# Investigating the Involvement of Astrocytic Functions in Brain Energy Homeostasis and Cognitive Behavior

---

Dissertation

zur

Erlangung der naturwissenschaftlichen Doktorwürde
(Dr. sc. nat.)

vorgelegt der

Mathematisch-naturwissenschaftlichen Fakultät

der

Universität Zürich

von

Ladina Hösli

von

Glarus-Süd GL

**Promotionskomission**

Prof. Dr. Bruno Weber (Vorsitz)
Prof. Dr. Hanns Ulrich Zeilhofer
Prof. Dr. Fritjof Helmchen

Zürich, 2020

# Abstract

The brain consumes immense amount of energy mainly obtained from glucose oxidation. Among the most energetically expensive processes in neurons is the recovery of ion gradients after activity. Mitochondrial respiration, fueling ATP to energy-demanding processes, is thought to be tightly regulated via homeostatic feedback loops involving adenine nucleotide pools or $Ca^{2+}$. Glial cells - and astrocytes in particular - are known to contribute to the regulation of neuronal functions and energy homeostasis. Astrocytes contain glycogen stores and are located between brain vasculature and neuronal compartments, therefore, perfectly positioned to bridge energy supply to local energy demand. Indeed, astrocytes are suggested to increase glycolysis and glycogenolysis to release lactate in response to neuronal activity to fuel neuronal metabolic needs. A potential route of glial lactate delivery to neurons is thought to occur via gap junction channels, that interconnect astrocytes to form large organized networks. Indeed, by decoupling astrocytes during brain development, functions including synaptic plasticity and cognitive abilities were attributed to the astroglial network.

However, it remains unclear, how neurons adjust their metabolic machinery when encountering changes in workload. Also, the mechanisms underlying a neuron-directed lactate release from astrocytes *in vivo* are still unknown, as is the role of the gap junction coupled network in the adult brain.

Here, we first elucidated how neuronal energy homeostasis is regulated during neurotransmission using fluorescence resonance energy transfer (FRET) sensors and ionic dyes *in vitro* and *in vivo*. We discovered a novel, hitherto unknown regulatory mechanism for mitochondrial ATP production in neurons directly involving the $Na^{+}$ pump. Next, by means of genetically-encoded lactate sensors and various arousal protocols, we demonstrate activity-dependent lactate release from astrocytes towards neurons in awake mice and reveal the contribution of astrocytic glycogen as a reservoir for acute lactate mobilization *in vivo*. Finally, we generated a new mouse model to study the role of the astrocytic network in the adult brain. We demonstrate the functional importance of the network for normal synaptic activity and for learning and memory.

# Acknowledgements

First l would like to express my thanks and appreciation to Bruno Weber for giving me the opportunity, means, space and time to pursue my research in his lab. I am also grateful to my committee meeting members Uli Zeilhofer and Fritjof Helmchen for kind support and inputs during the PhD.

I very much appreciated Jean-Marc Fritsch's generosity for letting me use his staining lab and antibodies, and for his accessible knowledge about immunohistochemistry. A big thank you goes also to Conny Schwerdel for always being on hand with help and advice, for professional organisation of the staining lab and for countless interesting conversations.

A big thank you goes to Felipe Barros, who enriched us with his visits from Chile and vivid discussions about fluxes and ion gradients. Thank you for making your knowledge available to us at any moment needed.

I would also like to thank Christian Giaume - who was so kind to introduce us to the world of connexins during his visits - for calm and interesting discussions.

Special thanks goes to Aiman Saab. Thank you for relentless scientific guidance, supervision and support. Your enthusiasm is contagious (almost pandemic) and you always had an open door and ear for my concerns. Zoe and Laeti, thank you for vivid discussions during our meetings, for scientific support and help, and for personal/emotional support.

I would also like to thank current and former teammates for scientific help and support – especially Matthias Wyss for always helping out and managing the lab, Noemi Binini for conducting ephys experiments and for organising the lab, Martin Holub for writing the mouse tracking software, Michael Stobart for help with qPCRs, and Luca Ravotto for endless efforts to improve data analysis. I am grateful to having met Stew, thanks for your help with the biocytin filling experiments, your enthusiasm for science and for life, and the fun day out cross-country skiing. You are missed. I am especially grateful for the friendship with Marc, Kim and Eva. I enjoyed spending time in and out of the lab with you. Thanks for many hours of experimental help, coffee drinking, running, listening, discussing, laughing and crying, that made these 6 PhD years so enjoyable! Also, special thanks to Kim and Marc for carefully reading my thesis and for helpful inputs.

I would also like to express my appreciation to the workshop - Stefan, Harald and Alex - for their expertise and good work; to the viral vector facility – Jean-Charles, Melanie, Jürg and Zsuzsanna – for providing us with infinite viral vectors; to Zvoni, for his boundless efforts in supporting the institute and who is always encountered with a smile; and to the animal caretakers for caring for our breedings. I am indebted to my friends and family for their support over all these years. First and foremost to my parents, for their love and kindness, their confidence and belief in me, and for their encouragement during stressful times. You made me who I am. Finally, I am very grateful to Philipp, for selfless support and critical advice. Thank you for being here, for listening, for the hug after a difficult day, for the glass of wine to celebrate achievements, and for making me feel home!

# Contents

# List of Figures

# List of Abbreviations

| | |
|---|---|
| **A/A** | astrocyte-to-astrocyte |
| **ADP** | adenosine diphosphate |
| **ALDH1L1** | aldehyde dehydrogenase 1 family member L1 |
| **AMP** | adenosine monophosphate |
| **ANLS** | astrocyte-neuron lactate shuttle |
| **A/O** | astrocyte-to-oligodendrocyte |
| **ATP** | adenosine triphosphate |
| **BBB** | blood-brain barrier |
| **cKO** | conditional knock out |
| **Cldn5** | Claudin5 |
| **CNS** | central nervous system |
| **Cx** | connexin |
| **dpi** | days post-injection |
| **ECS** | extracellular space |
| **EEG** | electroencephalography |
| **EMG** | electromyography |
| **fEPSP** | field excitatory postsynaptic potential |
| **FLIM** | fluorescence-lifetime imaging microscopy |
| **FRET** | fluorescence resonance energy transfer |
| **GABA** | $\gamma$-aminobutyric acid |
| **GFAP** | glial fibrillary acidic protein |
| **GFP** | green fluorescent protein |
| **GJ** | gap junction |
| **GLAST** | glutamate aspartate transporter |

| | |
|---|---|
| **GLT-1** | glutamate transporter 1 |
| **GLUT** | glucose transporter |
| **GYS1** | gylcogen synthase 1 |
| **hGFAP** | human glial fibrillary acidic protein |
| **KO** | knock out |
| **mEPSC** | miniature excitatory postsynaptic current |
| **mGFAP** | murine glial fibrillary acidic protein |
| **fEPSP** | field excitatory postsynaptic potential |
| **HR** | high range |
| **ISO** | isoflurane |
| **MAS** | malate-aspartate shuttle |
| **MCT** | monocarboxylate transporter |
| **O/O** | oligodendrocyte-to-oligodendrocyte |
| **STB** | short theta burst |
| **TCA** | tricarboxylic acid cycle |

# General Introduction

# 1

Intelligence, consciousness, the thinking mind. What do these terms describe? Where are they located? These questions have always fascinated mankind. While the old Egyptians thought of the heart as the seat of intelligence, the Greeks and Romans reseated intelligence and consciousness to the brain. Since then, the mysterious organ has been studied extensively. Ideas and concepts were formulated, overruled, reformed and discarded. However, modern neuroscience, the study of the nervous system, probably started with the formulation of the "neuron doctrine" by Santiago Ramón y Cajal (1852-1934), who used the famous silver-chromate staining technique to characterize the neuron as an individual functional unit of the brain. These neuronal working units were described to be embedded in a sort of "cement" or "glue". Later, the individual components of the "glue" were demonstrated to be astrocytes, oligodendrocytes and microglia. Their purpose and functions, however, remained unknown and underestimated for a long time after their discovery.

The following work will focus on the role of astrocytes in metabolic homeostasis. It will research the way neurons adapt to unforeseeable changes in workload and investigate the role of astrocytes in metabolic support of neurons. In addition the contributions of intercellular astroglial coupling - the astrocytic gap junction coupling - on normal brain function will be studied.

## 1.1 The Astrocyte - From Brain Glue to the Star of the Brain

The name astrocyte derives from the Greek words "astron"= *star* and "kytos" = *cavity* or *cell*. The word suitably describes the characteristic shape of this glial cell in the brain and spinal cord. In first descriptions, astrocytes were stated to be part of Nervenkitt (neuroglia; *nerve glue*), a term/concept first defined by Rudolph Virchow (1821-1902), who pictured it as some kind of connective tissue “glueing“ neurons together, rather than consisting of different cell types (Virchow, 1858). However, during following years, individual components of the *nerve glue* were described, such as the Bergmann glia in the cerebellum (Bergmann, 1857) or networks of stellate cells in the spinal cord (Henle and Merkel, 1869). Camillo Golgi (1843-1926) was then the first to demonstrate that glial cells are distinct from neurons (Golgi, 1870). Interestingly, he described a connection of the stellate cells with the vasculature that is nowadays known as *astrocytic end-feet* (Golgi, 1872). The discovery of astrocytic end-feet led to the formulation of a concept known as *glial metabolic support*, that is being discussed until this day. In 1893, Michael von Lenhossék (1863-1937) finally termed the stellate cells “astrocytes“ (Lenhossék, 1893). A year later Carl Ludwig Schleich (1859-1922) proposed that glia play a role in controlling neuronal excitability. He also presented the importance of neuron-glia interaction for normal brain function (Schleich, 1894). Refined versions of glial concepts formulated during this time are still valid today. A new era of experimental approaches, including chemical and electrophysiological techniques, began in the mid 20th century, leading to important functional attributions to glia. Hild and Tasaki, (1962) were the first ones to demonstrate that astrocytes have a distinct electrophysiological profile from neurons. Shortly after, it was demonstrated that unlike neurons, astrocytes do not fire action potentials, but “special low-resistance connections were found between glial cells“ (Kuffler and Potter, 1964). Several years later gap junctions were identified as the underlying molecular structures of the “low-resistance connections” (Brightman, 1969). Leif Hertz recognized the importance of astrocytes in potassium clearance during neuronal activity (Hertz, 1965), while Holger Hydén showed the effect of learning on RNA levels in neurons *and* glial cells (Hydén and Egyházi, 1963). He also postulated a biochemical and functional neuron-glia unit (Hydén, 1962). The perception of astrocytes was changed from mere Nervenkitt to a dynamic and functional unit by these pioneers. Nevertheless, neurons remained the active players in the central nervous system (CNS), while glial cells were thought to be their passive counterparts, playing a supportive role and providing the ideal environment for cell function.

Some years later and progressing to this day the classical view of the passive, supporting astrocyte has been changing to one of an active and vital player of the functioning brain. The finding that receptors for neurotransmitters (Bowman and Kimelberg, 1984) as well as voltage-gated channels (Bevan and Raff, 1985) are expressed by astrocytes opened up the possibility for astrocytes to be involved in intercellular communication. The concept of the tripartite synapse (Araque *et al.*, 1999) finally resulted from observations that astrocytes not only sense neurotransmitter release, but also react to it with calcium signaling and release of chemical transmitters, termed gliotransmitters (Cornell-Bell and Finkbeiner, 1991; Do *et al.*, 1997). By participating in the bidirectional communication of the three partners, pre-, postsynapse and astrocytic processes, astrocytes are located in a very powerful position to modify neuronal activity. It was shown that spontaneous activity in astrocytes leads to activation of nearby neurons (Parri *et al.*, 2001). Along this line, chemogenetic activation of astrocytes, but not neurons, enhances memory acquisition and specifically promotes memory allocation (Adamsky *et al.*, 2018).

Indeed, astrocytes in some way have become the stars of the brain, considerably involved in vital brain processes.

## 1.2 Astrocyte Physiology and Heterogeneity

> *What is the function of glial cells in neural centers? The answer is still not known, and the problem is even more serious because it may remain unsolved for many years to come until physiologists find direct methods to attack it.*
>
> Santiago Ramón y Cajal, 1911

As mentioned by Ramón y Cajal in 1911, resolving the functions of astrocytes requires cutting-edge science, hence, this section will first tackle quantity instead of quality.

A simple glia-to-neuron ratio in the brain should be a straightforward number to obtain. However, after 150 years of cell counting, literature unveils astrocyte-to-neuron ratios ranging from 1:1 to 50:1 (Bear *et al.*, 2007; Hilgetag and Barbas, 2009; Bartheld *et al.*, 2016) and the notion that astrocytes outnumber all other glial cells is widely spread in the field (e.g. Pekny and Pekna, 2014; Hu *et al.*, 2016, and many more). In the last decade several new approaches using various techniques tried to unravel the mystery. Only recently it was proposed that astrocytes account for 10-20% of total brain cells in the mouse (Sun *et al.*, 2017). Others report a (total) glia to neuron ratio of about 1 in the human brain and suggest that astrocytes account for 20% of all glial cells, while oligodendrocytes appear to be the most abundant glial cells (Azevedo *et al.*, 2009; Pelvig *et al.*, 2008). These new numbers differ drastically from the ones published decades ago and the question arises: What is the reason for the before-mentioned discrepancy in numbers?

*Astrocytic identity and heterogeneity* - a plain answer to a simple question. Hence, this section will introduce astrocyte morphology, molecular identity and function and will try to put morphological and molecular features in relation to functional differences.

### 1.2.1 The Morphological Characteristics of Astrocytes

One of the reasons for the astrocyte-to-neuron-ratio-problem might be that astrocytes differ from each other by a complex and fundamentally distinct morphology. This makes it difficult to correctly distinguish astrocytes from other glial cells by visual inspection. Nonetheless, the existing diversity in morphology provides an obvious possibility for classification. A few years back, astrocytes were categorized into nine subpopulations based on their appearance (Emsley and Macklis, 2006). In an ongoing process of knowledge acquisition, these subdivisions were recently refined (Verkhratsky and Nedergaard, 2018).
The classic subdivision of astrocytes into protoplasmic and fibrous astrocytes was defined by Andriezen, (1893), who was the first to describe that white and grey matter astrocytes morphologically differ from each other:

Protoplasmic astrocytes are found in grey matter regions of the CNS. They are defined by a small, round soma and highly arborized branches with thousands of smaller processes, characterized by a sponge-like morphology. Their individual architecture differs between and within brain regions (Bushong *et al.*, 2002; Emsley and Macklis, 2006). Protoplasmic astrocytes were shown to occupy specific, non-overlapping territories, connecting to each other at the tips of their fine processes via gap junction coupling. They contact between 4 and 6 neurons in their domain, covering between 20’000 and 120’000 synapses (Bushong *et al.*, 2002; Halassa *et al.*, 2007b).

Fibrous astrocytes are found in white matter regions of the CNS, where their somas align with axon bundles. In contrast to protoplasmic astrocytes, they have a lower degree of arborization, have an elongated morphology and overlapping territories. Characteristically, they extend their so called perinodal processes to the Nodes of Ranvier in myelinated tissue. Also within fibrous astrocytes a highly diverse morphology can be found.

Today, astrocytes are further subdivided taking into account for instance the location of residence or specialized functions of astrocytes, e.g. Bergamnn glia in the cerebellum, ependymocytes lining ventricles or pituicytes in the neurohypophysis. For further details on morphological characteristics defining astrocytic subpopulations, please refer to the study of Emsley and Macklis, 2006 and the review of Verkhratsky and Nedergaard, 2018.

### 1.2.2 The Molecular Identity of Astrocytes

The molecular identity of a cell provides another way of classification. In the case of neurons, marker genes expressed in the entire neuronal population or just in a subset, have long been identified. Unfortunately, nothing comparable and robust exists for astrocytes yet. A long-standing difficulty adding to the neuron-to-astrocyte-ratio-problem from the beginning is the lack of a specific marker covering the complete astrocyte population.

Nevertheless, some largely specific astrocytic markers include glial fibrillary acidic protein (GFAP), glycoprotein S100β, the glutamate transporters EAAT-1 (GLAST) and EAAT-2 (GLT-1), glutamine synthetase (GS) and the key enzyme of the folate metabolism, aldehyde dehydrogenase 1 family member L1 (ALDH1L1). Yet, all of these markers share one or all of the following disadvantages: (1) Only part of the astrocytic population is represented, (2) differences in developmental, regional and/or functional expression, (3) expression in a subpopulation of other cell types, such as oligodendrocytes or ependymal cells (Tansey *et al.*, 1991; Xin *et al.*, 2019; Perego *et al.*, 2002; Santos *et al.*, 2018). SOX9 is the most recent marker found to be almost exclusively expressed in astrocytes (Sun *et al.*, 2017). It is a transcription factor and therefore a nuclear marker, which is found in both mouse and human brain. It might be a good alternative to other markers, as long as the visualization of astrocytic processes is not required.

The comparison of transcriptomics data represents another technique to study molecular identity and cellular diversity. Most recent studies used RNA sequencing as a method to study astrocytic molecular expression and found substantial inter- and intra-regional differences among astrocytes (Chai *et al.*, 2017; Lin *et al.*, 2017; Morel *et al.*, 2017; Lanjakornsiripan *et al.*, 2018). These findings reinforce the long-neglected fact of astrocyte heterogeneity.

Subdividing astrocytes with the use of molecular markers long seemed a straightforward technique. However, a general difference between neuronal and astrocytic molecular expression might be that the molecular differences among astrocytes do not seem to be an all or none situation, but rather a graded expression of the same markers between subpopulations (Khakh and Deneen, 2019). One of the remaining open questions that has only started to be investigated in the last few years is how morphological and molecular traits might translate into functional identity and diversity.

### 1.2.3 Astrocyte Functions

Even though numerous functions have been attributed to astrocytes, for a long time they had remained a neurobiological mystery. This section will indulge in some of the most important astrocytic functions.

Even before the brain develops its full functionality, immature and mature astrocytes are involved early in development, for example in neuronal migration and axon guidance (Kawauchi *et al.*, 2010; Katz *et al.*, 1983). Important to note, is that various developmental functions are exerted via connexins (Cxs) (see section "Gap Junction Coupling" for introduction of Cxs) expressed by immature and mature astrocytes (Kawauchi *et al.*, 2010; Cina *et al.*, 2009; Elias *et al.*, 2007; Ghézali *et al.*, 2018; Kunze *et al.*, 2009; Lagos-Cabré *et al.*, 2019).
Perisynaptic astrocytic processes are in close proximity to synapses in the developing as well as in the adult brain (Montagnese *et al.*, 1988; Witcher *et al.*, 2010). Numerous groups demonstrated the importance of astrocytes in synaptogenesis (Allen and Barres, 2009; Eroglu and Barres, 2010; Pfrieger, 2010; Allen and Barres, 2005), as well as in synaptic activity and plasticity in general. This includes synaptic strengthening, stabilization (Nishida and Okabe, 2007; Theodosis *et al.*, 2008) and elimination (Stevens *et al.*, 2007) and can be influenced via at least three interconnected ways: (1) synaptic morphological rearrangements, (2) neurotransmitter synthesis and removal, (3) gliotransmission (Santello *et al.*, 2019). By determining the scale of astrocytic ensheathment of synapses, the vicinity of membrane proteins expressed by astrocytes (e.g. GLT-1 and GLAST) is adjusted. This changes the rate of glutamate removal from the synaptic cleft and determines the length and strength of synaptic activity (Araque *et al.*, 2014). Interestingly, Cx30 expression can influence the degree of astrocyte protrusion into the synaptic cleft (Pannasch *et al.*, 2014). Additionally, astrocytes regulate synaptic activity by releasing gliotransmitters, such as glutamate, D-Serine, adenosine triphosphate (ATP) or $\gamma$-aminobutyric acid (GABA) (Bezzi and Volterra, 2001; Halassa *et al.*, 2007a; Koizumi, 2010) via SNARE-dependent vesicular release (Lalo *et al.*, 2014; Min and Nevian, 2012; Schell *et al.*, 1995), hemichannels or pannexins (Iglesias *et al.*, 2009; Lee *et al.*, 2010).
Astrocytes not only interact with excitatory synapses, but are also involved in the regulation of inhibitory synapses. Hereby, astrocytes can fundamentally influence the excitation/inhibition balance in the brain (Mederos and Perea, 2019; Lee *et al.*, 2010). Astrocytes sense GABA release from neurons and express GABA

transporters for GABA reuptake during high interneuron activity (Boddum *et al.*, 2016). Additionally, they are the main extrasynaptic source for GABA that exerts tonic inhibition, representing an important control of cell excitability (Yoon and Lee, 2014), but interestingly astrocytes may also convert an inhibitory signal into an excitatory signal by releasing glutamate upon GABA activation (Perea *et al.*, 2016).

In addition to controlling extracellular neurotransmitter concentrations, astrocytes also regulate extracellular ionic homeostasis. The hyperpolarized resting state of astrocytes is mainly controlled by inwardly rectifying $K^+$ (Kir) channels (Seifert *et al.*, 2009), which allow for $K^+$ uptake released during synaptic activity (Seifert *et al.*, 2018). Activation of astrocytic GABA receptors leads to a depolarization of the membrane potential and to an efflux of $Cl^-$. If needed, astrocytes can sustain and modulate intense GABAergic firing, by regulating extracellular $Cl^-$ concentrations (Egawa *et al.*, 2013; Lia *et al.*, 2019).

On the one hand astrocytes ensheath synapses with perisynaptic processes, on the other hand they extend so called end-feet towards vasculature and tightly wrap around blood vessels. Here, they participate in the formation of the blood-brain barrier (BBB; Stewart and Wiley, 1981). Microvessels are almost completely covered by astrocytic end-feet (Mathiisen *et al.*, 2010). However, to what extent the astrocytic population participates in BBB formation and maintenance is unknown. Together with endothelial cells, pericytes, neurons and glial cells they form the neurovascular unit and are the main mediators between endothelial cells and neuronal tissue.

There are various astrocytic functions not listed here, two of which will be introduced in greater detail in the sections "Brain Energy Metabolism" and "Gap Junction Coupling".

In summary, astrocytes perform countless vital functions in the immature and mature brain. They can be seen as an extension of the processing capacity of a neuronal network, actively modulating neuronal excitability, synaptic activity, extracellular homeostasis and metabolic supply (see following section "Brain Energy Metabolism"). However, the general validity of functions among astrocytes is still matter of investigation. Alterations in astrocyte morphology are correlated with functional modifications (Sun and Jakobs, 2012), and divergences in molecular identity mirror functional differences (Chai *et al.*, 2017; Lanjakornsiripan *et al.*, 2018; Lin *et al.*, 2017; Morel *et al.*, 2017). In addition, research suggests that functional differences in astrocytes are partly the result of plastic adaptations to specific microenvironments and changing requirements (Stogsdill *et al.*, 2017;

Hasel *et al.*, 2017; Farmer *et al.*, 2016). This is to be kept in mind when modifying this tightly regulated neuron-glia system, because the result will be an adaptation to the modification.

## 1.3 Brain Energy Metabolism

Brain energy metabolism is characterized by two peculiarities specific to the brain. One is the extraordinary amount of energy consumption compared to other organs and the other is the local, activity-dependent energy demand (Barros *et al.*, 2018).

Even though the brain makes up only 2% of the total body weight it uses 20% of all glucose, its primary but not its sole energy source (Kety, 1957). The major part of brain energy consumption is ascribable to the activity of plasma membrane ion pumps and postsynaptic receptors (Barros *et al.*, 2018). For a long time neurons were thought to be the primary source of energy expenditure. However, after discovering that astrocytes react to neurotransmitters and increased extracellular $K^+$ concentrations with energetically expensive membrane depolarization and intracellular signaling pathways (Amédée *et al.*, 1997; Kettenmann *et al.*, 1984; Rose and Karus, 2013), it was generally recognized that astrocytes, and likewise other glia, also contribute to energy consumption of the brain. The extent of glial contribution to the high energy expenditure of the brain still remains to be clarified. Nevertheless, glial cells are not energetically inert, as long assumed, and therefore play an important role in brain energy metabolism (Barros *et al.*, 2018).

In the following, some of the energetically most expensive processes in neurons, as well as the intracellular regulation of energy supply will be discussed. Further, the contribution of astroyctes and astrocytic glycogen to neuronal metabolic support will be evaluated.

### 1.3.1 Energy Sinks and Sources in the Synapse

The basal unit for computational power in the brain is the synapse. Synaptic transmission is the energetically most costly process in the brain (Harris *et al.*, 2012). In general, presynaptic mechanisms are thought to be energetically more affordable compared to postsynaptic processes. Figure 1.1 summarises the major energy expending processes in the pre- and postsynapse. Most of the ATP consumed in the presynapse is due to activity of the following pumps (1) the $Na^+/K^+$-ATPase, that rebalances intracellular $Na^+$ concentrations after arrival of an action potential and generates a favorable $Na^+$ gradient for the $Na^+/Ca^{2+}$ exchanger to extrude $Ca^{2+}$; (2) the $Ca^{2+}$-ATPase, that keeps cytosolic $Ca^{2+}$ concentrations low by deporting it to the extracellular space or by storing it in the endoplasmatic reticulum; (3) vacuolar $H^+$-ATPase, that establishes an electrochemical gradient to drive neurotransmitter uptake into vesicles and (4) motor proteins, that transport vesicles and mitochondria. In the postsynapse, the extrusion of ions entered through postsynaptic receptors are the main workload of the $Na^+/K^+$-ATPase and the $Ca^{2+}$-ATPase. In astrocytes ATP is mainly used by the $Na^+/K^+$-ATPase to maintain the resting potential and to eject $Na^+$ that was cotransported with the uptake of glutamate. Additionally, the conversion of glutamate to glutamine is also a cost-intensive process.

In neurons it is suggested that the majority of ATP supplied to synapses is generated by oxidative phosphorylation in mitochondria (Sokoloff, 1960; Harris *et al.*, 2012). However, opposing views argue that local glycolysis plays an important role in fueling synapses. The arguments for glycolysis include synpatic glucose transporter (GLUT) type 4 incorporation and relocation of glycolytic enzymes to the synapse under conditions of energy stress (Ashrafi *et al.*, 2017; Jang *et al.*, 2016).

ATP supply from mitochondria residing in synaptic boutons are regulated according to energy needs. Until recently it has been postulated that short-term regulation of mitochondrial respiration is mediated via two ways: ATP/ADP homeostasis and intracellular $Ca^{2+}$ levels. By the law of mass action, ATP formation by mitochondrial respiration would be encouraged as the ATP/ADP ratio decreases due to ATP consumption by processes depicted in figure 1.1 (Chance and Williams, 1955). In this homeostatic feedback-loop adenosine diphosphate (ADP) would be the regulating molecule (Brand and Nicholls, 2011). Increases in intracellular $Ca^{2+}$, that occur in the pre- and in the postsynapse during synaptic transmission, have also been implicated in regulating oxidative phosphorylation (Chouhan *et al.*, 2012; Glancy and Balaban, 2012). Intramitochondrial $Ca^{2+}$ rises promote tricarboxylic acid cycle (TCA) activity and, subsequently, mitochondrial respiration (Duchen, 1992; Duchen *et al.*, 2008). Cytosolic $Ca^{2+}$ rises, on the other hand, activate mitochondrial aspartate-glutamate exchanger aralar (Gellerich *et al.*, 2009) that directly links cytosolic $Ca^{2+}$ to mitochondrial ATP snythesis. However, this dogma was lately challenged by Baeza-Lehnert *et al.*, 2019, suggesting a

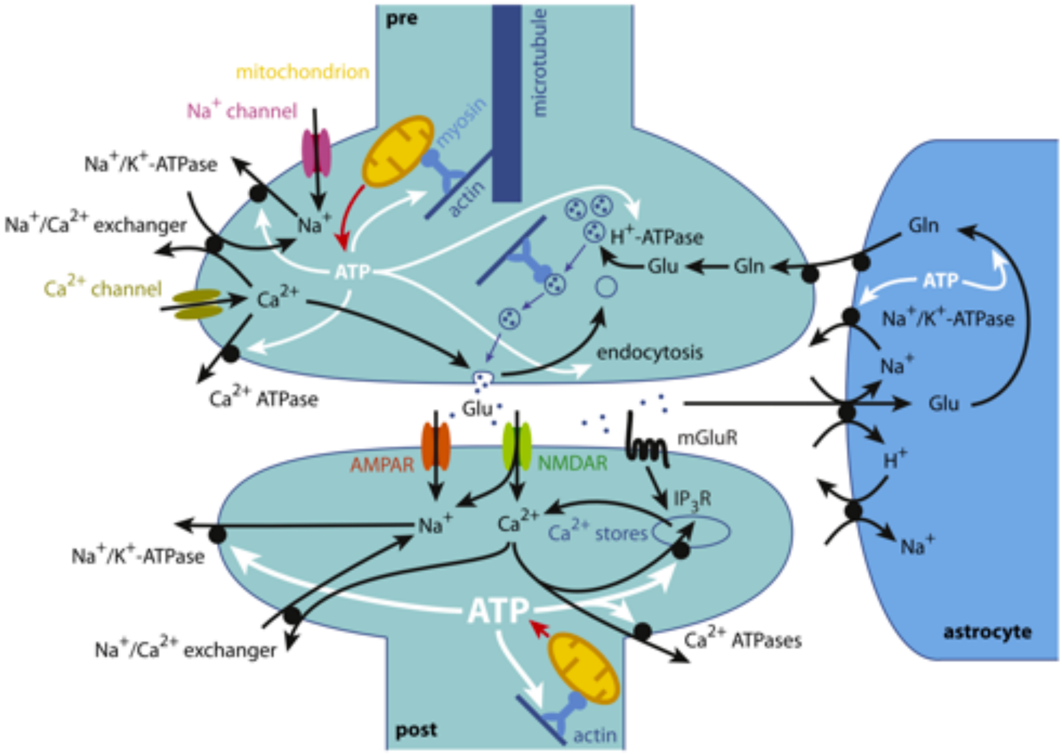

Figure 1.1.: **Summary of Energy-Requiring Processes in an Excitatory Synapse** ATP is required presynaptically and postsynaptically for reestablishment of ionic homeostasis after synaptic transmission. The postsynpase is thought to consume more energy compared to the presynapse, shown by thicker arrows. The main ATPases hydrolising ATP are the Na$^+$/K$^+$-ATPase, the Ca$^{2+}$-ATPase and the H$^+$-ATPase. Additionally, the transport machinery (kinesin, dynein, myosin) breaks down ATP. In astrocytes the conversion of glutamate to glutamine is also energy dependent. Figure taken from Harris *et al.*, 2012. Reuse License Number: 1046783-1.

novel mechanism for short-term regulation of oxidative phosphorylation (see chapter 3).

### 1.3.2 Astrocytes - Energy Suppliers?

Residing between brain vasculature and neuronal synapses, astrocytes are perfectly located to bridge energy supply to local brain activity. Astrocytic end-feet, which tightly enwrap blood vessels, are thought to be key players in functional hyperemia – the local increase of blood flow in response to elevated neuronal activity. The astrocytic release of prostaglandin E2 and other factors thereafter leads to a vasoconstriction or vasodilation (Attwell *et al.*, 2010; Gordon *et al.*, 2008). Additionally, end-feet express GLUT1 enabling the import of glucose

(Simpson *et al.*, 2007). Once inside astrocytes (or any other cell), glucose is phosphorylated to glucose-6-phosphate by hexokinase and can then be metabolized via different pathways: (1) glycolysis catalyzing pyruvate and/or lactate, (2) the pentose phosphate pathway generating reducing equivalents, such as NADPH and (3) glycogenesis producing glycogen – the storage form of glucose. Interestingly, neurons and astrocytes both have the capacity to metabolize glucose through all three pathways. However, they have different (but complementary) metabolic profiles and live in tight metabolic cooperation (Bélanger *et al.*, 2011). Astrocytes are keen glucose uptakers and are thought to be highly glycolytic cells, favoring the production and release of lactate over the shuttling of pyruvate to mitochondria for oxidative phosphorylation (see Baeza-Lehnert *et al.*, 2019, chapter 3). On the other hand neurons appear to be highly oxidative cells with the preference to process glucose through the pentose phosphate pathway to produce enough reducing equivalents. These are needed to scavenge reactive oxygen species, a byproduct of the high oxidative activity in neurons (Magistretti and Allaman, 2015). This labor division inevitably implies a shuttling of lactate from astrocytes to neurons (see figure 1.2; and see Zuend *et al.*, 2020, chapter 4). The mechanistic link between neuronal activity and glial energy metabolism is glutamate, whose synaptic action is terminated by energetically costly cellular uptake mainly by astrocytes (Danbolt *et al.*, 2016). This energetic burden is mainly due to the cotransport of glutamate with 3 $Na^+$, which triggers the activity of the $Na^+/K^+$-ATPase to reestablish the ionic gradient (Stobart and Anderson, 2013). Indeed, the mechanism known as astrocyte-neuron lactate shuttle (ANLS) describes a glutamate-stimulated increase of glucose uptake and its processing into lactate in astrocytes, which can then be released to fuel neurons (Magistretti, 2006; Pellerin and Magistretti, 1994, see also figure 1.2). Since the postulation of the ANLS considerable support for the lactate shuttling from astrocytes to neurons was published (Duran *et al.*, 2013; Gibbs *et al.*, 2006; Suzuki *et al.*, 2011; Wyss *et al.*, 2011; Zuend *et al.*, 2020; Mächler *et al.*, 2016), including work showing a decreasing lactate gradient starting from astrocytes to the extracellular space to neurons *in vivo* (Mächler *et al.*, 2016), and activity-dependent lactate release form astrocytes *in vivo* (Zuend *et al.*, 2020, see also chapter 4). Intriguingly, Volkenhoff *et al.*, (2015) demonstrate that glycolysis in glia is vital in *Drosophila*. Disrupting glycolysis in glia, but not in neurons, led to severe neurodegeneration, implying critical contribution of glial glycolysis for neuronal survival. However, the ANLS is highly debated (Bak and Walls, 2018; Dienel, 2017) and the truth may lie somewhere in the middle, with neurons consuming glucose as well as lactate (Baeza-Lehnert *et al.*, 2019, see also chapter 3).

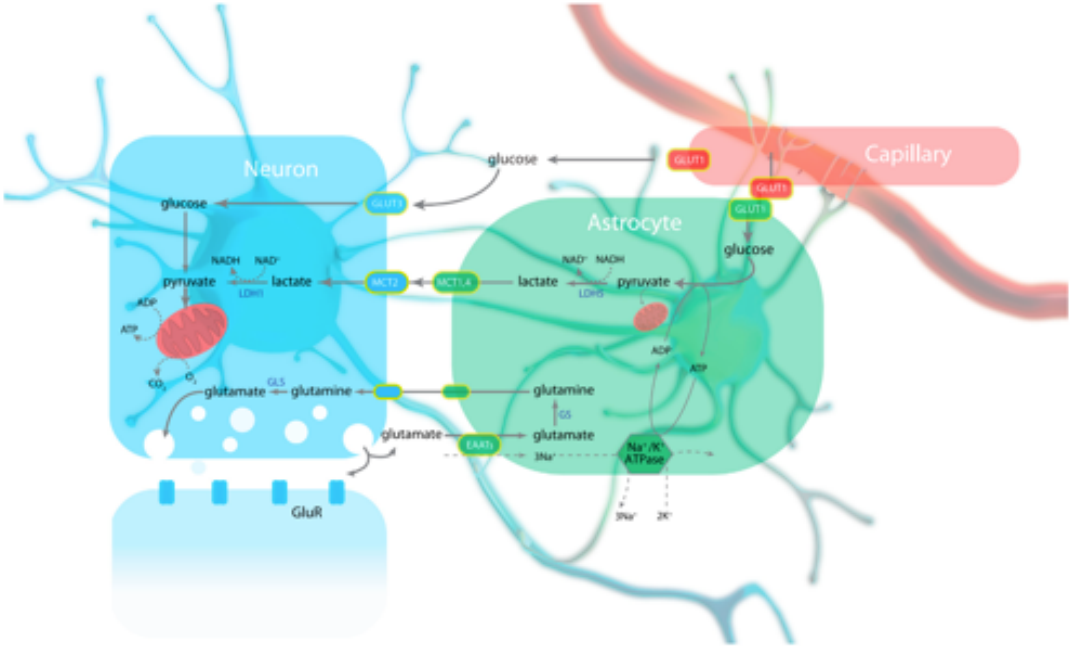

**Figure 1.2.: The Astrocyte-Neuron Lactate Shuttle**
Glutamate released at an excitatory synapse activates postsynaptic glutamate receptors (GluR) and is taken up by astrocyte perisynaptic processes via excitatory amino acid transporters (EAATs). Along with glutamate 3 $Na^+$ are cotransported, which activates the $Na^+/K^+$-ATPase to reestablish the disrupted $Na^+$ homeostasis. This is an energetically expensive process. Concurrantly, glutamate is transformed to glutamine (also an ATP-consuming process), which is then recycled back to neurons for vesicle filling, after reconversion to glutamate. This is the so called glutamate-glutamine cycle. Glutamate-induced ATP deficit in astrocytes leads to an increased glucose uptake via GLUT, and to accelerated glycolysis that produces pyruvate. After conversion of pyruvate to lactate, it is shuttled to neurons via monocarboxylate transporter (MCT) 4 and MCT2, where it is reconverted to pyruvate to enter oxidative phosphorylation in mitochondria for ATP production. Neurons express GLUT3 that enables neuronal glucose uptake. GS glutamine synthetase, GLS glutaminases, LDH5 lactate dehydrogenase 5, LHD1 lactate dehydrogenase 1. Figure taken from Magistretti and Allaman, 2015, Reuse License Number: 4854221063789

Under certain conditions the brain is able to use alternative metabolites for energy production. The major part of glutamate is converted into glutamine and then recycled back to neurons for replenishment of the glutamate vesicles. This cycle is also known as glutamate-glutamine cycle (Waagepetersen *et al.*, 2008; Schousboe *et al.*, 2013). However, astrocytes can use excess glutamate for ATP generation by converting it to $\alpha$-ketoglutarate and then processing it in the TCA cycle (Bak *et al.*, 2006; McKenna, 2007). Additionally, liver-derived ketone bodies (e.g. $\beta$-hydroxybutyrate, acetone, acetoacetate) transported into the brain via monocarboxylate transporters (MCTs) can be metabolized by neurons and glia.

This alternative energy source is mainly used during suckling in newborns, brain maturation in young children or under caloric restriction (Achanta *et al.*, 2017; Schönfeld and Reiser, 2017). Interestingly, and in contrast to other organs with high energy expenditure, the brain only poorly uses long-chain fatty acids (C14:0 – C18:0) for β-oxidation. However, the degree of β-oxidation in the brain seems to be a matter of debate, with some scientists showing evidence for the capacity of mitochondrial β-oxidation and others against (Attwell and Laughlin, 2001; Panov *et al.*, 2014; Sayre *et al.*, 2017; Speijer, 2011).

### 1.3.3 Glycogen - The Energy Store in Astrocytes

Glycogen – a macromolecule consisting of numerous glucose molecules – is the storage form of glucose and largely present in liver hepatocytes and skeletal muscle myocytes (Berg *et al.*, 2002). The liver regulates systemic glucose levels by glycogen degradation and release of glucose into blood circulation, while muscle glycogen represents a more local energy reservoir (Berg *et al.*, 2002). Glycogen content in the brain is vanishingly low compared to the amounts stored in liver and musculature, which might be the reason for its long-lived neglect (Brown and Ransom, 2007). The topic of glycogen metabolism in the brain gained interest from the moment that neuronal activity was linked to glycogen degradation (glycogenolysis; Swanson *et al.*, 1992; Magistretti *et al.*, 1981).

Brain glycogen is mainly stored in astrocytes and shows a patchy and age-dependent distribution throughout the brain. Highest amounts are found in hippocampus, striatum, cortex and cerebellar molecular layer and seem to decline with aging (Oe *et al.*, 2016). Glycogenolysis shares most of the intermediate steps and enzymes with glycolysis, including the starting molecule glucose-6-phosphate and the end product pyruvate (or lactate). Glucose-6-phosphate is either directly metabolized through glycolysis or is added to glycogen via the intermediate glucose-1-phosphate. During glycogenolysis glucose-1-phosphate is again recovered and reconverted to glucose-6-phosphate for lactate production (Wiesinger *et al.*, 1997). This degradation of glucose via its temporary incorporation into glycogen is referred to as the glycogen shunt (Shulman *et al.*, 2001). Importantly, even though similar pathways are involved in pyruvate/lactate production by glycolysis and glycogenolysis, they proceed compartmentalized without intermixture of the respective intermediates. This results in two separate lactate pools that cannot deputize for each other (Sickmann *et al.*, 2005). *In vivo* evidence for this hypothesis derives from memory impairments in chicks and rats after disruption of glycogenolysis that cannot be rescued by glucose supply (Gibbs *et al.*, 2006; Suzuki *et al.*, 2011). It is specifically the glycogen-derived lactate released by astrocytes that is implicated in memory formation (Alberini *et al.*, 2018). Studies in mice with brainwide deletion of gylcogen synthase 1 (GYS1), the enzyme generating glycogen, further confirmed the importance of glycogen in memory formation (Duran *et al.*, 2013). Using GYS1 knock out (KO) mice, Zuend *et al.*, (2020) also show that glycogen-derived lactate contributes to lactate surges in neurons and astrocytes during arousal (see chapter 4). Additionally, glycogenolysis is thought to also be required for glutamate and GABA de novo synthesis by astrocytes. These two neurotransmitters play a crucial role for brain plasticity, such as learning and memory (Gibbs *et al.*, 2006; Hertz and Chen, 2018).

To summarize, synaptic transmission is the most cost-intensive process in the brain. It is mainly fueled by neuronal oxidative phosphorylation. However, pyruvate entering mitochondrial respiration can be of neuronal or astrocytic origin. The ANLS describes the lactate release by astrocytes in response to neuronal activity to ensure adequate energy supply to neurons. Astrocyte-derived lactate is then converted into pyruvate in neurons and fed into mitochondrial respiration. The existence of two independent astrocytic lactate pools is suggested, one derived from glucose directly and the other metabolized from glycogen. Astrocytic lactate is implicated in the modulation of typical neuronal features, including excitability and plasticity. However, specifically the glycogen-derived lactate is implicated in learning and memory.

## 1.4 Gap Junction Coupling

Another typical feature of astrocytes is their intercellular communication by direct cell-to-cell connections. This is provided by gap junctions (GJs) and is not only a characteristic of astrocytes, but of many tissues in the body, such as the epithelial cells of the gastrointestinal tract or the myocardial cells in the heart (Bosco *et al.*, 2011). A GJ channel formed between two neighboring cells consists of two opposing connexons (hemichannels), which themselves are assembled from six Cxs (see figure 1.3). Together these elements build the basis for astrocytic GJ communication and the so called panglial syncytium, known to connect glial cells (Theis and Giaume, 2012; Wasseff and Scherer, 2011). The following section will explore the individual components involved in glial GJ communication and its functions.

### 1.4.1 Connexins – The smallest Entity of Gap Junctions

There are 21 Cx members in the human genome and 20 in the mouse genome, which differ in their molecular mass between 26 and 62kDa. Their nomenclature derives from these mass differences e.g. Cx26, Cx30, Cx43 etc. (Söhl and Willecke, 2004). There is a variety of different types of Cxs expressed in the brain, offering a variety of possible combinations: Hemichannels can assemble into homo- or heteromers, depending on whether one or several Cx types are involved. GJs can be homotypic or heterotypic, depending on whether the identity of the opposing hemichannels is identical or not (see figure 1.3). Additionally, GJs can connect the same (homocellular) or different (heterocellular) cell types as well as connect parts of the same cell (reflexive GJs) (Wolff *et al.*, 1998). So far, only *in vitro* data describes the existence of heteromeric hemichannels and GJs, but whether these combinations are also functional *in vivo* is not known.

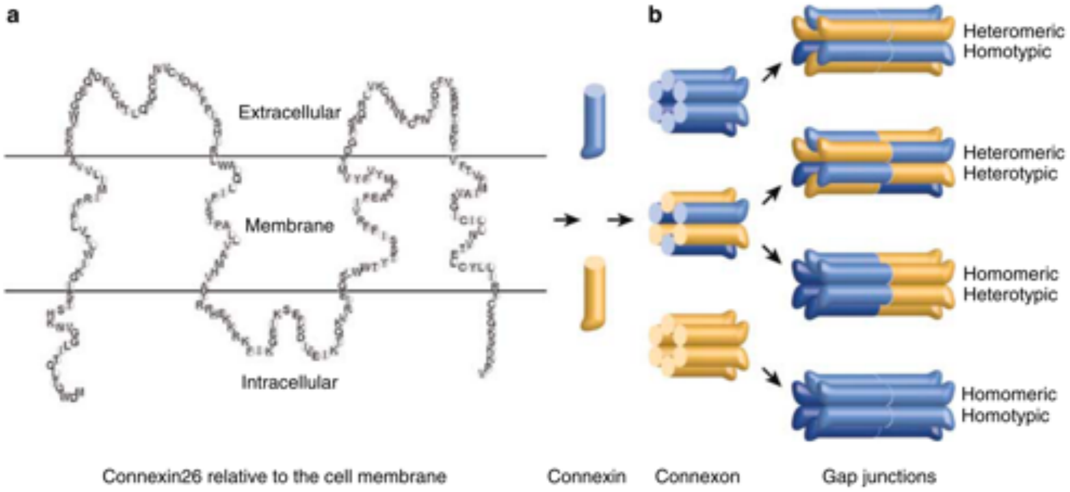

**Figure 1.3.: Schematic Structure and Composition of Cxs, Connexons and GJ Channels**
Cx26 is represented as an example. (a) Cxs have four transmebrane domains. The N- and C-terminus are positioned intracellularly. (b) A connexon (hemichannel) is formed by a hexameric ring of Cxs. Two opposing hemichannels form a gap junction channel. Depending on their composition they are called homo- or heteromeric and homo- or heterotypic. Figure taken from Mese et al, 2007. Reuse License Number: 1043898-1

### 1.4.2 Gap Junctions - Connecting The Syncytium

Glial cells express several types of Cxs, however, each glial cell type expresses its own specific set of Cxs, e.g. astrocytes mainly express Cx30 and Cx43, while oligodendrocytes express mainly Cx32 and Cx47 (Giaume and Liu, 2012). Due to this vast expression of Cxs among glial cells, the concept of a panglial syncytium, interconnecting astrocytes, oligodendrocytes and ependymocytes, was proposed (Mugnaini, 1986). As astrocytes show the highest level of Cx expression and a very high degree of astrocyte-to-astrocyte (A/A) interconnection, they were thought to serve as "mediators" in this panglial syncytium, connecting glial cells to each other via A/A coupling (Giaume and Liu, 2012). This may be true for grey matter, where studies failed to detect direct oligodendrocyte-to-oligodendrocyte (O/O) coupling (Mugnaini, 1986; Rash *et al.*, 2001), but astrocyte-to-oligodendrocyte (A/O) coupling was found to be present in several brain regions. Experiments in recent years demonstrated A/O coupling in the hippocampus, cortex and thalamus (Griemsmann *et al.*, 2015; Tanti *et al.*, 2019; Wasseff and Scherer, 2011; Claus *et al.*, 2018). Interestingly, there seem to be differences in the network size, identity of coupled cells and Cxs involved in the syncytium in these different brain regions (Griemsmann *et al.*, 2015). For instance, while astrocytes in the hippocampus express both Cx30 and Cx43, the thalamus is almost devoid of Cx43. This changes the network's composition from mainly astrocytic participation in the hippocampus, to a mix of astrocytes and oligodendrocytes in the thalamus. Thus, not only astrocytes themselves are heterogeneous, but also the panglial network structure shows differences between brain regions.

In white matter tracts, such as the corpus callosum, researchers seem to agree on the presence of an O/O network, that also includes A/O and A/A coupling (Wasseff and Scherer, 2011; Maglione *et al.*, 2010; Meyer *et al.*, 2018). This puts oligodendrocytes on equal footing as astrocytes regarding the coupling in the panglial syncytium.

There are multiple ways to regulate permeability, shape and size of a panglial syncytium: (1) The different Cx types can be selective for the passage of several molecules or ions. This not only depends on the molecule's size, but also its shape, charge and specific interactions with the Cxs in the channel (Giaume and Liu, 2012). Recently, a directional coupling between heterotypic channels formed by Cx47 and Cx43 was observed, with movement of ions and molecules from cells expressing Cx47 to cells expressing Cx43 (Fasciani *et al.*, 2018). Given that

Cx type expression is not homogeneous between and even within brain regions, the extent of GJ coupling can be well defined by controlling Cx type expression (Giaume *et al.*, 2010; Griemsmann *et al.*, 2015). (2) GJ communication can be modified posttranslationally by e.g. phosphorylation, which can regulate several Cx processes, including trafficking, assembly/disassembly or gating of GJ channels (Lampe and Lau, 2000). This allows for important adaptations to changes in the environment. (3) The size of the network can be limited by neuronal functional units, such as the barrel cortex in the somatosensory cortex or the barreloids in the thalamus, where the boarders of the A/O syncytium are mainly formed by weakly coupled oligodendrocytes (Claus *et al.*, 2018; Houades *et al.*, 2008). (4) Additionally, the GJ network in these units can be modulated in shape and size by neuronal activity (Claus *et al.*, 2018; Roux *et al.*, 2011). This not only applies for glial networks in confined anatomical structures, but was also observed in the hippocampus, where the astroglial network was shown to extend towards the site of increased neuronal activity (Rouach *et al.*, 2008). (5) Surrounding cells other than neurons can also alter GJ channel activity by releasing cell adhesion molecules, cytokines, endogenous lipids or peptides (Giaume and Liu, 2012). During inflammatory processes for example, astrocytes react to proinflammatory cytokines released by microglia by reducing Cx43 expression and GJ coupling (Bolaños and Medina, 1996; Karpuk *et al.*, 2011; Retamal *et al.*, 2007), while increasing hemichannel activity.

In summary, permeability, shape and size of the panglial syncytium seem to be unique depending on the brain region or the neuronal networks surrounding it. It can be regulated according to the brain's needs and can adapt to changing conditions.

### 1.4.3 The Syncytium – Connecting the Single Cell to a Coordinated Network

This section will mainly focus on the functions of the GJ coupled network in grey matter and, thus, will mainly mention astrocytes and the astrocytic network. The reason why the functions of the GJ coupled network in grey matter is mainly attributed to an astrocytic network is, that there was awareness of the high degree of A/A connections, while oligodendrocytes were only recently found to also be part of this complex network (see previous subsection 1.4.2). Many studies started from the premise that the glial network in grey matter areas mainly exists of A/A connections and neglected oligodendrocytes. Certainly, this does not imply that oligodendrocytes do not contribute to the functions of the network, it is just not known how and to what extent.

Unlike neurons that usually share overlapping dendritic fields, protoplasmic astrocytes occupy their own territory and, thus, depend on a fast, direct way of communication. Obviously, this is what GJ channels provide: the intercellular passage of ions, amino acid, glucose, lactate, ATP and small signaling molecules (Giaume *et al.*, 2010). The shape and degree of GJ communication can be modified and regulated by neuronal activity. An increase in extracellular $K^+$ can increase astrocytic dye coupling (Kristian Enkvist and McCarthy, 2002) and glutamate release increases glucose transport in the astrocytic network (Rouach *et al.*, 2008). However, as already mentioned previously (see subsection "Astrocyte Functions"), astrocytes can react to neuronal activity with elevated intracellular $Ca^{2+}$, which triggers gliotransmission. Importantly, this is not only the case on a single-astrocyte-level. The whole astrocytic network associated with a neuronal functional unit could act and react in synch and, hence, could affect neuronal network activity (Giaume *et al.*, 2010). Indeed, a recent study indicated that the astroglial network coordinates neuronal population bursts in the hippocampus (Chever *et al.*, 2016). In addition, Adamsky *et al.*, (2018) indicate that specific astrocytic activation results in memory enhancement by allocating neurons to the engram, leading to the formation of a neuronal ensemble in a task-specific way. GJ coupling is also implicated in complex behaviours, like learning and memory. Indeed, mice lacking Cx30 and Cx43, from development or deleted during adulthood, show impairments in spatial learning and memory (Lutz *et al.*, 2009; and see chapter 5).

During neuronal activity extracellular $K^+$ and glutamate concentrations can rapidly increase and astrocytes are crucial for the clearing of $K^+$ and glutamate. The functional interaction of two mechanisms during neuronal activity is required to balance extracellular $K^+$ concentrations: $K^+$ uptake and spatial $K^+$ buffering. A requirement for $K^+$ buffering is the extensive GJ coupling, that allows the astrocytes to redistribute $K^+$ from locations of high concentrations to sites of low extracellular concentrations (Kofuji and Newman, 2004). A recent paper suggests that GJ coupling enables electrical coupling of astrocytes and allows them to quickly equilibrate differences in membrane potential, which results in syncytial isopotentiality (Ma *et al.*, 2016). As a consequence, extracellular $K^+$-induced local membrane potential depolarization is immediately equilibrated in the astrocytic network, sustaining $K^+$ uptake and thereby making $K^+$ clearance more efficient. Most studies have investigated the role of astrocytes and glial GJ coupling on excitatory neurotransmission. However, astrocytes are also involved in GABAergic signaling and regulation of extracellular $Cl^-$ concentrations (Mederos and Perea, 2019; Yoon and Lee, 2014; Egawa *et al.*, 2013; Lia *et al.*, 2019; see also subsection "Astrocyte Functions"). Accordingly, astrocytic GJ coupling seems to be essential for extracellular $Cl^-$ buffering (Egawa *et al.*, 2013). With the ability to buffer ions relevant for excitation and inhibition, as well as to release excitatory and inhibitory transmitters, astrocytic GJ coupling may play a crucial role in the excitation/inhibition balance (Markram *et al.*, 2004; Mederos and Perea, 2019). As already mentioned earlier, processing of information is metabolically expensive and astrocytes are known for their function as energy suppliers. A working model for metabolic support is the ANLS (Pellerin and Magistretti, 1994). There is evidence that astrocytic metabolic support to neurons not only occurs on a single cell level, but also on the network level. However, whether every astrocyte maintains its own vascular connection for metabolite uptake or whether some astrocytes entirely rely on distribution by the network is a matter of investigation (see Preview, chapter 6). Nevertheless, extracellular glutamate appears to generate intercellular $Na^+$ and metabolic waves in the astrocytic network, leading to a concerted increase in glucose uptake (Bernardinelli *et al.*, 2004). In addition, glucose diffusion through the network seems to be increased after neuronal glutamate release (Rouach *et al.*, 2008). Data from the lateral hypothalamic area also confirm that the astrocytic network is crucial for metabolic support of the wake-promoting orexin neurons. Orexin neurons were silenced upon astrocytic decoupling, leading to disturbances of the sleep/wake cycle (Clasadonte *et al.*, 2017). GJ coupling is not only important for metabolic support in grey matter but is also crucial in white matter tracts. Due to the close proximity of myelinating oligodendrocytes to axons, oligodendrocytes play a vital role in metabolic support of axons (Fünfschilling *et al.*, 2012; Lee *et al.*, 2012; Saab *et al.*, 2013), as recently also illustrated in the corpus callosum (Meyer *et al.*, 2018).

### 1.4.4 Hemichannels – The Connection to The Extracellular Space

Cxs are not only the basis of GJ channel communication, but they also form hemichannels that allow for an exchange of ions and signaling molecules with the extracellular space. In this sense, they are a means for autocrine and paracrine communication and may play a role in gliotransmission (Giaume *et al.*, 2013).

Next to GJ coupling, also hemichannels can be modified by signaling molecules, such as pro-inflammatory cytokines (Retamal *et al.*, 2007). Similarly to GJ channels, also hemichannels play a role in $Ca^{2+}$ wave propagation (Arcuino *et al.*, 2002). Many contradictory results obtained by altering Cx expression could be explained by their dual function as gap junctions channels and as hemichannels (Orellana *et al.*, 2009). In contrary to GJ channels, which are widely accepted to be indispensable for proper brain function, the function of hemichannels is less clear (Nielsen *et al.*, 2017). This discrepancies might arise from the fact that it is extraordinarily challenging to distinguish GJ channel functions from those of hemichannels. Neither pharmacological inhibitors, nor antibodies or genetic manipulations of Cxs target only hemichannels without affecting GJ coupling or other membrane transport mechanisms (Nielsen *et al.*, 2017).

To summarize, astrocytic (or in general glial) GJ coupling clearly plays a crucial role in brain homeostasis, neuronal function and natural behavior (see also chapter 5). Many functions attributed to single astrocytes equally apply to the glial network and vice versa. As astrocytes, the network also appears to be very heterogeneous and plastic, adapting to the needs of the surrounding tissue. Moreover, the extent of GJ coupling varies in different brain regions and even adjusts to neuronal functional units. Due to the before mentioned astroplasticity, astrocytes will likely react to any changes exerted on the system, which makes it very challenging to investigate astrocytes and the glial syncytium. Nevertheless, this is a very intriguing topic and this work tries to contribute some information on the roles of astrocytic gap junction coupled networks for neuronal function.

# 2

# Aims

The first aim of this thesis was to better understand the basic regulatory mechanisms of neuronal energy homeostasis. Then neuron-astrocyte metabolic coupling in form of lactate release from astrocytes to neurons was investigated *in vivo*. Finally the importance of an intact astrocytic network for neuronal functions was studied.

- **Article 1** (see chapter 3) aimed at understanding the balance and regulation of ATP consumption and production. Using FRET sensors and ion-sensitive dyes *in vitro* and *in vivo* the $Na^+$ pump was discovered as a novel direct regulator of mitochondrial respiration. These findings challenge the dogmatic view on the mechanistic control by adenine nucleotides and $Ca^{2+}$.

- **Article 2** (see chapter 4) investigated mechanisms involved in astrocytic lactate release in dependence of neuronal activity *in vivo*. By means of genetically encoded sensors and two-photon microscopy astrocytic and neuronal lactate dynamics were studied during a state of arousal. In addition the dependence of the lactate surge on β-adrenergic signaling and glycogen stores was examined.

- **Article 3** (see chapter 5) aimed at exploring astrocytic network functions in the adult brain. We generated and characterized a new mouse model that circumvents developmental perturbations by decoupling the astrocytic network in the mature brain. We demonstrate the importance of astrocyte gap junction coupling in modulating neuronal activity and its impact on cognitive functions.

# 3

# Non-Canonical Control of Neuronal Energy Status by the $Na^+$ Pump

Originally published in Cell Metabolism (2019) 29(3), pp. 668-680.e4
DOI 10.1016/j.cmet.2018.11.005

## Authors and Affiliations

Felipe Baeza-Lehnert [1], Aiman S Saab [2], Valeria Larenas [3], Esteban Díaz [1], Melanie Horn [3], Ladina Hösli [2], Jillian Stobart [2], Johannes Hirrlinger [4], Bruno Weber [2] and L Felipe Barros [5]

[1]Centro de Estudios Científicos (CECs), Casilla 1469, 5110466 Valdivia, Chile; Universidad Austral de Chile, Valdivia, Chile
[2]Institute of Pharmacology and Toxicology, University and ETH Zurich, Switzerland; Neuroscience Center Zurich, Zurich, Switzerland
[3]Centro de Estudios Científicos (CECs), Casilla 1469, 5110466 Valdivia, Chile
[4]Carl-Ludwig-Institute for Physiology, Faculty of Medicine, University of Leipzig, 04103 Leipzig, Germany; Department of Neurogenetics, Max-Planck-Institute for Experimental Medicine, Hermann-Rein-Str. 3, 37075 Göttingen, Germany
[5]Centro de Estudios Científicos (CECs), Casilla 1469, 5110466 Valdivia, Chile. Electronic address: fbarros@cecs.cl

Correspondence: L Felipe Barros fbarros@cecs.cl

## Personal Contribution

Performance of *in vivo* two-photon imaging experiments, data analysis and preparation of respective figure. Reviewing of the manuscript.

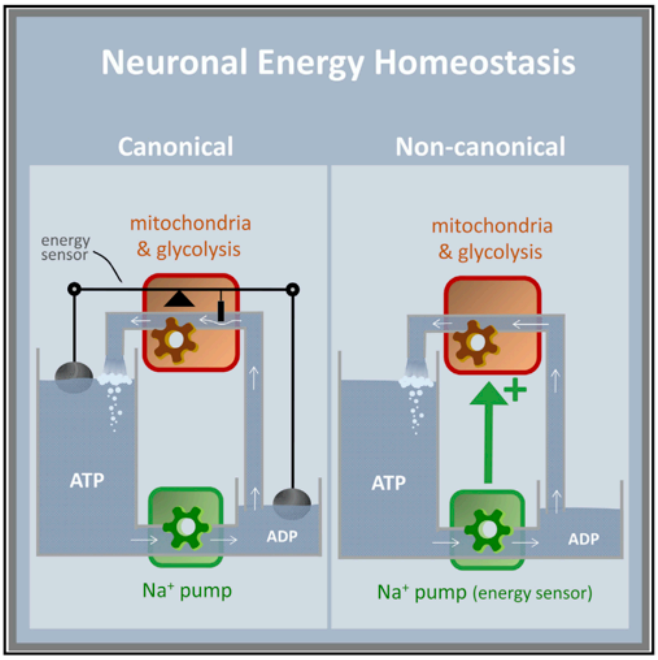

Graphical Abstract

## In Brief

Using fluorescent sensors for ions and metabolites Baeza-Lehnert et al. mapped the metabolic response to synaptic transmission *in vitro* and *in vivo*. Neurons showed perfect energetic stability that was attributed to control of ATP production by the $Na^+$ pump, as opposed to conventional homeostasis mediated by ADP, ATP, and $Ca^{2+}$.

## Highlights

- Neuronal ADP:ATP is not affected by neurotransmission despite strong $Na^+$ pumping
- Stimulated mitochondrial pyruvate flux precedes glucose consumption
- Energy stability is not explained by conventional homeostasis (ADP:ATP or $Ca^{2+}$)
- $Na^+$ pump activity controls glycolysis and mitochondrial ATP production

# Summary

Neurons have limited intracellular energy stores but experience acute and unpredictable increases in energy demand. To better understand how these cells repeatedly transit from a resting to active state without undergoing metabolic stress, we monitored their early metabolic response to neurotransmission using ion-sensitive probes and FRET sensors *in vitro* and *in vivo*. A short theta burst triggered immediate $Na^+$ entry, followed by a delayed stimulation of the $Na^+/K^+$ ATPase pump. Unexpectedly, cytosolic ATP and ADP levels were unperturbed across a wide range of physiological workloads, revealing strict flux coupling between the $Na^+$ pump and mitochondria. Metabolic flux measurements revealed a "priming" phase of mitochondrial energization by pyruvate, whereas glucose consumption coincided with delayed $Na^+$ pump stimulation. Experiments revealed that the $Na^+$ pump plays a permissive role for mitochondrial ATP production and glycolysis. We conclude that neuronal energy homeostasis is not mediated by adenine nucleotides or by $Ca^{2+}$ , but by a mechanism commanded by the $Na^+$ pump.

# Introduction

The brain consumes energy at a rate 10 times faster than the rest of the body. Over half of this energy is used by neuronal pumps to restore ion gradients challenged by excitatory synaptic potentials and action potentials (Erecinska and Silver, 1994; Harriset al., 2012). Neurons are unique insofar as they lack energy stores while being exposed to acute unpredictable increases in energy demand. It is not clear how these cells can transit from resting to active state time and again over a lifetime without undergoing metabolic stress. The details of such adaptive response seem particularly relevant because acute energy shortage has a quick and profound impact on brain cell function and viability, as exemplified by hypoxia and hypoglycemia. Neurons may be particularly susceptible to small ATP deficits, with possible consequences for neurodegeneration (Le Massonet al., 2014; Zilberter and Zilberter, 2017).

ATP bridges the gap between energy usage by biochemical processes and energy production by mitochondria and glycolysis. The neuronal ATP pool is highly dynamic, with typical turn-over times in the order of seconds (Barros et al., 2013). Different control systems contribute to balance energy demand and sup-

ply at different time scales. For example, the AMP-activated protein kinase takes minutes to signal the expression of proteins involved in fuel supply and ATP turnover (Hardie et al., 2012). Isotopic studies of purified enzymes and respirometry assays of isolated mitochondria suggested that mitochondrial respiration is controlled also in the short term by homeostatic feedback loops, in which ADP is the controlling variable (Chance and Williams,1956; Brand and Nicholls, 2011). Accordingly, studies in intact cells and tissues reported fast depletion of ATP in response to energy demand and/or decreased fuel/oxygen delivery (Erecin-ska and Silver, 1994; Jekabsons and Nicholls, 2004; Connollyet al., 2014; Lange et al., 2015; Rangaraju et al., 2014; Toloeet al., 2014; Rueda et al., 2015), and therefore the control of mitochondrial respiration by adenine nucleotide feedback has become standard in mathematical models of cell metabolism (Aubert et al., 2007; Jolivet et al., 2015; Le Masson et al., 2014; Berndt et al., 2015). However, low-resolution measurements showed that bulk tissue ATP in skeletal muscle, heart, and brain is relatively insensitive to workload (Hill, 1950; Hochachka and McClelland, 1997; Heineman and Balaban, 1990; Du et al., 2008). These findings have prompted alternative hypotheses, namely that mitochondrial respiration is controlled by local adenine nucleotide pools (Saks et al., 2008) or by $Ca^{2+}$, either intramitochondrial or cytosolic (Duchen et al., 2008; Glancy and Balaban, 2012; Denton, 2009; Llorente-Folch et al., 2013).
Genetically encoded fluorescence resonance energy transfer (FRET) reporters are allowing real-time measurement of metabolite concentrations and fluxes in intact cells and in minimally invasive fashion (Takanaga et al., 2008; Imamura et al., 2009; Bittner et al., 2010; Tantama et al., 2013; San Martín et al., 2013, 2014; Barros et al., 2013; Diaz-Garcia et al., 2017). Taking advantage of these tools in combination with ion-sensitive dyes and a novel protocol to evaluate ATP flux in real-time, we have approached the question of short-term control of energy metabolism in neurons.

# Results

To study the energetics of neurotransmission, we first used cultured neurons, which provide precise control of experimental variables and easier visualization of dyes and sensors. Neurons were cultured in the presence of astrocytes (Figure S3.1A), which promote their functional and metabolic differentiation (Barreset al., 1990; Mamczur et al., 2015).

## Resting Hippocampal Neurons Consume Both Glucose and Lactate

It is well established that neurons consume glucose but the role of lactate as fuel is contentious (Pellerin and Magistretti, 1994; Barros and Weber, 2018; Bak and Walls, 2018). Here, we addressed this issue with the FRET sensor Laconic and a transport-stop protocol based on the monocarboxylate transporter (MCT)1-2 blocker AR-C155858 (Figures S3.1B–S3.1D; San Martín et al., 2013). In the presence of physiological concentrations of glucose and lactate, the majority of neurons behaved as lactate consumers, whereas all astrocytes were lactate producers (Figures S3.1B and S3.1C). Additional characterization showed that as the cultures became more mature, the transport and consumption of glucose diminished in neurons and increased in astrocytes and that astrocytic enrichment of the cultures reduced the consumption of glucose by neurons (Figures S3.1E–S3.1L). Thus, under our experimental conditions, both glucose and lactate contribute to the fueling of neurons.

Neurotransmission was triggered by field stimulation of the cultures with a short theta burst (STB, Figure 3.1A), an electrical stimulation protocol of 40 pulses in a pattern that resembles hippocampal activity (Albensi et al., 2007). The STB elicited a $Ca^{2+}$ signal of similar amplitude to that produced by spontaneous firing (3.1B). The cytosolic $Ca^{2+}$ transient peaked 4 s after stimulation onset, lasted for 20 s, was strongly inhibited by a cocktail of DNQX and MK801, and was abolished by TTX (Figures 3.1C–3.1F), demonstrating predominant glutamatergic neurotransmission driven by action potentials. Using the high-affinity probes Rhod2 or mito-GCaMP6s (Li et al., 2014), we did not find sizable increases in intramitochondrial $Ca^{2+}$ in response to the STB (Figures 3.1G–3.1J).

## Quantitation of the Workload Elicited by Synaptic Activity

The cytosolic $Ca^{2+}$ transient was accompanied by a much slower $Na^+$ transient that peaked at 30 s and lasted for several minutes (3.2A). The $Na^+$ transient was similar in amplitude and timecourse to spontaneous $Na^+$ fluctuations recorded in brain tissue slices (Rose and Ransom, 1997), as detected with $Na^+$-binding benzofuran isophthalate (SBFI) or Asante Natrium Green probes (Figure S3.2).

Both $Ca^{2+}$ and $Na^+$ transients could be elicited repeatedly in the same preparation (Figure S3.2). The return of $Na^+$ toward pre-stimulation levels reveals a metabolic load, but the extent of the load may not be computed directly from the $Na^+$ concentration curve, because of unknown simultaneous contributions from $Na^+$ influx and pumping (as exemplified in Figure S3.3A). To circumvent this limitation, a protocol was devised based on $Na^+$ pump blockage. Figures 3.2A and 3.2B show that the curves of $Na^+$ accumulation with and without ouabain were virtually superimposable during the first 15 s after STB onset and sharply diverged afterward. The difference between the two curves was computed as $Na^+$ extruded, and its instant slope as the rate of extrusion, that is, the activity of the $Na^+$ pump (3.2C). One limitation of this approach is that the accumulation

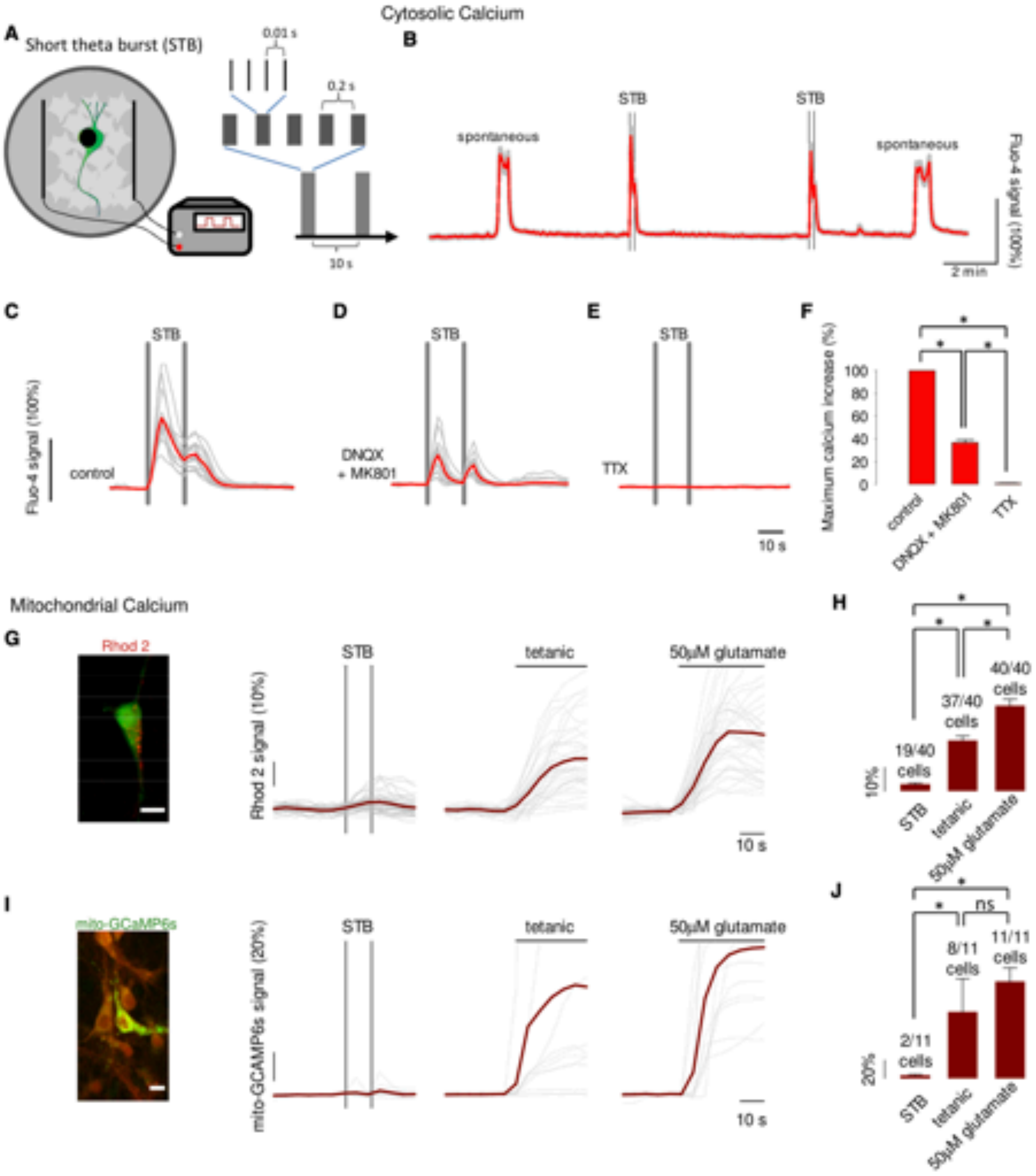

of intracellular $Na^+$ may interfere with the influx of $Na^+$, for example via the $Na^+/Ca^{2+}$ exchanger, a possibility supported by the observation that cytosolic $Ca^{2+}$ did not return to control levels after the STB in the ouabain-treated cells (Figure S3.3B). Therefore, to minimize underestimation of the rate of $Na^+$ pumping, analyses were restricted to the first 30 s after stimulation, a period in which $Na^+$ levels are still in the low millimolar range. Neuronal pH was not affected by the STB, either in the absence or presence of ouabain (Figure S3.3C), which is against a confounding effect of the $Na^+/H^+$ exchanger.

To determine the relative importance of $Na^+$ pumping on overall ATP expenditure, glucose metabolism was measured using a transport-stop protocol based on the FRET sensor FLII$^{12}$Pglu700µΔ6 (see schematic in Figure 3.4E; Takanaga et al., 2008; Bittner et al., 2011). The rate of glucose consumption by resting neurons was 0.8 µM/s in the presence of lactate and 1.7 µM/s in its absence, with a negligible change in cytosolic ADP:ATP after lactate removal (Figures S3.4B and S3.4C). As lactate has been shown to sustain *in vivo* neurotransmission as well as does glucose (Wyss et al., 2011), we assumed that the sum of glucose and lactate amounted to 1.7 µM/s of glucose equivalents, that is, that lactate contributes about 50% of resting fuel (Bouzier-Sore et al., 2006). With a stoichiometry of 31 ATPs per glucose, this fueling rate translated into an ATP production of 53 µM/s. Considering the measured $Na^+$ pumping rate of 46 µM/s (3.2A), and a 3:1 $Na^+$:ATP stoichiometry, the resting ATP consumption of the $Na^+$ pump was 15

Figure 3.1.: **Cytosolic and Mitochondrial $Ca^{2+}$ in Response to Neurotransmission.**
**(A)** Field stimulation of mixed hippocampal cultures with a short theta burst (STB) protocol (see details in STAR★Methods).
**(B)** The response of neuronal $Ca^{2+}$ to STB stimulation was monitored in Fluo4-loaded cultures. Spontaneous $Ca^{2+}$ transients are indicated. Mean ± SEM (17 cells).
**(C-E)** $Ca^{2+}$ responses to STB under control conditions **(C)**, in the presence of 30 µM DNQX and 15 µM MK801 **(D)**, or in the presence of 2 µM TTX **(E)**. Individual traces from 17 cells (gray), with averages in bold (red).
**(F)** Summary of three experiments similar to that shown in (C–E). Mean ± SEM (43 cells, $^*p < 0.05$).
**(G and I)** The response of mitochondrial $Ca^{2+}$ to STB stimulation, tetanic stimulation (20 Hz for 30s) and 50 µM glutamate was monitored in cells loaded with Rhod-2 (G, 49 cells in three experiments) or mito-GCaMP6s (I, 11 cells in eleven experiments). Insets show a neuron loaded with Rhod-2 (red) and Calcein (green), and a neuron expressing mito-GCaMP6s (green) in a culture loaded with Calcein Orange (red). Bars represent 10 mm.
**(H and J)**. Summary of amplitudes (mean ± SEM) of the Rhod-2 **(H)** and mito-GCaMP6s **(J)** responses to STB, tetanic and glutamate. The number of responsive cells is indicated on top of each bar. Mean ± SEM; $^*p < 0.05$.

μM/s. We conclude that housekeeping functions in these cells consumed ATP at a rate of 38 μM/s (from 53 μM/s minus 15 μM/s). Taken together, the $Na^+$ and glucose measurements show that a moderate level of neurotransmission stimulated neuronal ATP consumption to a large extent, from 53 μM/s to a maximum 155 μM/s, an increase of 1.9 fold (Figures 3.2D and S3.4D). Still, this figure is an underestimate, as neurotransmission also involves ATP usage by minor processes such as $Ca^{2+}$ pumping, synaptic vesicle recycling, and actin remodeling (Harris et al., 2012).

## Invariance of Cytosolic ATP and ADP and Estimation of ATP Production

How the large increase in ATP expenditure brought about by synaptic activity impacts the energy status of neurons was first gauged using the genetically encoded

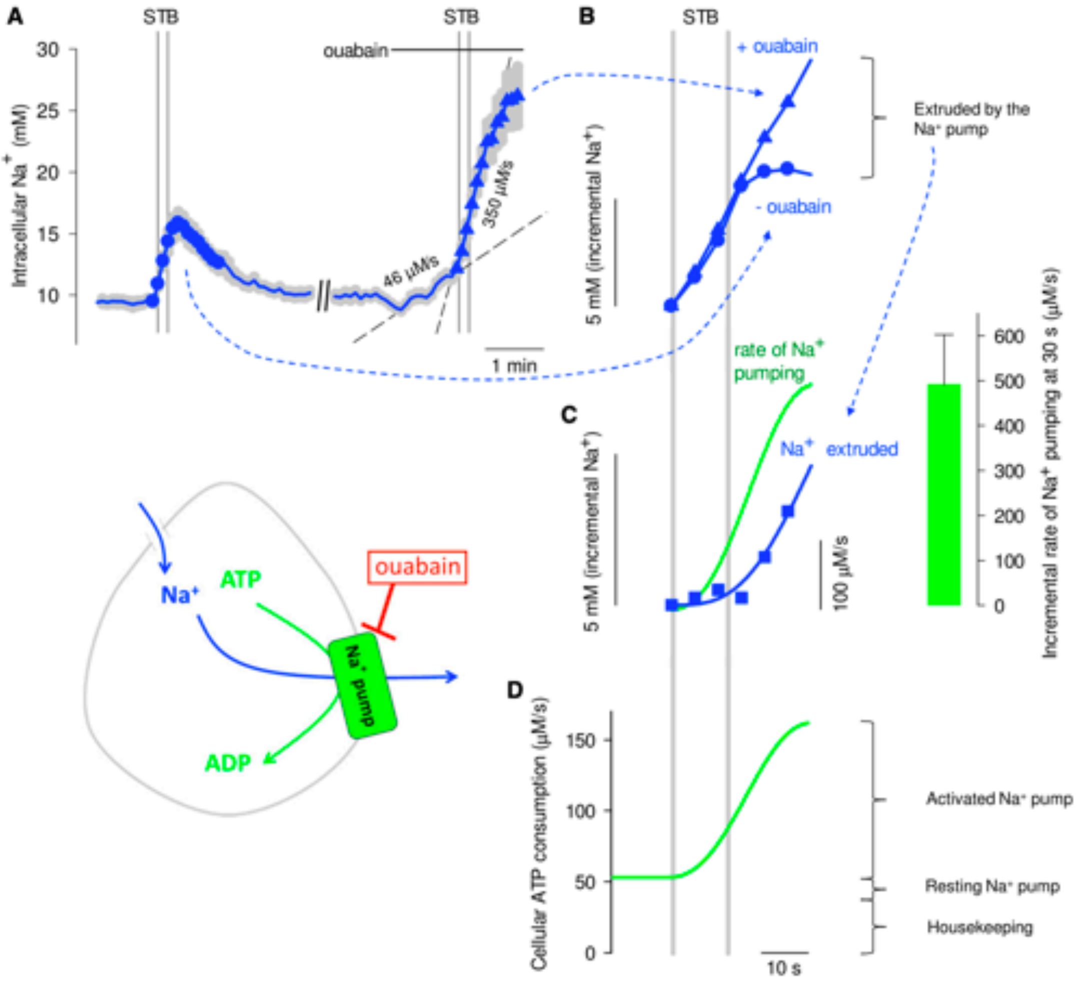

ATP sensor ATeam 1.03 (Imamura et al., 2009). According to a mathematical simulation based on the conventional homeostatic model of ADP feedback with a Hill coefficient of 1 (see STAR Methods), the estimated 1.9-fold rise in ATP demand should have resulted in substantial depletion of the cytosolic ATP pool. However, experiments showed no detectable change (Figure 3.3A). With ATP as constant, an estimated cytosolic ADP was obtained with the ADP:ATP reporter Perceval HR (Tantama et al., 2013). Again, the ADP:ATP ratio was unaffected by the STB (Figure 3.3B), showing that cytosolic ADP is also insensitive to synaptic activity. Similar changes in adenine nucleotides were predicted by an alternative feedback model based on explicit set points (Figure S3.5; Le Mas-son et al., 2014). A possible confounding effect of pH on Perceval HR (Tantama et al., 2013) was ruled out as the STB did not affect cytosolic pH in these cells to a measurable extent (Figures S3.3C and S3.5C). The large responses of both ATeam and Perceval HR to OXPHOS inhibition (Figures 3.3A, 3.3B, and S3.5) and to supra-physiological stimulation (see below), confirm previous reports that neuronal ATP and ADP concentrations lie in the sensing range of the probes (Imamura et al., 2009; Rangaraju et al., 2014; Toloe et al., 2014; Lange et al., 2015). No ADP:ATP change was detected in cells fueled exclusively with lactate (Figure S3.6), although there was a small but statistically significant change in glucose fueled cells. These results confirm that neurons may signal efficiently in

Figure 3.2.: **Quantification of the Metabolic Load Triggered by Nerotransmission.**
**(A)** The response of neuronal $Na^+$ concentration to STB stimulation under control conditions (circles) and in presence of 0.1 mM ouabain (triangles) was estimated with SBFI. Mean ± SEM (10 cells from a single experiment). $Na^+$ accumulation rates reflecting $Na^+$ entry (interrupted lines), were estimated before and after STB.
**(B)** The time courses of $Na^+$ accumulation induced by the STB in the absence (circles) and presence of 0.1 mM ouabain (triangles) are plotted together. Note the divergence between the two time courses, attributed to $Na^+$ pumping.
**(C)** The amount of $Na^+$ extruded (squares) was calculated as the point-by-point difference between $Na^+$ accumulation in the absence and presence of 0.1 mM ouabain illustrated in **(B)**. The continuous blue line corresponds to the fitting of three-parameter logistic curve to the data, $r2 > 0.99$. The green curve shows the instant rate of $Na^+$ extrusion calculated as the first derivative of the $Na^+$ extrusion curve. The bar graph summarizes data from four experiments (27 cells), including the one illustrated in **(A)** and **(B)**.
**(D)** The total rate of neuronal ATP consumption was obtained by adding the ATP consumption related to $Na^+$ pumping (from C) to the ATP consumption devoted to housekeeping functions, estimated from the rate of glucose consumption (Figure S3.4).

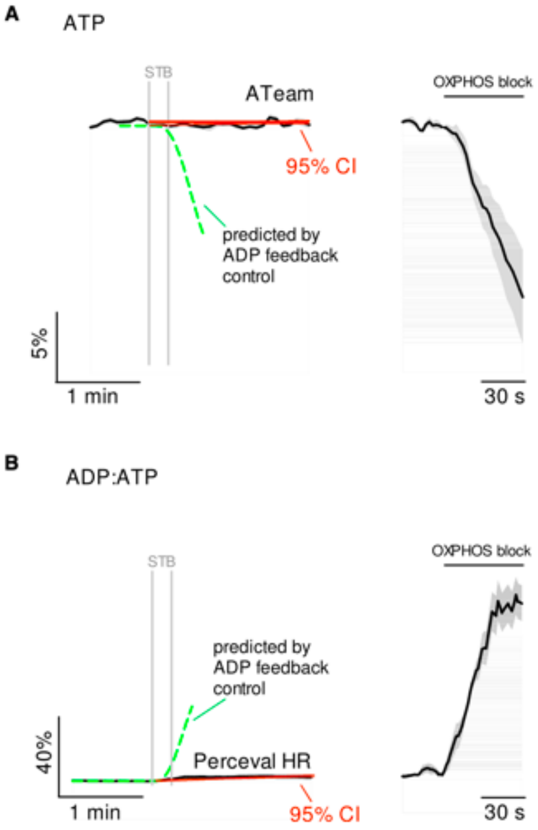

Figure 3.3.: **Invariance of Neuronal ATP and ADP After Neurotransmission.**
**(A)** Left, ATP response to STB stimulation measured with ATeam. Mean ± SEM (16 cells in ten experiments, black line). The interrupted green line shows a mathematical simulation of the response as it should have been observed with ATeam in cell governed by a negative feedback controlled by ADP. Right, effect of OXPHOS blockage with 5 mM azide on ATP as measured with ATeam. Mean ± SEM (16 cells in ten experiments). The 95% confidence interval (CI) of the mean is shown.
**(B)** Left, ADP:ATP ratio response to STB stimulation measured with Perceval high range (HR). Mean ± SEM (15 cells in 15 experiments, black line). The interrupted green line shows a mathematical simulation of the response as it should have been observed with Perceval HR in cell governed by a negative feedback controlled by ADP. Right, Effect of OXPHOS blockage with 5 mM azide on ADP:ATP ratio as observed with Perceval HR. Mean ± SEM (15 cells in 15 experiments). The 95% confidence interval (CI) of the mean is shown.

either substrate and that a robust glycolytic flux in neurons is not necessary for neuronal energy homeostasis, at least in the short term (Wyss et al., 2011).

The stability of cytosolic ATP was very informative, as it revealed that ATP consumption by the $Na^+$ pump is matched, second-by-second, by a commensurate increase in ATP production, defined as the release of ATP to the cytosol (Figure 3.4C). The invariance also suggested that ATP and ADP may not account for the tight coupling between ATP demand and production, a conclusion substantiated by a sensitivity analysis based on numerical simulation (Figure S3.6). For example, to account for the observed energy invariance, the stimulation of $Na^+$ pumping would have to be less than a 10th of what was measured or, reciprocally, resting ATP consumption would have to be more than 10 times larger than that estimated. These two unfavorable scenarios are not only inconsistent with our measurements, but also with the relative weight of signaling versus housekeeping in the neuronal energy budget (Harris et al., 2012) and with the strong stimulation of glucose and pyruvate consumption by STB described below. Alternatively, mitochondria would have to sense [ADP] with a Hill coefficientof $>$100, way beyond the reported range of 1–4 (Wilson, 2017). Figure S3.6 also shows that even a 1-s delay between $Na^+$ pumping and ATP production would lead to detectable fluctuations in ATP and ADP. Neurons possess substantial levels of phosphocreatine in equilibrium with the ATP pool (Hertz et al., 1988; Jolivet et al., 2015). As this pool is a fixed reservoir, it slightly slows down the onset of the predicted ATP depletion but does not change its amplitude (Figure S3.7). The predicted time course of AMP, phosphocreatine and other metabolites in response to the STB is shown in Figure S3.7.

## Early Metabolic Responses to Synaptic Activity

The cytosolic pools of pyruvate, lactate, and glucose were unperturbed by the STB (Figures 3.4A and 3.4B). However, when transport-stop protocols (Bittner et al., 2010; San Martín et al., 2014) were applied, large underlying changes in metabolic fluxes became visible. The stimulation of mitochondrial pyruvate uptake was immediate (Figures 3.4C and 3.4D). The median stimulation of pyruvate consumption was 2.6-fold and showed a half-time of 4 s, much shorter than that of stimulated ATP production (18 s; Figure 3.4G), revealing that mitochondria accumulate energy in some form before releasing ATP to the cytosol. Electrical stimulation of neurons is known to induce a biphasic change in mitochondrial NAD(P)H autofluorescence, characterized by a fast transient dip (oxidation) and a secondary overshoot (reduction) in which autofluorescence surpasses the baseline (Shuttleworth, 2010). The early phase of mitochondrial energization together with the delayed production of ATP described here, may provide an explanation for the overshoot phase of NAD(P)H autofluorescence. The consumption of glucose was also stimulated by synaptic activity, with a median of 1.9-fold, and its onset was delayed with respect to mitochondrial pyruvate uptake

(Figures 3.4E and 3.4F). This first direct demonstration of glycolysis stimulation by neurotransmission provides a straightforward explanation for the rise in cytosolic NADH/NAD$^+$ measured in hippocampal slice neurons, which also peaked about 30 s after the onset of synaptic activity (Diaz-Garcia et al., 2017). It is not possible at this stage to tell how much of the stimulated glucose flux was diverted through the pentose phosphate pathway (Herrero-Mendez et al., 2009). The delay between pyruvate uptake and glucose consumption implies that the pyruvate pool is sustained by lactate, at least during the first 10 to 20 s in which glycolysis has not been fully activated. A limitation of the present mitochondrial pyruvate uptake assay is that it requires the absence of glucose. Activation of the malate-aspartate shuttle (MAS) by Ca$^{2+}$ may control the utilization of glycolytic

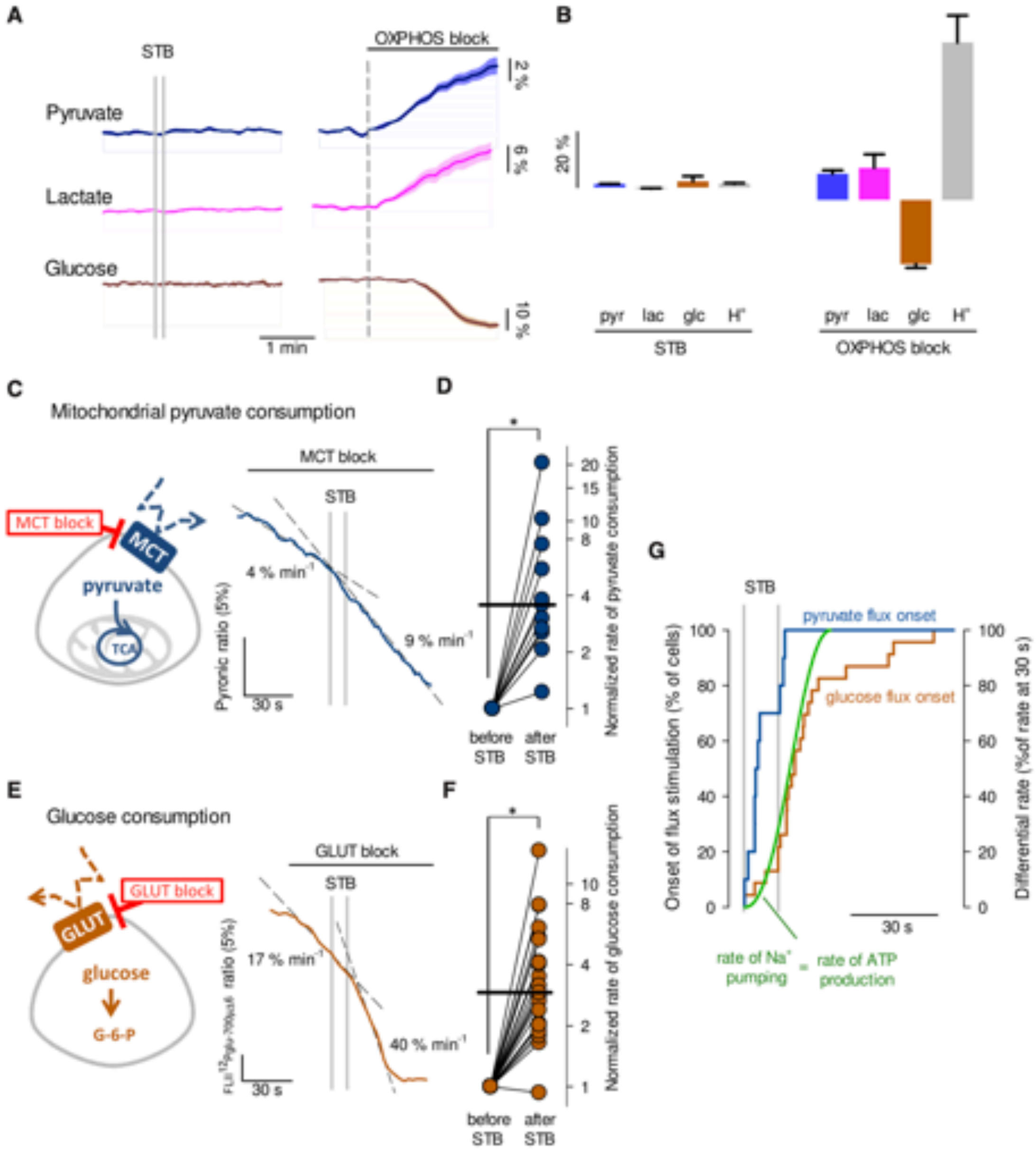

pyruvate (Llorente-Folch et al., 2013), which may not start at the same time as that of external pyruvate.

## Control of Mitochondrial ATP Production by the $Na^+$ Pump

The two signals that have been involved in the control of mitochondrial ATP production by workload are cytosolic ADP and $Ca^{2+}$, both intramitochondrial (Glancy and Balaban, 2012; Den-ton, 2009) and cytosolic (Llorente-Folch et al., 2013; Gellerichet al., 2013). As shown in Figures 3.1G–3.1J, only a small increase in mitochondrial matrix $Ca^{2+}$ was observed in response to the STB. A larger mitochondrial $Ca^{2+}$ increase was elicited by tetanic stimulation (20 Hz for 30 s), but this resulted in inhibition of mitochondrial pyruvate influx (Figure S3.7). This was in register with a reduced pyruvate-fueled respiration by intramitochondrial $Ca^{2+}$ (Gellerich et al., 2013; Pandya et al., 2013). Mitochondrial metabolism

Figure 3.4.: **Metabolic Response to Neurotransmission.**
**(A)** Left, effect of STB on the levels of pyruvate, lactate and glucose in neurons superfused with 2 mM glucose and 1 mM lactate. Right, effect of OXPHOS blockage with 5 mM azide. Mean ± SEM.
**(B)** Summary of the data in **(A)**, showing in the left graph the change induced by the STB for pyruvate (pyr, 10 cells in six experiments), lactate (lac, 9 cells in eight experiments), glucose (glc, 8 cells in three experiments) and $H^+$ concentration (24 cells in three experiments). Right, summary of the data for the effect of OXPHOS inhibition with 5 mM azide on pyruvate (7 cells in four experiments), lactate (6 cells in three experiments), glucose (16 cells in four experiments) and $H^+$ concentration (24 cells in three experiments). Mean ± SEM.
**(C)** Effect of STB on the rate of mitochondrial pyruvate consumption as measured with a transport-stop protocol based on the MCT blocker AR-C155858 (1 μM), in the presence of 400 μM extracellular pyruvate and absence of glucose and lactate. Rates were obtained by linear regression using the points preceding the STB (resting) or starting 30 s after the onset of the STB (stimulated).
**(D)** Mitochondrial pyruvate consumption rates before and after STB stimulation (13 neurons in seven experiments). The median stimulation of the rate is represented by a thick horizontal line. $^*p < 0.05$.
**(E)** Effect of STB on the rate of glucose consumption as measured with a transport-stop protocol based on the GLUT blocker cytochalasin B (20 μM), in the presence of 2 mM glucose and 1 mM lactate. Rates were obtained by linear regression using the points preceding the STB (resting) or starting 30 s after the onset of the STB (stimulated).

is sensitive to cytosolic $Ca^{2+}$ via proteins that expose $Ca^{2+}$-binding sites to the mitochondrial intermembrane space, such as the aspartate/glutamate transporter ARALAR, a key component of the MAS (Llorente-Folch et al., 2013). However, the time courses of both cytosolic and mitochondrial $Ca^{2+}$ preceded that of ATP production (Figure 3.5A). Although there was a good correlation between ATP production and cytosolic $Na^+$ (Figure 3.5A), mild $Na^+$ elevations caused by pharmacological or functional inhibition of the $Na^+$ pump (3.2A) did not increase neuronal ATP (Figure 3.5B), despite reduced ATP usage. Moreover, the large $Na^+$ elevation triggered by the STB in the presence of ouabain (3.2A) also failed to stimulate ATP production (Figure 3.5C). While discarding a direct role for $Na^+$, these results demonstrate that mitochondrial ATP production requires an active $Na^+$ pump. Consistently, a reduction of the $Na^+$ load triggered by the STB did not affect the coupling between ATP usage and production (Figure 3.5D). The neuronal $Na^+$ pump was also found to play a permissive role over glycolysis, a phenomenon previously described in astrocytes (Pellerin and Magistretti, 1994, 1997; Bittner et al., 2011). These findings suggest that mitochondrial and glycolytic ATP production in neurons is controlled by $Na^+$ via the $Na^+$ pump (Figure 3.5F).

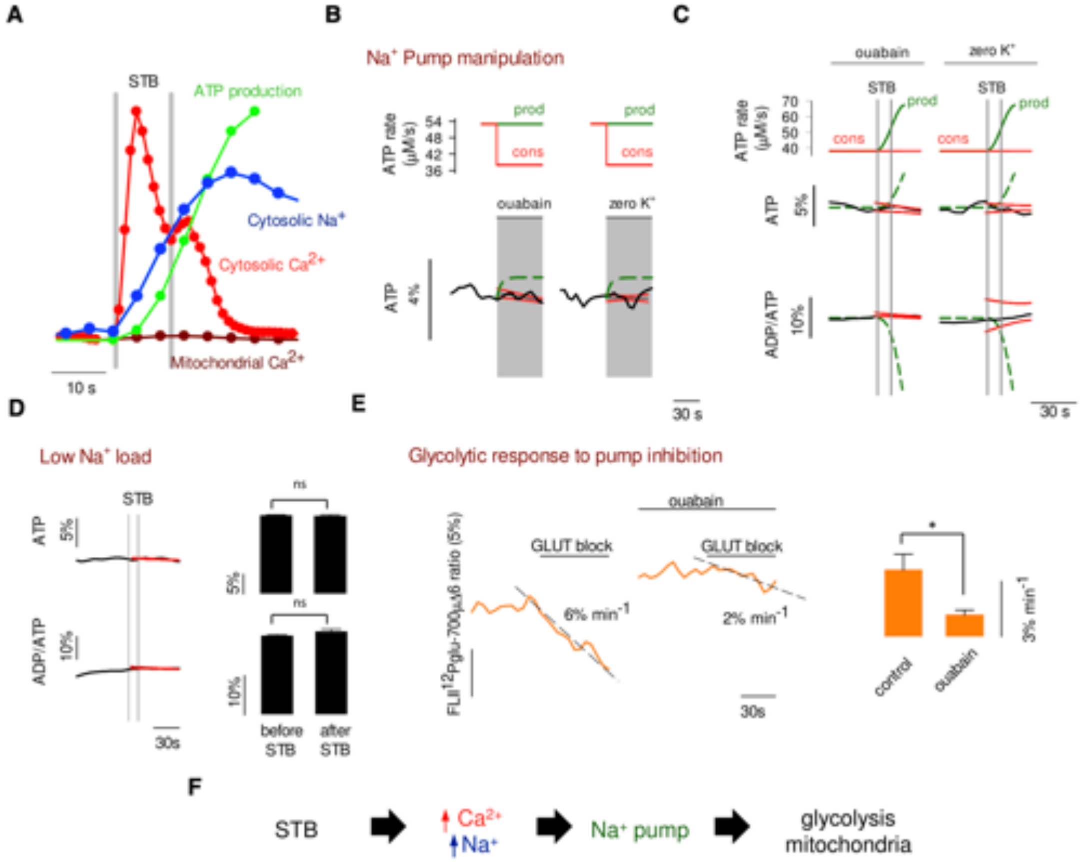

## ATP Invariance in Cortical Neurons *In Vivo*

Next, ATP dynamics were investigated in neurons of the somatosensory cortex using B6-Tg(Thy1.2-ATeam1.03$^{\mathrm{YEMK}}$)$^{\mathrm{AJhi}}$, a transgenic mouse expressing ATeam under the Thy1 promoter (Trevisiol et al., 2017), and two-photon imaging (Figure 3.6A). Under light anesthesia, neurons displayed considerable spontaneous activity as evidenced by the $Ca^{2+}$-sensitive sensor RCaMP1.07, but parallel recordings in ATeam mice showed no detectable ATP fluctuations (Figure 3.6B). The $Ca^{2+}$ activity increased in response to whisker stimulation but again, no ATPchanges were observed (Figure 3.6C). The sensitivity of the sensor in vivo was illustrated by direct electrical stimulation of the tissue, which produced a much larger $Ca^{2+}$ signal, and was accompanied by a significant drop in ATP that depended on both frequency (Figure 3.6E) and intensity (Figure 3.6F). These observations showed that ATP consumption and mitochondrial ATP production are also tightly coupled *in vivo*.

**Figure 3.5.:** **$Na^+$ Pump Involvement in Activity-Metabolism Coupling.**
**(A)** Time courses of cytosolic $Ca^{2+}$ (from Figure 3.1C), mitochondrial $Ca^{2+}$ (from Figure 3.1I), cytosolic $Na^+$ (from Figure 3.2A), and ATP production (from Figure 3.4G). Vertical scales are arbitrary.
**(B)** Effect of direct manipulation of $Na^+$ pump activity on ATP. Top, expected impact of full $Na^+$ pump blockage on neuronal ATP consumption (cons) and $Na^+$ pump-independent production (prod). Bottom, mean ATP levels measured with ATeam in response to 0.1 mM ouabain (nine cells in seven experiments) or zero extracellular $K^+$ (ten cells in ten experiments); 95% confidence intervals are shown in red. Predicted changes in ATP level are shown as broken green lines.
**(C)** Effect of STB on ATP and ADP:ATP ratio in the absence of $Na^+$ pump activity. Top, expected impact of STB on neuronal ATP consumption (cons) and $Na^+$ pump-independent production (prod). Bottom, mean traces for cells pre-incubated for 1 min in 0.1 mM ouabain (ATeam: nine cells in seven experiments. Perceval HR: nine cells in nine experiments), or zero $K^+$ (ATeam: ten cells in ten experiments. Perceval HR: ten cells in ten experiments). 95% confidence intervals are shown in red. Predicted changes in ATP and ADP:ATP ratio are shown as broken green lines.
**(D)** Cells were stimulated in the presence of 80 mM extracellular $Na^+$, equimolarly replaced with N-methyl-D-glucamine (ATeam: eight cells in eight experiments. Perceval HR: nine cells in eight experiments). Bars represent readings before and after the STB (mean ± SEM; ns, $p > 0.05$).
**(E)** Glucose consumption was measured in the absence and presence of 0.1 mM ouabain. Bars represent the results of 13 neurons in six experiments (mean ± SEM; $^*p < 0.05$).
**(F)** Proposed sequence of metabolic control in neurons.

To investigate the dynamic range of the novel homeostatic system, cultured neurons were exposed to graded workloads. Direct exposure to glutamate, which induced maximum increases in cytosolic $Na^+$ and $Ca^{2+}$, as well as in mitochondrial $Ca^{2+}$ (Figure 3.7A), resulted in substantial depletion of ATP (Figure 3.7B), an effect likely compounded by inhibition of glucose transport by glutamate (Porras et al., 2004; Tescarollo et al., 2014). Intermediate workloads were applied by changing the number of electric pulses or by applying NMDA. The changes in ATP and ADP:ATP ratio were plotted as a function of the cytosolic $Ca^{2+}$ increase, used as a proxy of the ATP demand (Figure 3.7C). This representation, together with the inhibition of mitochondrial pyruvate uptake by tetanic stimulation (Figure S3.7) suggests that in cultured hippocampal neurons, the workload imposed by the STB is near the maximum that may be tolerated without metabolic stress.

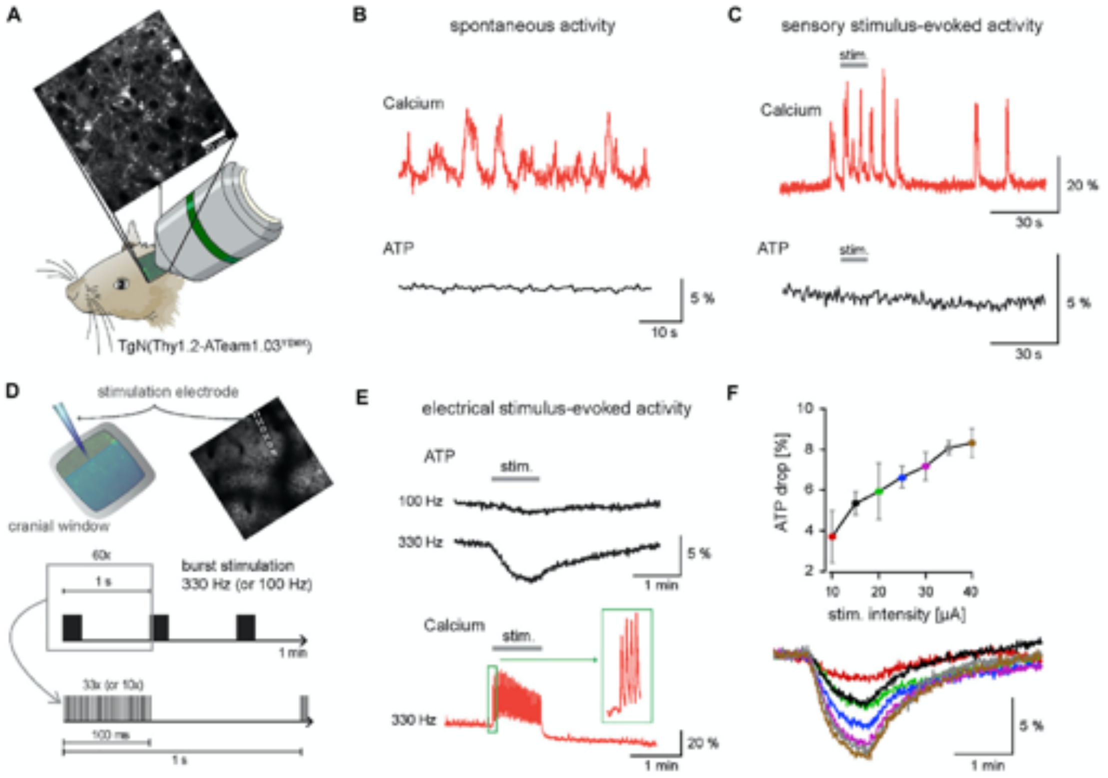

# Discussion

We have addressed the fundamental question of how neurons adapt to workload, using technologies that allowed a quantitative survey of the first seconds that follow neurotransmission. Our main conclusion is that mitochondrial ATP production in neurons is exquisitely regulated by the $Na^+$ pump, but not via adenine nucleotides or $Ca^{2+}$, at least in response to moderate levels of synaptic activity. Other important findings were the joint consumption of glucose and lactate by resting neurons, the stimulation of both pyruvate flux and glucose flux by synaptic activity and a "priming" phase of mitochondrial energization that precedes the production of ATP.

## Control of Mitochondrial ATP Production

Neurotransmission is well suited to the study of fast metabolic coupling because a strong ATP flux occurs in a predictable fashion between a single identified source (mitochondria) and a single identified sink ($Na^+$ pump), which can be manipulated in graded fashion. Our conclusions rest on the following: (1) *Quantitation of ATP consumption*. By monitoring the activity of the $Na^+/K^+$ ATPase and glucose consumption in real time, we made it possible, for the first time, to estimate the flux of ATP. (2) *Detection of ADP:ATP*. Being one order of magnitude smaller than the ATP pool, the ADP pool sustains the same flux, which makes it much more sensitive to possible mismatches between source and sink. The combination of no detectable ATP changes with invariance of Perceval HR and cytosolic pH revealed that ADP was also stable. This is important because OXPHOS is thought to be controlled by ADP, the levels of which had not been hitherto accessible. (3) *Spatiotemporal resolution*. Transient changes may be missed by low resolution

**Figure 3.6.:** **ATP Invariance In Vivo.**
**(A)** In vivo two-photon imaging of neuronal ATP levels in B6-Tg(Thy1.2-ATeam1.03 ) . Bar represents 20 mm.
**(B–F)** In addition to ATP levels, neuronal activity was monitored by calcium imaging using RCaMP1.07 (Ohkura et al., 2012) cortically expressed by viral-mediated delivery (AAV9-hSYN-RCaMP1.07). **(B)** ATP levels (lower trace) were unchanged during spontaneous activities revealed by calcium transients (upper trace). **(C)** Sensory-evoked activity following electrical whisker-pad stimulation (2 Hz for 10 s, at 400 mA) showed clear calcium responses in neurons, although ATP levels remained unchanged. **(D)** Scheme for microelectrode insertion and intracortical stimulation (top row). Burst stimulation paradigm for 1 min (1 Hz burst frequency, 100 ms trains at 100 or 330 Hz). **(E)** ATP level changes (top) in response to burst stimulations of 100 or 300 Hz (each at 15 mA). Local microstimulations evoke robust calcium transients (bottom). Depicted are example traces. **(F)** Average ATP level changes following 1 min burst stimulation of 330 Hz at different current intensities (n = 3 mice, mean ± SEM). Lower traces represent example recordings for each corresponding stimulus intensity (color-coded).

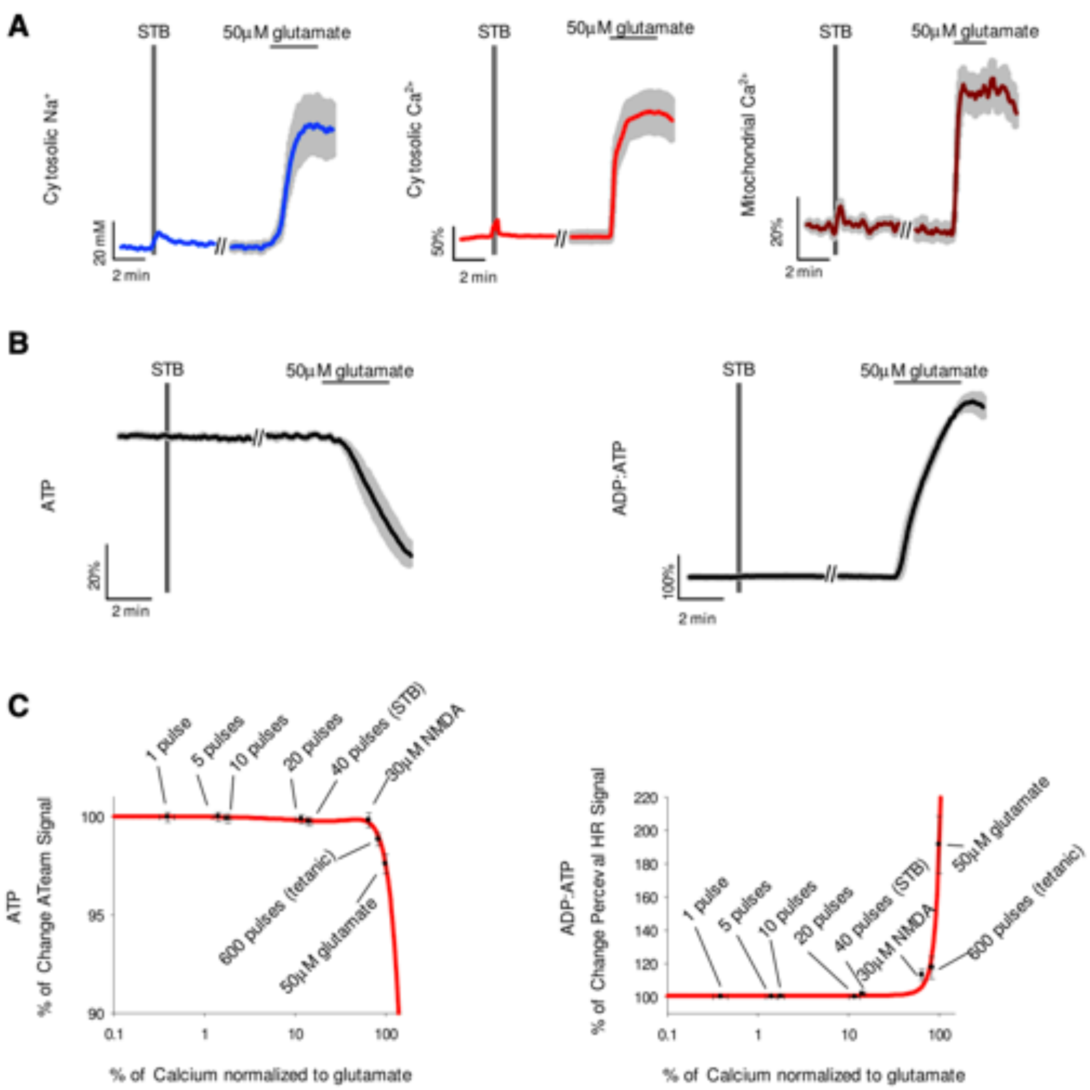

**Figure 3.7.: Supraphysiological Metabolic Uncoupling.**
**(A)** Comparison between the effects of STB and 50 µM glutamate on cytosolic $Na^+$ (10 cells), cytosolic $Ca^{2+}$ (19 cells) and mitochondrial $Ca^{2+}$ (15 cells). Mean ± SEM, representative of more than three experiments per parameter.
**(B)** Comparison between the effects of STB and 50 µM glutamate on ATP (eight cells) and ADP:ATP ratio (ten cells). Mean ± SEM, representative of more than eight experiments per parameter.
**(C)** Neurons were stimulated with an increasing number of electric pulses or exposed to 30 µM NMDA or 50 µM glutamate, while measuring intracellular $Ca^{2+}$, ATP or ADP:ATP. The plots express the change in nucleotide levels as a function of the maximum $Ca^{2+}$ increase evoked in at least six experiments per stimulation protocol. Mean ± SEM.

techniques such as MRS, which need extended integration times and average the behavior of many cells, a particular concern for heterogeneous tissues like brain. (4) *Physical separation between ATP source and ATP sink*. The existence of metabolite microdomains has been hypothesized in skeletal muscle, where mitochondria are close to contractile elements (Saks et al., 2008). Mitochondria can also make contact with the plasma membrane (Westermann, 2015), but most of them are buried within the cell (Deitch and Banker, 1993), whereas most $Na^+$ pumps reside at the cell surface (Juhaszova and Blaustein, 1997). This separation means that the crosstalk between $Na^+$ pump and mitochondria can be accurately monitored with sensors interposed in the bulk cytosol. Incidentally, according to Brownian diffusion the cytosol of mammalian cells is a well-mixed compartment for ATP and ADP, even in the immediate vicinity (1 nanometer) of sinks and sources (Barros and Martinez, 2007). With quantitative knowledge of metabolite levels and fluxes in real time, it was possible to rule out adenine nucleotides as mediators of the energetic adaptation to synaptic activity.

The alternative candidate for activity-dependent control of mitochondrial metabolism has been $Ca^{2+}$ (Duchen et al., 2008; Glancy and Balaban, 2012; Tarasov et al., 2012; Llorente-Folch et al., 2013). $Ca^{2+}$ may regulate mitochondrial metabolism by acting on matrix dehydrogenases or at the cytosolic side of mitochondrial transporters. The current finding of substantial stimulation of pyruvate uptake and ATP production without significant increases in matrix $Ca^{2+}$ argues against a necessary role for this cation in the control of neuronal energetics, at least in the short term. Moreover, mitochondrial $Ca^{2+}$ was not correlated with ATP production in response to the STB, whereas a larger increase in mitochondrial $Ca^{2+}$ induced by tetanic stimulation resulted in inhibition of pyruvate consumption. Matrix dehydrogenases require micromolar $Ca^{2+}$, and it is not clear that respiration can be stimulated by $Ca^{2+}$ when fed with pyruvate, the physiological substrate for dehydrogenases in neurons (Gellerich et al., 2013; Pandya et al., 2013). It was recently reported that a major fraction of the 2-oxoglutarate dehydrogenase expressed in brain cells is insensitive to $Ca^{2+}$ (Denton et al., 2016). ARALAR, a key component of the MAS, is sensitive to cytosolic $Ca^{2+}$ in the nanomolar range, and should have been activated during the $Ca^{2+}$ transient elicited by the STB. The modulation of ARALAR by $Ca^{2+}$ is direct and reversible, and therefore expected to follow the kinetics of $Ca^{2+}$. Considering the divergent time courses of cytosolic $Ca^{2+}$ and ATP production, a major role for the MAS in controlling ATP production is hard to envisage, although it likely contributes to mitochondrial energization.

## Control of the ATP Source by the ATP Sink

How is information conveyed between synaptic activity and mitochondria? The dynamics of a putative signal responsible for matching ATP production to ATP consumption should mimic the complex time course of $Na^+$ pumping, including delay, rapid rise, and slow return to resting level. This was certainly not the behavior of ATP, ADP, Ca , or even Na . Perfect correlation between stimulated $Na^+$ pumping and ATP production and instant adjustment of mitochondrial ATP production to $Na^+$ pump inhibition suggests that the top controller is the $Na^+$ pump itself. But how could the $Na^+$ pump modulate mitochondria if not via adenine nucleotides? One possible clue may be found in the striking coincidence between the time courses of Na pumping and glycolysis (Figure 3.4E). In brain cells, the rate-limiting glycolytic enzyme hexokinase is attached to mitochondria, where it interacts with several proteins including the adenine nucleotide translocator ANT, the transporter in charge of ATP export to the cytosol (Genda et al., 2011). Whereas the functional role of this hexokinase location is unclear, its forced relocation to the cytosol has been associated with neurodegeneration (Hauser et al., 2017). There is ample evidence that the $Na^+$ pump plays a permissive role in glycolysis of astrocytes (Pellerin and Magistretti, 1994; Bittner et al., 2011; Fernandez-Moncada and Barros, 2014), specifically the minority alpha2 subunit of the pump (Pellerin and Magistretti, 1997), which is also expressed by neurons (Dobretsov and Stimers, 2005). A possible role for alpha2 is consistent with the high sensitivity of glutamate transport to ouabain and the physical interaction between glutamate trans- porters, the $Na^+$ pump, hexokinase, and the mitochondrial ATP exporters ANT and VDAC (Rose et al., 2009; Genda et al., 2011). Conceivably, the pump may regulates mitochondria through hexokinase and/or through the downstream glycolytic intermediates glucose-6-phosphate and fructose-1,6-bisphospate (Diaz-Ruiz et al., 2008). Alternatively, the modulation may be direct, as neurons have invaginations of the plasma membrane that penetrate deep into the cytoplasm (Morris et al., 2003), plus there is a subpopulation of $Na^+$ pumps within the cell (Juhaszova and Blaustein, 1997; Blom et al., 2011), some of which have been found in association with mitochondria (Hashimoto et al., 2008).

## A Priming Phase of Mitochondrial Activation

The delay observed between stimulation of pyruvate consumption and ATP production means that the response to workload occurs in two steps: a priming phase, in which the organelle is energized, and an export phase, in which ATP is released "on demand" to the cytosol through the ANT. The priming phase explains why in the first seconds of activation there is an accumulation of reducing equivalents in mitochondria, visualized as the NADH overshoot (Chance and Williams, 1956; Shuttleworth, 2010) and may also help to explain the persistence of the NADH overshoot in the presence of the ATP synthase blocker oligomycin (Duchen, 1992). Putting together the available data, we propose the following timeline: first, synaptic activity stimulates OXPHOS, possibly via cytosolic $Ca^{2+}$ (Fein and Tsacopoulos, 1988) and causes the initial “dip” in matrix NADH (Shuttleworth, 2010). Seconds later, pyruvate oxidation is stimulated, leading to the mitochondrial NADH overshoot, likely compounded by the activation of ARALAR by cytosolic $Ca^{2+}$, which drives pyruvate into mitochondria and promotes respiration at moderate workloads (Llorente-Folch et al., 2013). By 10 s after the onset of stimulation, mitochondria are well energized with NADH, and perhaps also with ATP. Then, ATP is released to the cytosol through the ANT/VDAC under the fine control of the $Na^+$ pump, which is stimulated in a delayed fashion together with glycolysis.

Is ATP a physiological variable in neurons? The STB protocol represents a moderate degree of stimulation (Albensi et al., 2007) and did not affect ATP. Tetanic stimulation and glutamate further augmented the workload but failed to stimulate mitochondrial flux beyond that achieved by the STB, resulting in ATP depletion. Similar depletion has been reported in response to seizure-like activity or NMDA application (Toloe et al., 2014; Rueda et al., 2015; Lange et al., 2015; Rangaraju et al., 2014). It will be important to clarify whether ATP depletion occurs under strong physiological stimulation or whether it is a pathognomonic sign of neuronal dysfunction. According to computational modeling, a small decrease in cellular ATP may lead to runaway energy failure, a possible factor in the pathogenesis of neurodegeneration (Le Masson et al., 2014; Zilberter and Zilberter, 2017)

## Limitations of Study

This work addressed neurons from hippocampus and somatosensory cortex of mice and it may not be representative of other types of neurons, or other species. Another caveat is that all measurements were on somata, which makes the metabolic behavior of distal dendrites and axons a matter of future enquire.

# STAR★Methods

## Key Resources Table

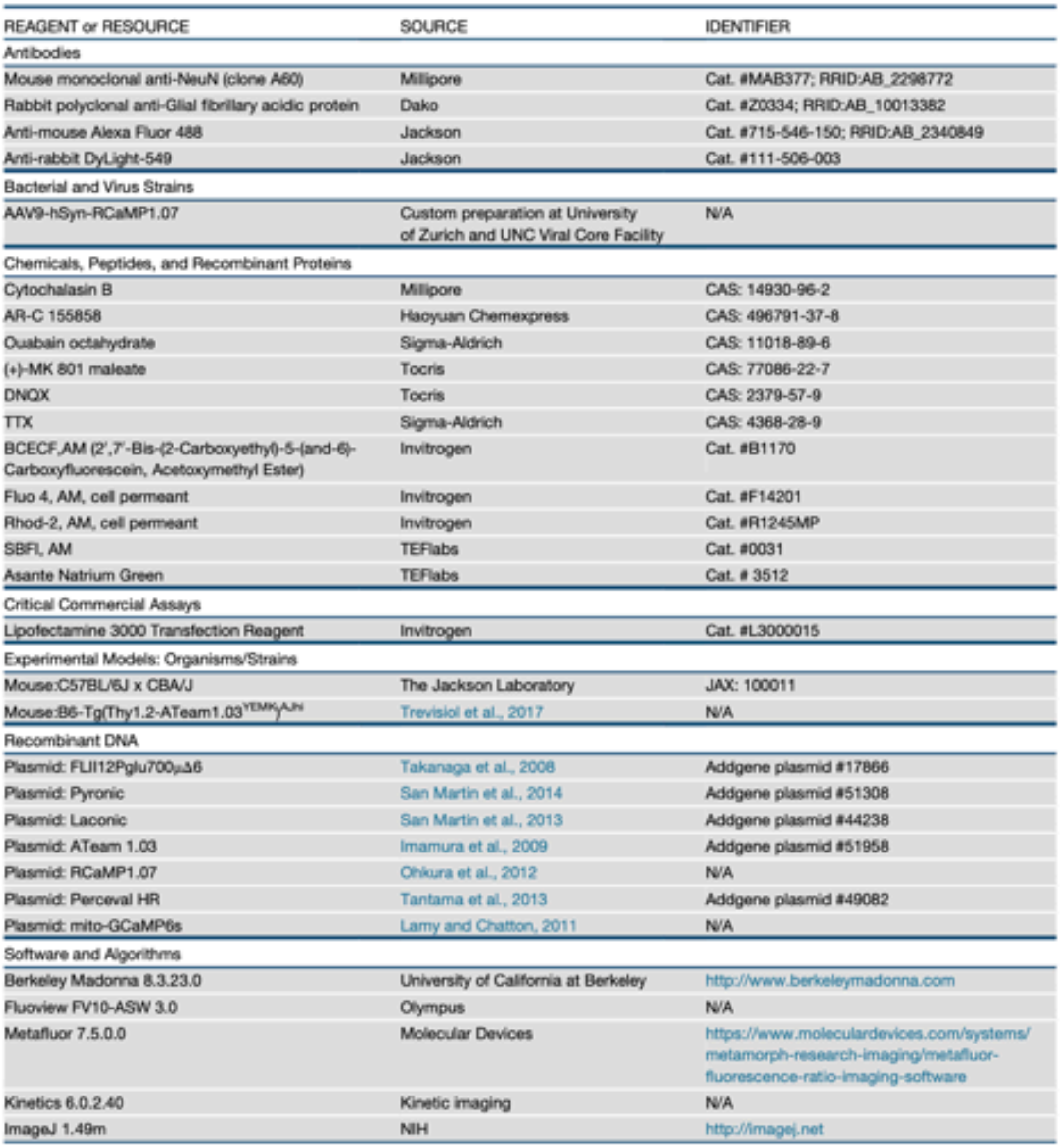

| REAGENT or RESOURCE | SOURCE | IDENTIFIER |
|---|---|---|
| Antibodies | | |
| Mouse monoclonal anti-NeuN (clone A60) | Millipore | Cat. #MAB377; RRID:AB_2298772 |
| Rabbit polyclonal anti-Glial fibrillary acidic protein | Dako | Cat. #Z0334; RRID:AB_10013382 |
| Anti-mouse Alexa Fluor 488 | Jackson | Cat. #715-546-150; RRID:AB_2340849 |
| Anti-rabbit DyLight-549 | Jackson | Cat. #111-506-003 |
| Bacterial and Virus Strains | | |
| AAV9-hSyn-RCaMP1.07 | Custom preparation at University of Zurich and UNC Viral Core Facility | N/A |
| Chemicals, Peptides, and Recombinant Proteins | | |
| Cytochalasin B | Millipore | CAS: 14930-96-2 |
| AR-C 155858 | Haoyuan Chemexpress | CAS: 496791-37-8 |
| Ouabain octahydrate | Sigma-Aldrich | CAS: 11018-89-6 |
| (+)-MK 801 maleate | Tocris | CAS: 77086-22-7 |
| DNQX | Tocris | CAS: 2379-57-9 |
| TTX | Sigma-Aldrich | CAS: 4368-28-9 |
| BCECF,AM (2',7'-Bis-(2-Carboxyethyl)-5-(and-6)-Carboxyfluorescein, Acetoxymethyl Ester) | Invitrogen | Cat. #B1170 |
| Fluo 4, AM, cell permeant | Invitrogen | Cat. #F14201 |
| Rhod-2, AM, cell permeant | Invitrogen | Cat. #R1245MP |
| SBFI, AM | TEFlabs | Cat. #0031 |
| Asante Natrium Green | TEFlabs | Cat. # 3512 |
| Critical Commercial Assays | | |
| Lipofectamine 3000 Transfection Reagent | Invitrogen | Cat. #L3000015 |
| Experimental Models: Organisms/Strains | | |
| Mouse:C57BL/6J x CBA/J | The Jackson Laboratory | JAX: 100011 |
| Mouse:B6-Tg(Thy1.2-ATeam1.03$^{YEMK}$)$^{AJH}$ | Trevisiol et al., 2017 | N/A |
| Recombinant DNA | | |
| Plasmid: FLII12Pglu700µΔ6 | Takanaga et al., 2008 | Addgene plasmid #17866 |
| Plasmid: Pyronic | San Martin et al., 2014 | Addgene plasmid #51308 |
| Plasmid: Laconic | San Martin et al., 2013 | Addgene plasmid #44238 |
| Plasmid: ATeam 1.03 | Imamura et al., 2009 | Addgene plasmid #51958 |
| Plasmid: RCaMP1.07 | Ohkura et al., 2012 | N/A |
| Plasmid: Perceval HR | Tantama et al., 2013 | Addgene plasmid #49082 |
| Plasmid: mito-GCaMP6s | Lamy and Chatton, 2011 | N/A |
| Software and Algorithms | | |
| Berkeley Madonna 8.3.23.0 | University of California at Berkeley | http://www.berkeleymadonna.com |
| Fluoview FV10-ASW 3.0 | Olympus | N/A |
| Metafluor 7.5.0.0 | Molecular Devices | https://www.moleculardevices.com/systems/metamorph-research-imaging/metafluor-fluorescence-ratio-imaging-software |
| Kinetics 6.0.2.40 | Kinetic imaging | N/A |
| ImageJ 1.49m | NIH | http://imagej.net |

## Contact for Reagent and Resource Sharing

Further information and requests for resources and reagents should be directed to the Lead Contact, L. Felipe Barros (fbarros@cecs.cl).

# Experimental Model and Subject Details

## Mice

For *in vivo* experiments, animals used were mixed F1 2-6 month-old female and male mice (C57BL/6J x CBA/J), which were kept in under SPF conditions at room temperature (20 ± 2°C) in a 12/12 h light/dark cycle with free access to food and water. In vivo 2-photon imaging in transgenic ATP sensor mice (B6-Tg(Thy1.2-ATeam1.03$^{YEMK}$)$^{AJhi}$ (Trevisiol et al., 2017) were approved by the local veterinary authorities in Zurich and conformed to the guidelines of the Swiss Animal Protection Law, Veterinary Office, Canton of Zurich (Act of Animal Protection 16 December 2005 and Animal Protection Ordinance 23 April 2008). Surgery was performed in female mice of 10-12 weeks of age (20– 25 g bodyweight). Mice were housed in groups of 2-4, had free access to food and water and were kept under an inverted 12 hour light/dark cycle. For *in vitro* experiments, animals used were 17.5 days-old embryos of mixed sex (C57BL/ 6J x CBA/J). Pregnant female mice were kept in under SPF conditions at room temperature (20 ± 2°C) in a 12/12 h light/dark cycle with free access to food and water. Experiments were approved by the Centro de Estudios Cientificos Animal Care and Use Committee.

## Embryonic Hippocampal Cultures

Pregnant mice were sacrificed by cervical dislocation and 6-8 embryos were transferred to ice-cold HBSS medium supplemented with 5mM glucose. The brains were extracted and the hippocampus was dissected free of meninges. The tissue was enzymatically dissociated in HBBS containing 1% trypsin-EDTA (Sigma-Aldrich) for 15 minutes at 37°C and then the digestion was stopped by addition of Neurobasal medium (Gibco) containing 10mM glucose, 2% B-27 supplement, 1% glutamax and 5% FBS. After mechan- ical dissociation, cells were plated in poly-D-lysine-coated glass coverslips for three hours, followed by removal of medium and addition of 2ml of serum-free Neurobasal Medium (Gibco) containing 10 mM glucose, 2% B-27 supplement, 1% glutamax, 2.5 mg/ml fungizone and 10 mg/ml penicillin/streptomycin. Cultures were kept at 37°C in a humid atmosphere (95% air/ 5% CO2) and 2/3 of the medium was replaced every three days. Cells were transfected at days 10-12 with Lipofectamine 3000 (Invitrogen) using 3 mg of sensor plasmid DNA, 6 mg of lipofectamine reagent and 3 mg of P300 reagent. Experiments were performed at days 11-15. To test for their effect on neuronal glucose dynamics (Figure S3.1), 8-10 day old mouse cortical astrocytes (Bittner et al., 2010) from a single 35 mm dish were trypsinized, washed 3 times in 10% serum medium for trypsin inactivation, and seeded on three 35 mm dishes with neurons, 24 hours before fluorescence measurements.

# Method Details

## Head Post, Chronic Window Implantation and Virus Injection

Head post and chronic window implantation were performed as previously described (Machler at al., 2016). Head post implantation was conducted under isoflurane anesthesia (4% for induction, 1-2% for maintenance). Animals were fixed in a stereotaxic frame and following a midline incision the skull was exposed. After careful cleaning of the bone, several layers of light-cured dental cement (Tectric EvoFlow) were used to attach an aluminum head post to the back of the head. The skull over the left somatosensory cortex was left exposed for craniotomy. Two days after head post implantation a craniotomy was cut over the primary sensory cortex under midazolam (5 mg/kg), fentanyl (0.05 mg/kg) and medetomidine (0.5 mg/kg) anesthesia. Intrinsic optical imaging was used to map the somatosensory regions for proper localization before craniotomy. 150 – 200 nl of virus vector AAV9-hSYN-RCaMP1.07 (titer 2.4 E12 VG/ml) was injected with a pipette and a hydraulic pump into the hindpaw and/or whisker barrel areas at a depth of 350 – 400 nm. Following virus injection a 3 x 3 mm square coverslip was gently placed over the exposed brain and fixed with dental cement to the head cap. Mice were allowed to recover for at least 3 weeks before *in vivo* imaging experiments.

## Immunofluorescence Staining

Cultures were fixed for 30 min in 2% paraformaldehyde at 4°C, washed 3 times with 2ml of PBS, and permeabilized with 3% Triton X100 in PBS containing 2% normal goat serum. Cells were incubated overnight at 4°C with mouse anti-NeuN (0.1 mg/ml; Millipore) and rabbit anti-GFAP (4 mg/ml; DAKO) antisera. Secondary antibodies were Alexa-488 and DyLight-549, both from Jackson. Images were captured using an Olympus FV1000 fluorescence microscope.

## Fluorescent Measurements

### Primary Culture Imaging

Cells were imaged at room temperature (22 - 25°C) in a 95% air/5% CO2-gassed solution of the following composition (in mM): 112 NaCl, 3 KCl, 1.25 CaCl2, 1.25 MgSO4, 1-2 glucose, 1 lactate, 10 HEPES, 24 NaHCO3, pH 7.4, using an upright Olympus FV1000 Confocal Microscope equipped with a water immersion objectives (10x, NA 0.3; 20x, NA 0.95) and 440, 488 and 543 nm lasers. Alternatively, cells were imaged with an Olympus IX70 or with an Olympus BX51 microscope equipped with a 40x oil-immersion objectve (NA 1.3) or with a 20x water immersion objective (NA 1.0). Bright field microscopes were equipped with CAIRN monochromators (Faversham, UK), and either a Hamamatsu Orca camera controlled by Kinetics software or a Rollera camera controlled with MetaFluor software, respectively. FRET sensors (FLII$^{12}$Pglu700$\mu\Delta$6, Laconic, Pyronic and ATeam) were excited at 440 nm (Confocal) or 430 nm (monochromator). Perceval HR and BCECF were excited at 430 and 490 nm (monochromator). Mito-GCaMP6s, Fluo4, Asante Natrium Green and Calcein were excited at 488 nm (Confocal) or 490 nm (monochromator). Rhod2 and Calcein Orange were excited at 543 nm. The effect of pH on Perceval HR (Tantama et al., 2013) during

OXPHOS inhibition was corrected as explained in Figure S3.5. FRET data are presented as the ratio between CFP or mTFP emission and YFP or Venus emission respectively, normalized with respect to the minimum ratio obtained in the absence of glucose for the FLII$^{12}$Pglu700µΔ6 sensor, and the initial steady state kept by a reference buffer containing 2mM glucose and 1mM lactate for Pyronic, Laconic, ATeam and Perceval HR sensors. Full calibration of FLII$^{12}$Pglu700µΔ6 in neurons is not practical because they express the high affinity transporter GLUT3, which slows down glucose equilibration at high concentrations. Figure S3.4 shows that the change of FRET ratio of the sensor expressed in neurons is similar to that previously described *in vitro* (Takanaga et al., 2008) and in several other cell types (Bittner et al., 2010).

AM dyes were loaded in 0.02% pluronic acid. Fluo4, Calcein and Calcein Orange were ester loaded at 4 µM in culture medium for 30 minutes. Asante Natrium Green was ester loaded under the same conditions for 1 hour. SBFI was ester loaded at 20 µM for 1 hour. BCECF was ester loaded at 2 µM at room temperature for 5 minutes. Rhod-2 was ester loaded at 4 µM at 4°C for 15 minutes in HEPES buffer supplemented with glucose and lactate, and then incubated overnight in culture medium before experiments. Calibration of SBFI and Asante Natrium Green was done at the end of each experiment in the presence of gramicidine, nigericine and ouabain, as described by Rose and Ransom (1997). At the time indicated, the $Na^+$ concentration of the recording solution was reduced to 80 mM (referred to as Low $Na^+$) and the osmolarity was compensated with N-methyl-D-glucamine.

### In vivo Imaging

In vivo imaging of cortical neurons (layers 2/3, 150-200 mm below the dura) was carried out in transgenic mice B6-Tg(Thy1.2- ATeam1.03$^{YEMK}$)$^{AJhi}$, which express ATeam specifically in neurons (Trevisiol et al., 2017). Anesthesia, head-post implantation, craniotomy and virus injection have been performed as described previously (Machler et al., 2016). In order to monitor neuronal calcium changes in addition to cytosolic ATP dynamics, we injected 150 – 200 nl of virus vector AAV9-hSYN-RCaMP1.07 (titer 2.4 E12 VG/ml) into the somatosensory cortex. Following robust RCaMP1.07 sensor expression calcium and ATP imaging started around 3 weeks after virus injection. Mice were imaged using a custom-built two-photon laser scanning microscope (2PLSM; (Mayrhofer et al., 2015) with a tunable pulsed laser (MaiTai eHP DS system or InSight$^{TM}$ DeepSee system, Spectra-Physics) at 870 and 1100 nm wavelength (for ATP sensor and calcium sensor imaging, respectively) equipped with a 20x water immersion objective (W-Plan-Apochromat 20x/1.0 Differential Interference Contrast, Zeiss). During measurements, animals were head-fixed and kept under isoflurane (1.5%) anesthesia. Unidirectional frame scans at 11.84 or 1.53 Hz and 128 x 128 or 512 x 512 pixel resolution, respectively, were acquired with ScanImage (r3.8.1, Janelia Research Campus; Pologruto et al., 2003). The following Semrock bandpass filters were used 475/64, 542/50 and 607/70, to detect emission of the FRET pair mseCFP and cp173-mVenus as well as emission of RCaMP1.07. For ATP FRET analysis the Venus channel was divided by the CFP channel and the ratio normalized to the corresponding baseline. Images were processed using ImageJ software (1.49m; NIH, USA) and mainly on whole frames. For neuronal calcium RCaMP1.07 emission analysis, time acquisition curves were normalized to initial frames to monitor relative changes in calcium transients. ATP channel acquisitions and calcium imaging of the same neurons were performed sequentially by changing excitation wavelengths accordingly. Three to five mice, each having up to 3 different regions of interest (containing 6-15 neurons), were analyzed for spontaneous, sensory-evoked activities and cortical microstimulations.

## Electrical Stimulation

### Field Stimulation

Mixed cultures of hippocampal neurons and astrocytes grown on 25 mm coverslips were field-stimulated using a RC-21BRFS chamber (Warner Instruments) and a PRO-4 device (World Precision Instruments, WPI). Pulses (50mA output) were generated with a WPI A385 High Current Stimulus Isolator connected to a WPI A382 Battery Charger. The stimulation protocol was a short theta burst that mimics hippocampal activity, consisting of two trains of impulses separated by 10 seconds. Each train lasted for 1 second and was composed of twenty pulses of 1 ms duration, distributed into five groups of four pulses (illustrated in Figure 3.1A). Alternatively, cultures were subjected to tetanic stimulation (20 Hz for 30s).

### Mice Stimulation

In vivo cortical neuronal activity was evoked either by sensory stimulation (whisker-pad or hind-limb) or by micro-stimulation with a glass electrode inserted into cortical layers 2 to 3. Whisker-pad and hind-limb were stimulated with 400 mA either at 2 or 4 Hz for various durations of 2, 4, 8 and 10 s or for 1 min and the corresponding cortical area was imaged. For intracortical microstimulations a 16x water-immersion objective (LWD 16x/0.80 DIC N2, Nikon) was used. Glass capillaries (Science Products; GB120F-8P 0.69 3 1.20 3 80 mm with filament) were pulled to achieve an impedance of 1.5 MU at 1 kHz, backfilled with Artificial Cerebrospinal Fluid, ACSF (containing in mM: 140 NaCl, 4 KCl, 2 CaCl2, 2 MgCl2, 10 glucose and 10 HEPES) and inserted below the remaining cranial glass window into the cortex. The glass of the cranial window was partly removed after carefully splitting it with a diamond glass cutter. Local stimulation was applied with a square-wave constant current stimulus (ranging from 5 to 50 mA) for 1 min (1 Hz train frequency, 100 ms trains at 330 or 100 Hz) using a constant-current isolator (STG 4002, Multi Channel Systems).

## Transport-Stop and Pump-Inhibition Assays for Flux Measurements

Fluxes were measured using genetically-encoded FRET sensors by acute pharmacological interruption of metabolite steady states with transport blockers as reported (Bittner et al., 2010; Barros et al., 2013). Glucose consumption rate was computed in the presence of the GLUT blocker cytochalasin B (20 μM) before (3 min) and after STB stimulation. Mitochondrial pyruvate consumption was measured in the presence of the MCT blocker AR-C155858 (1 μM) before (3 min) and after STB stimulation. Lactate depletion/accumulation was detected by exposure to 1 μM AR-C155858. Linear regressions were used to estimate fluxes. The onset of flux stimulation was computed as the intersection between linear regressions before and after STB. The effect of $Na^+$ pump inhibition over ATP and the ADP:ATP ratio was estimated by exposing cells to either 0.1mM ouabain or a potassium-free buffer before (1 min) and after STB stimulation

## Mathematical Modeling of ATP Homeostasis

The predicted response of neuronal energy status to electrical stimulation (STB) and $Na^+$ pump inhibition under a homeostatic control system was determined by numerical simulation using

Berkeley Madonna software. Metabolite pools were modeled according to (Aubert et al., 2007; Jolivet et al., 2015) and the following equations:

$$dATP/dt = Prod – (pump+housekeeping) + K_{off}*PCr*ADP - K_{on}*ATP*Cr$$

$$ADP = ATP/2 * (-ak+ (ak^2 + 4*ak*(A/ATP-1))^{1/2}$$

$$AMP= A- (ATP+ADP)$$

$$dCr/dt = K_{off}*PCr*ADP - K_{on}*ATP*Cr$$

$$dPCr/dt = K_{on}*ATP*Cr - K_{off}*PCr*ADP$$

where *prod* is the sum of glycolytic and mitochondrial ATP production, *pump* is the ATP consumption of the $Na^+/K^+$ ATPase, *housekeeping* is the ATP consumption of other processes, $K_{on}$ and $K_{off}$ are the kinetic constants of creatine kinase, *PCr* is phosphocreatine, *Cr* is creatine, *ak* is adenylate kinase, and *A* is the full nucleotide pool (ATP +ADP+ AMP). A was set at 1.554 mM and ak at 1 to obtain a resting ATP of 1.4 mM (Rangaraju et al., 2014). *Prod* was set at 0.53*ADP/(1.26+ADP) to obtain a sensitive negative feedback in which resting ATP production is 10% of maximum ATP production. Alternatively, *prod* was set at 0.053+ 0.001*(1.4-ATP) + 0.001*(ADP- 0.14) (Le Masson et al., 2014; Figure S3.5). To simulate ultrasensitivity while setting ATP production at 10% of maximum ATP production using the equation Prod = 0.53*ADPH/(KMH+ADPH), the respective values of the Hill coefficient and the affinity constant (H, Km) where (1, 1.26; 2, 0.42; 4, 0.2425; 10, 0.17441; 100, 0.1431103). Resting ATP production (53 μM/s) was inferred from the resting glucose plus lactate consumption of 1.7 μM/s glucose equivalents (Figure S3.4B) and 31 ATPs generated per each glucose equivalent. Resting *PCr* and *Cr* were respectively set at 2.7 and 0.09 mM (Hertz et al., 1988; Jolivet et al., 2015). $K_{on}$= 3.9 mM-1*s-1 and $K_{off}$ = 1.3 mM-1*s-1 were set at high values to maximize the buffering effect of creatine kinase. ATeam and Perceval HR signals were simu- lated according to their saturation parameters:

ATeam = $1+1.3*ATP^{2.1}/(3.3^{2.1}+ATP^{2.1})$; (Imamura et al., 2009).
Perceval HR = $1+ 2.5*ratio^{0.97}/(3.5^{0.97}+ratio^{0.97})$; (Tantama et al., 2013).

## Statistical Analysis

Statistical analyses were carried out with SigmaPlot software (Jandel). For normally distributed variables, differences were assessed with the Student's t-test (pairs) and with ANOVA followed by the Tukey-Kramer ad hoc test (groups). For variables that failed the normality test, differences were assessed with the Mann Whitney-Wilcoxon signed rank test (pairs) or with the Kruskal-Wallis one way ANOVA on ranks (groups). *, $p < 0.05$; ns (non-significant), $p > 0.05$). The number of experiments and cells is detailed in each figure.

# Acknowledgements

We thank Karen Everett for critical reading of the manuscript, Francisco V. Sepúlveda for helpful comments, and Giovanni Marsicano, Bordeaux, for mito-GCaMP6s. This work was partly supported by FONDECYT grant 1160317 to L.F.B. B.W. is supported by the University of Zurich and the National Science Foundation and is a member of the Clinical Research Priority Program of the University of Zurich on Molecular Imaging. A.S.S. was supported by a longterm EMBO fellowship and a Synapsis Foundation career fellowship award. J.H. would like to thank Klaus-Armin Nave, Göttingen, for longstanding collaboration and ongoing support. The Centro de Estudios Cient íficos (CECs) is funded by the Chilean Government through the Centers of Excellence Basal Financing Program of CONICYT.

# Author Contributions

F.B.-L. conceived, designed and performed most of the *in vitro* experiments. R.G., V.L., E.D., M.H., M.V., and L.H. performed experiments. J.H. and J.S. contributed to the setting up of *in vivo* experiments. A.S.S. and B.W. conceived and designed experiments *in vivo* and prepared the respective figure. L.F.B. conceived and designed experiments *in vitro* and *in vivo*. F.B-L. and L.F.B. analyzed data, prepared figures, and drafted the text. All authors discussed the data and critically revised the manuscript

# Declaration of Interest

Authors declare no competing interests.

Received: January 31, 2018
Revised: August 1, 2018
Accepted: November 12, 2018
Published: December 6, 2018

# References

Albensi, B.C, Oliver, D.R, Toupin, J., and Odero, G. (2007). Elecgtrical stimulation protocols for hippocampal synaptic plasticity and neuronal hyperexcitability: are they effective or relevant? Exp. Neurol. 204, 1-13.

Aubert, A., Pellerin, L., Magistretti, P.J., and Costalat, R. (2007). A coherent neurobiological framework for functional neuroimaging provided by a model integrating compartmentalized energy metabolism. Proc. Natl. Acad. Sci. U S A 104, 4188–4193.

Bak, L.K., and Walls, A.B. (2018). CrossTalk opposing view: lack of evidence supporting an astrocyte-to-neuron lactate shuttle coupling neuronal activity to glucose utilisation in the brain. J. Physiol. 596, 351–353. Barres, B.A., Koroshetz, W.J., Chun, L.L., and Corey, D.P. (1990). Ion channel expression by white matter glia: the type-1 astrocyte. Neuron 5, 527–544.

Barros, L.F., and Martinez, C. (2007). An enquiry into metabolite domains. Biophys. J. 92, 3878–3884. Barros, L.F., San Martin, A., Sotelo-Hitschfeld, T., Lerchundi, R., Fernandez-Moncada, I., Ruminot, I., Gutierrez, R., Valdebenito, R., Ceballo, S., Alegria, K., et al. (2013). Small is fast: astrocytic glucose and lactate metabolism at cellular resolution. Front. Cell Neurosci. 7, 27.

Barros, L.F., and Weber, B. (2018). CrossTalk proposal: an important astro- cyte-to-neuron lactate shuttle couples neuronal activity to glucose utilisation in the brain. J. Physiol. 596, 347–350.

Berndt, N., Kann, O., and Holzhutter, H.G. (2015). Physiology-based kinetic modeling of neuronal energy metabolism unravels the molecular basis of NAD(P)H fluorescence transients. J. Cereb. Blood Flow Metab. 35, 1494–1506.

Bittner, C.X., Loaiza, A., Ruminot, I., Larenas, V., Sotelo-Hitschfeld, T., Gutierrez, R., Cordova, A., Valdebenito, R., Frommer, W.B., and Barros, L.F. (2010). High resolution measurement of the glycolytic rate. Front. Neuroenergetics 2, 1–11.

Bittner, C.X., Valdebenito, R., Ruminot, I., Loaiza, A., Larenas, V., Sotelo- Hitschfeld, T., Moldenhauer, H., San Martinn, A., Gutierrez, R., Zambrano, M., and Barros, L.F. (2011). Fast and reversible stimulation of astrocytic glycolysis by $K^+$ and a delayed and persistent effect of glutamate. J. Neurosci. 31, 4709–4713.

Blom, H., Ronnlund, D., Scott, L., Spicarova, Z., Widengren, J., Bondar, A., Aperia, A., and Brismar, H. (2011). Spatial distribution of $Na^+$-$K^+$-ATPase in dendritic spines dissected by nanoscale superresolution STED microscopy. BMC Neurosci. 12, 16.

Bouzier-Sore, A.K., Voisin, P., Bouchaud, V., Bezancon, E., Franconi, J.M., and Pellerin, L. (2006). Competition between glucose and lactate as oxidative energy substrates in both neurons and astrocytes: a comparative NMR study. Eur. J. Neurosci. 24, 1687–1694.

Brand, M.D., and Nicholls, D.G. (2011). Assessing mitochondrial dysfunction in cells. Biochem. J. 435, 297–312.

Chance, B., and Williams, G.R. (1956). The respiratory chain and oxidative phosphorylation. Adv. Enzymol. Relat. Subj. Biochem. 17, 65–134.

Connolly, N.M., Dussmann, H., Anilkumar, U., Huber, H.J., and Prehn, J.H. (2014). Single-cell imaging of bioenergetic responses to neuronal excitotoxic- ity and oxygen and glucose deprivation. J. Neurosci. 34, 10192–10205.

Deitch, J.S., and Banker, G.A. (1993). An electron microscopic analysis of hip- pocampal neurons developing in culture: early stages in the emergence of po- larity. J. Neurosci. 13, 4301–4315. Denton, R.M. (2009). Regulation of mitochondrial dehydrogenases by calcium ions. Biochim. Biophys. Acta 1787, 1309–1316.

Denton, R.M., Pullen, T.J., Armstrong, C.T., Heesom, K.J., and Rutter, G.A. (2016). Calcium-insensitive splice variants of mammalian E1 subunit of 2-oxo- glutarate dehydrogenase complex with tissue-specific patterns of expression. Biochem. J. 473, 1165–1178.

Diaz-Garcia, C.M., Mongeon, R., Lahmann, C., Koveal, D., Zucker, H., and Yellen, G. (2017). Neuronal stimulation triggers neuronal glycolysis and not lactate uptake. Cell Metab. 26, 361–374.

Diaz-Ruiz, R., Averet, N., Araiza, D., Pinson, B., Uribe-Carvajal, S., Devin, A., and Rigoulet, M. (2008). Mitochondrial oxidative phosphorylation is regulated by fructose 1,6-bisphosphate. A possible role in Crabtree effect induction? J. Biol. Chem. 283, 26948–26955.

Dobretsov, M., and Stimers, J.R. (2005). Neuronal function and alpha3 isoform of the Na/K-ATPase. Front. Biosci. 10, 2373–2396.

Du, F., Zhu, X.H., Zhang, Y., Friedman, M., Zhang, N., Ugurbil, K., and Chen, W. (2008). Tightly coupled brain activity and cerebral ATP metabolic rate. Proc. Natl. Acad. Sci. U S A 105, 6409–6414.

Duchen, M.R. (1992). Ca(2+)-dependent changes in the mitochondrial energetics in single dissociated mouse sensory neurons. Biochem. J. 283 (Pt 1), 41–50.

Duchen, M.R., Verkhratsky, A., and Muallem, S. (2008). Mitochondria and cal- cium in health and disease. Cell Calcium 44, 1–5.

Erecinska, M., and Silver, I.A. (1994). Ions and energy in mammalian brain. Prog. Neurobiol. 43, 37–71.

Fein, A., and Tsacopoulos, M. (1988). Activation of mitochondrial oxidative metabolism by calcium ions in Limulus ventral photoreceptor. Nature 331, 437–440.

Fernandez-Moncada, I., and Barros, L.F. (2014). Non-preferential fuelling of the $Na^+/K^+$ ATPase pump. Biochem. J. 460, 353–361.

Gellerich, F.N., Gizatullina, Z., Gainutdinov, T., Muth, K., Seppet, E., Orynbayeva, Z., and Vielhaber, S. (2013). The control of brain mitochondrial energization by cytosolic calcium: the mitochondrial gas pedal. IUBMB Life 65, 180–190.

Genda, E.N., Jackson, J.G., Sheldon, A.L., Locke, S.F., Greco, T.M., O'Donnell, J.C., Spruce, L.A., Xiao, R., Guo, W., Putt, M., et al. (2011). Co- compartmentalization of the astroglial glutamate transporter, GLT-1, with glycolytic enzymes and mitochondria. J. Neurosci. 31, 18275–18288.

Glancy, B., and Balaban, R.S. (2012). Role of mitochondrial $Ca^{2+}$ in the regu- lation of cellular energetics. Biochemistry 51, 2959–2973.

Hardie, D.G., Ross, F.A., and Hawley, S.A. (2012). AMPK: a nutrient and energy sensor that maintains energy homeostasis. Nat. Rev. Mol. Cell Biol. 13, 251–262.

Harris, J.J., Jolivet, R., and Attwell, D. (2012). Synaptic energy use and supply. Neuron 75, 762–777. Hashimoto, T., Hussien, R., Cho, H.S., Kaufer, D., and Brooks, G.A. (2008). Evidence for the mitochondrial lactate oxidation complex in rat neurons: demonstration of an essential component of brain lactate shuttles. PLoS One 3, e2915.

Hauser, D.N., Mamais, A., Conti, M.M., Primiani, C.T., Kumaran, R., Dillman, A.A., Langston, R.G., Beilina, A., Garcia, J.H., Diaz-Ruiz, A., et al. (2017). Hexokinases link DJ-1 to the PINK1/parkin pathway. Mol. Neurodegener. 12, 70.

Heineman, F.W., and Balaban, R.S. (1990). Phosphorus-31 nuclear magnetic resonance analysis of transient changes of canine myocardial metabolism in vivo. J. Clin. Invest. 85, 843–852.

Herrero-Mendez, A., Almeida, A., Fernandez, E., Maestre, C., Moncada, S., and Bolanos, J.P. (2009). The bioenergetic and antioxidant status of neurons is controlled by continuous degradation of a key glycolytic enzyme by

APC/C-Cdh1. Nat. Cell Biol. 11, 747–752.

Hertz, L., Drejer, J., and Schousboe, A. (1988). Energy metabolism in glutama- tergic neurons, GABAergic neurons and astrocytes in primary cultures. Neurochem. Res. 13, 605–610.

Hill, A.V. (1950). A challenge to biochemists. Biochim. Biophys. Acta 4, 4–11.

Hochachka, P.W., and McClelland, G.B. (1997). Cellular metabolic homeosta- sis during large-scale change in ATP turnover rates in muscles. J. Exp. Biol. 200, 381–386.

Imamura, H., Nhat, K.P., Togawa, H., Saito, K., Iino, R., Kato-Yamada, Y., Nagai, T., and Noji, H. (2009). Visualization of ATP levels inside single living cells with fluorescence resonance energy transfer-based genetically encoded indicators. Proc. Natl. Acad. Sci. U S A 106, 15651–15656.

Diaz-Ruiz, R., Averet, N., Araiza, D., Pinson, B., Uribe-Carvajal, S., Devin, A., and Rigoulet, M. (2008). Mitochondrial oxidative phosphorylation is regulated by fructose 1,6-bisphosphate. A possible role in Crabtree effect induction? J. Biol. Chem. 283, 26948–26955.

Dobretsov, M., and Stimers, J.R. (2005). Neuronal function and alpha3 isoform of the Na/K-ATPase. Front. Biosci. 10, 2373–2396.

Du, F., Zhu, X.H., Zhang, Y., Friedman, M., Zhang, N., Ugurbil, K., and Chen, W. (2008). Tightly coupled brain activity and cerebral ATP metabolic rate. Proc. Natl. Acad. Sci. U S A 105, 6409–6414.

Duchen, M.R. (1992). Ca(2+)-dependent changes in the mitochondrial energetics in single dissociated mouse sensory neurons. Biochem. J. 283 (Pt 1), 41–50.

Duchen, M.R., Verkhratsky, A., and Muallem, S. (2008). Mitochondria and cal- cium in health and disease. Cell Calcium 44, 1–5.

Erecinska, M., and Silver, I.A. (1994). Ions and energy in mammalian brain. Prog. Neurobiol. 43, 37–71.

Fein, A., and Tsacopoulos, M. (1988). Activation of mitochondrial oxidative metabolism by calcium ions in Limulus ventral photoreceptor. Nature 331, 437–440.

Fernandez-Moncada, I., and Barros, L.F. (2014). Non-preferential fuelling of the $Na^+/K^+$ ATPase pump. Biochem. J. 460, 353–361.

Gellerich, F.N., Gizatullina, Z., Gainutdinov, T., Muth, K., Seppet, E., Orynbayeva, Z., and Vielhaber, S. (2013). The control of brain mitochondrial energization by cytosolic calcium: the mitochondrial gas pedal. IUBMB Life 65, 180–190.

Genda, E.N., Jackson, J.G., Sheldon, A.L., Locke, S.F., Greco, T.M., O'Donnell, J.C., Spruce, L.A., Xiao, R., Guo, W., Putt, M., et al. (2011). Co- compartmentalization of the astroglial glutamate transporter, GLT-1, with glycolytic enzymes and mitochondria. J. Neurosci. 31, 18275–18288.

Glancy, B., and Balaban, R.S. (2012). Role of mitochondrial $Ca^{2+}$ in the regu- lation of cellular energetics. Biochemistry 51, 2959–2973.

Hardie, D.G., Ross, F.A., and Hawley, S.A. (2012). AMPK: a nutrient and energy sensor that maintains energy homeostasis. Nat. Rev. Mol. Cell Biol. 13, 251–262.

Harris, J.J., Jolivet, R., and Attwell, D. (2012). Synaptic energy use and supply. Neuron 75, 762–777. Hashimoto, T., Hussien, R., Cho, H.S., Kaufer, D., and Brooks, G.A. (2008). Evidence for the mitochondrial lactate oxidation complex in rat neurons: demonstration of an essential component of brain lactate shuttles. PLoS One 3, e2915.

Hauser, D.N., Mamais, A., Conti, M.M., Primiani, C.T., Kumaran, R., Dillman, A.A., Langston, R.G., Beilina, A., Garcia, J.H., Diaz-Ruiz, A., et al. (2017). Hexokinases link DJ-1 to the PINK1/parkin pathway. Mol. Neurodegener. 12, 70.

Heineman, F.W., and Balaban, R.S. (1990). Phosphorus-31 nuclear magnetic resonance analysis of transient changes of canine myocardial metabolism in vivo. J. Clin. Invest. 85, 843–852.

Herrero-Mendez, A., Almeida, A., Fernandez, E., Maestre, C., Moncada, S., and Bolanos, J.P. (2009). The bioenergetic and antioxidant status of neurons is controlled by continuous degradation of a key glycolytic enzyme by APC/C-Cdh1. Nat. Cell Biol. 11, 747–752.

Hertz, L., Drejer, J., and Schousboe, A. (1988). Energy metabolism in glutama- tergic neurons, GABAergic neurons and astrocytes in primary cultures. Neurochem. Res. 13, 605–610.

Hill, A.V. (1950). A challenge to biochemists. Biochim. Biophys. Acta 4, 4–11.

Hochachka, P.W., and McClelland, G.B. (1997). Cellular metabolic homeosta- sis during large-scale change in ATP turnover rates in muscles. J. Exp. Biol. 200, 381–386.

Imamura, H., Nhat, K.P., Togawa, H., Saito, K., Iino, R., Kato-Yamada, Y., Nagai, T., and Noji, H. (2009). Visualization of ATP levels inside single living cells with fluorescence resonance energy transfer-based genetically encoded indicators. Proc. Natl. Acad. Sci. U S A 106, 15651–15656.

Jekabsons, M.B., and Nicholls, D.G. (2004). In situ respiration and bioenergetic status of mitochondria in primary cerebellar granule neuronal cultures exposed continuously to glutamate. J. Biol. Chem. 279, 32989–33000.

Jolivet, R., Coggan, J.S., Allaman, I., and Magistretti, P.J. (2015). Multi-time- scale modeling of activity-dependent metabolic coupling in the neuron-glia- vasculature ensemble. PLoS Comput. Biol. 11, e1004036.

Juhaszova, M., and Blaustein, M.P. (1997). $Na^+$ pump low and high ouabain affinity alpha subunit isoforms are differently distributed in cells. Proc. Natl. Acad. Sci. U S A 94, 1800–1805.

Lamy, C.M., and Chatton, J.Y. (2011). Optical probing of sodium dynamics in neurons and astrocytes. Neuroimage 58, 572–578.

Lange, S.C., Winkler, U., Andresen, L., Byhro, M., Waagepetersen, H.S., Hirrlinger, J., and Bak, L.K. (2015). Dynamic changes in cytosolic ATP levels in cultured glutamatergic neurons during NMDA-induced synaptic activity supported by glucose or lactate. Neurochem. Res. 40, 2517–2526.

Le Masson, G., Przedborski, S., and Abbott, L.F. (2014). A computational model of motor neuron degeneration. Neuron 83, 975–988.

Li, H., Wang, X., Zhang, N., Gottipati, M.K., Parpura, V., and Ding, S. (2014). Imaging of mitochondrial $Ca^{2+}$ dynamics in astrocytes using cell-specific mitochondria-targeted GCaMP5G/6s: mitochondrial $Ca^{2+}$ uptake and cyto- solic $Ca^{2+}$ availability via the endoplasmic reticulum store. Cell Calcium 56, 457–466.

Llorente-Folch, I., Rueda, C.B., Amigo, I., del, A.A., Saheki, T., Pardo, B., and Satrustegui, J. (2013). Calcium-regulation of mitochondrial respiration main- tains ATP homeostasis and requires ARALAR/AGC1-malate aspartate shuttle in intact cortical neurons. J. Neurosci. 33, 13957–13971, 13971a.

Machler, P., Wyss, M.T., Elsayed, M., Stobart, J., Gutierrez, R., von Faber- Castell, A., Kaelin, V., Zuend, M., San, M.A., Romero-Gomez, I., et al. (2016). In vivo evidence for a lactate gradient from astrocytes to neurons. Cell Metab. 23, 94–102.

Mamczur, P., Borsuk, B., Paszko, J., Sas, Z., Mozrzymas, J., Wisniewski, J.R., Gizak, A., and Rakus, D. (2015). Astrocyte-neuron crosstalk regulates the expression and subcellular localization of carbohydrate metabolism enzymes. Glia 63, 328–340.

Mayrhofer, J.M., Haiss, F., Haenni, D., Weber, S., Zuend, M., Barrett, M.J., Ferrari, K.D., Maechler, P., Saab, A.S., Stobart, J.L., et al. (2015). Design and performance of an ultra-flexible two-photon microscope for in vivo research. Biomed. Opt. Express 6, 4228–4237.

Morris, C.E., Wang, J.A., and Markin, V.S. (2003). The invagination of excess surface area by shrinking neurons. Biophys. J. 85, 223–235.

Ohkura, M., Sasaki, T., Sadakari, J., Gengyo-Ando, K., Kagawa-Nagamura, Y., Kobayashi, C., Ikegaya, Y., and Nakai, J. (2012). Genetically encoded green fluorescent $Ca^{2+}$ indicators with improved detectability for neuronal $Ca^{2+}$ signals. PLoS One 7, e51286.

Pandya, J.D., Nukala, V.N., and Sullivan, P.G. (2013). Concentration depen- dent effect of calcium on brain mitochondrial bioenergetics and oxidative stress parameters. Front. Neuroenergetics 5, 10.

Pellerin, L., and Magistretti, P.J. (1994). Glutamate uptake into astrocytes stimulates aerobic glycolysis: a mechanism coupling neuronal activity to glucose utilization. Proc. Natl. Acad. Sci. U S A 91, 10625–10629.

Pellerin, L., and Magistretti, P.J. (1997). Glutamate uptake stimulates $Na^{+}$,$K^{+}$- ATPase activity in astrocytes via activation of a distinct subunit highly sensitive to ouabain. J. Neurochem. 69, 2132–2137.

Pologruto, T.A., Sabatini, B.L., and Svoboda, K. (2003). ScanImage: flexible software for operating laser scanning microscopes. Biomed. Eng. Online 2, 13.

Porras, O.H., Loaiza, A., and Barros, L.F. (2004). Glutamate mediates acute glucose transport inhibition in hippocampal neurons. J. Neurosci. 24, 9669–9673.

Rangaraju, V., Calloway, N., and Ryan, T.A. (2014). Activity-driven local ATP synthesis is required for synaptic function. Cell 156, 825–835.

Rose, C.R., and Ransom, B.R. (1997). Regulation of intracellular sodium in cultured rat hippocampal neurons. J. Physiol. 499 (Pt 3), 573–587.

Rose, E.M., Koo, J.C., Antflick, J.E., Ahmed, S.M., Angers, S., and Hampson, D.R. (2009). Glutamate transporter coupling to Na,K-ATPase. J. Neurosci. 29, 8143–8155.

Rueda, C.B., Traba, J., Amigo, I., Llorente-Folch, I., Gonzalez-Sanchez, P., Pardo, B., Esteban, J.A., del, A.A., and Satrustegui, J. (2015). Mitochondrial ATP-Mg/Pi carrier SCaMC-3/Slc25a23 counteracts PARP-1-dependent fall in mitochondrial ATP caused by excitotoxic insults in neurons. J. Neurosci. 35, 3566–3581.

Ruminot, I., Gutierrez, R., Pena-Munzenmeyer, G., Anazco, C., Sotelo-Hitschfeld, T., Lerchundi, R., Niemeyer, M.I., Shull, G.E., and Barros, L.F.(2001) NBCe1 mediates the acute stimulation of astrocytic glycolysis by extracellular $K^{+}$. J. Neurosci. 31, 14264–14271.

Saks, V., Beraud, N., and Wallimann, T. (2008). Metabolic compartmentation - a system level property of muscle cells: real problems of diffusion in living cells. Int. J. Mol. Sci. 9, 751–767.

SanMartín, A.,Ceballo, S.,Baeza-Lehnert, F.,Lerchundi, R.,Valdebenito, R., Contreras-Baeza, Y., Alegria, K., and Barros, L.F. (2014). Imaging mitochondrial flux in single cells with a FRET sensor for pyruvate. PLoS One 9, e85780.

SanMartín, A., Ceballo, S., Ruminot, I., Lerchundi, R., Frommer, W.B., and Barros, L.F. (2013). A genetically encoded FRET lactate sensor and its use to detect the Warburg effect in single cancer cells. PLoS One 8, e57712.

Shuttleworth, C.W. (2010). Use of NAD(P)H and flavoprotein autofluorescence transients to probe neuron and astrocyte responses to synaptic activation. Neurochem. Int. 56, 379–386.

Takanaga, H., Chaudhuri, B., and Frommer, W.B. (2008). GLUT1 and GLUT9 as major contributors to glucose influx in HepG2 cells identified by a high sensitivity intramolecular FRET glucose sensor. Biochim. Biophys. Acta 1778, 1091–1099.

Tantama, M., Martinez-Francois, J.R., Mongeon, R., and Yellen, G. (2013). Imaging energy status in live cells with a fluorescent biosensor of the intracel- lular ATP-to-ADP ratio. Nat. Commun. 4, 2550.

Tantama, M., and Yellen, G. (2014). Imaging changes in the cytosolic ATP-to- ADP ratio.

Methods Enzymol. 547, 355–371.

Tarasov, A.I., Semplici, F., Ravier, M.A., Bellomo, E.A., Pullen, T.J., Gilon, P., Sekler, I., Rizzuto, R., and Rutter, G.A. (2012). The mitochondrial $Ca^{2+}$ uni- porter MCU is essential for glucose-induced ATP increases in pancreatic beta-cells. PLoS One 7, e39722.

Tescarollo, F., Covolan, L., and Pellerin, L. (2014). Glutamate reduces glucose utilization while concomitantly enhancing AQP9 and MCT2 expression in cultured rat hippocampal neurons. Front. Neurosci. 8, 246.

Toloe, J., Mollajew, R., Kugler, S., and Mironov, S.L. (2014). Metabolic differ- ences in hippocampal 'Rett' neurons revealed by ATP imaging. Mol. Cell Neurosci. 59, 47–56.

Trevisiol, A., Saab, A.S., Winkler, U., Marx, G., Imamura, H., Mobius, W., Kusch, K., Nave, K.A., and Hirrlinger, J. (2017). Monitoring ATP dynamics in electrically active white matter tracts. Elife 6, https://doi.org/10.7554/eLife.24241.

Westermann, B. (2015). The mitochondria-plasma membrane contact site. Curr. Opin. Cell Biol. 35, 1–6.

Wilson, D.F. (2017). Oxidative phosphorylation: regulation and role in cellular and tissue metabolism. J. Physiol. 595, 7023–7038.

Wyss, M.T., Jolivet, R., Buck, A., Magistretti, P.J., and Weber, B. (2011). In vivo evidence for lactate as a neuronal energy source. J. Neurosci. 31, 7477–7485. Zilberter, Y., and Zilberter, M. (2017). The vicious circle of hypometabolism in neurodegenerative diseases: ways and mechanisms of metabolic correction. J. Neurosci. Res. 95, 2217–2235.

# Supplemental Information

Supplemental Information includes seven figures and can be found with this article online at https://doi.org/10.1016/j.cmet.2018.11.005

# Supporting Citations

The following references appear in the Supplemental Information: Ruminot et al., 2011, Tantama and Yellen, 2014.

# Supplementary Figures

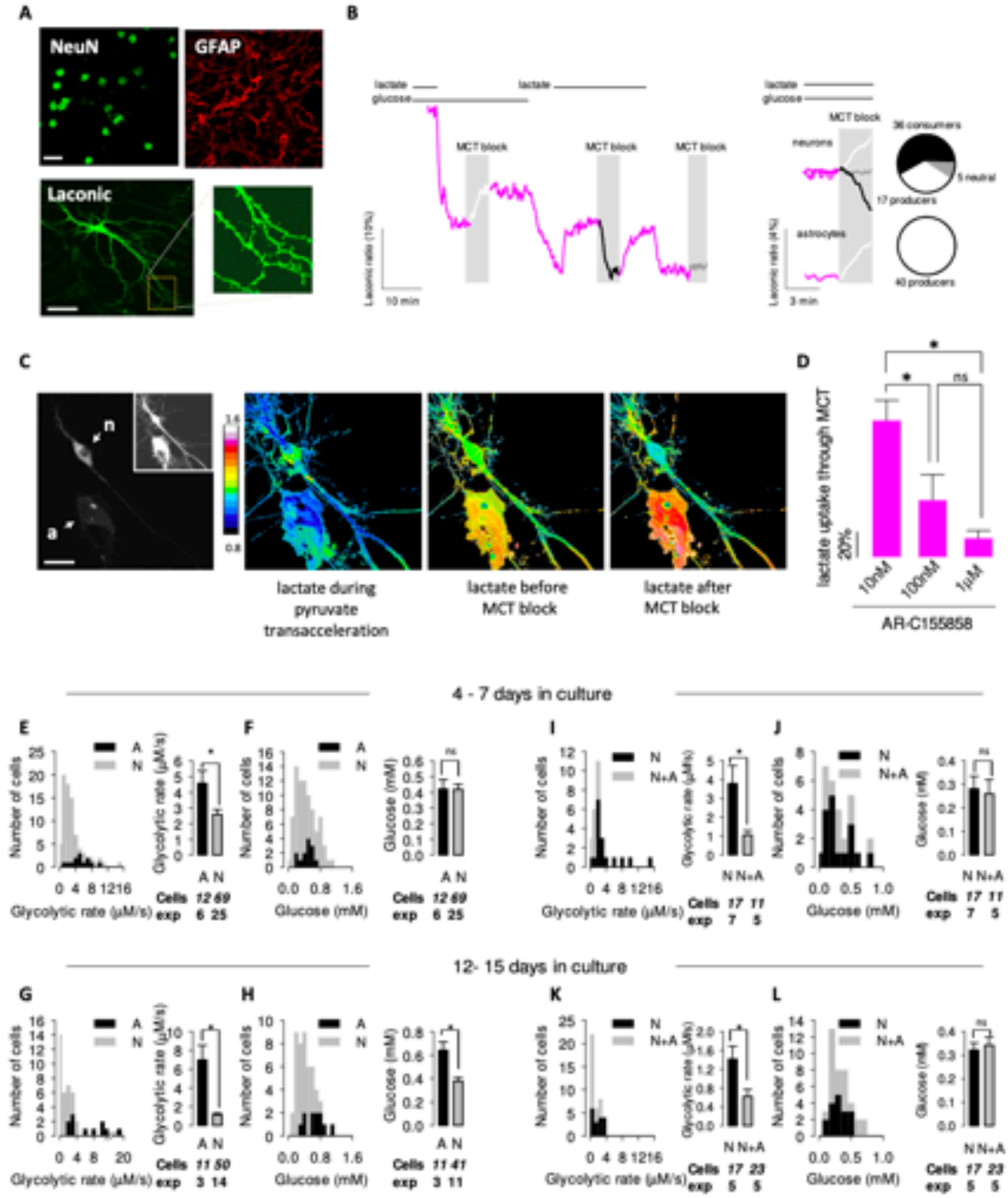

Figure S3.1.: **(related to Fig. 3.1) Characterization of Lactate and Glucose Dynamics in Resting Neurons.**

**(A)** Top panels show a mixed hippocampal culture stained for the neuronal marker NeuN (left) and the astrocytic marker GFAP (right). Bottom panels show a neuron expressing Laconic (Venus channel), with dendritic spines visible in the inset. Scale bars represent 30 μm.

**(B)** Left, differential behavior of neuronal lactate in response to the MCT blocker AR- C155858 (1 μM) in the presence of glucose (2 mM) or lactate (0.1 mM). Data are representative of 7 neurons in three experiments. Right, representative responses of neuronal and astrocytic lactate to 1 μM AR-C155858 in the presence of both glucose (2 mM) and lactate (1 mM). Pie charts summarize the behavior of 58 neurons and 40 astrocytes.

**(C)** Left, a neuron (n) and an astrocyte (a) expressing Laconic. Sensor density is shown as the average of mTFP and Venus intensities. A saturation image of the same field reveals neuronal processes (inset). Scale bar represents 20 $\mu$m. Right, Laconic mTFP/Venus ratios were obtained first in the presence of 5 mM pyruvate, which through accelerated substrate exchange (transacceleration) drives intracellular lactate to a minimum (explained in San Martin et al., 2013; Machler et al., 2016), and then in the presence of 2 mM glucose and 1 mM lactate before and 7 minutes after the addition of 1 μM AR-C155858.

**(D)** The Laconic ratio was measured after a pulse of 1 mM lactate in the absence and presence of the MCT inhibitor AR-C155858, at 10 nM, 100 nM or 1 μM (expressed as % of control, 8 neurons).

**(E-F)** Young cultures. The rate of glucose consumption and the steady-state concentration of glucose concentration were measured in neurons (N, 69 cells in twenty five experiments) and astrocytes (A, 12 cells in six experiments) at 4-7 days in culture using FLII$^{12}$Pglu700μΔ6.

**(G-H)** Mature cultures. The rate of glucose consumption and the steady-state concentration of glucose concentration were measured in neurons (N, 41 cells in eleven experiments for glucose concentration and 50 cells in fourteen experiments for glucose consumption rate) and astrocytes (A, 11 cells in three experiments) at 12-15 days in culture using FLII$^{12}$Pglu700μΔ6. Neuronal cultures were enriched with astrocytes as described in the Methods section.

**(I-J)** Young cultures. Neuronal glucose consumption and glucose concentration were measured in control neuronal cultures (N, 17 cells in seven experiments) or astrocyte- enriched cultures (N+A, 11 cells in five experiments) at 4-7 days in culture using FLII$^{12}$Pglu700μΔ6.

**(K-L)** Mature cultures. Neuronal glucose consumption and glucose concentration were measured in control neuronal cultures (N, 17 cells in five experiments) or astrocyte- enriched cultures (N+A, 23 cells in five experiments) at 12-15 days in culture using FLII$^{12}$Pglu700μΔ6.

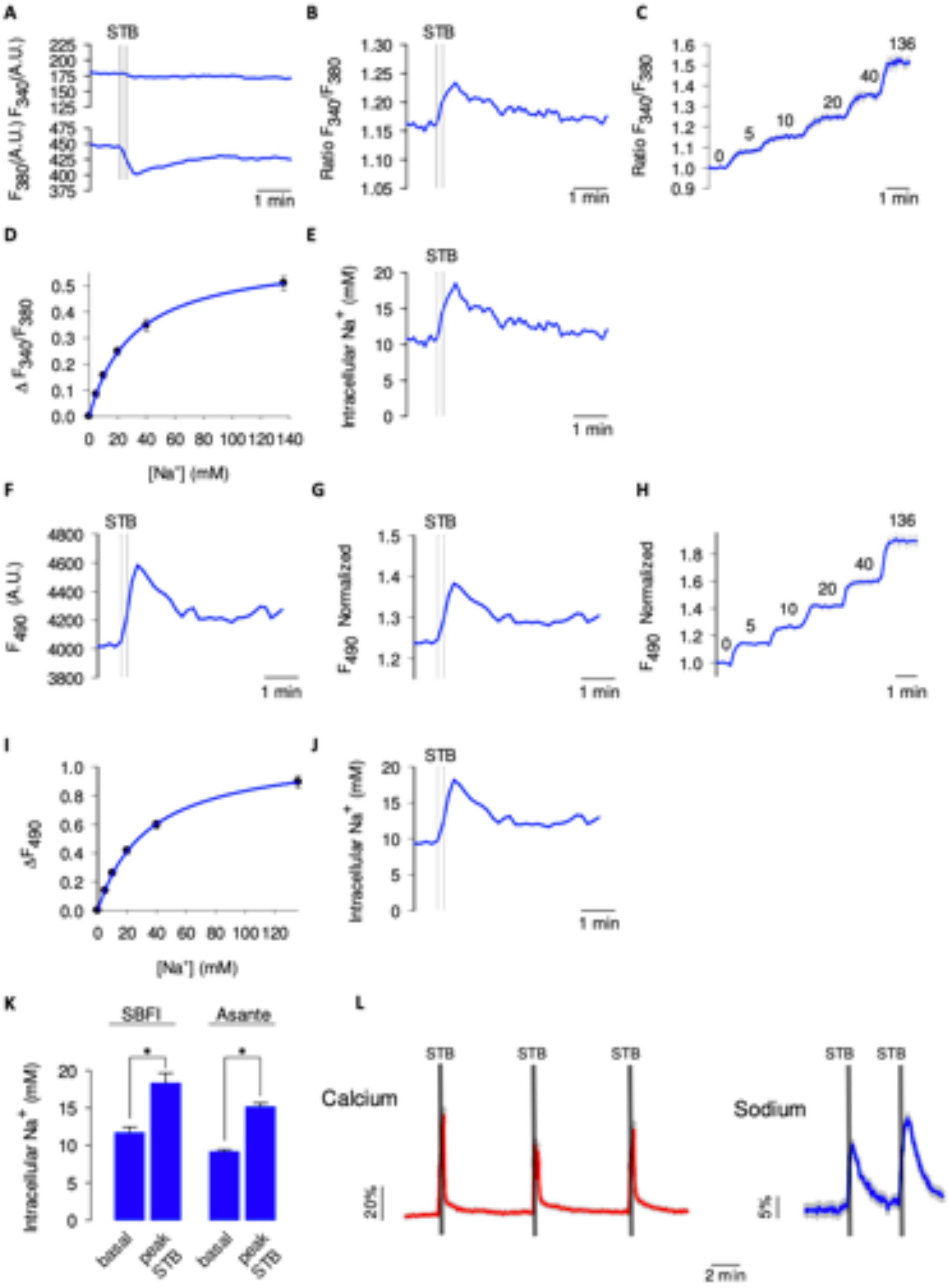
A
STB
$F_{380}$(A.U.) $F_{340}$(A.U.)
225
200
175
150
125
475
450
425
400
375
1 min
B
STB
Ratio $F_{340}/F_{380}$
1.30
1.25
1.20
1.15
1.10
1.05
1 min
C
Ratio $F_{340}/F_{380}$
1.6
1.5
1.4
1.3
1.2
1.1
1.0
0.9
0
5
10
20
40
136
1 min
D
$\Delta F_{340}/F_{380}$
0.5
0.4
0.3
0.2
0.1
0.0
0 20 40 60 80 100 120 140
$[Na^+]$ (mM)
E
STB
Intracellular $Na^+$ (mM)
20
15
10
5
0
1 min
F
STB
$F_{490}$ (A.U.)
4800
4600
4400
4200
4000
3800
1 min
G
STB
$F_{490}$ Normalized
1.5
1.4
1.3
1.2
1 min
H
$F_{490}$ Normalized
1.8
1.6
1.4
1.2
1.0
0
5
10
20
40
136
1 min
I
$\Delta F_{490}$
1.0
0.8
0.6
0.4
0.2
0.0
0 20 40 60 80 100 120
$[Na^+]$ (mM)
J
STB
Intracellular $Na^+$ (mM)
20
15
10
5
0
1 min
K
SBFI
Asante
*
*
Intracellular $Na^+$ (mM)
20
15
10
5
0
basal
peak STB
basal
peak STB
L
Calcium
STB
STB
STB
20%
Sodium
STB
STB
5%
2 min

**Figure S3.2.:** **(related to Fig. 3.2). Quantitation of Intracellular Na$^+$ with SBFI and no Apparent Desensitization in Response to STB Stimulation.**
**(A)** Fluorescence traces of a single SBFI-loaded neuron excited at 340 and 380 nm.
**(B)** Ratio between the traces in A.
**(C-D)** Calibration curve obtained by exposing a group of 8 Na$^+$-permeabilized SBFI-loaded neurons (including the cell in A) to increasing extracellular Na$^+$ concentrations, equimolarly balanced with K$^+$.
**(E)** Transformation of the ratio in B into Na$^+$ concentration using the calibration curve in D.
**(F)** Fluorescence trace of a single Asante-loaded neuron excited at 488 nm.
**(G)** Normalized background-corrected data.
**(H-I)** Calibration curve obtained by exposing a group of 8 Na$^+$-permeabilized Asante- loaded neurons (including the cell in A) to increasing extracellular Na$^+$ concentrations, equimolarly balanced with K.
**(J)** Transformation of the fluorescence data in B into Na$^+$ concentration using the calibration curve in D.
**(K)** Na$^+$ concentrations before and at the peak of the elevation induced by the STB (19 neurons in four experiments with SBFI and 26 cells in three experiments with Asante).
**(L)** Neurons loaded Fluo4 (left, 16 cells) or with SBFI (right, 14 cells) were STB stimulated at the times indicated. Mean ± SEM.

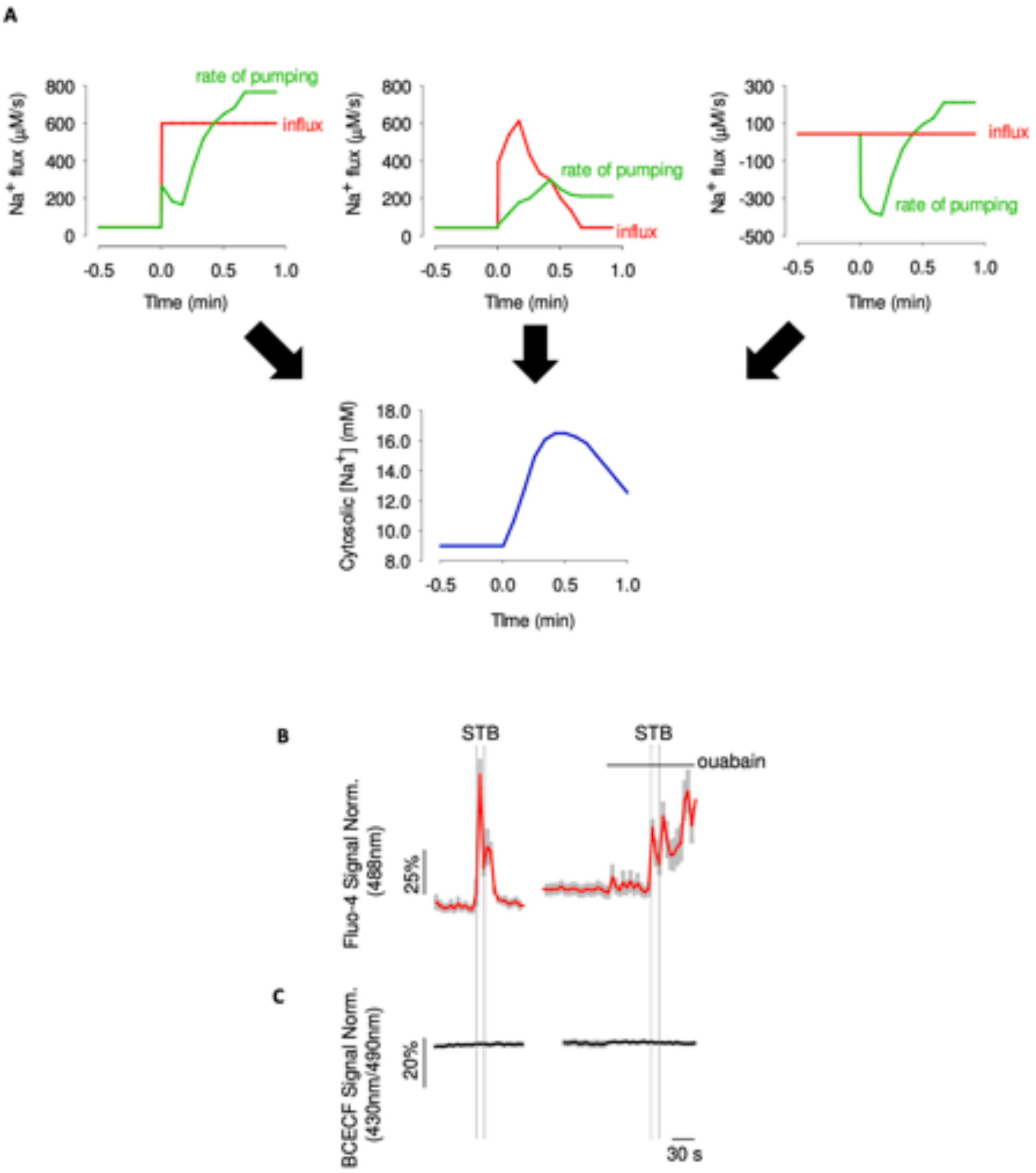

**Figure S3.3.:** **(related to Fig. 3.2). Accompanying Data for the Na$^+$ Pumping Protocol.**

**(A)** The extent of the Na$^+$ load may not be deduced from Na$^+$ concentration alone. Three combinations of influx (Na$^+$ load) and pumping were simulated to render exactly the same time course of Na$^+$ concentration. The example in the middle graph is similar to that estimated in STB-stimulated neurons as measured with the ouabain protocol (Fig. 3.2).

**(B)** The effect of STB on cytosolic Ca$^{2+}$ was measured using Fluo4 in the absence and presence of 0.1 mM ouabain (Mean ± SEM, 11 cells, representative of three paired experiments).

**(C)** The effect of STB on cytosolic pH was measured using BCECF in the absence and presence of 0.1 mM ouabain (Mean ± SEM, 16 cells, representative of three paired experiments).

---

Blank page to keep figures and captions aligned

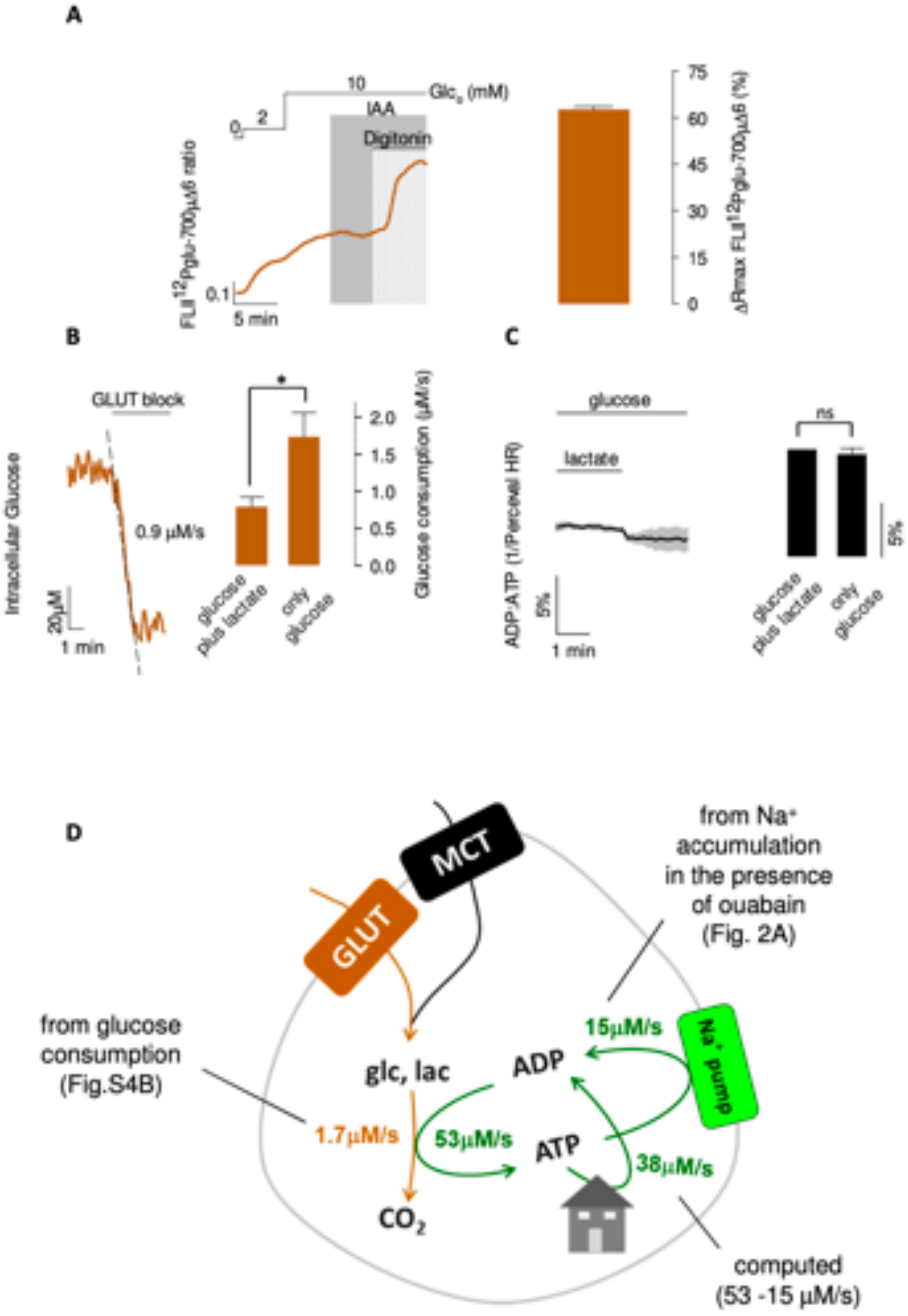
A
0
2
10
Glc$_o$ (mM)
IAA
Digitonin
FLII$^{12}$Pglu-700µΔ6 ratio
0.1
5 min
75
60
45
30
15
0
ΔRmax FLII$^{12}$Pglu-700µΔ6 (%)
B
GLUT block
Intracellular Glucose
0.9 µM/s
20µM
1 min
*
2.0
1.5
1.0
0.5
0.0
Glucose consumption (µM/s)
glucose plus lactate
only glucose
C
glucose
lactate
ADP:ATP (1/Perceval HR)
5%
1 min
ns
5%
glucose plus lactate
only glucose
D
MCT
GLUT
from Na+ accumulation in the presence of ouabain (Fig. 2A)
from glucose consumption (Fig.S4B)
glc, lac
ADP
15µM/s
Na+ pump
1.7µM/s
53µM/s
ATP
38µM/s
CO$_2$
computed (53 -15 µM/s)

**Figure S3.4.:** **(related to Fig. 3.2). Estimation of Housekeeping ATP Consumption.** **(A)** Dynamic range of FLII$^{12}$Pglu700µΔ6 in neurons. Cells were exposed to increasing extracellular glucose followed by the glycolytic blocker iodoacetic acid (IAA, 0.5 mM) and permeabilization with 0.002% digitonin. The FRET ratio change estimated in this manner was about 60%, similar to that described *in vitro* (Takanaga et al., 2008) and in other mammalian cell types (Bittner et al., 2010; 5 cells in five experiments). **(B)** Left, example of glucose consumption measurement in a single neuron using the GLUT blocker cytochalasin B (20 µM) in the presence of 2 mM glucose and 1 mM lactate. The bar graph represents paired rates of glucose consumption (Mean + SEM) in the presence of 2 mM glucose alone or in 2 mM glucose plus 1 mM lactate (16 cells in six experiments). **(C)** Effect of lactate removal on Perceval HR, Mean ± SEM (12 cells from twelve experiments). Bars represent mean + SEM before and 30 seconds after lactate removal. **(D)** Procedure to calculate housekeeping ATP consumption. Assuming 31 molecules of ATP generated per each fully oxidized glucose, the measured rate of 1.7 µM/s (from B) translates into 53 µM/s of ATP. Assuming a stoichiometry of 3 $Na^+$ ions pumped per ATP, the measured rate of resting $Na^+$ pumping of 46 µM/s (Fig. 3.2A) translates into 15 µM/s of ATP consumption. The rest of ATP consumption (38 µM/s) is attributed to housekeeping functions.

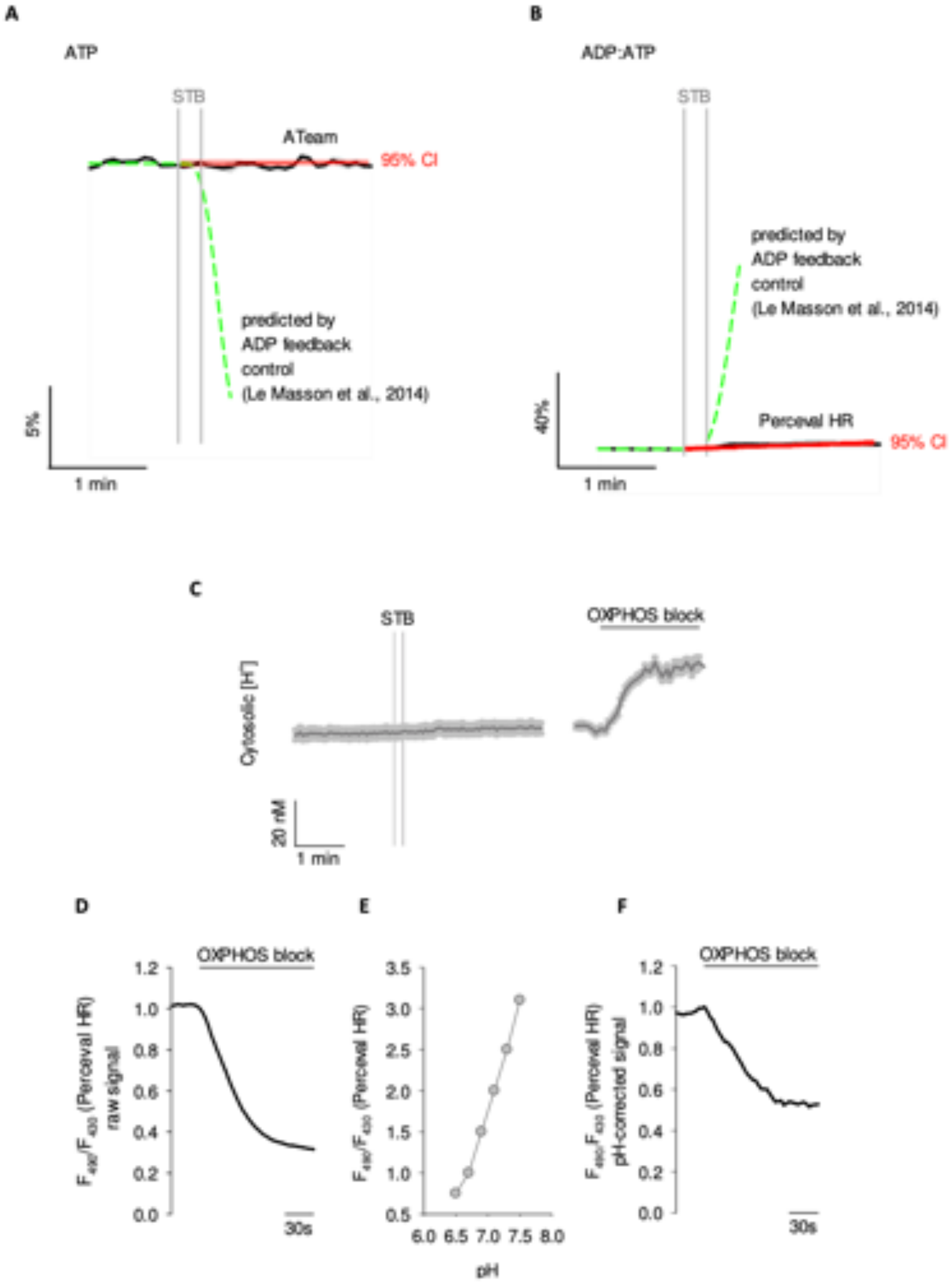
A
ATP
STB
ATeam
95% CI
predicted by
ADP feedback
control
(Le Masson et al., 2014)
5%
1 min
B
ADP:ATP
STB
predicted by
ADP feedback
control
(Le Masson et al., 2014)
Perceval HR
95% CI
40%
1 min
C
STB
OXPHOS block
Cytosolic [H+]
20 nM
1 min
D
OXPHOS block
F490/F430 (Perceval HR)
raw signal
1.2
1.0
0.8
0.6
0.4
0.2
0.0
30s
E
F490/F430 (Perceval HR)
3.5
3.0
2.5
2.0
1.5
1.0
0.5
6.0 6.5 7.0 7.5 8.0
pH
F
OXPHOS block
F490/F430 (Perceval HR)
pH-corrected signal
1.2
1.0
0.8
0.6
0.4
0.2
0.0
30s

Figure S3.5.: **(related to Fig. 3.3). The Invariance of ATP and ADP After Neurotransmission is not Explained by Adenine Nucleotide Feedback Based on Explicit Setpoints and no Detectable pH Effect of STB and pH Correction of Perceval HR.**

**(A-B)** Black lines illustrate the ATP **(A)** and ADP:ATP **(B)** responses to STB stimulation respectively measured with ATeam (Mean ± SEM; 16 cells in ten experiments) and Perceval HR (Mean ± SEM; 15 cells in fifteen experiments). The interrupted green lines correspond to the responses predicted by negative adenine nucleotide feedbacks operating through explicit setpoints, as described by Le Masson et al., 2014 (see Methods).

**(C)** Effects of STB and OXPHOS blockage (5mM azide) on cytosolic $H^+$ concentration measured with BCECF as detailed in Ruminot et al. (2011), 12 cells in a single experiment, representative of four separate experiments.

**(D)** Raw signal of Perceval HR after exposure to 5mM azide.

**(E)** pH-sensitivity of Perceval HR, data are from (Tantama and Yellen, 2014).

**(F)** Data in B is shown after correction according to the pH-sensitivity relationship of C.

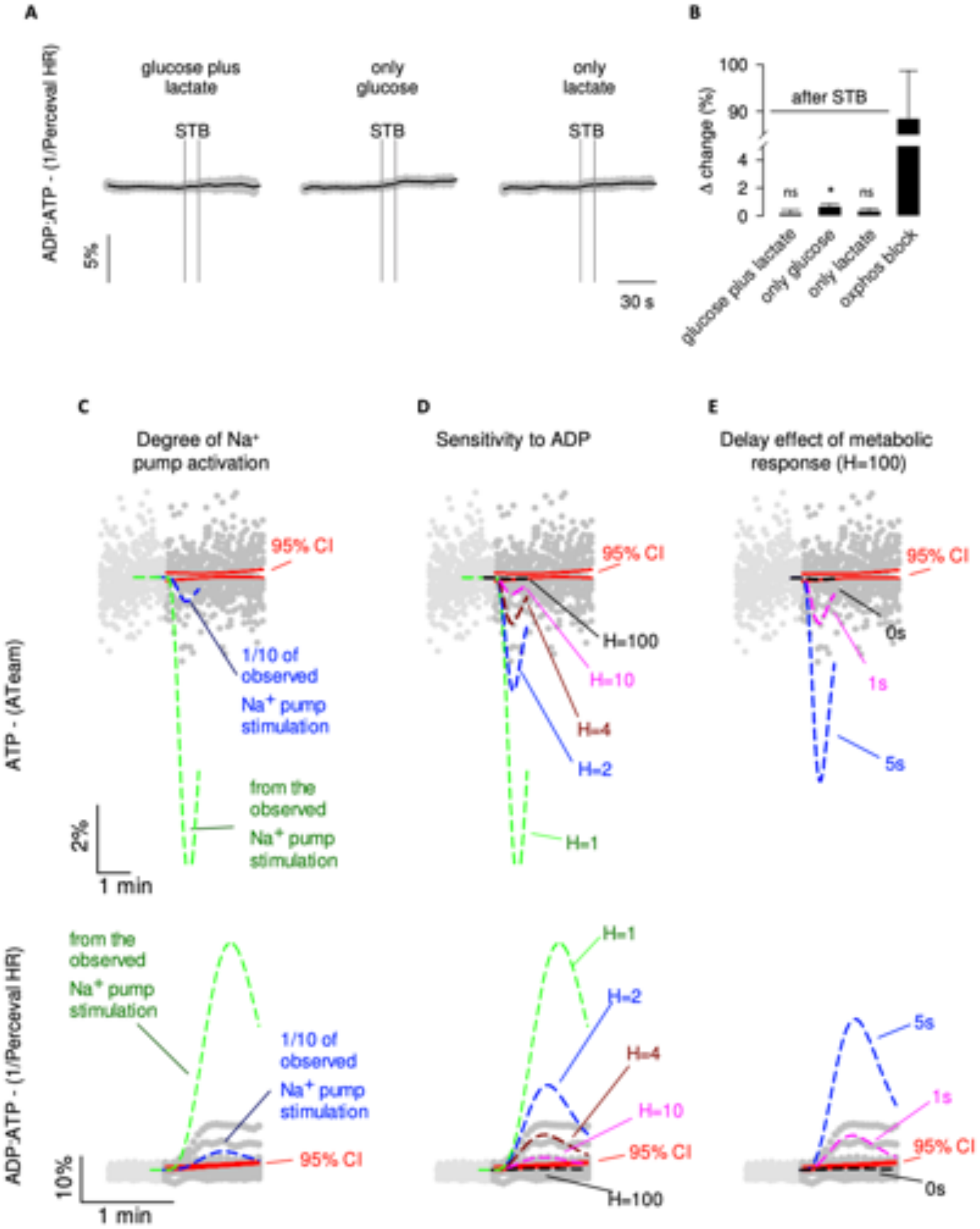
A
ADP:ATP - (1/Perceval HR)
glucose plus lactate
only glucose
only lactate
STB
STB
STB
5%
30 s
B
Δ change (%)
100
90
4
2
0
after STB
ns
*
ns
glucose plus lactate
only glucose
only lactate
oxphos block
C
Degree of Na+ pump activation
D
Sensitivity to ADP
E
Delay effect of metabolic response (H=100)
ATP - (ATeam)
95% CI
1/10 of observed Na+ pump stimulation
from the observed Na+ pump stimulation
2%
1 min
95% CI
H=100
H=10
H=4
H=2
H=1
95% CI
0s
1s
5s
ADP:ATP - (1/Perceval HR)
from the observed Na+ pump stimulation
1/10 of observed Na+ pump stimulation
95% CI
10%
1 min
H=1
H=2
H=4
H=10
95% CI
H=100
5s
1s
95% CI
0s

**Figure S3.6.:** **(related to Fig. 3.3). Effect of STB on Neuronal Energetics in the Presence of Different Fuels and Sensitivity Analysis of the Homeostatic Response to the $Na^+$ Load.**

**(A)** Perceval HR-expressing neurons fueled with 2 mM glucose plus 1 mM lactate, only 2 mM glucose or only 1mM lactate were exposed to STB (Mean ± SEM; 12 cells in twelve experiments).

**(B)** Summary of the data shown in A, expressed as the change (%) in ratio from before to 30s after the onset of the STB. The large change in ratio elicited by OXPHOS inhibition is shown as a reference. Scatter plots show data obtained with ATeam (middle row) and Perceval HR (bottom row), before (light grey) and after (dark grey) STB stimulation. 95% confidence intervals for the average are shown in red.

**(C)** The impact of ATP expenditure by the $Na^+$ pump on ATP and ADP:ATP was simulated under conventional ADP feedback assuming the observed degree of $Na^+$ pump stimulation (green lines) or in a hypothetical scenario in which $Na^+$ pumping increased one tenth of what was observed (blue lines).

**(D)** The ADP feedback response to ATP expenditure by the $Na^+$ pump was simulated at Hill coefficients **(H)** of 1 (green), 2 (blue), 4 (brown), 10 (pink) and 100 (black). For equations, see Methods.

**(E)** The ADP feedback response to ATP expenditure by the $Na^+$ pump was simulated at a Hill coefficient of 100 assuming instant activation (0 s; black) or introducing delays of 1 s (pink) or 5 s (blue).

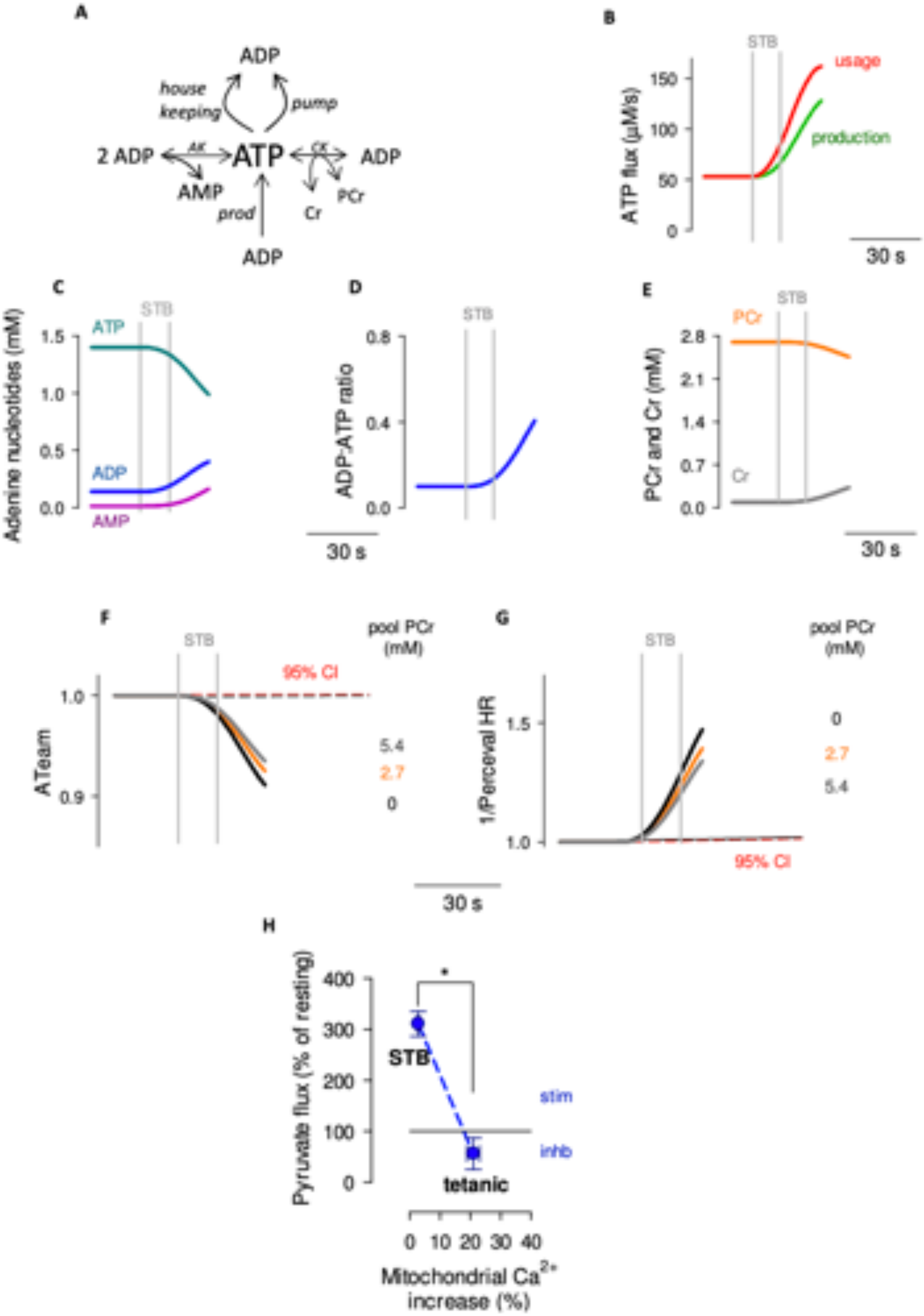
A
ADP
house keeping
pump
2 ADP
AK
ATP
CK
ADP
AMP
PCr
Cr
prod
ADP
B
STB
usage
production
ATP flux (μM/s)
150
100
50
0
30 s
C
STB
ATP
ADP
AMP
Adenine nucleotides (mM)
1.5
1.0
0.5
0.0
D
STB
ADP:ATP ratio
0.8
0.4
0.0
30 s
E
STB
PCr
Cr
PCr and Cr (mM)
2.8
2.1
1.4
0.7
0.0
30 s
F
STB
95% CI
pool PCr (mM)
ATeam
1.0
0.9
5.4
2.7
0
30 s
G
STB
pool PCr (mM)
1/Perceval HR
1.5
1.0
0
2.7
5.4
95% CI
H
*
Pyruvate flux (% of resting)
400
300
200
100
0
STB
stim
inhb
tetanic
0 10 20 30 40
Mitochondrial Ca2+ increase (%)

**Figure S3.7.:** **(related to Fig. 3.3). Simulation of Conventional Energy Homeostasis Based on Linear ADP Feedback and Negative Correlation Between the Magnitude of the Mitochondrial Ca$^{2+}$ Increase and the Stimulation of Mitochondrial Pyruvate Flux.**

**(A)** Kinetic model of adenine nucleotide homeostasis, in which the ATP pool is fed by the sum of glycolytic and mitochondrial production (prod) and consumed by the activity of the Na$^{+}$/K$^{+}$ ATPase (pump) and other processes (housekeeping). The ATP pool is buffered by the actions of adenylate kinase (AK) and creatine kinase (CK). See equations and parameters in Methods.

**(B)** Homeostatic response of ATP production (green) to the increase in ATP usage (red) measured after STB (from Fig. 3.2D).

**(C-E)** Variation of adenine nucleotides, ADP:ATP ratio, phosphocreatine (PCr) and creatine (Cr).

**(F-G)** Impact of STB on the relative ATeam signal **(F)** and reciprocal Perceval HR signal **(G)** at increasing phosphocreatine concentrations. The interrupted lines show the 95% confidence intervals of the observed ATeam and Perceval HR signals (from Figs. 3A-B). **(H)** Neurons expressing Pyronic and loaded with Rhod2 were exposed to STB (11 neurons in five experiments) or to tetanic stimulation (20 Hz for 30s), 8 neurons in seven experiments) during measurement of mitochondrial pyruvate uptake using 1 µM AR- C155858.

# 4

# Arousal-Induced Cortical Activity Triggers Lactate Release From Astrocytes

Originally published in Nature Metabolism, 2, 179-191 (2020)
DOI 10.1038/s42255-020-0170-4

## Authors and Affiliations

Marc Zuend[1,2], Aiman S Saab[1,2,7], Matthias T Wyss[1,2,7], Kim David Ferrari[1,2], Ladina Hösli[1,2], Zoe J Looser[1,2], Jillian L Stobart[1,2], Jordi Duran[4,6], Joan J Guinovart[4,5,6], L Felipe Barros[3] and Bruno Weber[1,2*]

[1] Institute of Pharmacology and Toxicology, University of Zurich, 8057 Zurich, Switzerland
[2] Neuroscience Center Zurich, University of Zurich and ETH Zurich, 8057 Zurich, Switzerland
[3] Centro de Estudios Científicos, Valdivia 5110466, Chile
[4] Institute for Research in Biomedicine, Barcelona, Spain
[5] Department of Biochemistry and Molecular Biology, University of Barcelona, Barcelona, Spain
[6] Centro de Investigación Biomédica en Red de Diabetes y Enfermedades Metabólicas Asociadas, Barcelona, Spain
[7] These authors contributed equally to this work.

Correspondence: Bruno Weber bweber@pharma.uzh.ch

## Personal Contribution

Characterization of the GYS1 KO mutants. Reviewing the manuscript.

# Summary

It has been suggested that, in states of arousal, release of noradrenaline and β-adrenergic signalling affect long-term memory formation by stimulating astrocytic lactate production from glycogen. However, the temporal relationship between cortical activity and cellular lactate fluctuations upon changes in arousal remains to be fully established. Also, the role of β-adrenergic signaling and brain glycogen metabolism on neural lactate dynamics *in vivo* is still unknown. Here, we show that arousal-induced increase in cortical activity triggers lactate release into the extracellular space that correlates with a fast and prominent lactate dip in astrocytes. The immediate drop in astrocytic lactate concentration and the parallel increase in extracellular lactate levels underline an activity-dependent lactate release from astrocytes. Moreover, when β-adrenergic signaling is blocked or brain is depleted of glycogen, the arousal-evoked cellular lactate surges are significantly reduced. We provide *in vivo* evidence that cortical activation upon arousal triggers lactate release from astrocytes, a rise in intracellular lactate levels mediated by β-adrenergic signaling and the mobilization of lactate from glycogen stores.

# Introduction

The brain is almost exclusively fueled by glucose oxidation[1]. Acute elevations in brain activity are met with a transient net increase in aerobic glycolysis and the production of lactate that is released into the extracellular space[2,3]. However, the primary cellular source of this activity-driven lactate release remains a matter of debate[4-7]. A long-standing hypothesis is that astrocytes increase their glycolysis in response to neuronal activity to cover neuronal ATP demand with lactate[5-8]. Many studies have expanded this metabolic support model (see references in[7]). Nevertheless, *in vivo* evidence of activity-evoked lactate release from astrocytes to neurons is still unavailable. Clearly, neurons are able to maintain their activity *in vivo* with a lactate supply[9] and an *in vivo* lactate gradient from astrocytes to neurons favors astrocytic shuttling of lactate to neurons[10]. However, recent studies suggest that neurons increase their glycolytic activity upon stimulation and may also release lactate[11].

At a behavioral level, lactate mobilization from glycogen, primarily stored in astrocytes, has been shown to promote long-term memory formation[3, 12-14]. In particular, emotionally-driven memory formation induced by stress or arousal, involves β-adrenergic signaling and lactate release from astrocytes[15,16]. During arousal, noradrenaline released from locus coeruleus projections strongly activates astrocytes[17] and could have diverse metabolic functions, including activation of glycogenolysis[18-20]. Apart from serving as an energy substrate, lactate also regulates neuronal excitability by modulating ATP-sensitive potassium (KATP) channels[21,22] or direct action on membrane receptors[23,24]. Despite evidence that lactate has various functions including the regulation of wakefulness, brain plasticity and memory consolidation, the pathways and mechanisms that mediate astrocytic lactate release *in vivo* remain to be determined.

In this paper, we have addressed the way in which fast changes in cortical activity modulate lactate dynamics in astrocytes and neurons in awake behaving mice. We found that a startle response triggers a rapid lactate release from astrocytes, which is followed by increased lactate levels in neurons. The startle-evoked lactate surges were in part mediated by β-adrenergic signaling and derived from glycogen stores. Our results show that cortical astrocytes integrate local neurosensory input and brain-wide neuromodulatory signals to cover immediate ambient energy needs *in vivo*.

# Results

## Lactate Dynamics in Neurons and Astrocytes in Response to Acute Isoflurane Exposure

We studied how state-dependent changes in cortical activity impact neuronal and astrocytic lactate levels in awake behaving mice. Mice were trained for head-restrained, awake two-photon imaging of genetically encoded sensors for lactate (called Laconic[25]) and calcium (GCaMP6s[26] and RCaMP1.07 (ref.[27]) (Figure 4.1a and Extended Data S4.1). Volatile anesthetics like isoflurane are known to induce changes in cortical activity[28-30]. We exposed mice to isoflurane for 20 minutes (1.5%) while monitoring lactate level changes in cortical neurons and astrocytes (Extended Data S4.2). Prolonged exposure to isoflurane caused a significant increase in intracellular lactate levels in both astrocytes and neurons, which remained elevated during the isoflurane period. Critically, at the onset

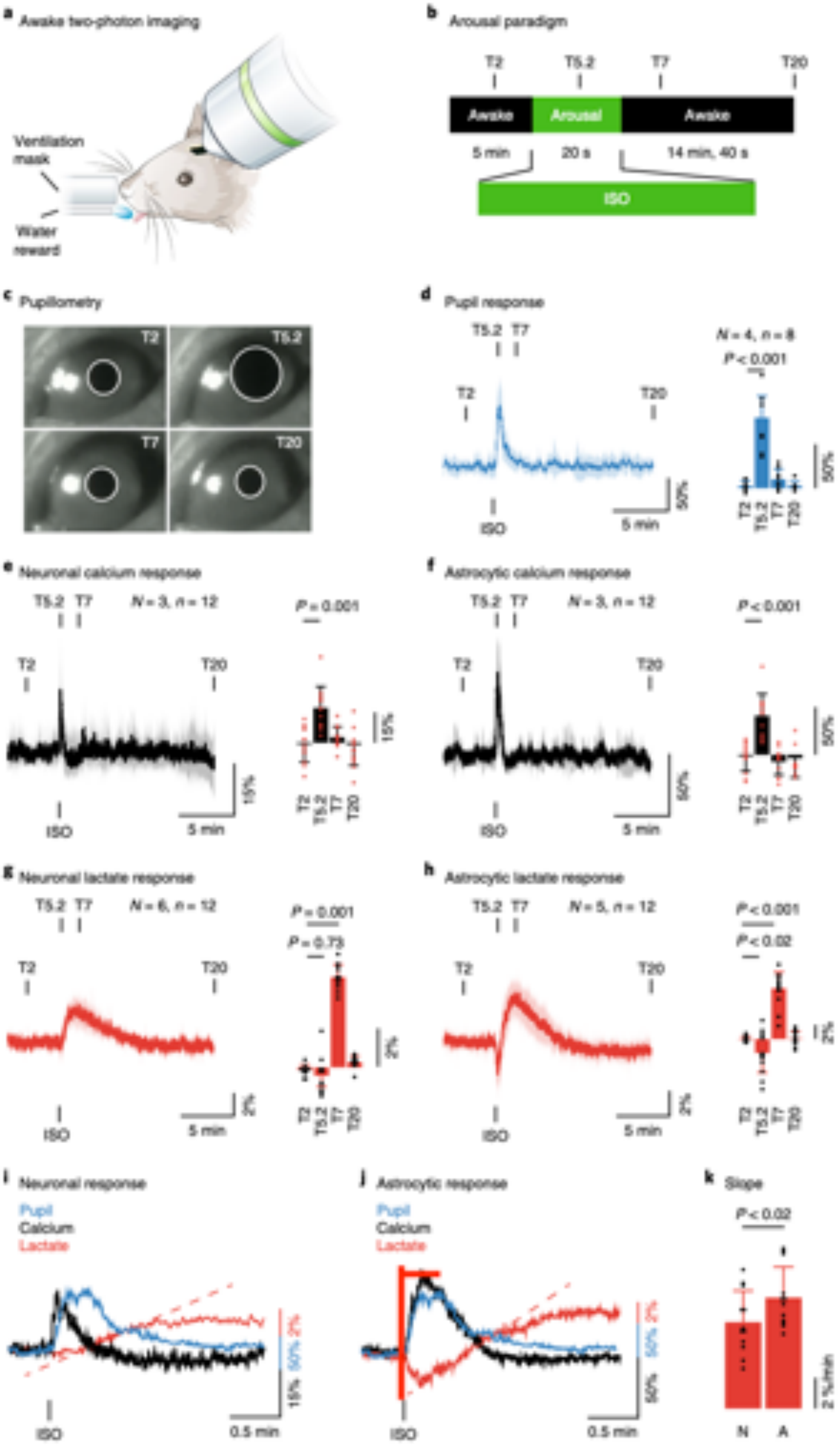
a Awake two-photon imaging
Ventilation mask
Water reward
b Arousal paradigm
T2
T5.2
T7
T20
Awake
Arousal
Awake
5 min
20 s
14 min, 40 s
ISO
c Pupillometry
T2
T5.2
T7
T20
d Pupil response
T5.2 T7
T2
T20
ISO
5 min
50%
N = 4, n = 8
P < 0.001
50%
T2
T5.2
T7
T20
e Neuronal calcium response
T5.2 T7
N = 3, n = 12
T2
T20
ISO
5 min
15%
P = 0.001
15%
T2
T5.2
T7
T20
f Astrocytic calcium response
T5.2 T7
N = 3, n = 12
T2
T20
ISO
5 min
50%
P < 0.001
50%
T2
T5.2
T7
T20
g Neuronal lactate response
T5.2 T7
N = 6, n = 12
T2
T20
ISO
5 min
2%
P = 0.001
P = 0.73
2%
T2
T5.2
T7
T20
h Astrocytic lactate response
T5.2 T7
N = 5, n = 12
T2
T20
ISO
5 min
2%
P < 0.001
P < 0.02
2%
T2
T5.2
T7
T20
i Neuronal response
Pupil
Calcium
Lactate
ISO
0.5 min
2%
50%
15%
j Astrocytic response
Pupil
Calcium
Lactate
ISO
0.5 min
2%
50%
50%
k Slope
P < 0.02
2 %/min
N
A

Figure 4.1.: **Startle-Induced Calcium and Lactate Elevations in Neurons and Astrocytes.**
**a,** Animals were trained for head-restrained, awake two-photon imaging. A water spout was used for reward delivery and a ventilation mask for isoflurane supply. **b,** Paradigm to induce arousal in awake mice. **c,d,** A brief isoflurane pulse (ISO) induces pupil dilation (T5.2) without a subsequent miosis. White circles indicate pupil size approximation **(c)** used to calculate percentage changes from baseline values at T2 (d). The time point of isoflurane onset (T5) is indicated by ISO. **e,f,** Neurons **(e)** and astrocytes **(f)** immediately respond with an increase in calcium (T5.2) upon ISO pulse. Relative calcium changes normalized to baseline are quantified at time points T2, T5.2, T7 and T20 (bar graphs). **g,h,** Lactate level changes in neurons **(g)** and astrocytes **(h)**. Arousal induces lactate level elevations in both cell types (T7). Note that only astrocytes reveal a significant dip in lactate levels immediately after the ISO pulse (T5.2). Quantification of relative lactate level changes at time points T2, T5.2, T7 and T20 (bar graphs). The time point of isoflurane onset (T5) is indicated by ISO. Data set comprised 226 neurons and 236 astrocytes. **i,j,** Overlay of pupil (blue), calcium (black) and lactate responses (red) in neurons **(i)** and astrocytes **(j)**. Note that in astrocytes the evoked calcium response strongly coincides with the immediate, initial drop in lactate levels. Dashed lines are indicated for slope analysis shown in **(k)**. **k,** Response slopes of the evoked lactate rise. Astrocytes revealed a faster lactate level rise (8.3 ± 1.1 %/min) compared to neurons (4.7 ± 3.3 %/min; $p < 0.02$). T indicates time points in minutes. N = number of animals, n = number of experiments. Data is represented as mean ± SD. m = 8 experiments for pupil, 12 for calcium and 12 for lactate used to derive statistics. Mean statistics were calculated using two-sided linear mixed-effects models and Tukey post hoc tests.

of isoflurane exposure (within 10-20 s) we observed a significant and transient drop in lactate levels specifically in astrocytes but not in neurons (Extended Data S4.2b, c). After stopping isoflurane, lactate levels completely recovered to baseline levels within 20.2 ± 6.0 min and 17.7 ± 7.1 min, in neurons and astrocytes respectively.

## Isoflurane Exposure Causes an Initial Arousal Response Before Induction of Anesthesia

The biphasic lactate response observed in astrocytes upon isoflurane exposure, consisting of an initial dip, followed by a rise in lactate concentration (Extended Data S4.2c), could be triggered by distinct phases of isoflurane-induced brain states[29]. Isoflurane and other general anesthetics are known to cause an initial arousal before the anesthetized state[30,31]. Hence, we investigated the way in which our isoflurane protocol impacts overall brain activity (Extended Data S4.3) and cortical calcium dynamics in neurons and astrocytes (Extended Data S4.4). First, we studied brain activity patterns with electroencephalography (EEG) recordings (Extended Data S4.3a-d). Indeed, exposure to isoflurane elicited

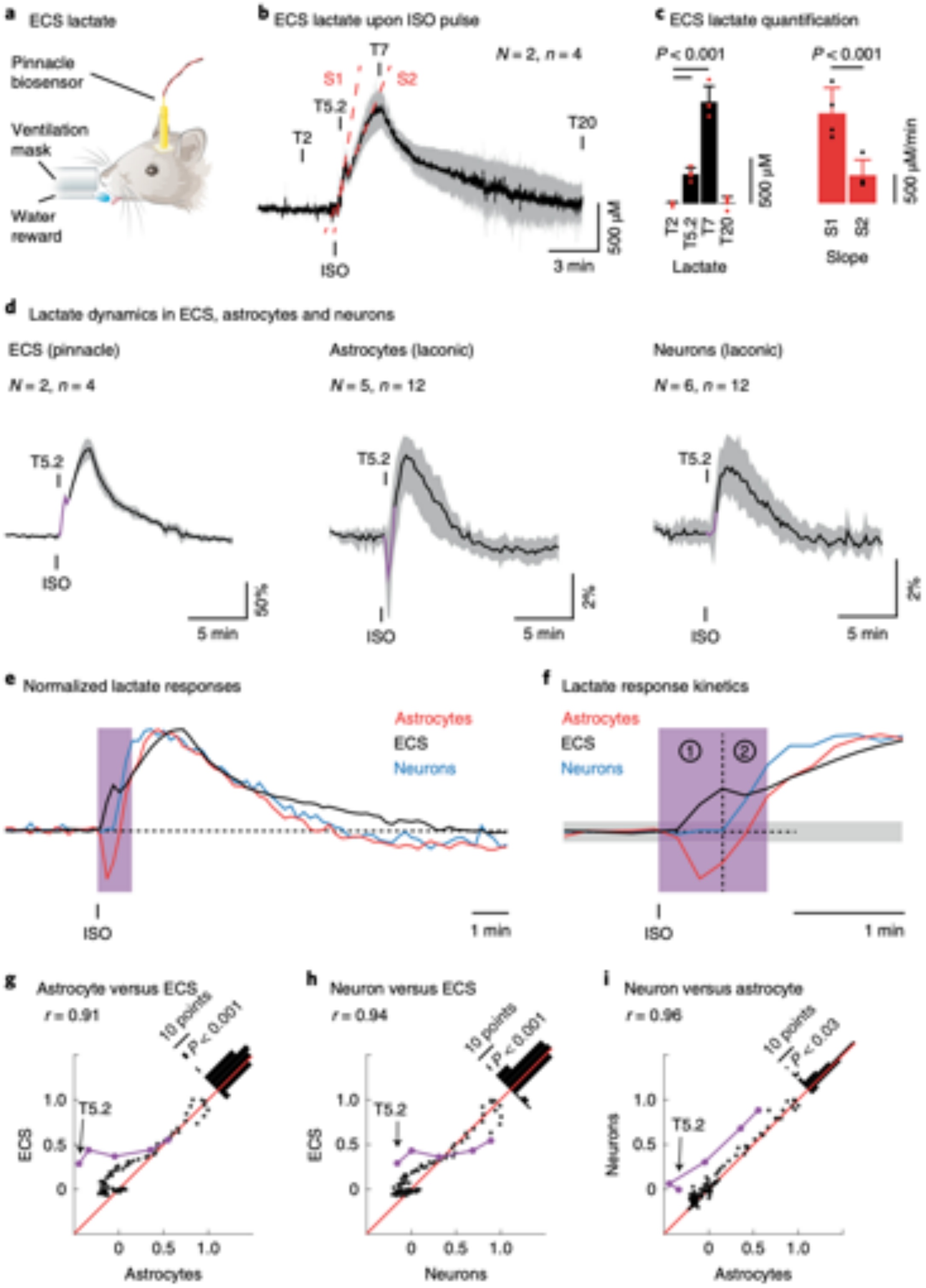

changes in EEG patterns (Extended Data S4.3a, b). Within seconds of isoflurane exposure, we observed a significant increase in high-frequency spectrum typically associated with cortical desynchronization[32,33]. Cortical desynchronization was followed by an increase in slow-wave oscillations until EEG patterns reached the burst suppression found during deep anesthesia[34,35]. The initial EEG band shifts observed upon isoflurane exposure (Extended Data S4.3c, d) strongly correlated with changes normally observed during an arousal response[32,36]. This was further corroborated with electromyography (EMG) recordings and by monitoring the pupil response (Extended Data S4.3e, f). Acute pupil dilations are a non-invasive estimate of changes in brain states and neuromodulatory inputs to the cortex. Consistent with our EEG recordings, shortly upon isoflurane exposure, EMG

Figure 4.2.: **Lactate Response Kinetics Suggest an Activity-Dependent Release of Lactate From Astrocytes.**
**a,** Scheme of extracellular space (ECS) lactate recordings using a pre-calibrated Pinnacle lactate biosensor inserted into the somatosensory cortex. **b,** ECS lactate level changes in response to isoflurane (ISO) pulse. Note that the ECS lactate surge has two distinct slopes (S1 and S2; $p < 0.001$) indicated by dashed red lines. **c,** Quantification of ECS lactate surges. m = 4 experiments used to derive statistics. Mean statistics were calculated using two-tailed linear mixed-effects models and Tukey post hoc tests at different time points. **d,** Direct comparison of the arousal-evoked lactate responses of the three compartments. Purple section of curves indicates the first 60 s upon ISO pulse. T5.2 represents the first data point 12 s after ISO pulse. Data is represented as mean ± SD. **e,** Normalized lactate responses from astrocytes, neurons and ECS. **f,** Magnification of the time course depicted in **(e)** around the ISO pulse to better visualize lactate response kinetics. Purple shaded area indicates first 60 s upon ISO pulse and gray shaded area indicates margins of 2 standard deviations (SD) from the baseline of all 3 recordings. Two distinct phases are highlighted. First phase (1): Lactate level drop in astrocytes parallels rise in the ECS; Second phase (2): Neuronal lactate rise slows down ECS lactate surge. **g-i,** Time series comparison of normalized data from **(d)** between neuronal, astrocytic and ECS responses. Direct comparison of ECS with astrocytes upon arousal (T5.2 onwards) shows a decrease in association, a significant left shift from the identity line (red), in favor of ECS lactate increases, as revealed by the distribution of data points in the histogram (top right corner). Overall comparison reveals that ECS shows the fastest increase in lactate levels followed by astrocytes and neurons. Arrow indicates first data point after ISO pulse (T5.2). m = 12 for neurons, m = 12 for astrocytes and m = 4 experiments used to derive statistics. Correlation (R) was computed with Pearson's linear correlation coefficient at a significance level of 0.05. Histogram (top right) showing data distribution of mean values compared to identity line (correlation of 1; red) and statistical analysis of differences between compartments (two-tailed paired t-test).

electrical activity significantly increased by 67.6 ± 21.5% and pupils dilated by 51.3 ± 31.7 % (Extended Data S4.3g, i). In the subsequent anesthetized state, muscle activity (EMG) and pupil size were strongly reduced by 40.1 ± 16.5 % and 47.0 ± 17.1 %, respectively (Extended Data S4.3g, i). Taken together, our EEG, EMG and pupil size measurements confirmed a rapid and transient arousal response before the onset of the anesthetized state.

The state of elevated arousal has been shown to evoke cortical calcium bursts in astrocytes[17] and neurons[36]. We therefore examined the cortical calcium activity during prolonged isoflurane exposure by monitoring cellular calcium dynamics using a combination of two calcium sensors, RCaMP 1.07 (ref. [27]) in neurons and GCaMP6s[26] in astrocytes, expressed in the same field of view (Extended Data S4.4). Immediately upon isoflurane exposure there was a significant and transient calcium whole frame fluorescence intensity elevation in both neurons and astrocytes (Extended Data S4.4b, c). Moreover, automated analysis of calcium signals[237,38] revealed a two-fold increase in calcium events in response to isoflurane exposure in both neurons and astrocytes (Extended Data S4.4d, e). Noteworthy, during the subsequent anesthetized state calcium signal intensity and spontaneous activity in neurons and astrocytes were substantially reduced (Extended Data S4.4b-e). Both calcium fluorescence intensities and event frequencies returned to baseline values when isoflurane application was stopped. We find that the overall calcium dynamics observed in astrocytes and neurons are in line with our EEG, EMG and pupillometry measurements showing an initial increase in cellular activity upon isoflurane administration.

## Arousal Triggers Lactate Release From Astrocytes

Our EEG, EMG and pupil size measurements, as well as our cortical calcium recordings, provide convincing evidence that when administered, isoflurane initially causes an immediate, strong arousal response. Thus, we wondered whether brief isoflurane pulses would lead to arousal-evoked cortical lactate fluctuations. We therefore adapted our protocol and exposed awake mice to a brief 20 s isoflurane pulse (ISO pulse; Figure 4.1b). As expected, the ISO pulse triggered a large pupil dilation without causing subsequent pupil constriction, indicating that we were only inducing a startle response (Figure 4.1c, d). This was further corroborated by measuring cortical calcium dynamics. Indeed, the

ISO pulse elicited a significant calcium transient in both neurons and astrocytes (Figure 4.1e, f).

Next, we examined how arousal impacts lactate levels in cortical neurons and astrocytes. Arousal-induced calcium and lactate recordings were each performed in the same animal using a multi-viral injection approach (Extended Data S4.1d, e). In both neurons and astrocytes, lactate levels were significantly increased by 2.4 ± 1.3 % and 3.6 ± 1.4 % respectively, in response to the ISO pulse (Figure 4.1g, h). Strikingly, only astrocytes revealed a prominent lactate dip by 2.1 ± 1.4 % before the subsequent lactate surge (Figure 4.1h).

We then compared the time course of the evoked changes in EMG, pupil radius, calcium and lactate response in the arousal paradigm and revealed the relationship between the initial dip and cortical states (Figure 4.1i, j and Supplementary Figure S4.1). In neurons, the evoked lactate surge appeared after the induced pupil dilation and calcium transients (Figure 4.1i). In contrast, astrocytic changes in pupil radius, calcium and lactate levels occurred almost simultaneously (Figure 4.1j). The minimum of the astrocytic lactate dip coincided with the peak of the astrocytic calcium response (lactate dip: 0.26 ± 0.14 min vs. calcium peak: 0.18 ± 0.08 min; $p = 0.24$; unpaired t-test; Figure 4.1j). To further compare response kinetics between neurons and astrocytes, we computed the response slopes (Figure 4.1k) of the lactate elevations. Notably, despite the initial lactate dip, astrocytes displayed a significantly faster lactate rise compared to neurons (Figure 4.1i-k). These time courses highlight the rapid initiation of the astrocytic dip that correlates strongly with the onsets of pupil, EMG and neuronal calcium responses (Supplementary Figure S4.1) suggesting a role of arousal.

To test for a role of a general increase in arousal in triggering the cellular lactate responses, we compared the ISO pulse protocol to other stimulation paradigms, such as single whisker stimulation, air puff to the whisker pad, a short pulse of air and amyl acetate (Extended Data S4.5a-f), and varied the dose (Extended Data S4.5g-l) and time of the ISO pulse (Extended Data S4.5m-r). The 20 s ISO pulse elicited the strongest pupil response (Extended Data S4.5b, n) and cellular activation (Extended Data S4.5h) which resulted in nearly 60% of 104 imaged astrocytes showing a lactate dip (Extended Data S4.5e). Whereas, all astrocytes and nearly all neurons (120 cells) showed a lactate surge (Extended Data S4.5e). In addition, quantification of the percentage of responsive cells (i.e. cells showing a stimulus-evoked lactate dip and/or surge larger than 2 x SD from baseline values) revealed that the numbers of lactate responding astrocytes and neurons strongly increased (Extended Data S4.5e, f, k, l, q, r) when the evoked relative pupil dilation and calcium response was larger (Extended Data S4.5b, h, n). Like the ISO pulse, the other stimuli triggered a pupil response (indicative of an increase in arousal; Extended Data S4.5b). They also induced cortical lactate fluctuations in both astrocytes and neurons (Extended Data S4.5c, d), confirming that our portrayed arousal-mediated lactate dynamics are not isoflurane-specific. However, compared to the other stimulus paradigms the ISO pulse revealed to be the strongest arousal-inducing paradigm and astrocytic lactate dips and surges become larger and more frequent compared to weaker stimulations. Thus, the ISO pulse seems to be an effective and robust paradigm for which to study arousal-mediated global cortical lactate dynamics in awake mice.

The immediate arousal-mediated decrease in astrocytic lactate suggests an activity-dependent lactate consumption or release. If it were the latter, we might expect to detect an arousal-evoked lactate release from astrocytes with a concomitant increase in extracellular lactate levels. We therefore measured changes in ECS lactate levels using a pre-calibrated lactate biosensor inserted into the somatosensory cortex (Figure 4.2a). A brief isoflurane pulse caused a significant extracellular lactate rise of 1.10 ± 0.15 mM (Figure 4.2b, c). Two distinct slopes were seen in these elevated ECS lactate elevations. There was an initial, rapid lactate rise (S1: 25.8 ± 6.3 μM per s) that peaked around 35 s post stimulus, which was followed by a second, significantly slower component (S2: 8.1 ± 3.8 μM M per s; Figure 4.2b, c). We went on to compare the kinetics of lactate dynamics in the ECS, astrocytes, and neurons (Figure 4.2d-f). Two distinct phases in lactate dynamics were identifiable during the first 60 seconds: (I) A fast initial ECS lactate rise that coincided with the lactate decrease in astrocytes and (II) a slow delayed ECS lactate rise that coincided with the neuronal lactate increase (Figure 4.2f). The differences in lactate dynamics between the three compartments were further corroborated by direct comparison of the time series of lactate level changes and kinetics within the initial 60 s of the arousal response (Figure 4.2g-i). Hence, our data implies that astrocytes rapidly release lactate in an activity-dependent manner upon arousal.

## β-Adrenergic Signaling Mediates Arousal-Induced Lactate Level Surges

Changes in arousal are linked to the release of the neuromodulator noradrenaline in cortex, from neuronal locus coeruleus projections. In astrocytes, β-adrenergic signaling has been reported to shape emotionally-driven memory formation[15] and β-signaling-mediated lactate shuttling from astrocytes to neurons plays a key role in associative learning[3,12,39]. Our experiments show that arousal impacts cortical lactate dynamics and that astrocytes are likely to release lactate upon cortical activation (Figures 4.1 and 4.2). To assess if noradrenergic inputs mediate the arousal-evoked cortical lactate mobilization, we tested the non-selective β-adrenergic receptor blocker propranolol in the arousal paradigm. Arousal-evoked lactate and calcium (Figure 4.3 and Extended Data S4.6) responses in astrocytes and neurons were recorded before (0 h) and at several time points (1, 3, 6 and 24 h) after administering propranolol (10 mg per kg (body weight), i.p.). With accurate, repetitive imaging, we followed arousal-evoked responses in the same cells over time (Supplementary Figure S4.2). Blocking β-adrenergic receptors with propranolol did neither impair evoked calcium transients in neurons nor astrocytes (Extended Data S4.6b-f), a finding in line with previous reports[17]. In contrast, propranolol had a significant impact on the induced lactate surges in both neurons and astrocytes (Figure 4.3b, c, e, f and Extended Data S4.6g, i), but caused no overt changes in the astrocytic lactate dip (Figure 4.3d and Extended Data S4.6g, i). Lactate surges (Figure 4.3e), response slopes (Figure 4.3f), the percentage of responding cells with a surge (Extended Data S4.6h) and surge size of responding cells (Extended Data S4.6i) started to decrease compared to baseline responses within the first hour after drug injection. Twenty-four hours after injection of propranolol, lactate responses recovered completely. Control experiments with saline injections did not show any changes in the arousal-evoked calcium and lactate responses (Extended Data S4.7). These results suggest that β-adrenergic signaling appears to primarily regulate de novo lactate production and lactate mobilization from glucose or glycogen stores rather than acting directly on the astrocytic lactate release machinery.

## Brain Glycogen Fuels Lactate Responses in Astrocytes and Neurons

The arousal-evoked increase in cerebral activity-induces cellular lactate fluctuations that partly derived from β-adrenergic signaling (Figure 4.3). We wondered whether β-adrenergic signaling might regulate lactate mobilization from glycogen stores, as it has been proposed to occur in cultured astrocytes[20.40]. To test this possibility, we studied cortical metabolite dynamics and cellular activity in mice lacking brain glycogen[14] using gylcogen synthase 1 (GYS1) knockout mice ($GYS1^{flox/flox}$ x Nestin-Cre = GYS1 KO; Figure 4.4 and Extended Data S4.8). However, before studying cortical activity-evoked lactate dynamics in GYS1 KO mice, we first questioned whether absence of brain glycogen by itself may have altered plasma metabolite levels, cellular activity and intracellular lactate levels which may indirectly hamper the arousal-evoked cortical lactate dynamics. However, blood plasma glucose and lactate levels (Extended Data S4.8c) as well as cellular activity (Extended Data S4.8d) showed no difference among mutant and control mice. To asses possible changes in steady-state intracellular lactate levels we first established the previously described pyruvate trans-acceleration protocol[10] in awake wildtype mice (Extended Data S4.9). Indeed, the trans-acceleration protocol with a systemic pyruvate injection confirmed that astrocytes have higher lactate levels compared to neurons[10] also in awake mice (Extended Data S4.9b, c). Moreover, with this one-point calibration protocol we determined that intracellular lactate levels are not overtly changed in GYS1 KO mice compared to littermate controls (Extended Data S4.8e, f).

Next, we studied arousal-evoked cortical calcium and lactate dynamics in the absence of brain glycogen using the ISO pulse paradigm. The evoked calcium responses of astrocytes and neurons in GYS1 mutants and littermate controls were similar in amplitude (Figure 4.4a, b). However, the arousal-evoked lactate

Figure 4.3.: **β-Adrenergic Signaling Mediates Startle-Evoked Lactate Surges.**
**a,** Scheme to investigate propranolol (β-adrenergic antagonist) effects on arousal-induced lactate responses. Propranolol (10 mg per kg (body weight), i.p.) was injected after baseline acquisition (0 h). **b,c,** Evoked lactate responses in neurons **(b)** and astrocytes **(c)** before (0 h) and after propranolol injection (1, 3, 6 and 24 h). The same 113 neurons and 118 astrocytes were monitored per time point. **d,** Quantification of the area under the curve (AUC) of the evoked lactate dip in astrocytes before (0 h) and after propranolol (1 h - 24 h) showed no change in the dip response. **e,f,** Quantification of startle-induced lactate surges **(e)** and response slopes **(f)** in neurons (left) and astrocytes (right) gradually decreased after propranolol injection (1 h - 6 h) and recovered 24 hours later. 6 h after propranolol injection, arousal-evoked lactate surges, measured as the area under curve (AUC), were reduced by 49.4 ± 40.2 % and 31.2 ± 32.5 % (both $p < 0.001$; Tukey post-hoc test). We also saw that the response slopes decreased by 35.3 ± 28.6 % and 34.7 ± 25.3 % compared to baseline responses in neurons and astrocytes, respectively ($p < 0.001$ and $p = 0.004$). N = number of animals, n = experiments. Data is represented as mean ± SD. m = 113 neurons and 118 astrocytes used to derive statistics. Mean statistics were calculated using two-tailed linear mixed-effects models and Tukey post hoc tests.

surges were significantly reduced in both astrocytes and neurons in GYS1 KO mice compared to controls (Figure 4.4c, d). Importantly, both GYS1 KO and controls revealed a similar number of lactate responsive astrocytes and neurons

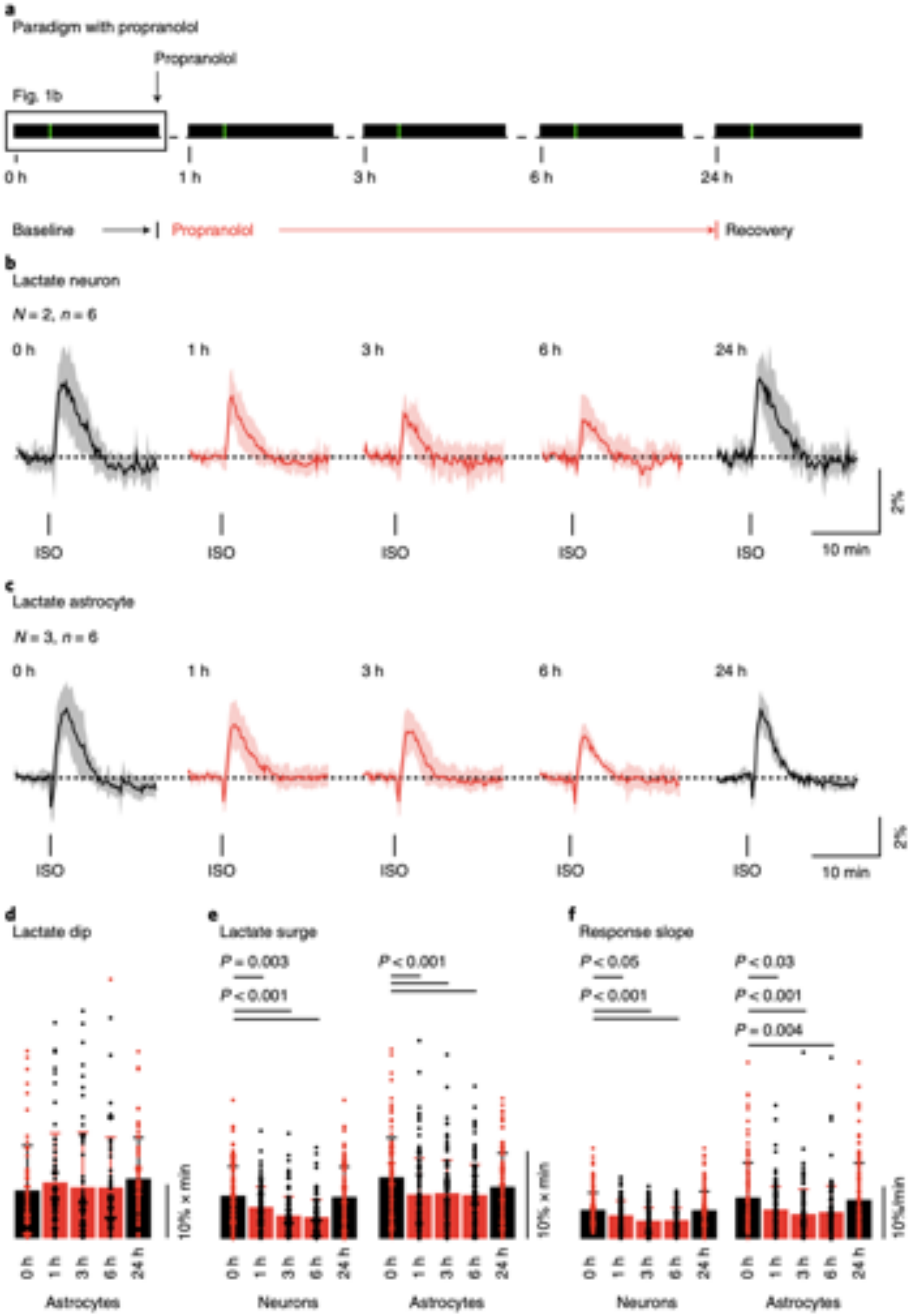

to the ISO pulse, emphasizing that the decreased lactate surges in GYS1 KO are mainly due to impaired intracellular lactate mobilization (Extended Data S4.10a, b). The lactate dip in astrocytes was not significantly altered in GYS1 KO (Figure 4.4d and Extended Data S4.10b). Overall, the changes in lactate fluctuations observed in GYS1 KO mice resemble the data when the β-adrenergic receptors were inhibited. Moreover, and consistent with previous findings[3,12,41], GYS1 deficient mice revealed impairments in associative learning (Extended Data S4.10c, d).

In summary, β-adrenergic signaling appears to primarily regulate lactate production and mobilization from glycogen stores rather than acting directly on the astrocytic lactate release machinery that is most likely directly regulated by cellular depolarization (Figure 4.5). Additionally, these findings suggest that arousal-induced glycogen breakdown is critical to mobilize lactate that is required for higher cognitive functions.

## Discussion

Acute brain activation is accompanied by an increase in aerobic glycolysis and surges in extracellular lactate. Our work here shows that arousal caused a fast and transient decrease in astrocytic lactate and a corresponding increase in extracellular lactate followed by an increase in lactate in neurons and astrocytes (Figures 4.1, and 4.2). Neuronal activity was also increased at the same time (Figure 4.1). We show that neither inhibition of β-adrenergic signaling with propranolol (Figure 4.3) nor depletion of glycogen stores (Figure 4.4) affected the initial astrocytic lactate release, but both are critical in controlling neuronal and astrocytic lactate surges.

We have introduced a startle paradigm to elicit a robust and reproducible arousal response in awake mice combined with two-photon microscopy used for high spatiotemporal imaging. Acute exposure to isoflurane induces a rapid arousal response[29,30], which we identified carefully by measuring EEG, EMG, pupil size and cortical calcium responses. Pupil dilation occurred within seconds of an isoflurane stimulus. Tracking pupil diameter changes is a consistent method for monitoring wakefulness, switching between cortical states and arousal[36]. Our EEG recordings during the initial seconds of isoflurane exposure are also

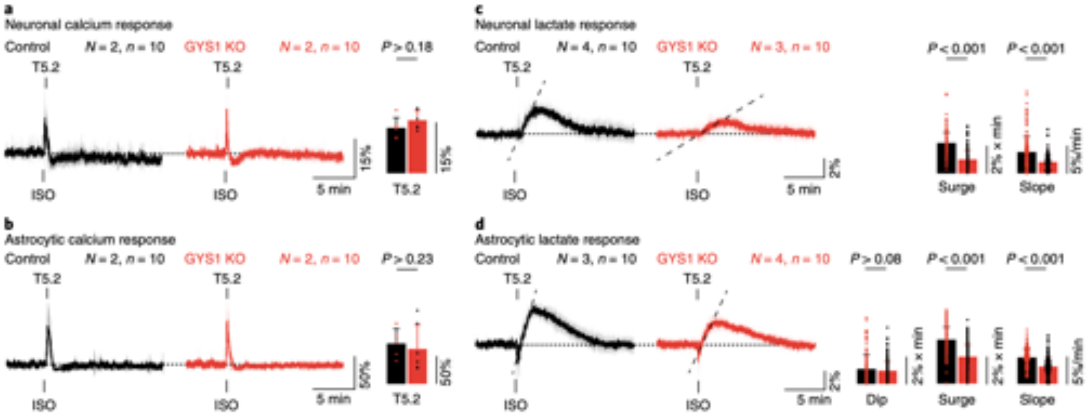

**Figure 4.4.: Lacking Brain Glycogen Leads to Impaired Lactate Responses in Cortical Neurons and Astrocytes.**
**a,b,** Isoflurane pulse-evoked calcium changes in neurons **(a)** and astrocytes **(b)** in control animals (black) and mice lacking glycogen synthase 1 ($GYS1^{flox/flox}$ x Nestin-Cre = GYS1 KO, red). Calcium response in control and GYS1 KO did not differ (bar graph). **c,d,** Lactate level fluctuations in control and GYS1 KO in neurons **(c)** and astrocytes **(d)**. Bar graphs illustrate quantification of the area under the curve (AUC) and slope responses. The dip was not affected when lacking glycogen, but lactate increases were less pronounced in GYS1 KO mice (neurons: 3.4 ± 2.0 vs. 5.0 ± 2.5 % x min; $p < 0.001$; astrocytes: 4.6 ± 2.3 vs. 6.6 ± 2.4 % x min; $p < 0.001$) and raised slower (neurons: 2.0 ± 1.4 vs. 3.8 ± 2.7 %/min; $p < 0.001$; astrocytes: 3.1 ± 1.6 vs. 4.7 ± 1.7 %/min; $p < 0.001$). Data set for control animals comprised 177 neurons and 146 astrocytes. Data set for GYS1 KO animals comprised 184 neurons and 192 astrocytes. Dashed lines are indicated for slope analysis. T indicates time points in minutes. N = number of animals, n = experiments. Data is represented as mean ± SD. m = 184 neurons and 192 astrocytes used to derive statistics. Mean statistics were calculated using two-tailed linear mixed-effects models and Tukey post hoc tests.

in line with EEG profiles obtained from cortical responses to locus coeruleus stimulation[42,43]. The activity of locus coeruleus projections is critical in the regulation of wakefulness and in promoting arousal[44,45]. Arousal induced by forced locomotion or by air puffs has been shown to evoke calcium transients in cortical astrocytes[17,46-48] and in neurons[36]. In a similar manner, our isoflurane-induced arousal protocol triggered a robust calcium response in both astrocytes and neurons. Important to note is that by limiting isoflurane exposure to a brief 20 s pulse (Figure 4.1), we only produce arousal, while avoiding the subsequent sedative state that appears after prolonged isoflurane administration. This is substantiated by EEG, EMG, pupillometry and cellular calcium measurements that clearly allow for differentiation between the arousal response and the anaesthetized state (Extended Data S4.3 and Extended Data S4.4). Moreover, directly upon isoflurane administration animals stopped performing the licking behavior of the suppression-response task (Extended Data S4.3h, i), which is in line with the initial induction of arousal as it has been recently described to occur with acute locus coeruleus activation[49].

To gain more mechanistic insight into how the lactate dip is possibly regulated *in vivo*, we could show that with increasing arousal-evoked cortical activity astrocytic lactate dips and surges are larger and more frequent (Extended Data S4.5). We compared single whisker stimulation (90 Hz, 8 s), air puffs on the whisker pad (5 Hz, 3 s), air flow for 20 s and the odorant amyl acetate 1:1000 for 20 s (ref. [50]) to our short pulse ISO paradigm (Extended Data S4.5a-f). Like the ISO pulse, the other stimuli triggered a pupil response indicative of an increase in arousal. They also induced cortical lactate fluctuations in both astrocytes and neurons, confirming that our portrayed arousal-mediated lactate dynamics are not isoflurane-specific. However, the signal changes were markedly smaller when compared to the ISO pulse (Extended Data S4.5c, d). In addition, when looking at the number of responsive cells showing a dip and/or surge, the ISO pulse protocol showed the highest number of responsive cells (Extended Data S4.5e). Also, lower doses (Extended Data S4.5g-l) and less administration time (Extended Data S4.5m-r) reduced the arousal response, lactate mobilization and reduced the number of responsive cells. On a more general note, since isoflurane is commonly used as an anesthetic in neurophysiology, the initial effect of arousal should be considered when interpreting the data.

In summary, all paradigms elicited a lactate response but only the ISO pulse evoked a strong, robust and reproducible global cortical activation. We could show that the arousal-induced lactate response in astrocytes and neurons was independent of isoflurane. We successfully established the isoflurane pulse paradigm to reliably evoke arousal and global cortical activation that can be easily combined with behavioral training (water licking performance) during awake two-photon imaging.

We used genetically-encoded sensors for calcium[26,27] and lactate[25] in cortical astrocytes and neurons to examine intracellular calcium and lactate dynamics in response to isoflurane-induced arousal (Figure 4.1). Moreover, with a pre-calibrated Pinnacle lactate biosensor[10] inserted into the cortex, we also studied arousal-evoked lactate fluctuations in the ECS (Figure 4.2). While monitoring lactate dynamics with high temporal resolution, we detected a rapid and significant lactate level decrease only in astrocytes upon arousal. The astrocytic lactate dip occurred almost simultaneously with the arousal-evoked calcium transients in neurons and astrocytes (Figure 4.1). In principle, this dip in astrocytic lactate could either be due to an increase in lactate consumption (conversion to pyruvate) or to an increased release of lactate. If the latter, then we would expect a corresponding, rapid increase in ECS lactate levels. Indeed, arousal-evoked ECS lactate dynamics revealed two distinct lactate response slopes. Strikingly, to see was an initial, fast increase in ECS lactate of about 26 μM per s that coincided with the astrocytic lactate dip, suggesting that the rapid extracellular lactate rise is promoted by lactate release from astrocytes (Figure 4.2). A very similar fast lactate release from astrocytes has been reported in response to acute extracellular [$K^+$] elevations *in vitro*, to electrical stimulation *in vivo* and in hippocampal slices[51,52]. Hence, a rise in extracellular [$K^+$] during neuronal activity could rapidly stimulate neighboring astrocytes to release lactate, either through a lactate channe[51], monocarboxylate transporters[53] or possibly via pannexins or hemichannels[54]. The initial decrease in astrocytic lactate was much steeper when animals were startled compared to intracellular lactate depletion by trans-acceleration with pyruvate (Extended Data S4.9g, h). This result might indicate that cellular depolarization mediates a fast channel-mediated lactate export, whereas trans-acceleration mainly acts on carrier-mediated intracellular lactate depletion through monocarboxylate transporters as described by others[10]. The overshoot in the ISO paradigm may result from *de novo* lactate synthesis, whereas pyruvate conversion by lactate dehydrogenase leads to increased lactate levels in neurons and astrocytes. Interestingly, with electrical stimulation *in vitro* mainly a dip is observed without a subsequent increase in intracellular lactate[51,52] suggesting that a dip is not a prerequisite to induce a lactate rise and that the dip and surge might be mechanistically independent from each other. Important to note is that without cellular activity neither lactate dip nor surge occurred strongly suggesting a cell depolarization-dependent lactate release mechanism[51,52]. Resolving the molecular mechanisms of these respective signaling modalities will require further studies, using a combination of specific pharmacological agents and advanced genetic tools.

Arousal strongly induced cortical circuit activation as revealed by EEG and neuronal calcium recordings (Extended Data S4.3 and S4.4), in line with other studies[17,29,36,46]. Neuronal stimulation was recently suggested to trigger neuronal lactate release[11]. However, arousal-induced neuronal activation did not have a neuronal lactate dip that corresponded with an extracellular lactate rise. On the contrary, neurons mainly showed increased lactate levels after the initial astrocytic lactate release (Figures 4.1 and 4.2). In fact, the neuronal lactate increase coincides with a significant slowing of the extracellular lactate rise

(3-fold decrease), suggesting that the neuronal lactate rise is driven by lactate uptake (Figure 4.2). Although neuronal activity may also stimulate glycolysis in neurons[11], it seems unlikely that neurons contain sufficient lactate for it to be released instantaneously (Extended Data S4.9). On the one hand, astrocytes have a higher basal glycolytic activity[55], as well as higher *in vivo* intracellular lactate levels than neurons[10] (Extended Data S4.9). On the other hand, astrocytes maintain an intracellular lactate pool (Extended Data S4.9c), a phenomenon also observed in astrocytes *in vitro* even at low lactate levels[51,52]. Thus, lactate release from this "pressure reservoir" in astrocytes could be rapidly triggered for export in an activity-dependent manner[56].

The arousal-evoked lactate dip in astrocytes is directly followed by a lactate overshoot. This is most likely the reason why more cells were detected showing a dip *in vitro*[52] whereas more cells showed lactate surges *in vivo* (Extended Data S4.5). This is best explained by having a fast lactate production (aerobic glycolysis) surpassing lactate release covering the initial dip response *in vivo*. The extracellular lactate elevation period parallels the astrocytic and neuronal lactate surges, suggesting that an increased lactate production is strongly linked to lactate release and uptake respectively (Figure 4.5). Many activity-dependent neuronal signals have been shown to trigger lactate production by glycogenolysis and glycolysis in astrocytes. Astrocytic glycolysis has been seen to be promoted by glutamate, ammonium, nitric oxide and $K^+$ (ref. [8,51,57,58]) and glycogen breakdown is stimulated by vasoactive intestinal peptide, adenosine, noradrenaline and $K^+$ (ref. [20,59]). However, in response to arousal, the primary signal responsible for the astrocytic lactate production may well be noradrenaline as we discuss below.

During arousal, noradrenaline is released throughout the brain from locus coeruleus projections[60]. Noradrenergic signaling has been implicated in cognition and memory formation, particularly involving β-adrenergic receptors[61-63]. A recent study highlighted that β2-adrenergic signaling in astrocytes is critical for emotionally-driven memory consolidation in mice[15]. Blocking β-adrenergic signaling either pharmacologically with propranolol or by shRNA-mediated knockdown in astrocytes but not in neurons, impaired long-term memory formation, which could be rescued by administering extracellular lactate[15,16].

We hypothesized that if β-adrenergic signaling is required to mobilize lactate in astrocytes, then we should see a perturbation of arousal-evoked cortical lactate dynamics with pharmacological inhibition. Indeed, 1 to 6 hours after a single intraperitoneal injection of propranolol (10 mg per kg (body weight)),

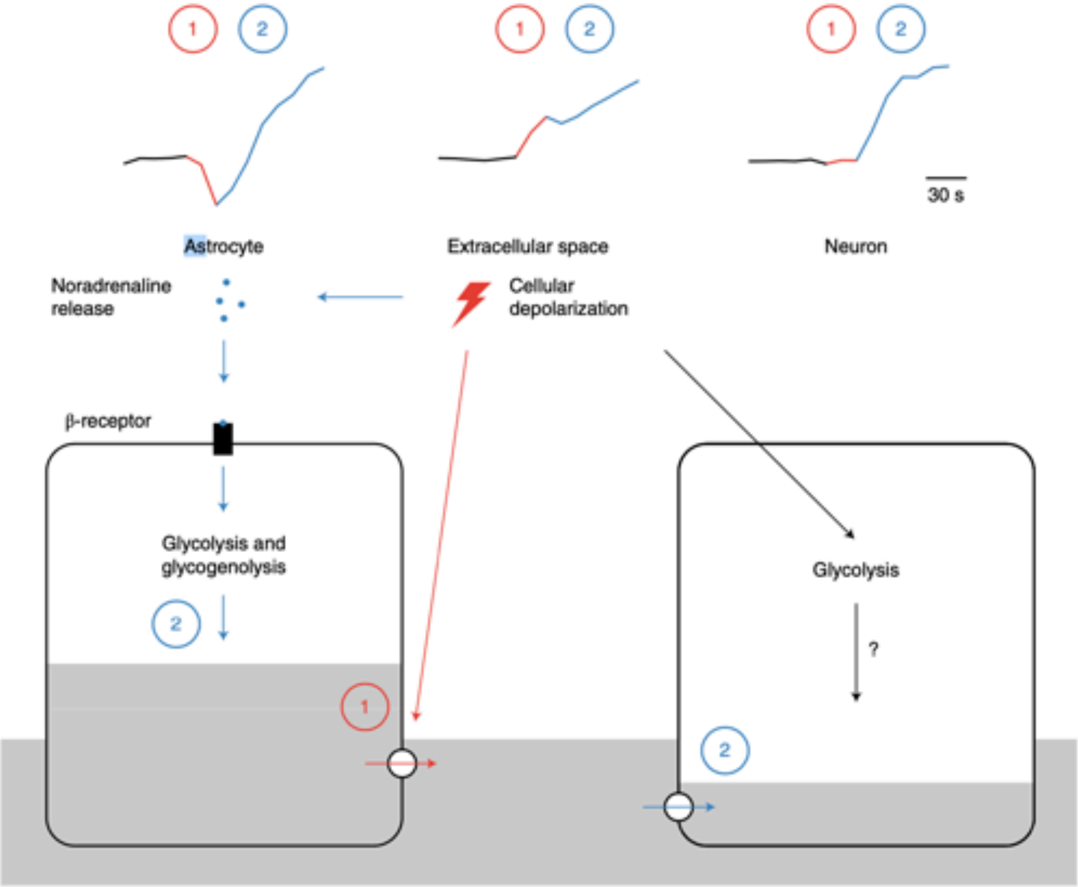

Figure 4.5.: **Model of Startle-Induced Lactate Mobilization From Astrocytes** Arousal-induced cortical activity triggers an immediate lactate release from the astrocytic “pressure reservoir”[56]. The gray shaded area represents steady-state lactate levels in all three compartments and highlights the lactate gradient from astrocytes to neurons[10]. The activity-evoked drop in astrocytic lactate is paralleled by a rapid rise in extracellular lactate levels (I, red). This initial astrocytic lactate release is most likely driven by cellular depolarization and a rise in extracellular $[K^+]$[51]. Moreover, arousal induces release of noradrenaline (NA) that activates β-adrenergic receptors on astrocytes. β-adrenergic signaling stimulates glycogenolysis in astrocytes[75], thereby promoting additional lactate production and release (II, blue). Neurons increase their lactate levels most likely by uptake of lactate, thereby slowing down the astrocyte-mediated extracellular lactate surge (II, blue). Neurons may already take up lactate in the initial phase (I, red) which may be directly used to fuel cellular activity (arousal-evoked calcium transients; Figure 4.2) resulting in balanced uptake and consumption. Neuronal depolarization may also stimulate glycolysis in neurons, which may also contribute to the neuronal lactate rise[11]

lactate surges in both astrocytes and neurons were strongly reduced (Figure 4.3). Notably, the astrocytic lactate dip was not overtly perturbed indicating that β-adrenergic signaling may not be necessary to facilitate lactate channel opening

and/or transporter activity. In fact, astrocytes and neurons remained responsive to arousal-induced cortical activation, as calcium transients were not diminished by blocking β-adrenergic receptors (Extended Data S4.6). This is in line with arousal-mediated astrocytic calcium transients being primarily mediated by α-adrenergic but not β-adrenergic receptors[17,46]. Hence, other activity-dependent mechanisms could stimulate the lactate release machinery in astrocytes, very likely mediated by an acute extracellular [$K^+$] rise[51,52]. High [$K^+$] may also participate in the delayed increase in astrocytic lactate, through NBCe1-mediated stimulation of glycolysis[52,64,65] and glycogen degradation[59], acting in concert with the slower stimulation of astrocytic glycolysis by glutamate[8,64].
Inhibition of β-adrenergic signaling via a single intraperitoneal propranolol injection (10 mg per kg (body weight)) reduced arousal-evoked lactate surges in astrocytes by about 35 % around 6 h post injection (Figure 4.3). It could well be that β-adrenergic receptors were not fully inhibited by a single intraperitoneal injection and that a higher or prolonged dose, or a locally administered dose may have an even stronger impact on glycogen or glucose metabolism, as previously suggested[15,66]. As discussed above, other activity-dependent mechanisms are also likely to be involved in promoting lactate production, such as $K^+$-mediated acceleration of glycolysis and glycogenolysis[59,64]. Important to note is that while both astrocytes and neurons remained similarly responsive to arousal, indicating that workload and energy demand were unchanged during propranolol treatment, the subsequent reductions in arousal-evoked lactate surges in neurons and astrocytes are primarily caused by a partial deficit in lactate production. Thus, we assume that reductions in arousal-evoked lactate elevations in neurons are directly linked to a reduced lactate mobilization presumably from glycogen stores in astrocytes (Figures 4.3 and 4.5). However, astrocytic β-adrenergic signaling may also impact glucose metabolism[19,67,68]. Nonetheless, it is most interesting that a minimal perturbation of β-adrenergic signaling has such a strong impact on cortical lactate dynamics.

Noradrenaline-mediated glycogen breakdown and lactate release[20] was reported to be important for long-term memory formation[3,12]. To obtain a more direct evidence for a functional role of glycogen, we used a mouse model lacking brain-specific glycogen synthase 1 (Figure 4.4 and Extended Data S4.8) to study the functional consequences of an absent glycogen store[14]. We found that mice lacking brain glycogen have deficits in associative learning when compared to littermate controls (Extended Data S4.10c-e). These results are consistent with previous reports showing that glycogen in the brain is critical in learning and memory processes[12,14,15]. GYS1 KO mice revealed neither differences in baseline cellular activity nor in blood plasma metabolites when compared to control littermates, making it unlikely that systemic changes affected the behavioral performance (Extended Data S4.8). Important to note is that GYS1 KO mice and littermates were similarly responsive to arousal. Hence, subsequent reductions in arousal-evoked lactate surges in neurons and astrocytes are primarily caused by the absence of glycogen stores (Figure 4.4). Since glycogen is predominantly stored in astrocytes, astrocytic β-adrenergic signaling possibly mobilizes lactate from glycogen and explains the arousal-evoked cortical lactate surges. Although direct effects of β-adrenergic signaling on lactate production in cortical neurons cannot be ruled out, it is more likely that astrocytes are critically involved in arousal-evoked lactate mobilization and lactate derived from glycogenolysis promotes associative learning and long-memory formation[12,16] with a common lactate-dependent mechanism that is mediated by β-adrenergic signaling in astrocytes[15].

Astrocytic networks are rapidly activated upon arousal in mice[17,46-48]. Also, astrocytes have been recently described to be critically involved in regulating startle-induced behaviors in Drosophila larvae[69]. It is well-known that sensory processing and behavioral responses are strongly influenced by brain state transitions and periods of increased arousal. Extracellular lactate elevations have been demonstrated to modulate neuronal excitability[21,22], to regulate neuronal signaling and expression of plasticity-related genes[16], and to play an important role in stress- or arousal-induced memory formation[12,15,16]. Our study demonstrates in awake behaving mice that astrocytes rapidly release lactate in response to a startle-induced increase in arousal. And we show that mice deficient of brain glycogen show reduced arousal-evoked lactate surges and deficits in associative learning behavior. It is therefore intriguing to speculate that astrocytes release lactate upon arousal not only to fuel neurons but also to modulate neuronal network activity which may contribute to brain state-dependent network signal processing. Future analysis of mice in which lactate channels are selectively removed from astrocytes will help to address the functional impact of startle-induced arousal, fast astrocytic lactate release in the modulation of neuronal network activity and animal behavior.

In summary, our data favors an activity-induced astrocyte-to-neuron lactate shuttle. We provide *in vivo* evidence to show that arousal triggers lactate release from astrocytes and that astrocytic lactate mobilization is partly mediated by β-adrenergic signaling and lactate mobilization from glycogen stores (Figure 4.5). Our study opens an exciting avenue for future studies to investigate the contribution of astrocytic lactate release in e.g. brain state-dependent sensory processing and in higher-order brain functions such as attention and decision making.

# Methods

## Animals

All experimental and surgical procedures were approved by the local veterinary authorities according to the guidelines of the Swiss Animal Protection Law, Veterinary Office, Canton Zurich (Act of Animal Protection, 16 December 2005 and Animal Protection Ordinance, 23 April 2008). Female C57BL/6J (Charles River) and GYS KO[14] mice weighing between 20 and 30 g were used in this study. For control experiments litter mates were used. All mice were kept in standardized single cages with food and water *ad libitum*. During experimental periods mice were subjected to water deprivation. Body weight was monitored before and after all training and experimental sessions. If body weight loss exceeded 15 % with respect to the baseline weight animals would be given free access to water until their weight had normalized. All housed animals were subjected to a 12/12 h light/dark cycle with the dark phase adjusted so that the animals were in their active phase during experimental periods. Surgical interventions were performed at age 10-15 weeks. Mean life span of mice for awake experiments was 439.6 ± 166.1 days.

## Surgical Interventions

Surgical interventions were performed on two separate days. On the first day, the animals were anesthetized with isoflurane 1.5-2.0 % in a mixture of O2 and air (30/70 %) at a flow rate of 400 ml/min. Vitamin A ointment was applied to avoid corneal desiccation. To prevent dehydration 0.2 ml of saline solution was subcutaneously injected every hour. Animals were fixed in a stereotaxic frame (Model 900; David Kopf Instruments) for the head-post implantation as previously described by others[70]. In short, fur from the head and neck area was removed and after disinfection (Kodan; Schülke & Mayr) a 2 cm long midline incision was made between the eyes to the neck. A bonding agent (Gluma Comfort; Heraeus Kulzer) was applied after cleaning the skull and carefully separating the temporal muscle. Next, a head-cap was formed, made of multiple layers of light-curing dental cement (Synergy D6 Flow, Coltene AG). Finally, a custom-made aluminum head-post was attached, and open skin was attached to the implant with acrylic glue (Histoacryl; Braun). On the second day, a craniotomy was performed using a dental drill (OSSEODOC; Bien-Air), above the left somatosensory cortex, for intracortical virus injection. Animals were anesthetized with a mixture of fentanyl (0.05 mg per kg bodyweight; Sintenyl, Sintetica), midazolam (5 mg per kg bodyweight; Dormicum, Roche), and medetomidine (0.5 mg per kg bodyweight; Domitor, Orion Pharma) injected intraperitoneally, and anesthesia was maintained with midazolam after 50 min (5 mg per kg bodyweight, subcutaneous). A facemask delivering oxygen was installed to prevent hypoxemia. For multi-viral injections in the somatosensory cortex, neighboring adeno-associated viral (AAV) injections (50-75 nl each) were delivered with a custom-made micro injector as described elsewhere[10] to achieve multiple non-overlapping loci in the somatosensory cortex. The neuronal construct included a human synapsin-1 (hSYN) promoter and the astrocyte-specific construct included a minimal GFAP promoter (gfaABC1D). Transfection was performed by injecting: (A) a lactate sensor Laconic[25] for neuronal (AAV6-hSYN-Laconic; titer 1.02 E13 VG/ml); (B) for astrocytic (AAV9-GFAP-Laconic; titer 3.1 E12 VG/ml); (C) calcium sensors RCaMP 1.07 (ref. [27]) for neuronal (AAV6-hSYN-RCaMP 1.07; titer 2.4 E13 VG/ml) and (D) GCaMP6s[26] for astrocytic (AAV9-GFAP-GCaMP6s; titer 3.2 E13 VG/ml) expression, diluted 5-30 times in physiological saline. Injections were performed via a glass capillary to a cortical depth of 300 μm through the intact dura. Large blood vessels were avoided to prevent bleeding and the absorption of light by hemoglobin during imaging. For later chronic optical measurements, a square sapphire glass (3x3 mm, Powatec GmbH) was gently placed on the dura mater and sealed with light-curing dental cement (Synergy D6 Flow, Coltene AG).

## Fluorescence Check

Three weeks after injection the animals were checked for sensor expression. Animals were anesthetized with 1.5% isoflurane as described above. Excitation light was delivered at 510 nm for an overview of the vessel structure, 490 nm for the excitation of Laconic and GCaMP6s and 600 nm for the excitation of RCaMP by a monochromatic-based illumination system (Polychrome V; Till Photonics). Fluorescence was collected with a fluorescence stereo microscope (Leica MZ16FA with a Planapo 1.0x objective; Meyer Instruments). Vessel images were recorded with a high-performance digital CCD camera system (Pixelfly; PCO) with an exposure time of 50 ms for the vessel images and 500 ms for fluorescence images. We used emission filters for yellow and green (F47-535; AHF Analysentechnik), and red (F47-623; AHF Analysentechnik) to detect fluorescence emission. Image acquisition was controlled by Camware software (V3.09; PCO). Vessels imagines and fluorescent maps were combined to determine the location of the expression site in respect to the vessel structure.

## Behavioral Setup

A custom-made head fixation box was built for chronic imaging and constant positioning of the animal. The response-suppression task used in this study was designed to suppress movement for 8 s periods while images from the cortex were acquired. After 8 s a tone was sounded to indicate the end of each period (reward stimulus). As a reward stimulus a 70 dB click noise of 1 ms duration with 2-18-kHz bandwidth was produced (background noise was 50 dB) and delivered by stereo speakers positioned 20 cm away from the animals' head. A drinking spout that included a piezo sensor (LDT0-028K; Measurement Specialties) was mounted in front of the animal. The spout was connected to a solenoid valve (Type 0330; Burkert) that controlled water delivery upon spout deflection. A custom-made piezo movement sensor for monitoring movement was positioned under the animals' body. A camera (191133; Conrad Electronic AG) with an infrared light source (BL0106-15-28; Kingbright Electronics) was used for monitoring animals. We used the custom-written LabVIEW program (Version 2012; National Instruments) and multifunctional data acquisition cards to control and monitor all components of the behavioral apparatus[71].

## Behavioral Paradigm, Training and Performance

Animals were first handled and familiarized with the experimenter, one week after implantation, for at least 3 times a day. They were adapted to water deprivation 12 h before training sessions and accustomed to tolerate head fixation and to drink water from a spout every 2 s during training sessions. Finally, the animals were trained in two daily sessions not to move for up to 8 s until the reward stimulus was presented. Occurrence of movement during this period led to a temporal delay of the reward stimulus. Delay was computed depending on the time point and the duration of movement within the normal movement-suppression window. After sounding of each tone, the animal was given a 1.5-second-long "window of opportunity" to lick on the spout. After the reward stimulus was triggered by a spout deflection (stimulus-response), there was a water release of 0.002 ml water per trial (referred to as "reward on lick"). All licks were registered. Licks within the suppression window were counted as false licks. Detected licks within the window of opportunity were counted as correct trials. We computed the number of correct trials for each training session to evaluate performance and training progress of all animals. Only mice that reached a 75 % correct trial performance during training were included for awake imaging. On average, mice performed 139 $\pm$ 33 trials per session and 2835 $\pm$ 1320 total trials.

## Isoflurane Experiments

In the first set of experiments we collected 10 min baseline (50 trials) where the animal was performing the behavioral paradigm, followed by isoflurane administration for 20 min (1.5 % isoflurane in O2 and air (1:2) and 400 ml/min total flow rate) and a recovery phase after turning isoflurane off, for 30 min. In the second set of experiments a baseline of 5 min was acquired followed by administration of isoflurane for 20 s (1.5 %) and a recovery phase of 14 min and 40 s (termed ISO pulse).

## Different Arousal Paradigms

For dose-response comparison the ISO pulse protocol was adapted such that either no isoflurane and just air (air pulse) or only 0.75 % of isoflurane was supplied through the ventilation mask for 20 s. The isoflurane pulse paradigm was also used for the administration of amyl acetate. Instead of isoflurane amyl acetate mixed with air (1:1000; W504009; Merck) was supplied through a ventilation mask for 20 s. For whisker stimulations whiskers were inserted into a glass capillary (GB120F-8P; 1.5x1.05x30 mm; Science Products) glued onto the piezo actuator. The whisker stimulus consisted of single-whisker deflections (90 Hz, 8s) generated by a piezo actuator (T223-H4CL-303X; Piezo Systems). Driving voltage was generated by a custom-written LabVIEW program (National Instruments) using a multi-functional data acquisition card (PCI-6259; National Instruments) and amplified with a piezo controller (MDT693A; Thorlabs). In all animals the right $\gamma$-whisker was stimulated. For the stimulation of the right whisker pad a Toohey

Spritzer (Toohey Company) was used to deliver air puffs at 5 Hz for 3 seconds. Driving voltage was generated by an MC stimulus (STG4001; Multi Channel Systems).

## Microscope Design and Imaging Parameters

A custom-made two-photon laser scanning microscope[72] equipped with a two-photon laser with <120 fs temporal pulse width (InSight DeepSee Dual; Spectra-Physics) with a 20x water immersion objective (W Plan-Apochromat 20x/1.0 DIC VIS-IR; Zeiss) was used for image acquisition. Excitation and emission beam paths were separated by a dichroic mirror (F73-825; AHF Analysentechnik). A dichroic mirror at 506nm (F38-506; AHF Analysentechnik) and 560 nm (F38-560; AHF Analysentechnik) separated the emission light beam. The emission light was focused on the photomultiplier (H9305-03, Hamamatsu) by two lenses (LA1050-A1 and AL5040-A2; Thorlabs). We used emission filters for blue (F39-477; AHF Analysentechnik), green and yellow (F37-545; AHF Analysentechnik) and red (F39-608; AHF Analysentechnik) for multi-color imaging. ScanImage[73] and custom-written LabVIEW software (Version 2012; National Instruments) were used for image control and data acquisition.

## Lactate Imaging Parameters

Anatomical imaging was performed at a resolution of 512x512 pixels at a frequency of 0.74 Hz. Emission signals were acquired at 5.94 Hz and with a 256x256-pixel resolution. ScanImage[73] and custom-written LabVIEW software (Version 2012; National Instruments) were used for image control and data acquisition. Laconic was excited with 870 nm with an overall mean power of 45.8 ± 12.6 mW for neurons and 42.0 ± 12.7 mW for astrocytes. Neurons were imaged 131.5 ± 27.1 µm and astrocytes 117.7 ± 25.2 µm below cortical surface. Power measurements were made close to the focal plane of the objective with a thermal power sensor (S370C; Thorlabs) and a digital optical power meter (PM120; Thorlabs).

## Lactate Analysis

For numerical integrations of the area under the curve (AUC), the MATLAB trapz function was used. Data processing and analysis was carried out with MATLAB 2018a (MathWorks) and ImageJÒ[74]. Ratiometric data was analyzed with the MATLAB toolbox Cellular and Hemodynamic Image Processing Suite CHIPS[37]. Regions of interest (ROIs) were manually selected in ImageJ using high resolution 512x512-pixel images.

## Calcium Imaging Parameters

Data was acquired from the somatosensory cortex 100-200 μm below the cortical surface. Anatomical imaging was performed at a resolution of 512x512 pixels at a frequency of 0.74 Hz. Emission signals were acquired at 11.84 Hz and with a 128x256-pixel resolution. GCaMP6s and RCaMP1.07 were excited simultaneously with a 940 nm and a power of 57.9 ± 8.1 mW at an imaging depth of 116.6 ± 26.0 μm. Power measurements were made close to the focal plane of the objective with a thermal power sensor (S370C; Thorlabs) and a digital optical power meter (PM120; Thorlabs).

## Calcium Analysis

Data processing and analysis was carried out with MATLAB 2018a (MathWorks) and ImageJ[74]. Calcium data was analyzed with the MATLAB toolbox Cellular and Hemodynamic Image Processing Suite CHIPS[37] as previously described by Stobart and al.[38]. In more detail, all calcium data was spectrally unmixed to reduce potential bleed through of GCaMP6s or RCaMP 1.07 and aligned using a 2D convolution engine to account for motion and x-y drift in time. Background noise was defined as the bottom first percentile pixel value in each frame and was subtracted from every pixel. Regions of interest (ROIs) were selected a by customized implementation of an activity-based algorithm for the automated identification of active neurons or astrocytes (FLIKA in CHIPS). In the activity-based algorithm, a 2D spatial Gaussian filter (sxy = 2 mm) and a temporal moving average filter (width = 0.1 s RCaMP 1.07 and 0.5 s for GCaMP6s) were applied to all images to reduce noise. Active pixels were identified as those that exceeded a moving threshold (mean pixel intensity plus 7 x SD for RCaMP 1.07 and 5 x SD for GCaM6s) and had a peak within a defined time window (0.0845 - 2 s for RCaMP 1.07 and 0.1689 - 8 s for GCaMP6s) compared to the preceding 5 s. Active pixels were grouped within space (minimum area of 3.78 mm2 for RCaMP 1.07 and GCaMP6s) and time (0.169 s for RCaMP 1.07 and 1.35 s for GCaMP6s). The 3D mask of active pixels was summed along the temporal dimension, normalized and thresholded ($q = 0.33$ for RCaMP 1.07 and $q = 0.2$ for GCaMP6s) to make a 2D activity ROI mask for each channel. Raw image data from pixels within each 2D ROI were statistically compared to pixels surrounding the ROI (p value $< 0.05$ by one-way Anova) to exclude false positives.

## EEG, EMG, ECS Recordings

Electroencephalogram (EEG), electromyogram (EMG) and extracellular glucose and lactate measurements were performed with a commercially available recording system (4-channel EEG/EMG/BIO Tethered System; Pinnacle Technology). All mice had a head-post mounted as previously described and regions of interest were spared from dental cement. Two to five days after the head-post was mounted, the skull was opened with a dental drill. Two EEG screws were implanted bilaterally in the frontal area, 2 screws (8403; Pinnacle Technology) in the occipital area, a guide cannula (7032; Pinnacle Technology) was implanted into the primary somatosensory cortex, wired with a head mount (8402; Pinnacle Technology) and fixed with dental cement.

Two EMG electrodes were placed in the neck muscle of the animal. After a recovery period of 2 weeks, the pre-calibrated lactate biosensor (7004; Pinnacle Technology) was inserted into the guide cannula. Prior to implantation each lactate biosensor was calibrated in vitro to ensure selectivity and sensitivity for lactate. Data was acquired at 250 Hz for EEG and 1 Hz for lactate measurements. Experimental means were used for time series comparison.

## Pupillometry

For recordings of the right pupil we used a Raspberry Pi NoIR Camera Module V2 night vision camera, an infrared light source (BL0106-15-28; Kingbright Electronics) and a Raspberry Pi 3 Model B (Raspberry Pi Foundation). Ambient light was mimicked with an UV-light source (NSPU510CS; Nichia Corporation) confined to the left eye to reduce interference with cortical imaging. Pupil diameter was measured using a custom-written MATLAB (MathWorks) script. Frames were binarized and an ellipse-fitting algorithm (Ellipse Fit; MATLAB; MathWorks) was used to approximate the pupil size.

## Blood Plasma Metabolite Measurements

The tail vein was used to measure blood plasma metabolite levels. A blood drop was collected with a test strip used for instant whole-blood glucose (Contour; Bayer) and lactate measurements (Lactate Pro 2, Arkray).

## Drug Application and Imaging Protocol

Propranolol, a β-adrenergic receptor antagonist, in saline, was injected intraperitoneally (i.p.) at a concentration of 10 mM per kg. For control experiments, only saline was injected. The ISO pulse protocol was used for five sequential imaging sessions at 1, 3, 6 and 24 h after the initial recording at 0 h.

## Trans-Acceleration With Pyruvate

For intravenous interventions (i.v.) injections, a 30 Gauge needle was connected to fine bore polyethylene tubing (0.28 mm ID; 0.61 mm OD; Portex; Smith medical), filled with 0.9% saline solution and inserted into one of the tail veins. The tubing was connected via an X connector (model SC25, Instech) to peristaltic pumps (Reglo digital ISM 831; Ismatec SA) operated with custom-written MATLAB (MathWorks) code. A 500 mM solution of sodium chloride (S7653, Sigma Aldrich, MO, USA) or sodium pyruvate (P2256; Sigma-Aldrich) at 4 mM per kg bodyweight was injected for 3 minutes.

## Immunohistochemistry

Mice were anaesthetized with pentobarbital and trans-cardially perfused directly with 4% PFA in PBS, pH 7.4. Brains were dissected and post fixed in 4% PFA in PBS for 3 hours. Tissue was cryoprotected in 30% sucrose in PBS, overnight at 4°C. Coronal sections (40 µm) were cut using a microtome (Hyrax, KS34) and then stored in antifreeze at -20°C until further usage. Free floating sections were washed in Tris-Triton (0.05% Triton-X, pH 7.4). For antigen retrieval slices were put in sodium citrate buffer (10mM, 0.05% tween20, pH 6) in a water bath in a commercially available microwave, twice 7 min at 40% of full microwave power. Sections were cooled downs and preincubated in Tris-Triton containing 5% donkey serum and 0.3% Triton-X for 1 hour at RT. Primary antibodies were dissolved in preincubation solution and slices were incubated overnight at 4°C. After washing in Tris-Triton, secondary antibodies were applied in Tris-Triton for 45 min at RT. Slices were washed in Tris-Triton, mounted on glass slides and covered with Dako Fluorescence Mounting Medium (Code S3023). Primary mouse anti-glutamine synthetase (BD Transduction Lab, # 610518) 1:500 and rabbit anti-glycogen synthase 1 (3886S, Cell Signaling) 1:300 antibodies were used. Alexa Fluor488-AffiniPure donkey anti-mouse IgG (H+L) (715-545-151, LucernaChem) 1:700, Cy3-conjugated AffiniPure donkey anti-rabbit IgG (H+L) (711-165-152, LucernaChem,) 1:700 were used as secondary antibodies. Images were taken with a Zeiss LSM 700 confocal microscope using a 40x oil immersion objective (Zeiss). Data was normalized to the mean of all control measurements. Two-tailed unpaired t-test was used for statistical comparison.

## Western Blot

GYS1 protein deletion in brain specific GYS1 knockout mice (GYS1 KO) was quantified from cortical protein extracts. Samples were prepared with sucrose buffer (320 mM sucrose, 10 mM Tris (pH 7.4), 1 mM NaHCO3, 1 mM MgCl2) with protease inhibitors (Roche) and bullet blender (Next Advance) with a 1:1 beads to sample volume ratio. The tissue was homogenized by mixing twice for 15 s on setting 4. After centrifugation of 3 min at 14’000 rpm the protein content in the supernatant was determined with the BCA Protein Assay Kit according to the micro scale assay protocol. For the western blot, 25 µg protein lysate was used per sample and run in a 12 % polyacrylamide separating gel and blotting was performed according to the manufacturer’s instructions (Abcam). Membranes were blocked with TBST (0.1% Tween, pH = 7.4) containing 5% BSA for 60 min at 4°C. Primary antibodies were used at the following dilutions GYS1 1:1’000 (rabbit; 3886; Cell Signaling Technology) and Actin 1:20’000 (rabbit, A2066; Sigma) and incubated overnight in the blocking solution. Membranes were washed with TBST (pH = 7.4) and incubated with an infrared fluorescence secondary antibody system (LI-COR, Odyssey imagers). The secondary antibody (anti rabbit, 800 nm, LI-COR) was dissolved in TBST containing 1% BSA at a dilution of 1:10’000 and incubated for one hour at room temperature before washing in TBST and in TBS. The fluorescent signal was detected by an Odyssey scanner (LI-COR).

## Statistics

Statistical analyses and calculations were performed in R (version 3.6.1) using the lme4 package for linear mixed-effects models and multivariate analysis. All data was reported and plotted as uncorrected means and standard deviation of the means (SD). P values for different parameter comparisons were obtained using the lsmeans or multcomp packages with Tukey post-hoc tests. Also, paired and unpaired t-test was used where appropriate. P values $< 0.05$ were considered significant. For data cross-correlation corrplot from MATLAB's econometrics toolbox was used, with a Pearson's linear correlation coefficient at a significance level of 0.05. The MATLAB ploterr function was used to compute data distribution histogram of correlated data. Estimates of effect sizes (Cohen's d) were calculated using the R package pwr.

## Reporting Summary

Further information on research design is available in the Nature Research Reporting Summary linked to this article.

## Data Availability

All data that support the findings of this study are available from the corresponding author upon request.

# Acknowledgements

We thank all lab members of the Weber group for support and frequent discussions. We would also like to thank Jean-Charles Paterna and the Viral Vector Facility of the Neuroscience Center Zurich (ZNZ) for viral productions. We further thank Johannes M. Mayrhofer and Wolfger von der Behrens for their initial support in establishing the suppression-response task. A.S.S. received support from a Synapsis Career Fellowship Award and the Cloëtta Foundation, M.T.W. is supported by the Hartmann-Müller Foundation, L.F.B. is funded by the Chilean Government through the Centers of Excellence Basal Financing Program of CONICYT, J.D. and J.J.G. are funded by the Spanish MINECO (BFU2017-82375-R) and the National Institutes of Health (NIH-NINDS) (P01NS097197) and B.W. is supported by the Swiss National Science Foundation (SNF Number: 31003A_156965).

# Author Contributions

Conceptualization, M.Z., A.S.S., M.T.W. and B.W.; Methodology, M.Z.; Software, M.Z. and K.D.F.; Formal Analysis, M.Z. and A.S.S.; Investigation, M.Z., Z.J.L. and L.H.; Resources: J.L.S., J.D., J. J. G. and L.F.B.; Writing - Original Draft M.Z. and A.S.S.; Visualization: M.Z. and A.S.S.; Writing - Review & Editing, M.Z., A.S.S., M.T.W., L.F.B. and B.W.; Supervision and Project Administration, M.T.W. and B.W.; Funding Acquisition, M.Z., A.S.S., M.T.W. and B.W.

# Competing Interests

The authors have no competing financial interest.

# References

1. Kety, S. S. and Schmidt, C. F. The nitrous oxide method for the quantitative determination of cerebral blood flow in man: theory, procedure and normal values. J. Clin. Invest. 27, 476–483 (1948).
2. Hu, Y. and Wilson, G. S. A temporary local energy pool coupled to neuronal activity: fluctuations of extracellular lactate levels in rat brain monitored with rapid-response enzyme-based sensor. J. Neurochem. 69, 1484–1490 (1997).
3. Newman, L. A., Korol, D. L. and Gold, P. E. Lactate produced by glycogenolysis in astrocytes regulates memory processing. PLoS ONE 6, e28427 (2011).
4. Yellen, G. Fueling thought: management of glycolysis and oxidative phosphorylation in neuronal metabolism. J. Cell Biol. 217, 2235–2246 (2018).
5. Magistretti, P. J. and Allaman, I. Lactate in the brain: from metabolic end-product to signalling molecule. Nat. Rev. Neurosci. 19, 235–249 (2018).
6. Dienel, G. A. Lack of appropriate stoichiometry: strong evidence against an energetically important astrocyte-neuron lactate shuttle in brain. J. Neurosci.Res. 95, 2103–2125 (2017).
7. Barros, L. F. and Weber, B. CrossTalk proposal: an important astrocyte-to-neuron lactate shuttle couples neuronal activity to glucose utilisation in the brain. J. Physiol. 596, 347–350 (2018).
8. Pellerin, L. and Magistretti, P. J. Glutamate uptake into astrocytes stimulatesaerobic glycolysis: a mechanism coupling neuronal activity to glucoseutilization. Proc. Natl Acad. Sci. USA 91, 10625–10629 (1994).
9. Wyss, M. T., Jolivet, R., Buck, A., Magistretti, P. J. and Weber, B. In vivo evidence for lactate as a neuronal energy source. J. Neurosci. 31, 7477–7485 (2011).
10. Machler, P. et al. In vivo evidence for a lactate gradient from astrocytes to neurons. Cell Metab. 23, 94–102 (2016).
11. Diaz-Garcia, C. M. et al. Neuronal stimulation triggers neuronal glycolysis and not lactate uptake. Cell Metab. 26, 361–374 e364 (2017).
12. Suzuki, A. et al. Astrocyte-neuron lactate transport is required for long-term memory formation. Cell 144, 810–823 (2011).
13. Zhang, Y. et al. Inhibition of lactate transport erases drug memory and prevents drug relapse. Biol. Psychiatry 79, 928–939 (2016).
14. Duran, J., Saez, I., Gruart, A., Guinovart, J. J. and Delgado-Garcia, J. M. Impairment in long-term memory formation and learning-dependent synaptic plasticity in mice lacking glycogen synthase in the brain. J. Cereb. Blood Flow Metab. 33, 550–556 (2013).
15. Gao, V. et al. Astrocytic β2-adrenergic receptors mediate hippocampal long-term memory consolidation. Proc. Natl Acad. Sci. USA 113, 8526–8531 (2016).
16. Descalzi, G., Gao, V., Steinman, M. Q., Suzuki, A. and Alberini, C. M. Lactate from astrocytes fuels learning-induced mRNA translation in excitatory and inhibitory neurons. Commun. Biol. 2, 247 (2019).
17. Paukert, M. et al. Norepinephrine controls astroglial responsiveness to local circuit activity. Neuron 82, 1263–1270 (2014).
18. Alberini, C. M., Cruz, E., Descalzi, G., Bessieres, B. and Gao, V. Astrocyte glycogen and lactate: new insights into learning and memory mechanisms. Glia 66, 1244–1262 (2018)
19. Dienel, G. A. and Cruz, N. F. Aerobic glycolysis during brain activation: adrenergic regulation and influence of nore-

pinephrine on astrocytic metabolism. J. Neurochem. 138, 14–52 (2016).

20. Sorg, O. and Magistretti, P. J. Characterization of the glycogenolysis elicited by vasoactive intestinal peptide, noradrenaline and adenosine in primary cultures of mouse cerebral cortical astrocytes. Brain Res. 563, 227–233 (1991)
21. Sada, N., Lee, S., Katsu, T., Otsuki, T. and Inoue, T. Epilepsy treatment. Targeting LDH enzymes with a stiripentol analog to treat epilepsy. Science 347, 1362–1367 (2015).
22. Clasadonte, J., Scemes, E., Wang, Z., Boison, D. and Haydon, P. G. Connexin 43-mediated astroglial metabolic networks contribute to the regulation of the sleep-wake cycle. Neuron 95, 1365–1380 (2017).
23. Tang, F. et al. Lactate-mediated glia-neuronal signalling in the mammalian brain. Nat. Commun. 5, 3284 (2014).
24. Morland, C. et al. The lactate receptor, G-protein-coupled receptor 81/ hydroxycarboxylic acid receptor 1: expression and action in brain. JJ. Neurosci. Res. 93, 1045–1055 (2015).
25. San Martin, A. et al. A genetically encoded FRET lactate sensor and its use to detect the Warburg effect in single cancer cells. PLoS ONE 8, e57712 (2013).
26. Chen, T. W. et al. Ultrasensitive fluorescent proteins for imaging neuronal activity. Nature 499, 295–300 (2013).
27. Ohkura, M., Sasaki, T., Kobayashi, C., Ikegaya, Y. and Nakai, J. An improved genetically encoded red fluorescent Ca2+ indicator for detecting optically evoked action potentials. PLoS ONE 7, e39933 (2012).
28. Franks, N. P. General anaesthesia: from molecular targets to neuronal pathways of sleep and arousal. Nat. Rev. Neurosci. 9, 370–386 (2008)
29. Liu, X. et al. Arousal transitions in sleep, wakefulness, and anesthesia are characterized by an orderly sequence of cortical events. NeuroImage 116, 222–231 (2015).
30. Kum, J. E., Han, H. B. and Choi, J. H. Pupil size in relation to cortical states during isoflurane anesthesia. Exp. Neurobiol. 25, 86–92 (2016).
31. Guedel, A. E. Inhalation Anesthesia; A Fundamental Guide (Macmillan, 1951).
32. Chen, C. R. et al. Roles of adrenergic alpha1 and dopamine D1 and D2 receptors in the mediation of the desynchronization effects of modafinil in a mouse EEG synchronization model. PLoS ONE 8, e76102 (2013).
33. McCormick, D. A. and Bal, T. Sleep and arousal: thalamocortical mechanisms. Annu. Rev. Neurosci. 20, 185–215 (1997)
34. Jameson, L. C. and Sloan, T. B. Using EEG to monitor anesthesia drug effects during surgery. J. Clin. Monit. Comput. 20, 445–472 (2006).
35. MacIver, M. B. and Bland, B. H. Chaos analysis of EEG during isoflurane- induced loss of righting in rats. Front. Syst. Neurosci. 8, 203 (2014).
36. Reimer, J. et al. Pupil fluctuations track fast switching of cortical states during quiet wakefulness. Neuron 84, 355–362 (2014).
37. Barrett, M. J. P., Ferrari, K. D., Stobart, J. L., Holub, M. and Weber, B. CHIPS: an extensible toolbox for cellular and hemodynamic two-photon image analysis. Neuroinformatics 16, 145–147 (2018).
38. Stobart, J. L. et al. Cortical circuit activity evokes rapid astrocyte calcium signals on a similar timescale to neurons. Neuron 98, 726–735 e724 (2018).
39. Gibbs, M. E., Anderson, D. G. and Hertz, L. Inhibition of glycogenolysis in astrocytes interrupts memory consolidation in young chickens. Glia 54, 214–222 (2006).
40. Lee, K., Makino, S., Imagawa, T., Kim, M. and Uehara, M. Effects of adrenergic agonists on glycogenolysis in primary

cultures of glycogen body cells and telencephalon astrocytes of the chick. Poult. Sci. 80, 1736–1742 (2001).

41. Duran, J. and Guinovart, J. J. Brain glycogen in health and disease. Mol. Asp. Med. 46, 70–77 (2015).
42. Berridge, C. W. and Foote, S. L. Effects of locus coeruleus activation on electroencephalographic activity in neocortex and hippocampus. J. Neurosci. 11, 3135–3145 (1991).
43. Carter, M. E. et al. Tuning arousal with optogenetic modulation of locus coeruleus neurons. Nat. Neurosci. 13, 1526–1533 (2010).
44. Aston-Jones, G. and Cohen, J. D. An integrative theory of locus coeruleus- norepinephrine function: adaptive gain and optimal performance. Annu. Rev. Neurosci. 28, 403–450 (2005).
45. Berridge, C. W. and Waterhouse, B. D. The locus coeruleus–noradrenergic system: modulation of behavioral state and state-dependent cognitive processes. Brain Res. Brain Res. Rev. 42, 33–84 (2003).
46. Ding, F. et al. α1-Adrenergic receptors mediate coordinated Ca2+ signaling of cortical astrocytes in awake, behaving mice. Cell Calcium 54, 387–394 (2013).
47. Srinivasan, R. et al. Ca2+ signaling in astrocytes from Ip3r2–/– mice in brain slices and during startle responses in vivo. Nat. Neurosci. 18, 708–717 (2015).
48. Slezak, M. et al. Distinct mechanisms for visual and motor-related astrocyte responses in mouse visual cortex. Curr. Biol. 29, 3120–3127 (2019).
49. Zerbi, V. et al. Rapid reconfiguration of the functional connectome after chemogenetic locus coeruleus activation. Neuron 103, 702–718 (2019).
50. Chaigneau, E., Oheim, M., Audinat, E. and Charpak, S. Two-photon imaging of capillary blood flow in olfactory bulb glomeruli. Proc. Natl Acad. Sci. USA 100, 13081–13086 (2003).
51. Sotelo-Hitschfeld, T. et al. Channel-mediated lactate release by K+-stimulated astrocytes. J. Neurosci. 35, 4168–4178 (2015).
52. Ruminot, I., Schmalzle, J., Leyton, B., Barros, L. F. and Deitmer, J. W. Tight coupling of astrocyte energy metabolism to synaptic activity revealed by genetically encoded FRET nanosensors in hippocampal tissue. J. Cereb. Blood Flow Metab. 39, 513–523 (2019).
53. Pierre, K. and Pellerin, L. Monocarboxylate transporters in the central nervous system: distribution, regulation and function. J. Neurochem. 94, 1–14 (2005).
54. Karagiannis, A. et al. Hemichannel-mediated release of lactate. J. Cereb. Blood Flow Metab. 36, 1202–1211 (2016).
55. Hung, Y. P., Albeck, J. G., Tantama, M. and Yellen, G. Imaging cytosolic NADH-NAD+ redox state with a genetically encoded fluorescent biosensor. Cell Metab. 14, 545–554 (2011).
56. Kasparov, S. Are astrocytes the pressure-reservoirs of lactate in the brain? Cell Metab. 23, 1–2 (2016).
57. Lerchundi, R. et al. NH4+ triggers the release of astrocytic lactate via mitochondrial pyruvate shunting. Proc. Natl Acad. Sci. USA 112, 11090–11095 (2015).
58. Bolanos, J. P., Delgado-Esteban, M., Herrero-Mendez, A., Fernandez-Fernandez, S. and Almeida, A. Regulation of glycolysis and pentose-phosphate pathway by nitric oxide: impact on neuronal survival. Biochim. Biophys. Acta 1777, 789–793 (2008).
59. Choi, H. B. et al. Metabolic communication between astrocytes and neurons via bicarbonate-responsive soluble adenylyl cyclase. Neuron 75, 1094–1104 (2012).
60. Schwarz, L. A. and Luo, L. Organization of the locus coeruleus-norepinephrine

system. Curr. Biol. 25, R1051–R1056 (2015).

61. Cahill, L., Prins, B., Weber, M. and McGaugh, J. L. β-adrenergic activation and memory for emotional events. Nature 371, 702–704 (1994).
62. Murchison, C. F. et al. A distinct role for norepinephrine in memory retrieval. Cell 117, 131–143 (2004).
63. Sun, H., Mao, Y., Wang, J. and Ma, Y. Effects of β-adrenergic antagonist, propranolol on spatial memory and exploratory behavior in mice. Neurosci. Lett. 498, 133–137 (2011).
64. Bittner, C. X. et al. Fast and reversible stimulation of astrocytic glycolysis by K+ and a delayed and persistent effect of glutamate. J. Neurosci. 31, 4709–4713 (2011).
65. Ruminot, I. et al. NBCe1 mediates the acute stimulation of astrocytic glycolysis by extracellular K+. J. Neurosci. 31, 14264–14271 (2011).
66. Savaki, H. E., Kadekaro, M., Jehle, J. and Sokoloff, L. α- and β-adrenoreceptor blockers have opposite effects on energy metabolism of the central auditory system. Nature 276, 521–523 (1978).
67. Catus, S. L., Gibbs, M. E., Sato, M., Summers, R. J. and Hutchinson, D. S. Role of β-adrenoceptors in glucose uptake in astrocytes using β-adrenoceptor knockout mice. Br. J. Pharmacol. 162, 1700–1715 (2011).
68. Dong, J. H. et al. β2-adrenergic receptor and astrocyte glucose metabolism. J. Mol. Neurosci. 48, 456–463 (2012).
69. Ma, Z., Stork, T., Bergles, D. E. and Freeman, M. R. Neuromodulators signal through astrocytes to alter neural circuit activity and behaviour. Nature 539, 428–432 (2016).
70. Mayrhofer, J. M., Haiss, F., Helmchen, F. and Weber, B. Sparse, reliable, and long-term stable representation of periodic whisker deflections in the mouse barrel cortex. NeuroImage 115, 52–63 (2015).
71. Mayrhofer, J. M. et al. Novel two-alternative forced choice paradigm for bilateral vibrotactile whisker frequency discrimination in head-fixed mice and rats. J. Neurophysiol. 109, 273–284 (2013).
72. Mayrhofer, J. M. et al. Design and performance of an ultra-flexible two-photon microscope for in vivo research. Biomed. Opt. Express 6, 4228–4237 (2015).
73. Pologruto, T. A., Sabatini, B. L. and Svoboda, K. ScanImage: flexible software for operating laser scanning microscopes. Biomed. Eng. Online 2, 13 (2003).
74. Schneider, C. A., Rasband, W. S. and Eliceiri, K. W. NIH Image to ImageJ: 25 years of image analysis. Nat. Methods 9, 671–675 (2012).
75. Coggan, J. S. et al. Norepinephrine stimulates glycogenolysis in astrocytes to fuel neurons with lactate. PLoS Comput. Biol. 14, e1006392 (2018).

# Additional Information

## Supplemental Information

is available for this paper at https://doi.org/10.1038/s42255-020-0170-4.

## Correspondence and Requests for Materials

should be addressed to B.W.

## Peer Review Information

Primary Handling Editor: Elena Bellafante.

## Reprints and Permissions Information

is available at www.nature.com/reprints.

## Publisher's Note

Springer Nature remains neutral with regard to jurisdictional claims in published maps and institutional affiliations.

# Extended Data

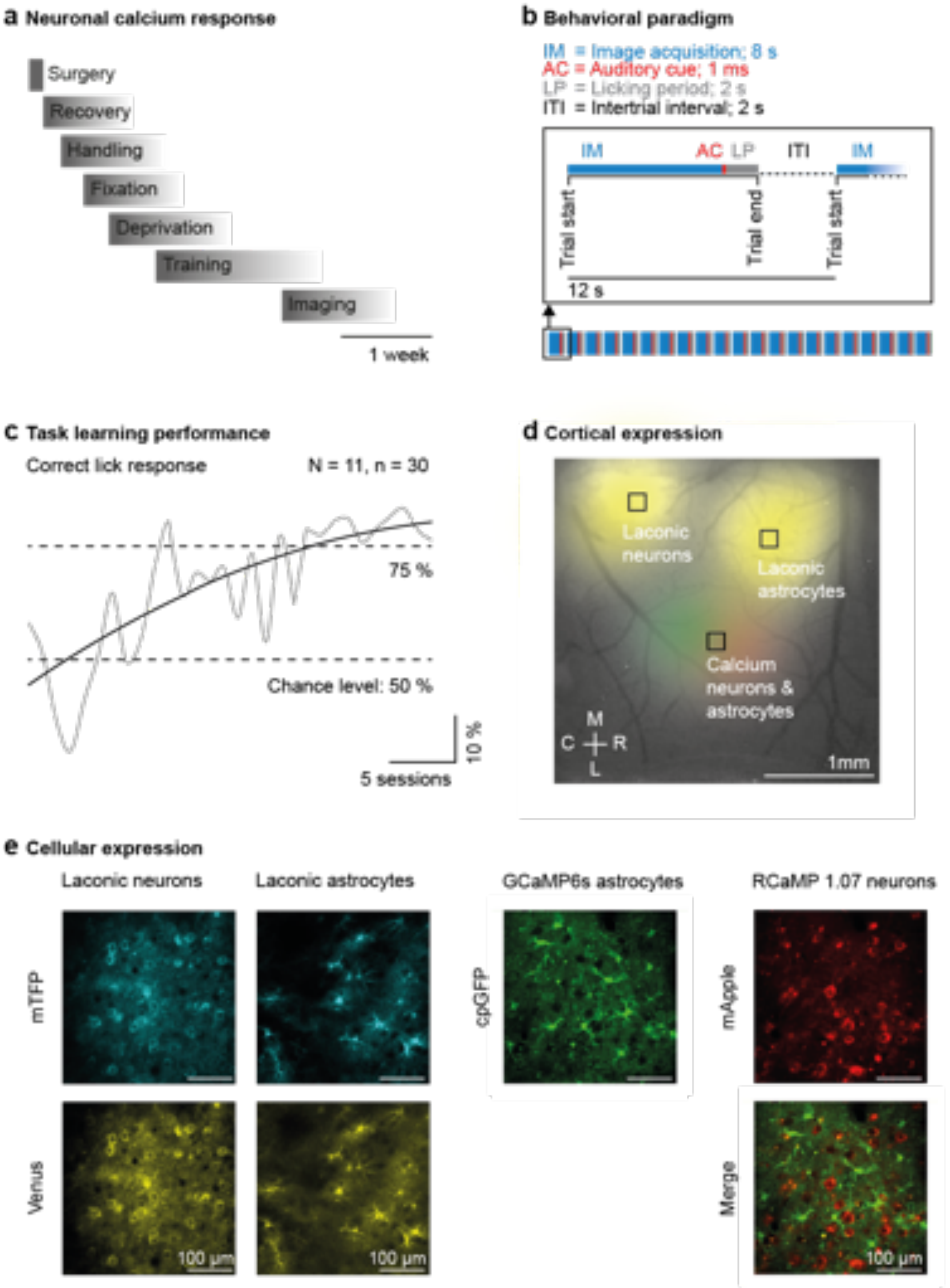

**Ext. Data S4.1.:** **Awake Two-Photon Imaging to Study Cortical Lactate and Calcium Dynamics in Neurons and Astrocytes. (Related to Figure 4.1.)**
**(a)** Workflow scheme of preparing mice for awake two-photon imaging. Following recovery from surgery and intracortical AAV injections, mice were trained for head-restrained imaging using a suppression-response task and a water reward. On average, mice were ready for imaging at around 4 weeks after surgery. This protocol was repeated for all animals in this study with similar results. **(b)** Behavioral paradigm used during awake imaging. Each trial consisted of an 8 s imaging period (IM) which ended with a 1 ms auditory cue (AC) indicating the mouse to collect the water reward within a lick period of 2 s (LP). Each trial had an intertrial interval (ITI) of 2 s before the next trial started. **(c)** Mean behavioral performance (gray) and learning progress (black) during training. A trial was counted correct when no licking occurred during image acquisition (IM). N = number of animals, n = number of sessions. **(d)** Cortical expression of genetically-encoded lactate sensor Laconic (San Martin et al.,[25]), calcium sensor RCaMP 1.07 (Ohkura et al.,[27]) and GCaMP6s (Chen et al.,[26,32]) imaged through a chronic cranial window. Visualization with single photon excitation. M = medial, L = lateral, C = cranial, R = rostral. **(e)** Representative images of Laconic expression in neurons and astrocytes (mTFP = blue; Venus = yellow), RCaMP 1.07 in neurons (mApple = red) and GCaMP6s in astrocytes (cpGFP = green) and a merge of calcium sensors expressed at the same site (neurons = red, astrocytes = green). Excitation wavelength for Laconic = 870 nm. Wavelength for simultaneous excitation of GCaMP6s and RCaMP 1.07 = 940 nm. Images were taken 121.4 ± 26.9$\mu$m below cortical surface.

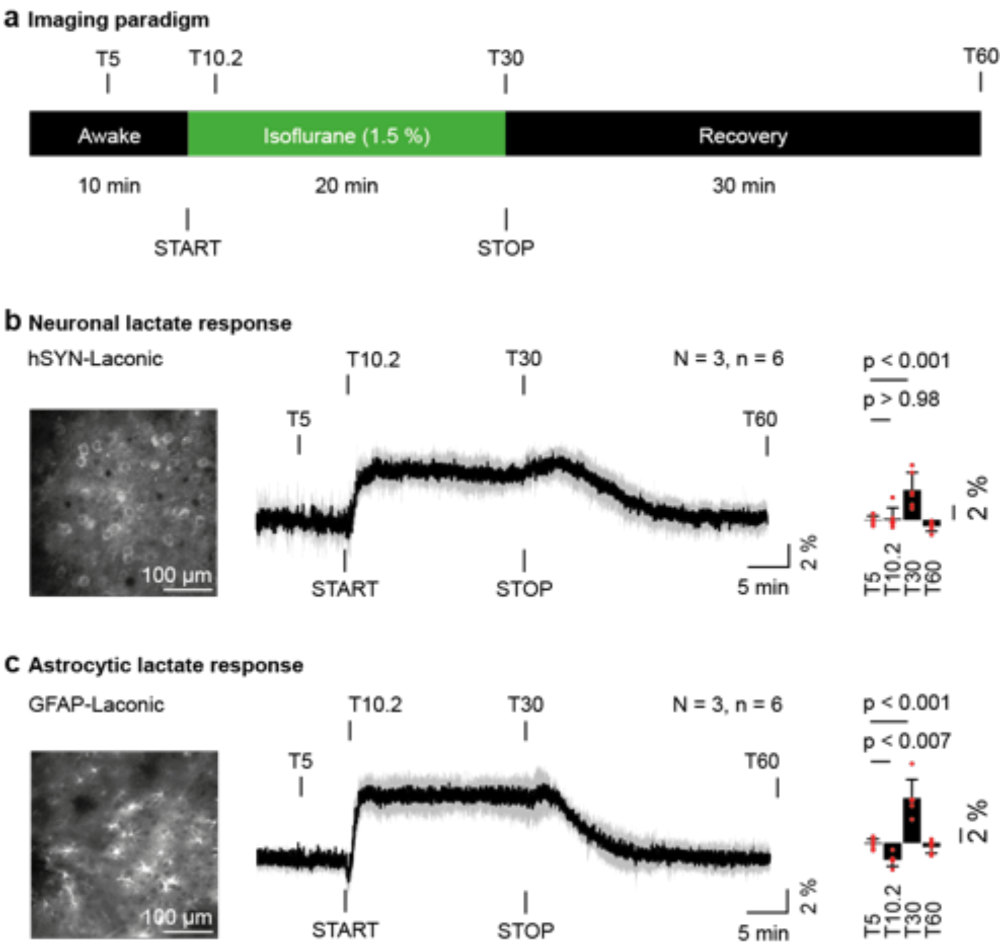

**Ext. Data S4.2.: Lactate Dynamics in Cortical Neurons and Astrocytes Upon Prolonged Isoflurane Exposure. (Related to Figure 4.1).**
**(a)** Scheme of the prolonged isoflurane imaging protocol. T indicates time points in minutes throughout the imaging session. Time points for the onset (T10) and end (T30) of isoflurane delivery are indicated by START and STOP. **(b, c)** Cortical neurons (b, left panel) and astrocytes expressing Laconic (c, left panel) in individual fields of view. Single cell fluorescence analysis of relative lactate changes (middle panels) during the prolonged isoflurane administration protocol. Both, neurons and astrocytes show a rise in lactate levels that persists during the isoflurane period (indicated at T30; relative lactate signal rose by 4.6 ± 1.6 % in neurons and 5.5 ± 2.0 % in astrocytes; $p < 0.001$). At T10.2 upon isoflurane induction relative lactate signal dropped by -1.8 ± 1.1 % ($p < 0.007$) in astrocytes only. In contrast, neurons showed no significant lactate decrease when compared to baseline ($p > 0.98$). Lactate levels return to baseline during recovery (indicated at T60). Bar graphs summarize relative changes at T5, T10.2, T30 and T60. Data set contained 104 neurons and 102 astrocytes. T indicates time points in minutes. N = number of animals, n = number of experiments. Data is represented as mean ± SD. m = 6 experiments used to derive statistics. Mean statistics were calculated using two-tailed linear mixed-effects models and Tukey post hoc tests.

---

Blank page to keep figures and captions aligned

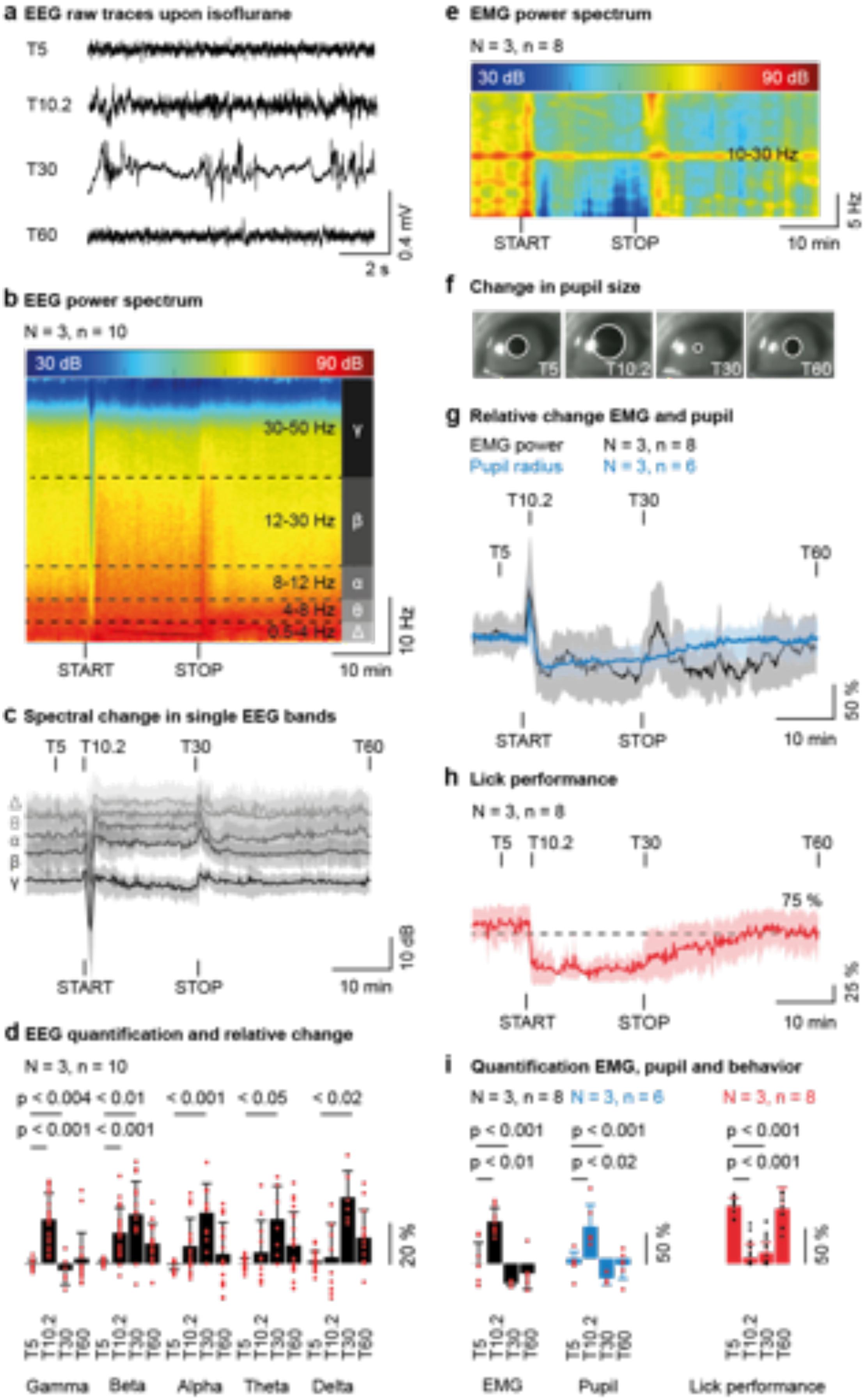
a EEG raw traces upon isoflurane
T5
T10.2
T30
T60
0.4 mV
2 s
b EEG power spectrum
N = 3, n = 10
30 dB
90 dB
30-50 Hz
γ
12-30 Hz
β
8-12 Hz
α
4-8 Hz
θ
0.5-4 Hz
Δ
10 Hz
START
STOP
10 min
C Spectral change in single EEG bands
T5
T10.2
T30
T60
Δ
θ
α
β
γ
10 dB
START
STOP
10 min
d EEG quantification and relative change
N = 3, n = 10
p < 0.004
< 0.01
< 0.001
< 0.05
< 0.02
p < 0.001
< 0.001
20 %
T5
T10.2
T30
T60
Gamma
Beta
Alpha
Theta
Delta
e EMG power spectrum
N = 3, n = 8
30 dB
90 dB
10-30 Hz
5 Hz
START
STOP
10 min
f Change in pupil size
T5
T10.2
T30
T60
g Relative change EMG and pupil
EMG power
N = 3, n = 8
Pupil radius
N = 3, n = 6
T10.2
T30
T5
T60
50 %
START
STOP
10 min
h Lick performance
N = 3, n = 8
T5
T10.2
T30
T60
75 %
25 %
START
STOP
10 min
i Quantification EMG, pupil and behavior
N = 3, n = 8
N = 3, n = 6
N = 3, n = 8
p < 0.001
p < 0.001
p < 0.001
p < 0.01
p < 0.02
p < 0.001
50 %
50 %
50 %
T5
T10.2
T30
T60
EMG
Pupil
Lick performance

**Ext. Data S4.3.: Isoflurane Exposure Causes an Initial Arousal Response Before Reaching the Anesthetized State. (Related to Figure 4.1).**
**(a)** EEG raw traces at different time points of the prolonged isoflurane imaging protocol (Extended Data S4.2a). Traces represent distinct states such as: T5 = awake behaving, T10.2 = induction and desynchronization, T30 = anesthetized and increased slow-wave activity leading to burst suppression, T60 = recovery and awake. **(b)** EEG power spectrum and EEG bands (delta: 0.5-4 Hz, theta: 4-8 Hz, alpha: 8-12 Hz, beta: 12-30 Hz and gamma: 30-50 Hz) show a clear shift upon isoflurane exposure. Blue = low power (30 dB) and red = high power (90 dB). **(c)** EEG bands according to their power display a biphasic EEG response when transiting from the awake state through the induction phase (increase in high-frequency power) to the anesthetized state (increase in low-frequency power). **(d)** Quantification of EEG bands as a relative change with respect to baseline at time points T5, T10.2, T30 and T60 derived from **(c)**. **(e)** EMG spectrum (10-30 Hz) recorded from neck muscles shows an increase in muscle activity with exposure to isoflurane and a reduced power in the anesthetized state. Blue = low power (30 dB) and red = high power (90 dB). **(f)** Pupillometry analysis reveals pupil dilation in the induction phase (T10.2), then a pupil constriction in the anesthetized state (T30). White circles indicate pupil size approximation. **(g)** Relative changes in EMG power (black) and pupil radius (blue) recorded during the isoflurane protocol. **(h)** Lick performance during the isoflurane protocol. Note that prolonged isoflurane administration immobilizes the animal and behavioral performance is absent. **(i)** Quantification of EMG and pupil radius and lick performance at time points T5, T10.2, T30 and T60. Note a significant increase in neuromuscular activity in the induction phase (T10.2) and a reduction in EMG power, pupil size and lick performance during the anesthetized state highlighting that prolonged isoflurane exposure first initiates an aroused state (within the first 60 s), which is then gradually followed by an anesthetized state and immobilization. T indicates time points in minutes. N = number of animals, n = number of experiments. START and STOP indicate the period of isoflurane administration. Data is represented as mean ± SD. m = 10 experiments for EEG, 8 for EMG, 6 for pupil and 8 for lick performance used to derive statistics. Mean statistics were calculated using two-tailed linear mixed-effects models and Tukey post hoc tests.

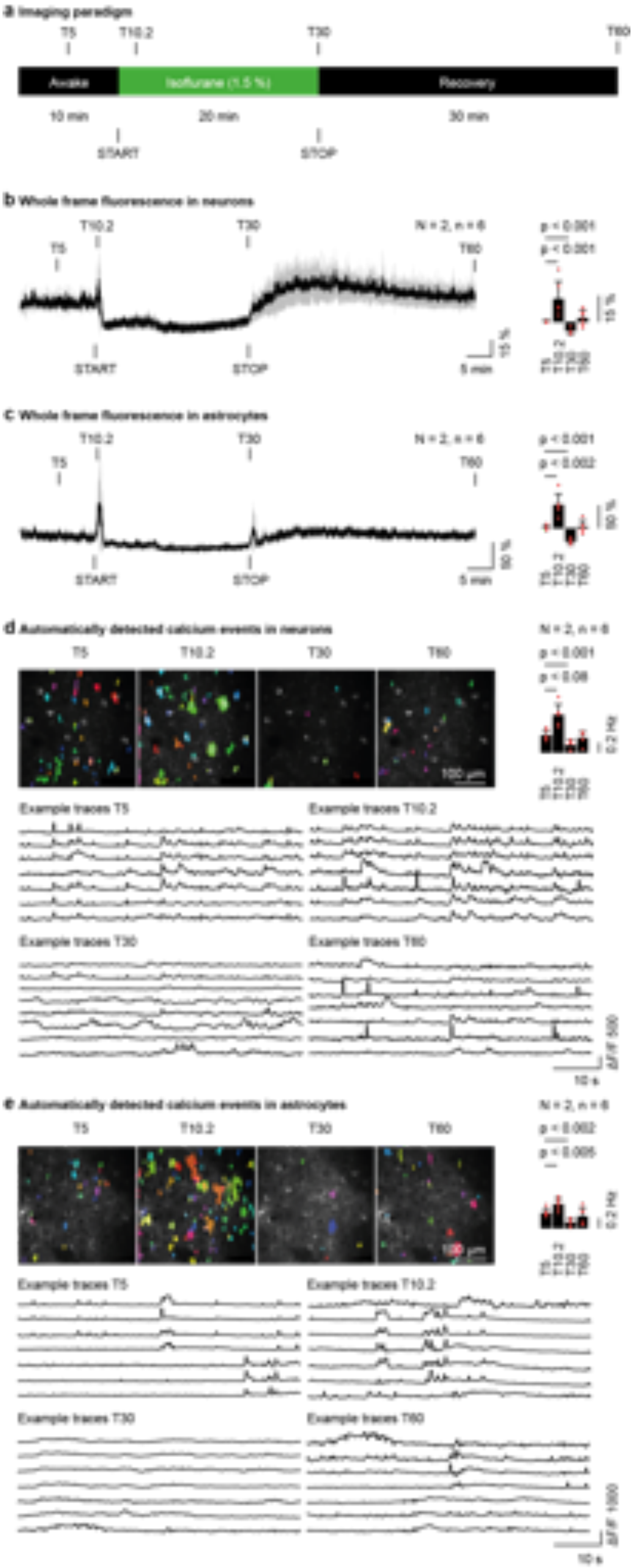a Imaging paradigm
T5
T10.2
T30
T60
Awake
Isoflurane (1.5 %)
Recovery
10 min
20 min
30 min
START
STOP
b Whole frame fluorescence in neurons
T5
T10.2
T30
T60
N = 2, n = 6
START
STOP
5 min
15 %
p < 0.001
p < 0.001
T5
T10.2
T30
T60
c Whole frame fluorescence in astrocytes
T5
T10.2
T30
T60
N = 2, n = 6
START
STOP
5 min
50 %
p < 0.001
p < 0.002
d Automatically detected calcium events in neurons
T5
T10.2
T30
T60
100 µm
N = 2, n = 6
p = 0.001
p = 0.08
0.2 Hz
Example traces T5
Example traces T10.2
Example traces T30
Example traces T60
ΔF/F 500
10 s
e Automatically detected calcium events in astrocytes
T5
T10.2
T30
T60
100 µm
N = 2, n = 6
p = 0.002
p = 0.005
0.2 Hz
Example traces T5
Example traces T10.2
Example traces T30
Example traces T60
ΔF/F 1000
10 s

**Ext. Data S4.4.:** **Calcium Activity in Neurons and Astrocytes Upon Isoflurane Administration (Related to Figure 4.1).**

**(a)** Scheme of the prolonged isoflurane imaging protocol consisting of a 10 min baseline (awake behaving), 20 min isoflurane and a 30 min recovery period. T indicates time in min for the course of the imaging session. Timepoints for the onset (T10) and end (T30) of isoflurane delivery are indicated by START and STOP. **(b, c)** Whole frame fluorescence analysis of relative calcium changes during the isoflurane administration protocol **(a)**. The onset of isoflurane exposure (START) caused a strong activation in cortical network and a significant rise in neuronal and astrocytic calcium levels (T10.2). In neurons, whole frame fluorescence intensity increased by 14.2 ± 7.3 % ($p < 0.001$) and in astrocytes, it increased by 50.1 ± 21.2 % ($p < 0.001$). During the anesthetized state (T30) overall calcium levels decreased in both cell types and recovered to baseline levels when mice returned to the awake state (T60). Bar graphs on the right summarize calcium level changes at time points T5, T10.2, T30 and T60. **(d, e)** Automated analysis to identify calcium events for neurons **(d)** and astrocytes **(e)** using MATLAB toolbox CHIPS (Barrett et al.,[37]). Detected signals are indicated by colored ROI masks for time points T5, T10.2, T30 and T60 of the isoflurane administration protocol **(a)**. ROIs represent cellular areas of calcium events detected by an automated activity-based algorithm and do not reflect specific manually selected cell structures. Quantification of the number of events detected during these time points are summarized in bar graphs (right). With isoflurane administration there is a significant increase in calcium events in both neurons and astrocytes (T10.2) compared to baseline (T5). Event frequencies are strongly reduced during the anesthetized state (T30) and recover back to baseline at T60. Example traces illustrate automatically detected events at T5, T10.2, T30 and T60 for neurons **(d)** and astrocytes **(e)**. ROI = region of interest. T indicates time points in minutes. N = number of animals, n = number of experiments. Data is represented as mean ± SD. m = 6 experiments used to derive statistics. Mean statistics were calculated using two-tailed linear mixed-effects models and Tukey post hoc tests.

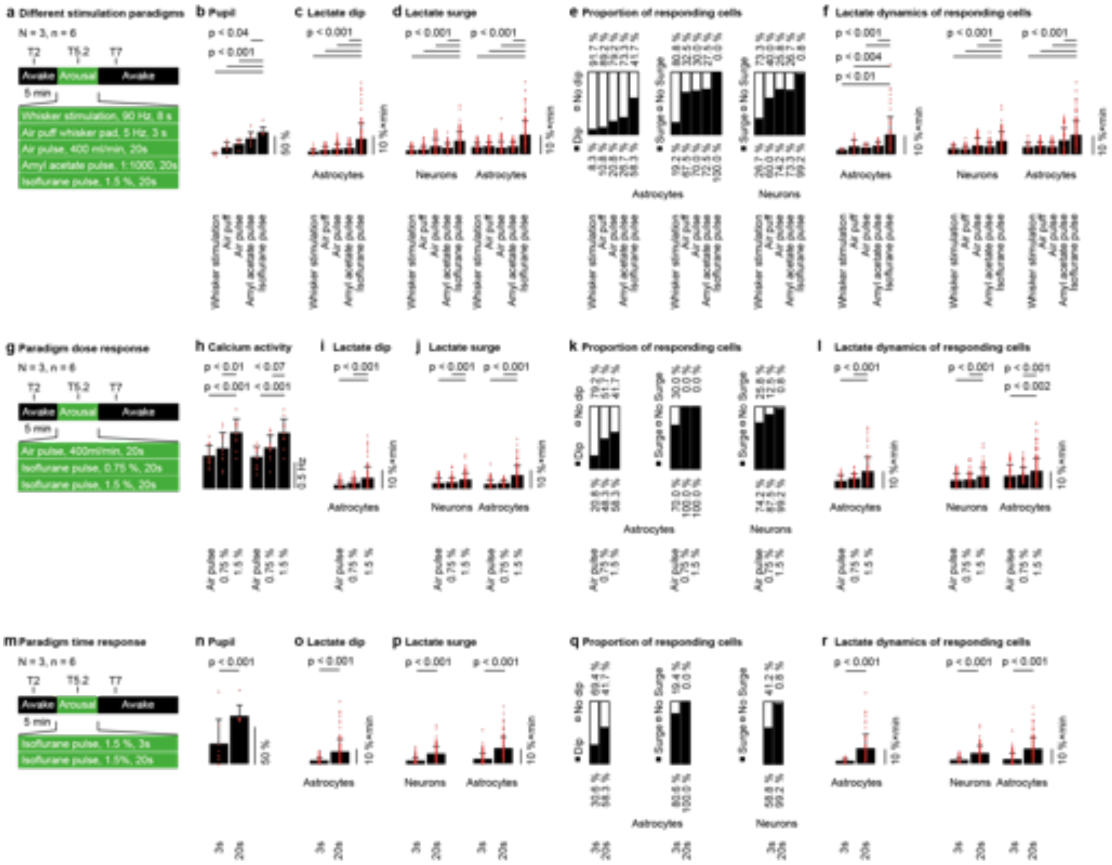
a Different stimulation paradigms
N = 3, n = 6
T2
T5.2
T7
Awake
Arousal
Awake
5 min
Whisker stimulation, 90 Hz, 8 s
Air puff whisker pad, 5 Hz, 3 s
Air pulse, 400 ml/min, 20s
Amyl acetate pulse, 1:1000, 20s
Isoflurane pulse, 1.5 %, 20s
b Pupil
p < 0.04
p < 0.001
50 %
c Lactate dip
p < 0.001
10 %•min
Astrocytes
d Lactate surge
p < 0.001
p < 0.001
Neurons
Astrocytes
e Proportion of responding cells
Dip
No dip
Surge
No Surge
Astrocytes
Neurons
f Lactate dynamics of responding cells
p < 0.001
p < 0.004
p < 0.01
Whisker stimulation
Air puff
Air pulse
Amyl acetate pulse
Isoflurane pulse
g Paradigm dose response
N = 3, n = 6
Air pulse, 400ml/min, 20s
Isoflurane pulse, 0.75 %, 20s
Isoflurane pulse, 1.5 %, 20s
h Calcium activity
p < 0.01
< 0.07
p < 0.001
< 0.001
0.5 Hz
i Lactate dip
j Lactate surge
k Proportion of responding cells
l Lactate dynamics of responding cells
p < 0.002
Air pulse
0.75 %
1.5 %
m Paradigm time response
N = 3, n = 6
Isoflurane pulse, 1.5 %, 3s
Isoflurane pulse, 1.5%, 20s
n Pupil
o Lactate dip
p Lactate surge
q Proportion of responding cells
r Lactate dynamics of responding cells
3s
20s

**Ext. Data S4.5.: Comparison of Different Stimulation Paradigms (Related to Figure 4.1).**
**(a)** Different paradigms to induce arousal in awake mice. **(b)** Comparison of pupil response strengths at T5.2 between the different paradigms. Whisker stimulation induced the smallest response (left) compared to a brief isoflurane pulse (strongest response; right). **(c, d)** Quantification of the area under the curve (AUC) of the stimulation evoked lactate dip in astrocytes **(c)** and the induced lactate surges in neurons (d; left) and astrocytes (d; right). Note that isoflurane pulse evoked the largest response when compared to other stimulation paradigms. **(e)** Comparison of stimulation paradigms and percentage of responding astrocytes and neurons. Only the ISO pulse mobilized the entire astrocytic and neuronal network. The threshold for a lactate dip (T5.2) or surge (T7) detection was set to 2 x SD from baseline values (T2). **(f)** Quantification of lactate dips and surges of only responding neurons and astrocytes identified in (e). **(g)** Dose-dependent stimulation with isoflurane (air pulse, 0.75 % isoflurane and 1.5 % isoflurane at 400 ml/min through a ventilation mask). **(h)** Quantification of evoked calcium events in astrocytes and neurons. Note that 1.5 % isoflurane evoked the highest number of events. The same field of view was monitored for each paradigm. **(i, j)** The AUC for the dip in astrocytes and the surge in both cell types. **(k)** Percentages of astrocytes and neurons with a lactate response. **(l)** Quantification of the AUC of responding neurons and astrocytes only. **(m)** Time-dependent stimulation with isoflurane. **(n)** Comparison of response strengths measured by pupil response. **(o, p)** Quantification of lactate dips in astrocytes (o), and lactate surges in neurons and astrocytes (p). Note that the 20 s isoflurane pulse evoked a stronger response in neurons and astrocytes when compared to the 3 s stimulation paradigm. **(q)** Comparison of 3 s and 20 s isoflurane pulse stimulation regarding percentages of responding cells. **(r)** Quantification of the AUC of responding neurons and astrocytes only. The threshold for a lactate dip (T5.2) or surge (T7) detection was set to 2 x SD from baseline values (T2). The same 120 neurons and 104 astrocytes were monitored for each paradigm. T indicates time points in minutes. N = number of animals, n = number of experiments. Data is represented as mean ± SD. m = 120 neurons and 104 astrocytes for lactate measurements or 6 experiments for calcium and pupil measurements used to derive statistics. Mean statistics were calculated using two-tailed linear mixed-effects models and Tukey post hoc tests.

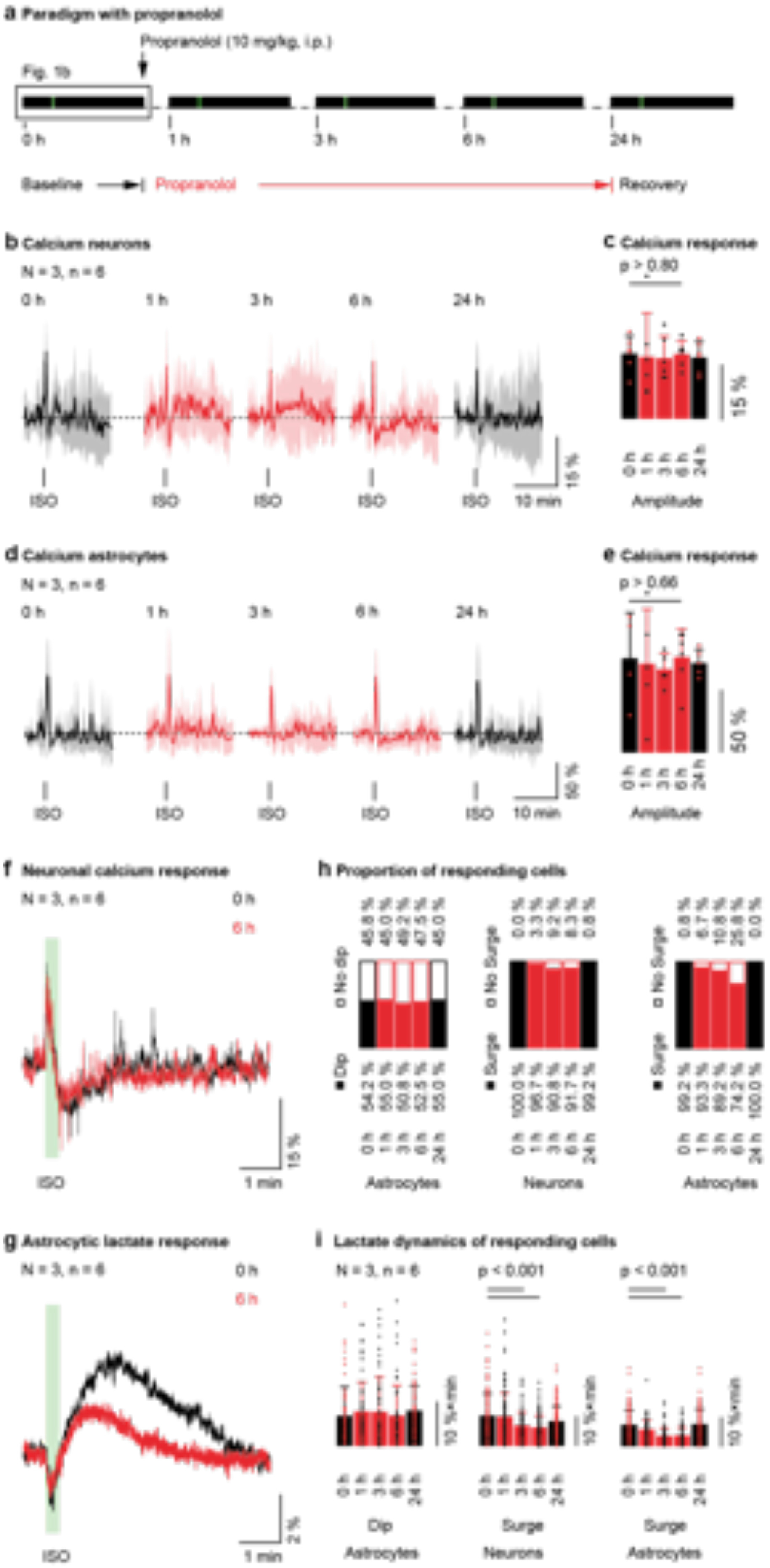
a Paradigm with propranolol
Propranolol (10 mg/kg, i.p.)
Fig. 1b
0 h
1 h
3 h
6 h
24 h
Baseline
Propranolol
Recovery
b Calcium neurons
N = 3, n = 6
0 h
1 h
3 h
6 h
24 h
ISO
ISO
ISO
ISO
ISO
10 min
15 %
c Calcium response
p > 0.80
15 %
0 h
1 h
3 h
6 h
24 h
Amplitude
d Calcium astrocytes
N = 3, n = 6
0 h
1 h
3 h
6 h
24 h
ISO
ISO
ISO
ISO
ISO
10 min
50 %
e Calcium response
p > 0.66
50 %
0 h
1 h
3 h
6 h
24 h
Amplitude
f Neuronal calcium response
N = 3, n = 6
0 h
6 h
ISO
1 min
15 %
h Proportion of responding cells
□ No dip
■ Dip
45.8 %
45.0 %
49.2 %
47.5 %
45.0 %
54.2 %
55.0 %
50.8 %
52.5 %
55.0 %
0 h
1 h
3 h
6 h
24 h
Astrocytes
□ No Surge
■ Surge
0.0 %
3.3 %
9.2 %
8.3 %
0.8 %
100.0 %
96.7 %
90.8 %
91.7 %
99.2 %
0 h
1 h
3 h
6 h
24 h
Neurons
□ No Surge
■ Surge
0.8 %
6.7 %
10.8 %
25.8 %
0.0 %
99.2 %
93.3 %
89.2 %
74.2 %
100.0 %
0 h
1 h
3 h
6 h
24 h
Astrocytes
g Astrocytic lactate response
N = 3, n = 6
0 h
6 h
ISO
1 min
2 %
i Lactate dynamics of responding cells
N = 3, n = 6
p < 0.001
p < 0.001
10 %/min
10 %/min
10 %/min
0 h
1 h
3 h
6 h
24 h
Dip
Astrocytes
0 h
1 h
3 h
6 h
24 h
Surge
Neurons
0 h
1 h
3 h
6 h
24 h
Surge
Astrocytes

**Ext. Data S4.6.: Propranolol Has no Effect on Cellular Calcium Activity but Reduces Lactate Surge in Astrocytes and Neurons (Related to Figure 4.3).**

**(a)** Protocol used to investigate the effects of propranolol in neurons and astrocytes. Propranolol (10 mg per kg, i.p.) was injected after baseline acquisition (0 h) and the same cells were imaged in subsequent sessions 1, 3, 6 and 24 h after injection. **(b-e)** ISO pulse-evoked calcium changes in neurons **(b,c )** and astrocytes **(d, e)** at different time points. Signal amplitudes did not differ from control experiments with saline injections (Extended Data S4.7). m = 6 experiments used for statistical analysis. **(f, g)** Temporal comparison of neuronal calcium and astrocytic lactate response before (0 h; black) and 6 h after (red) propranolol injection. Propranolol has no effect on neuronal calcium response **(f)** and the initial dip in astrocytic lactate upon arousal but reduces the second phase of lactate mobilization reducing the astrocytic lactate surge **(g)**. Only means are displayed. **(h)** The fraction of astrocytes showing a dip and the fraction of astrocytes and neurons showing an activity-dependent surge. **(i)** The area under the curve (AUC) in responding astrocytes and the AUC of the surge of responding astrocytes and neurons. The threshold for a lactate dip (T5.2) or surge (T7) detection was set to 2 SD from baseline values (T2). The same 113 neurons and 118 were monitored for each paradigm. N = number of animals, n = number of experiments. Data is represented as mean ± SD. m = 113 neurons and 118 astrocytes for lactate measurements used to derive statistics. Mean statistics were calculated using two-tailed linear mixed-effects models and Tukey post hoc tests.

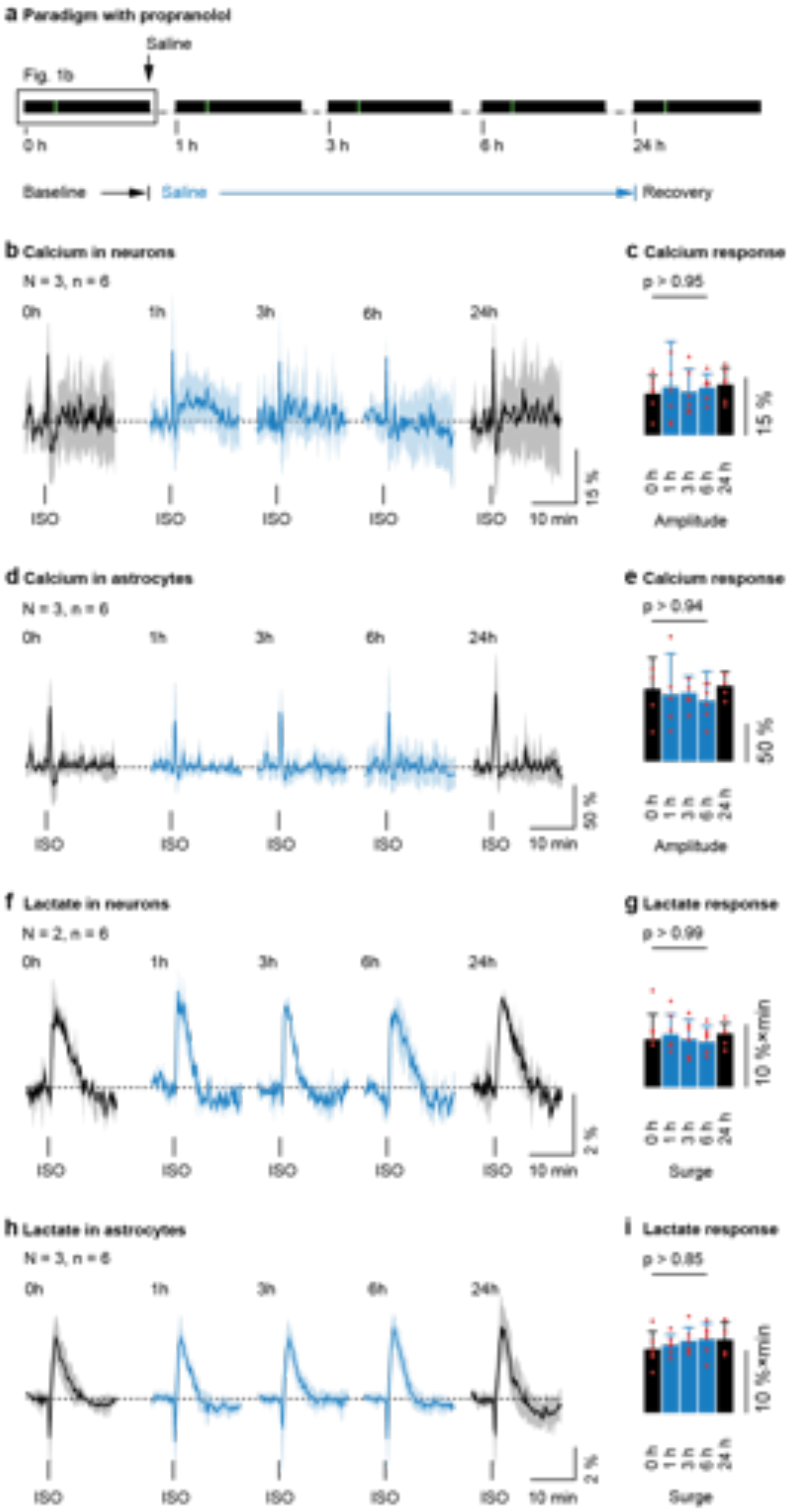
a Paradigm with propranolol
Saline
Fig. 1b
0 h
1 h
3 h
6 h
24 h
Baseline
Saline
Recovery
b Calcium in neurons
N = 3, n = 6
0h
1h
3h
6h
24h
ISO
10 min
15 %
c Calcium response
p > 0.95
15 %
0 h
1 h
3 h
6 h
24 h
Amplitude
d Calcium in astrocytes
N = 3, n = 6
0h
1h
3h
6h
24h
ISO
10 min
50 %
e Calcium response
p > 0.94
50 %
0 h
1 h
3 h
6 h
24 h
Amplitude
f Lactate in neurons
N = 2, n = 6
0h
1h
3h
6h
24h
ISO
10 min
2 %
g Lactate response
p > 0.99
10 %×min
0 h
1 h
3 h
6 h
24 h
Surge
h Lactate in astrocytes
N = 3, n = 6
0h
1h
3h
6h
24h
ISO
10 min
2 %
i Lactate response
p > 0.85
10 %×min
0 h
1 h
3 h
6 h
24 h
Surge

**Ext. Data S4.7.: Control Saline Experiments of Calcium and Lactate Responses in Neurons and Astrocytes (Related to Figure 4.3).**
**(a)** Scheme of the control protocol with saline for arousal-induced calcium and lactate responses in neurons and astrocytes. The same cells as in the propranolol paradigm were monitored in sequential imaging sessions. **(b-e)** Evoked calcium responses in neurons **(b, c)** and astrocytes **(d, e)** Calcium responses were not affected by saline injection. **(f-i)** Evoked lactate response in neurons **(f)** and astrocytes **(h)** before and after saline injection (0 h - 24 h). The same 113 neurons and 118 astrocytes were monitored in 6 experiments per time point. The isoflurane-induced lactate response in neurons **(g)** and astrocytes **(i)** was not affected by saline injection. Data is represented as mean ± SD. N = number of animals, n = number of experiments. Data was binned into 12 s fragments for data visibility in (b), (d), (f) and (h). m = 6 experiments used to derive statistics. Mean statistics were calculated two-tailed using linear mixed-effects models and Tukey post hoc tests.

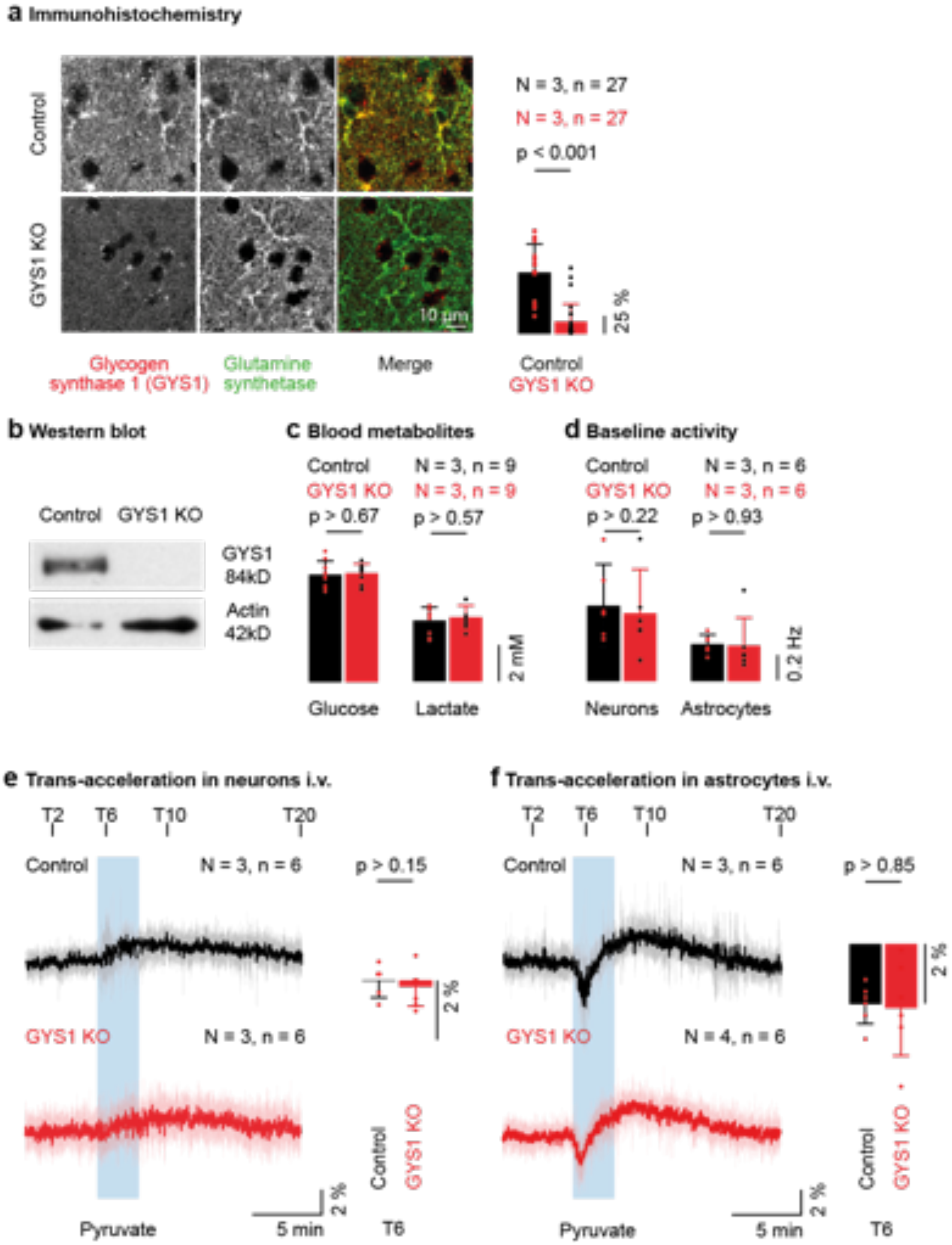
a Immunohistochemistry
Control
GYS1 KO
10 µm
Glycogen synthase 1 (GYS1)
Glutamine synthetase
Merge
N = 3, n = 27
N = 3, n = 27
p < 0.001
25 %
Control
GYS1 KO
b Western blot
Control
GYS1 KO
GYS1 84kD
Actin 42kD
c Blood metabolites
Control
GYS1 KO
N = 3, n = 9
N = 3, n = 9
p > 0.67
p > 0.57
2 mM
Glucose
Lactate
d Baseline activity
Control
GYS1 KO
N = 3, n = 6
N = 3, n = 6
p > 0.22
p > 0.93
0.2 Hz
Neurons
Astrocytes
e Trans-acceleration in neurons i.v.
T2
T6
T10
T20
Control
N = 3, n = 6
GYS1 KO
N = 3, n = 6
Pyruvate
5 min
2 %
p > 0.15
2 %
Control
GYS1 KO
T6
f Trans-acceleration in astrocytes i.v.
T2
T6
T10
T20
Control
N = 3, n = 6
GYS1 KO
N = 4, n = 6
Pyruvate
5 min
2 %
p > 0.85
2 %
Control
GYS1 KO
T6

Ext. Data S4.8.: **Comparison of Control Animals and GYS KO Mice (Related to Figure 4.4).**
**(a)** Immunohistological analysis of GYS1 KO (bottom) and control animals (litter mates; top) of cortical glycogen synthase 1 (GYS1; red) and glutamine synthetase (green). The merge illustrates loss of GYS1 in GYS1 KO mice. Graph represents quantification of the fluorescence intensity of GYS1 (17.2 ± 24.2 %) normalized to the mean of all control animals (100.0 ± 48.2 %; $p = < 0.001$). **(b)** Western blot analysis of GYS1 protein abundance in GYS1 KO and control cortical tissue. Actin was used as loading control. Experiment was repeated 3 times with similar result. **(c)** Blood plasma glucose (left panel) and lactate (right panel) do not differ between GYS1 KO and control animals. **(d)** Automatically detected calcium events in cortical neurons (left) and astrocytes (right) in GYS1 KO mice (red) and littermate control animals (black). Both have a similar resting state activity. **(e, f)** One-point calibration with trans-acceleration (3 min; 500 mM pyruvate; i.v.) did not differ between GYS1 KO and control mice. Data set for control animals comprised 110 neurons and 102 astrocytes. Data set for knock-out animals comprised 108 neurons and 87 astrocytes. N = number of animals, n = number of experiments. Data is represented as mean ± SD. m = number of experiments as stated in the representing figure used to derive statistics. Mean statistics were calculated using two-tailed linear mixed-effects models and Tukey post hoc tests.

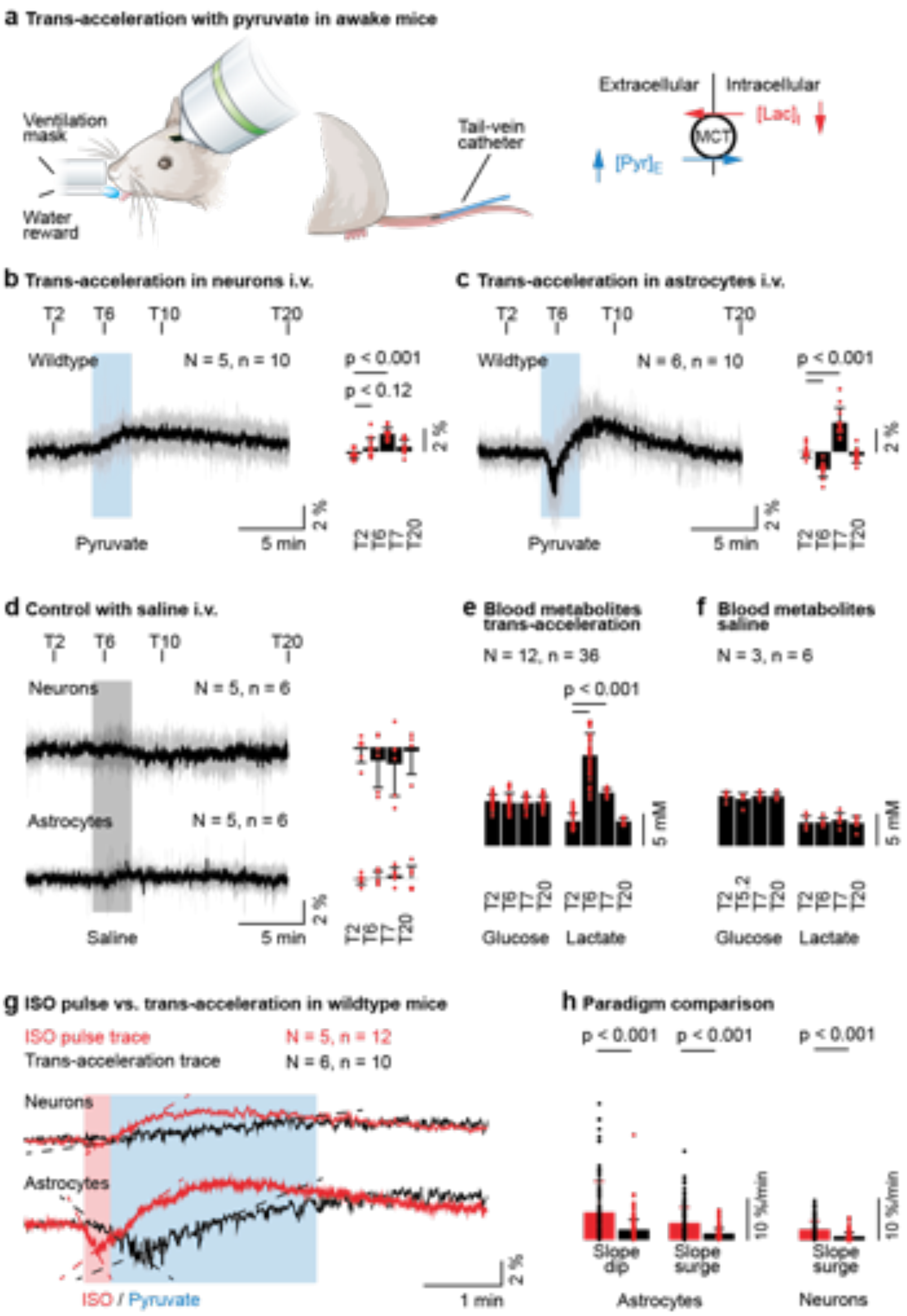
a Trans-acceleration with pyruvate in awake mice
Ventilation mask
Water reward
Tail-vein catheter
Extracellular
Intracellular
[Lac]I
MCT
[Pyr]E
b Trans-acceleration in neurons i.v.
T2 T6 T10 T20
Wildtype
N = 5, n = 10
p < 0.001
p < 0.12
2 %
Pyruvate
5 min
2 %
T2 T6 T7 T20
c Trans-acceleration in astrocytes i.v.
T2 T6 T10 T20
Wildtype
N = 6, n = 10
p < 0.001
2 %
Pyruvate
5 min
2 %
T2 T6 T7 T20
d Control with saline i.v.
T2 T6 T10 T20
Neurons
N = 5, n = 6
Astrocytes
N = 5, n = 6
Saline
5 min
2 %
T2 T6 T7 T20
e Blood metabolites trans-acceleration
N = 12, n = 36
p < 0.001
5 mM
T2 T6 T7 T20
T2 T6 T7 T20
Glucose
Lactate
f Blood metabolites saline
N = 3, n = 6
5 mM
T2 T5.2 T7 T20
T2 T6 T7 T20
Glucose
Lactate
g ISO pulse vs. trans-acceleration in wildtype mice
ISO pulse trace
N = 5, n = 12
Trans-acceleration trace
N = 6, n = 10
Neurons
Astrocytes
ISO / Pyruvate
1 min
2 %
h Paradigm comparison
p < 0.001
p < 0.001
p < 0.001
10 %/min
Slope dip
Slope surge
Astrocytes
10 %/min
Slope surge
Neurons

**Ext. Data S4.9.: One-Point Calibration of Lactate Levels in Neurons and Astrocytes. (Related to Figure 4.4)**.

**(a)** Trans-acceleration with pyruvate through a tail-vein catheter for one-point calibration of relative intracellular lactate levels in neurons and astrocytes in awake mice. A bolus injection of pyruvate (3 min; 500 mM; i.v.) artificially increases blood pyruvate levels that enters the brain through monocarboxylate transporter (MCT). Sudden increase in extracellular pyruvate (blue; top right) leads to a rapid extrusion and decrease in intracellular lactate (red; top right). This process is termed trans-acceleration. MCT = monocarboxylate transporter. **(b, c)** A bolus injection of pyruvate resulted in a significant decrease in astrocytic (c) but not neuronal lactate levels (b) indicating significantly higher lactate levels in astrocytes. **(d)** Saline bolus injections had no effect on intracellular lactate levels. For trans-acceleration and saline experiments, the same cells were imaged. m = 6 experiments used for statistical analysis. **(e)** Trans-acceleration increased blood plasma lactate levels (e; right panel) leading to an overshoot of lactate in neurons and astrocytes (b, c). Glucose plasma levels remained stable (e; left panel). **(f)** Saline had neither an effect on blood plasma glucose nor lactate levels. **(g, h)** Comparison of the temporal kinetics of the ISO pulse (red) and trans-acceleration (black) protocol illustrating significant differences in kinetics. N = number of animals, n = number of experiments. Data is represented as mean ± SD. For the comparison 226 neurons and 236 astrocytes for the ISO pulse, and 230 neurons and 200 astrocytes for the trans-acceleration paradigm were used to derive statistics. Mean statistics were calculated using two-tailed linear mixed-effects models and Tukey post hoc tests.

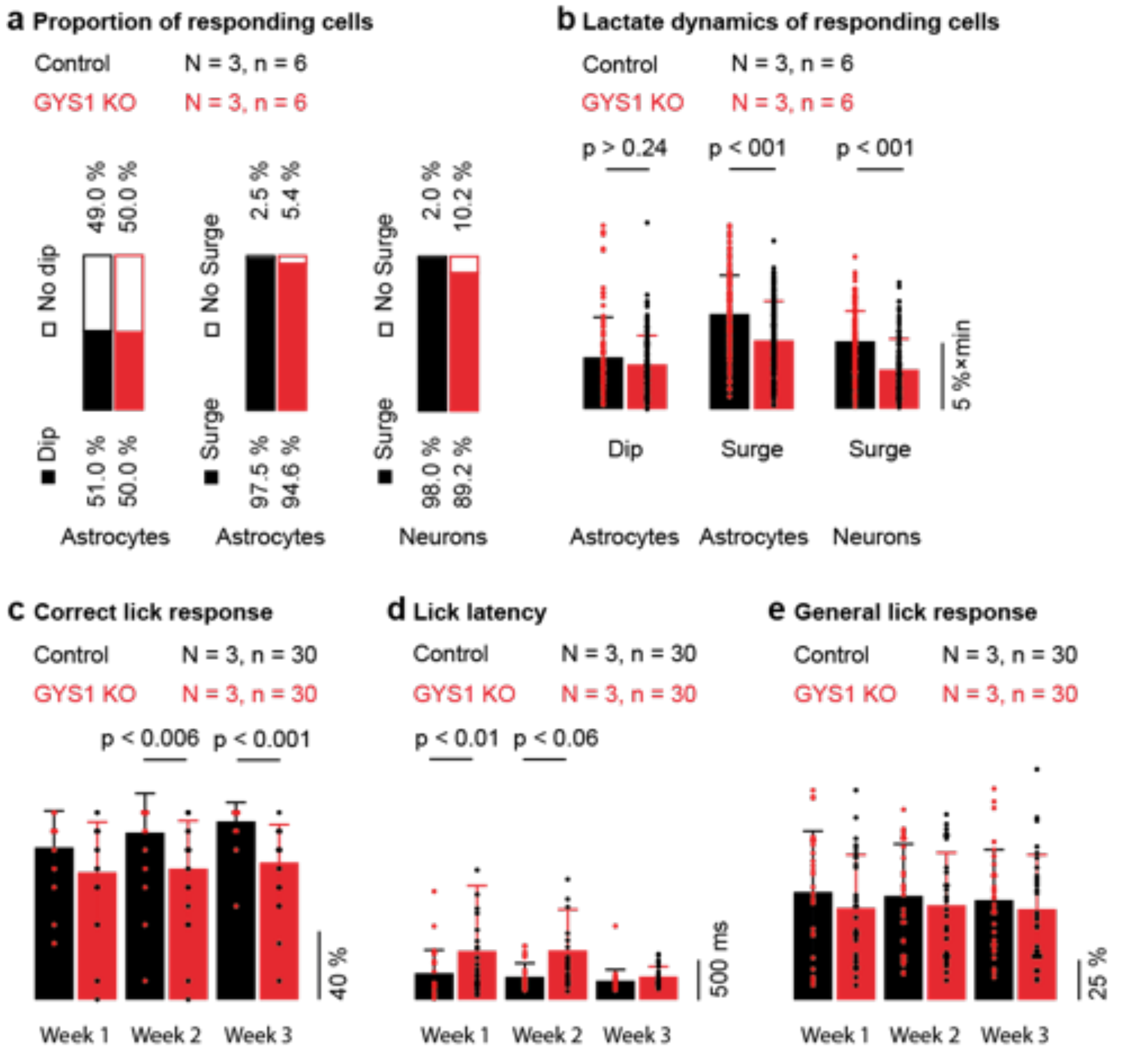

**Ext. Data S4.10.:** **Loss of Brain Glycogen Leads to Impaired Lactate Surges and Associative Learning in GYS1 KO Mice (Related to Figure 4.4).** **(a)** Comparison of responsive cells of control (black) and GYS1 KO mice (red). **(b)** Quantification of the area under the curve (AUC) of responding neurons and astrocytes for the dip and surge identified in a. Astrocytes and neurons with a surge had a lower AUC in GYS1 KO animals. For statistical analysis 177 neurons and 146 astrocytes were used. **(c)** GYS1 KO mice (red) showed impaired learning performance in the suppression-response task when compared to control animals (black) resulting in more errors per trial. **(d, e)** Both groups reduced the response latency to the auditory cue, however, GYS1 KO mice responded significantly slower than the control **(d)** although GYS1 KO were similarly responsive **(e)**. N = number of animals, n = number of experiments. Data is represented as mean ± SD. m = 30 sessions used to derive statistics. Mean statistics were calculated using two-tailed linear mixed-effects models and Tukey post hoc tests.

# 5

# Decoupling Astrocytes in Adult Mice Impairs Synaptic Plasticity and Spatial Learning

Submitted to eLife, July 2020

## Authors and Affiliations

Ladina Hösli[1,2], Noemi Binini[1,2], Laetitia Thieren[1,2], Zoe J. Looser[1,2], Kim David Ferrari[1,2], Marc Zuend[1,2], Stewart Berry[3†], Martin Holub[1,2,6], Wiebke Möbius[4], Torben Ruhwedel[4], Klaus-Armin Nave[4], Christian Giaume[5†], Bruno Weber[1,2*] and Aiman S. Saab[1,2*]

[1] Institute of Pharmacology and Toxicology, University of Zurich, Zurich, Switzerland
[2] Neuroscience Center Zurich, University and ETH Zurich, Zurich, Switzerland
[3] Brain Research Institute, University of Zurich, Zurich, Switzerland
[4] Max Planck Institute of Experimental Medicine, Göttingen, Germany
[5] Collège de France, Center for Interdisciplinary Research in Biology (CIRB), Paris, France
[6] Present address: Department of Bionanoscience, TU Delft, Delft, Netherlands
[†] Dedicated to the memory of Stewart Berry and Christian Giaume

[*] Correspondence: Bruno Weber bweber@pharma.uzh.ch and Aiman S. Saab asaab@pharma.uzh.ch

## Personal Contribution

Designing and performing immunohistological and behavioral experiments and data analysis. Writing, reviewing and editing manuscript.

# Summary

Astrocytes are coupled by gap junctions and form large networks. The role of astrocytic networks in regulating neurotransmission and mouse behavior is mainly derived from disrupting connexins 30 (Cx30) and 43 (Cx43), the two key astrocytic gap junction channel proteins, during brain development. But in the adult brain, the functional importance of astroglial coupling remains elusive. To circumvent developmental perturbations, we have generated inducible, astrocyte-specific Cx30 and Cx43 double knockout mice. We found that reducing astrocytic coupling in adult mice led to widespread activation of astrocytes and microglia, which was accompanied by deficits in sensorimotor performance and in spatial learning. Hippocampal CA1 neuron excitability, excitatory synaptic transmission and plasticity were also altered, without overt changes in glutamate clearance capacity. Our results demonstrate the vital contribution of the astroglial network in modulating neuronal and synaptic activity, and its impact on cognitive functions in the adult brain.

# Introduction

Neurons and astrocytes cultivate a highly dynamic dialogue with each other that is critical for normal brain function. Astrocytes are involved in a plethora of homeostatic processes, ranging from the regulation and modulation of synaptic transmission (Araque et al., 1999; Santello et al., 2019), neurotransmitter, ionic and energy homeostasis (Magistretti and Allaman, 2018; Weber and Barros, 2015), to network plasticity and cognitive abilities (Adamsky and Goshen, 2018; Suzuki et al., 2011). An important feature of astrocytes is that they are highly interconnected and organized in large networks via gap junction channels, which are mainly comprised of connexin 30 (Cx30) and connexin 43 (Cx43; Giaume et al., 2010; Pannasch et al., 2011; Theis et al., 2005). This astroglial channel network allows for intercellular communication, trafficking and redistribution of various neuroactive molecules such as ions, neurotransmitters and metabolites (Giaume et al., 2010).

Most of our current ideas on the function of the astroglial network have been obtained from research in mice in which Cx30 and Cx43 are inactivated during brain development (Pannasch and Rouach, 2013). These double-deficient mice have been generated by crossing Cx30 *null* mutants (Teubner et al., 2003) with mice having a conditional Cx43 deletion in astrocytes (Theis et al., 2003), driven by embryonically or perinatally active Cre transgenic lines under the control of the human glial fibrillary acidic protein promoter (hGFAP-Cre; Zhuo et al., 2001) or the murine GFAP promoter (mGFAP-Cre; Garcia et al., 2004). Postnatal studies in *Cx30*$^{-/-}$*:Cx43*$^{fl/fl}$*:hGFAP-Cre* mice showed that a lack of astrocytic connexin hemichannels and gap junctions in the developing brain produces defects in synaptic plasticity and network excitability, extracellular potassium and glutamate homeostasis, as well as in nutrient supply to neurons (Chever et al., 2016; Pannasch et al., 2012, 2011; Rouach et al., 2008; Wallraff et al., 2006). Moreover, early onset dysmyelination, axonal pathology and the formation of vacuoles in gray and white matter, are a striking feature of *Cx30*$^{-/-}$*:Cx43*$^{fl/fl}$*:mGFAP-Cre* mice (Lutz et al., 2009). Similar white matter pathology and myelin vacuolation were observed in mice deficient in the oligodendroglial connexins Cx32 and Cx47 (Menichella et al., 2006, 2003), suggesting that a lack of functional gap junction coupling between astrocytes and oligodendrocytes (Magnotti et al., 2011; Orthmann-Murphy et al., 2007; Rash, 2010) causes abnormal white matter development that disrupts axonal integrity.

Having numerous functions in development, Cx30 and Cx43 play a role in cell migration, proliferation and differentiation (Cina et al., 2009; Elias et al., 2007; Ghézali et al., 2018; Kunze et al., 2009; Lagos-Cabré et al., 2019). For instance, Cx43 in radial glial cells promotes neuronal migration and neocortical laminar formation during development (Cina et al., 2009; Elias et al., 2007). Cx30 contributes to astroglial polarization during postnatal maturation (Ghézali et al., 2018) and Cx30-deficient mice show impaired cochlear development and severe hearing loss (Cohen-Salmon et al., 2007; Teubner et al., 2003). Furthermore, depending on the genetic background of the mice, hGFAP-Cre-mediated, embryonic deletion of Cx43 impairs cellular organization of the cortex, hippocampus and cerebellum (Wiencken-Barger et al., 2007).

To disentangle these developmental connexin attributes with the early cellular adaptations in Cx30- and Cx43-deficient mice, from the later functional role of the astroglial gap junction network in the adult brain, we generated and studied inducible, astrocyte-specific Cx30 and Cx43 double knockout mice. We found that reducing astrocyte coupling in adult mice triggered a widespread activation of astrocytes and microglia. In both gray and white matter, we saw no sign of tissue damage, vacuolation, neuronal or myelin loss. Behavioral inspection revealed deficits in sensorimotor performance and in spatial learning and memory. In addition, hippocampal CA1 neuron excitability, excitatory synaptic transmission and long-term potentiation were altered in adult knockouts, whereas glutamate clearance appeared unaffected. Our *in vivo* findings demonstrate, for the first time, that an intact astroglial network is required for sensorimotor and cognitive abilities in the adult brain.

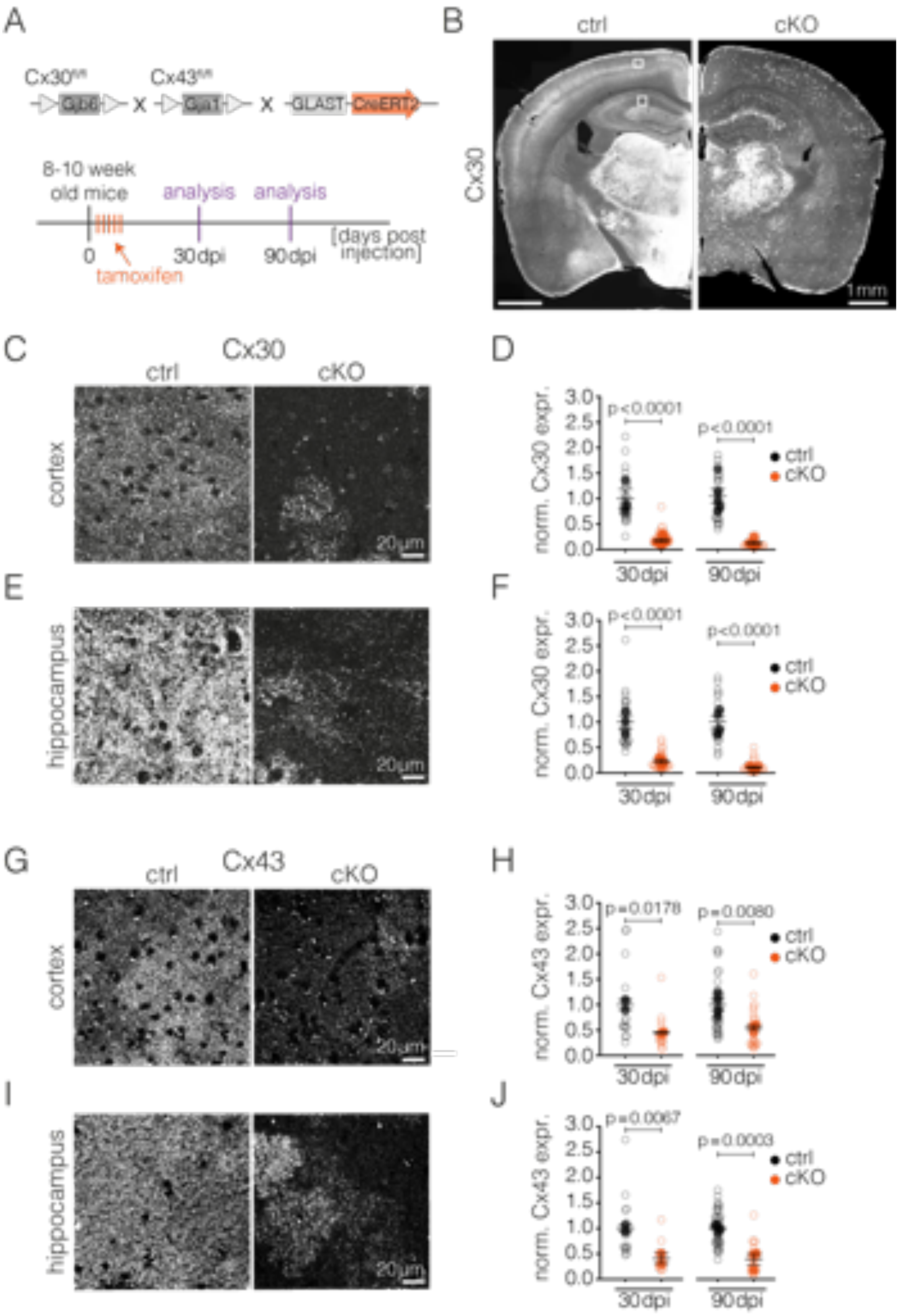

# Results

## Inducible Deletion of Cx30 and Cx43 Impairs Astrocytic Gap Junction Coupling

To study the role of the gap junction coupled astrocytic network in the fully developed brain, we generated inducible double knockouts to selectively delete Cx30 and Cx43 from astrocytes in adult mice. We crossbred mice carrying loxP-flanked *Gjb6* (Cx30$^{fl/fl}$ mice; Boulay et al., 2013) and *Gja1* (Cx43$^{fl/fl}$ mice; Theis et al., 2003) alleles with mice expressing the tamoxifen-sensitive Cre-recombinase CreERT2 under the endogenous GLAST(*Slc1a3*)-promoter (Mori et al., 2006;

**Figure 5.1.: Inducible Deletion of Astrocytic Cx30 and Cx43 in Adult Mice**
**(A)** Generation of $Cx30^{fl/fl}$:$Cx43^{fl/fl}$:$GLAST^{CreERT2/+}$ mice. Tamoxifen injections were given to adult 8-10 week old mice and analysis was performed at 30 and 90 days days post-injection (dpi).
**(B)** Overview images of Cx30 immunolabeled coronal sections from control (ctrl) and cKO at 90 dpi. White boxes indicate example regions used for quantifications, depicted in (C), (E), (G) and (I).
**(C, D)** Confocal images showing Cx30 in cortex of ctrl and cKO mice at 90 dpi **(C)** and quantification of Cx30 expression **(D)**. Compared to ctrl, Cx30 expression in cKO mice was reduced by 78 ± 19% at 30 dpi (n = 3-4, N = 27-36, r = 4.83, t(12.6) = 7.05, $p < 0.0001$) and by 92 ± 15% at 90 dpi (n = 4-5, N = 24-27, r = 9.4, t(21.0) = 10.07, $p < 0.0001$).
**(E, F)** Confocal images showing Cx30 in CA1 hippocampus of ctrl and cKO mice at 90 dpi **(E)** and quantification of Cx30 expression **(F)**. Compared to ctrl, Cx30 expression in cKO mice was reduced by 78 ± 13% at 30 dpi (n = 3-4, N = 27-36, r = 4.82, t(13.0) = 6.98, $p < 0.0001$) and by 90 ± 12% at 90 dpi (n = 4-5, N = 24-27, r = 11.33, t(21.9) = 10.66, $p < 0.0001$).
**(G, H)** Confocal images showing Cx43 in cortex of ctrl and cKO mice at 90 dpi **(G)** and quantification of Cx43 expression **(G)**. Compared to ctrl, Cx43 expression in cKO mice was reduced by 55 ± 10% at 30 dpi (n = 2, N = 18, r = 2.00, t(11.81) = 2.75, $p = 0.0178$) and by 45 ± 12% at 90 dpi (n = 3-4, N = 27-36, r = 1.98, t(9.51) = 3.34, $p = 0.0080$).
**(I, J)** Confocal images showing Cx43 in CA1 hippocampus of ctrl and cKO mice at 90 dpi **(I)** and quantification of Cx43 expression **(J)**. Compared to ctrl, Cx43 expression in cKO mice was reduced by 59 ± 12% at 30 dpi (n = 2, N = 18, r = 2.28, t(11.81) = 3.28, $p = 0.0067$) and by 61 ± 11% at 90 dpi (n = 3-4, N = 27-36, r = 3.04, t(9.51) = 5.42, $p = 0.0003$).
Data are presented as mean ± SEM of animal means (solid circles). Empty circles represent all images quantified. n = number of animals, N = number of images. Significance was tested using linear mixed effects models with post-hoc pairwise comparisons.

Figure 5.1A). Since Cx30 and Cx43 are the two main connexins that form gap junctions in astrocytes (Giaume et al., 2010), inactivation of both isoforms should disrupt astrocytic gap junction coupling (Pannasch et al., 2011; Wallraff et al., 2006).

We injected adult, 8-10 week old mice ($\mathrm{Cx30^{fl/fl}{:}Cx43^{fl/fl}{:}GLASTCre^{ERT2/+}}$, termed cKO) with tamoxifen for 5 consecutive days and studied the deletion of Cx30 and Cx43 at 30 and 90 days post-injection (dpi; Figure 5.1A). Littermate control mice ($\mathrm{Cx30^{fl/fl}{:}Cx43^{fl/fl}{:}GLASTCre^{+/+}}$) were identically treated with tamoxifen. At 30 dpi, we determined a significant reduction in *Gjb6* and *Gja1* mRNA expression from both gray and white matter-enriched brain regions (Fig. 5.1 – Fig. suppl. 1A, B). Immunostaining confirmed a clear loss of Cx30 and Cx43 expression in cKO mice at 30 and 90 dpi, as shown for cortex and hippocampus (Figure 5.1B-J). In brain sections of control mice, we observed a dense punctate staining of Cx30 and Cx43, but in cKO brains, only a few sparsely labeled cells remained visible (Figure 5.1B-J). These cells are likely astrocytes that were not targeted for recombination, as can be seen from GLAST-CreERT2-mediated reporter expression (Fig. 5.1 – Fig. suppl. 1C). We quantified the loss of Cx30 and Cx43 by confocal analysis in the somatosensory cortex and the CA1 region of the hippocampus at 30 and 90 dpi (Figure 5.1C-J). Cx30 expression was significantly reduced by 78 ± 19% (at 30 dpi, $p < 0.0001$) and 92 ± 15% (at 90 dpi, $p < 0.0001$) in the cortex (Figure 5.1C, D) and by 78 ± 13% (at 30 dpi, $p < 0.0001$) and 90 ± 12% (at 90 dpi, $p < 0.0001$) in the hippocampus of cKO mice compared to littermate controls (Figure 5.1E, F). Cx43 expression was also significantly reduced by 55 ± 10% (at 30 dpi, $p = 0.0178$) and 45 ± 12% (at 90 dpi, $p = 0.0080$) in the cortex (Figure 5.1G, H) and by 59 ± 12% (at 30 dpi, $p = 0.0067$) and 61 ± 11% (at 90 dpi, $p = 0.0003$) in the hippocampus (Figure 5.1I, J). Given the residual expression of connexins, we next examined the extent to which the astrocytic gap junction coupling is impaired in our inducible cKO mice. For this, we performed dye coupling experiments around 90 dpi in acute hippocampal slices (Figure 5.2A, B). The intercellular coupling assessed by biocytin diffusion was found to be significantly reduced by 74 ± 17% ($p = 0.0010$) in cKO mice compared to littermate controls (Figure 5.2B), without any overt changes in the intrinsic membrane properties of the whole-cell patched astrocytes from both genotypes (Figure 5.2C, D).

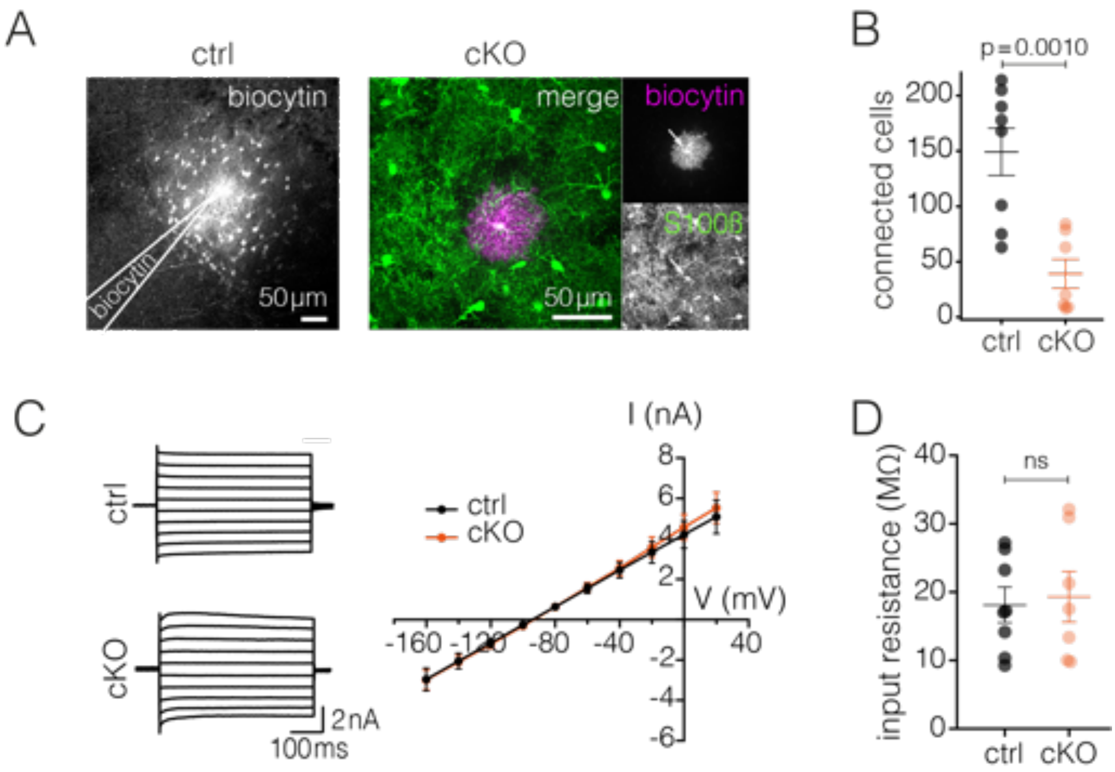

**Figure 5.2.: Disruption of Gap Junction Coupling in cKO Mice**
**(A, B)** Biocytin filling of astrocytes in hippocampal slices. **(A)** Example images (maximum projections) from ctrl (left) and cKO mice (right) co-stained with the astrocytic marker S100β. **(B)** Quantification of biocytin-coupled cells revealed a reduction of 74 ± 17% in cKO mice compared to ctrl (n = 7-8, t(11.4) = 4.40, $p$ = 0.001, unpaired $t$ test).
**(C, D)** No difference was found in current-voltage (I/V) plots **(C)** and input resistance **(D)** in astrocytes from ctrl and cKO mice (n = 7-8, t(10.1) = -0.27, $p$ = 0.7875, unpaired $t$ test).
Data are presented as mean ± SEM. n = number of cells from 4-5 animals per genotype.

## Astrocytic Decoupling Causes Widespread Activation of Astrocytes and Microglia

We asked whether disruption of the astroglial network in the adult brain impacts cellular functions and mouse behavior. With this in mind, we first inspected brains of cKO mice to see if they were developing any signs of pathology following astrocyte decoupling. In coronal brain sections from cKO mice, we observed, both in gray and white matter regions, an increased immunoreactivity against the astrocytic marker GFAP (Figure 5.3A-D) and the microglial marker Iba1 (Figure 5.3E-H), indicative of activated astrocytes and microglia, respectively. Noteworthy was that the increase in gliosis was already apparent at 30 dpi and became more pronounced at 90 dpi (Figure 5.3, Fig. 5.3 – Fig. suppl. 1A-C). Reactive astrocytes appeared more ramified with more elongated processes (Figure 5.3A), however, the density of astrocytes (S100β-positive) remained unchanged in cKO mice (Fig. 5.3 – Fig. suppl. 1D). An important finding was that despite the visible hypertrophy of astrocytes and microglia we did not detect any signs of tissue damage such as vacuolation (Figure 5.4A) as has been previously described in both gray and white matter regions from mice with developmental deletions of Cx30 and Cx43 (Lutz et al., 2009). In addition, the gross structural organization of neuronal layers appeared normal (Figure 5.4A, B) and neuronal density assessed by NeuN labeling remained unchanged in cKO

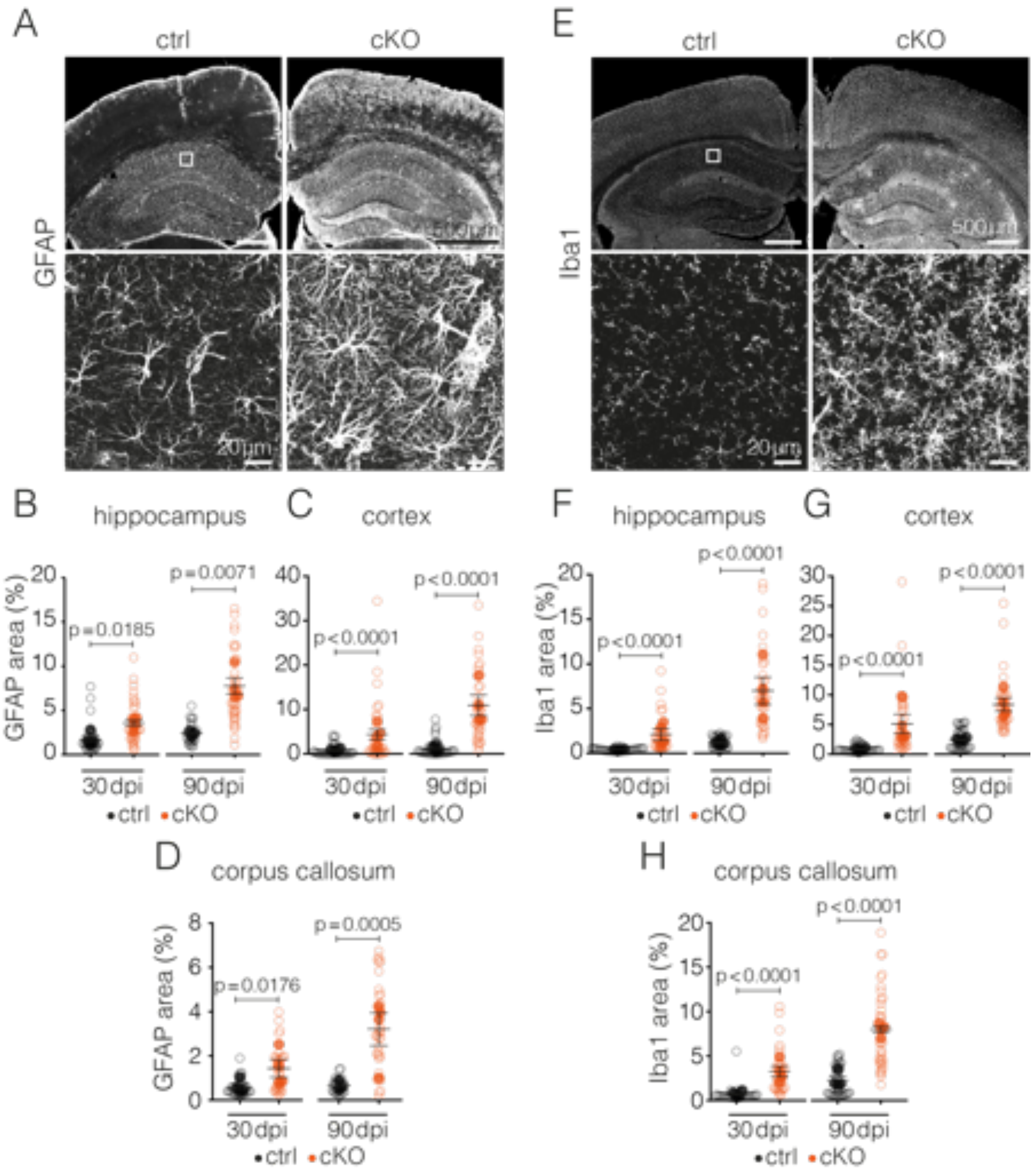

mice compared to littermate controls (Figure 5.4C, D). This means there was no apparent neuronal loss when the astroglial network was compromised, in line with earlier developmental knockout studies (Lutz et al., 2009; Pannasch et al., 2011). Indeed, we confirmed the absence of neurodegeneration in cKO mice by Fluoro-Jade C staining (Figure 5.4E), which is commonly used to detect degenerating neurons (Chao et al., 2019; Rook et al., 2015; Wang et al., 2003, 2008). Moreover, in contrast to previous observations in developmental double-deficient *Cx30*$^{-/-}$*:Cx43*$^{fl/fl}$*:mGFAP-Cre* mice (Lutz et al., 2009), white matter tracts

**Figure 5.3.: Activated Astrocytes and Microglia Following Decoupling of Astrocytes**
**(A)** Representative confocal images of GFAP immunolabeling from ctrl and cKO brain sections at 90 dpi. White box indicates magnified area depicted in lower panel.
**(B)** Quantification of GFAP-positive area in hippocampus. Compared to ctrl, cKO mice showed a significant increase in GFAP area at 30 dpi (n = 4, N = 36, r = 0.46, t(24.4) = -2.53, $p$ = 0.0185) and at 90 dpi (n = 3-4, N = 27-36, r = 0.39, t(28.3) = -2.90, $p$ = 0.0071).
**(C)** Quantification of GFAP-positive area in cortex. Compared to ctrl, cKO mice showed a significant increase in GFAP area at 30 dpi (n = 4, N = 36, r = 0.18, t(24.4) = -5.47, $p$ < 0.0001) and at 90 dpi (n = 4, N = 36, r = 0.07, t(24.4) = -8.87, $p$ < 0.0001).
**(D)** Quantification of GFAP-positive area in corpus callosum. Compared to ctrl, cKO mice showed a significant increase in GFAP area at 30 dpi (n = 4, N = 36, r = 0.46, t(24.4) = -2.55, $p$ = 0.0176) and a significant increase at 90 dpi (n = 3-4, N = 27-36, r = 0.27, t(28.3) = -3.95, $p$ = 0.0005).
**(E)** Representative confocal images of Iba1 staining from ctrl and cKO sections at 90 dpi. White box indicates magnified area depicted in lower panel.
**(F)** Quantification of Iba1-positive area in hippocampus. Compared to ctrl, cKO mice showed an increase in Iba1 area at 30 dpi (n = 4, N = 36, r = 0.24, t(14.7) = -5.71, $p$ < 0.0001) and at 90 dpi (n = 4 N = 36, r = 0.17, t(14.7) = -7.81, $p$ < 0.0001).
**(G)** Quantification of Iba1-positive area in cortex. Compared to ctrl, cKO mice showed an increase in Iba1 area at 30 dpi (n = 4, N = 36, r = 0.21, t(14.7) = -6.31, $p$ < 0.0001) and at 90 dpi (n = 4, N = 36, r = 0.26, t(14.7) = -5.37, $p$ < 0.0001).
**(H)** Quantification of Iba1-positive area in corpus callosum. Compared to ctrl, cKO mice showed an increase in Iba1 area at 30 dpi (n = 4 N = 36, r = 0.22, t(14.7) = -6.05, $p$ < 0.0001) and at 90 dpi (n = 4 N = 36, r = 0.24, t(14.7) = -5.72, $p$ < 0.0001).
Data are presented as mean ± SEM of animal means (solid circles). Empty circles represent all images quantified. n = number of animals, N = number of images. Significance was tested using linear mixed effects models with post-hoc pairwise comparisons.

of cKO mice revealed no signs of demyelination, myelinic or axonal pathology at 90 dpi (Figure 5.5).

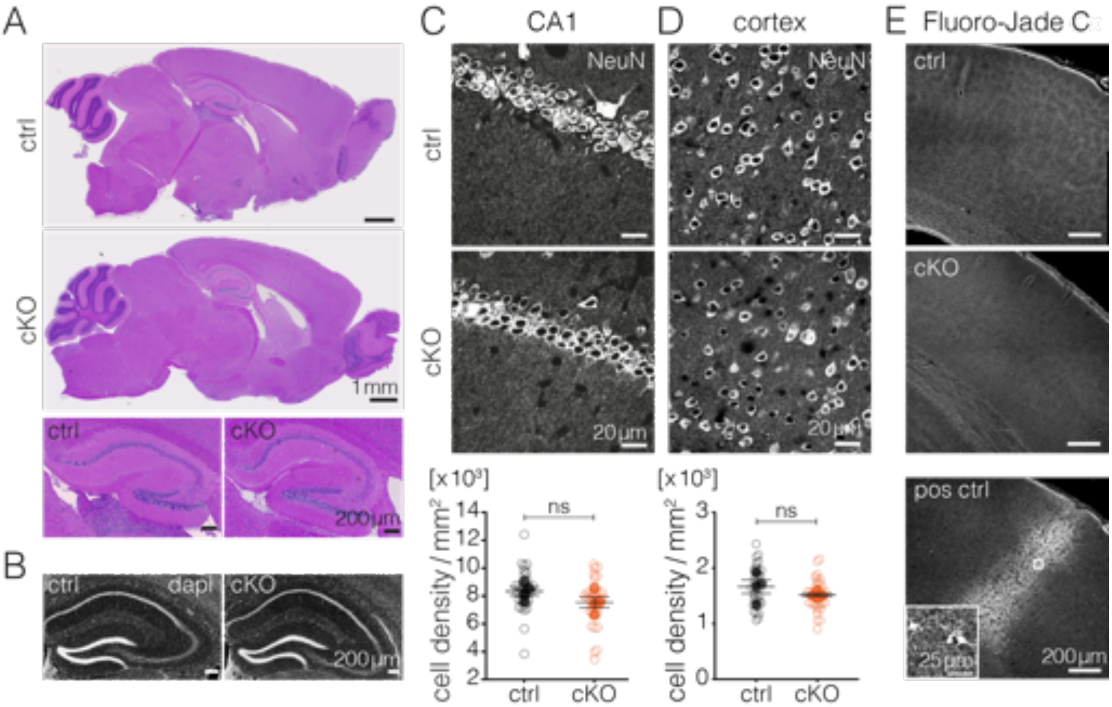

**Figure 5.4.:** **No Signs of Vacuolation or Neuronal Loss in cKO Mice**
**(A, B)** Representative H&E-stained sagittal brain sections **(A)** from ctrl and cKO mice at the age of 8 months (180 dpi) showing no signs of vacuolation or lesions, nor any overt structural changes in neuronal layers; see also exemplary images of hippocampal sections stained with nuclear marker DAPI **(B)**.
**(C, D)** No changes in neuronal density in cKO mice, determined by NeuN immunolabeling in CA1 hippocampus (C, n = 4, N = 36, r = 1.12, t(9.08) = 1.57, $p$ = 0.1496) and cortex (D, n = 4, N = 36, r = 1.09, t(9.08) = 1.25, $p$ = 0.2424).
**(E)** No sign of degenerating neurons in cKO mice, assessed by Fluoro-Jade C labeling (n = 4 mice per genotype). Brain sections from wildtype mice subjected to cortical microinfarcts were used as positive controls (pos ctrl, lower panel), showing a clear labeling of degenerating cells.
Data are presented as mean ± SEM of animal means (solid circles). Empty circles represent all images quantified. n = number of animals, N = number of images. Significance was tested using linear mixed effects models with post-hoc pairwise comparisons.

## Spatial Learning is Impaired Following Astrocyte Decoupling

Next, we examined whether astrocyte decoupling in adult mice causes any behavioral changes. To assess possible alterations in sensorimotor skills, we tested cKO mice and littermate controls before treatment with tamoxifen and 30, 60 and 90 days after treatment, using behavioral paradigms that included gait analysis, ledge test, hindlimb clasping and horizontal wire assays (Figure 5.6A). As expected, both groups of mice showed a similar score before tamoxifen treatment (pretam). However, starting from around 30 dpi, cKO mice developed subtle sensorimotor deficits that gradually became more pronounced at 90 dpi ($p = 0.0001$, Figure 5.6A). We then inspected whether cKO mice also develop deficits in learning and memory. For this, we tested cKO mice and littermate controls for object recognition memory (Figure 5.6B) and for spatial reference learning and memory (Figure 5.6C-J) before tamoxifen treatment and at 90 dpi. Rodents have a natural preference to explore novel objects rather than familiar ones (Goulart et al., 2010; Leger et al., 2013). We tested the ability of cKO animals to recognize and remember familiar objects using the novel object recognition test at retention intervals of 3 h and 24 h. Neither short-term nor long-term recognition memory was impaired in cKO mice at 90 dpi (Figure 5.6B). Of note, since novel objects replaced the familiar object at the same location in the box, the novel object recognition test did not require spatial working memory. To directly assess spatial learning and memory, which is primarily controlled by the hippocampus (Broadbent et al., 2004; Moser et al., 1998), we performed a Barnes maze test in which mice had to learn and remember the position of an escape hole on a round table guided by visual cues (Figure 5.6C). Before tamoxifen treatment, there was no difference between cKO mice and littermate controls in spatial learning and memory performance. Both groups of mice showed similar learning abilities to locate the target hole during the spatial acquisition phase (Figure 5.6D) and performed equally well during the memory recall phase at test day 5 (Figure 5.6F, G). However, 90 days after tamoxifen treatment, cKO mice revealed a significant deficit in spatial learning (Figure 5.6E) and a complete lack of memory for target location on test day 5 compared to littermate controls (Figure 5.6I, J). Important to note is that these results were not influenced by possible changes in motivation or locomotor activity since walking distance during the defined test period of 90 s was identical between the genotypes (Figure 5.6H, K).

Taken together, decoupling of astrocytes in adult mice led to an activation of astrocytes and microglia, which was accompanied by deficits in sensorimotor skills and in spatial reference learning and memory without any overt signs of tissue damage, vacuole formation, neuronal or myelin loss.

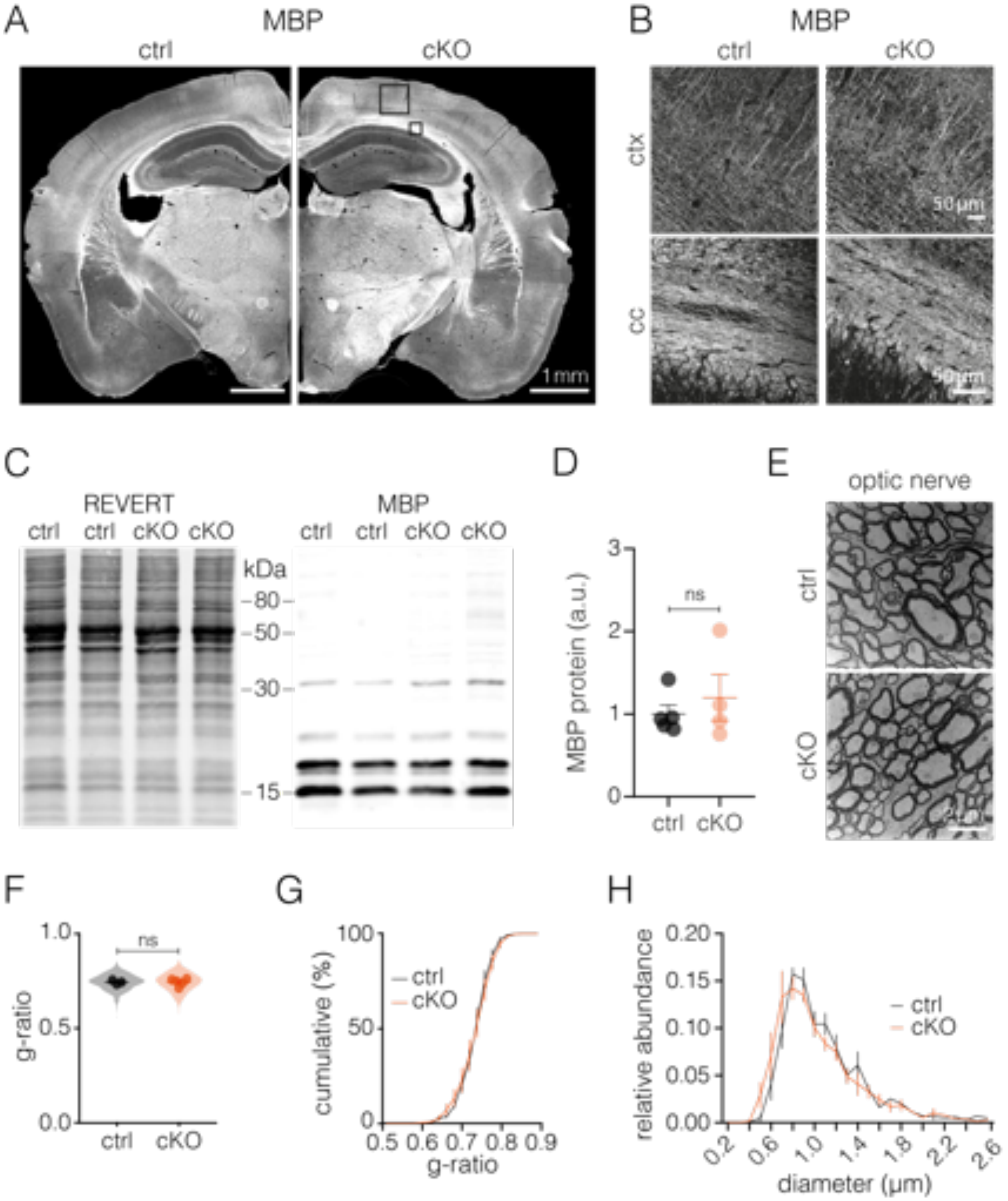

Figure 5.5.: **Unchanged Myelination and White Matter Integrity in cKO Mice**
**(A, B)** Overview pictures of brain sections immunostained for myelin basic protein (MBP), a marker for myelin **(A)** and magnifications **(B)** of regions indicated by black boxes, of cortex (ctx) and corpus callosum (cc). No overt difference in overall myelination was observed between ctrl and cKO brains.
**(C, D)** Western blot analysis of MBP expression in cortex extracts of ctrl (n = 5) and cKO mice (n = 4) at 90 dpi showed no difference in protein abundance (U = 9, $p$ = 0.9048, Mann Whitney). REVERT total protein stain was used as loading control.
**(E)** Electron microscopy images of optic nerves from ctrl and cKO mice at 90 dpi.
**(F-H)** Myelin sheath thickness, g-ratio **(F, G)** and axon size distribution of myelinated axons **(H)** were similar in ctrl and cKO nerves. **(F)** No difference was found in g-ratios (n = 3-4 mice, N = 1522-1958 axons, $\beta$= 0.01, t(5) = 0.73, $p$ = 0.4978, linear mixed effects models with post-hoc pairwise comparison), in cumulative distribution **(G)** of g-ratios ($F_{interaction}$(20, 126) = 0.16, $p > 0.999$, two-way ANOVA), nor in **(H)** axon size distribution ($F_{interaction}$(24, 150) = 0.87, $p$ = 0.6479, two-way ANOVA) between genotypes.
Data are presented as mean ± SEM.

## Disconnecting Astrocytes Alters Hippocampal CA1 Neuron Excitability, Excitatory Synaptic Transmission, and Plasticity

The spatial learning deficits observed in cKO mice may result from possible alterations in hippocampal synaptic activity and plasticity. We therefore conducted electrophysiological recordings from CA1 pyramidal neurons in acute hippocampal slices from cKO mice and littermate controls (Figures 5.7 and 5.8). Mice were injected with tamoxifen at the age of 4-5 weeks and all recordings were performed between 80 and 120 dpi. First, we examined intrinsic membrane properties of CA1 pyramidal cells and found no changes in resting membrane potential or input resistance in cKO mice (Figure 5.7A, B). However, when testing excitability with current injection steps, pyramidal cells from cKO mice showed a reduced excitability evident from lower firing rates in response to depolarizing current pulses (Figure 5.7C, D). This is also reflected in an increased rheobase, the minimal current required to evoke action potentials (Figure 5.7E), but there were no changes in action potential amplitudes or threshold in cKO mice (Figure 5.7F, G).

We went on to examine miniature excitatory postsynaptic currents (mEPSCs)

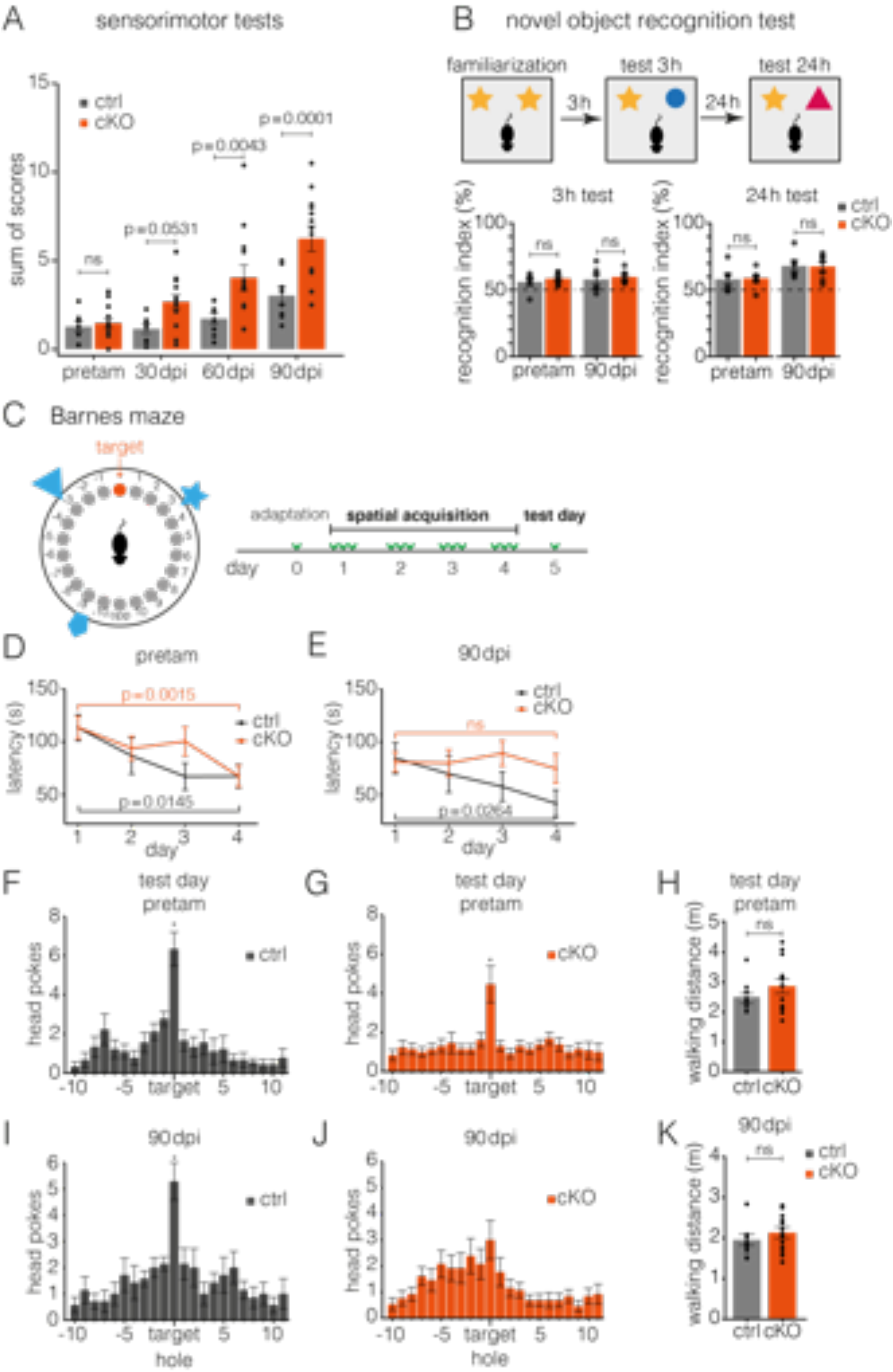
A
sensorimotor tests
sum of scores
15
10
5
0
ctrl
cKO
ns
p=0.0531
p=0.0043
p=0.0001
pretam
30dpi
60dpi
90dpi
B
novel object recognition test
familiarization
test 3h
test 24h
3h
24h
3h test
24h test
recognition index (%)
100
50
0
ns
pretam
90dpi
ctrl
cKO
C
Barnes maze
target
adaptation
spatial acquisition
test day
day
0
1
2
3
4
5
D
pretam
latency (s)
150
100
50
p=0.0015
p=0.0145
ctrl
cKO
1
2
3
4
day
E
90dpi
latency (s)
ns
p=0.0264
ctrl
cKO
day
F
test day
pretam
head pokes
ctrl
-10
-5
target
5
10
G
test day
pretam
head pokes
cKO
H
test day
pretam
walking distance (m)
ns
ctrl
cKO
I
90dpi
head pokes
ctrl
hole
J
90dpi
head pokes
cKO
hole
K
90dpi
walking distance (m)
ns
ctrl
cKO

mediated by AMPA receptors (AMPARs) recorded at -70 mV in the presence of 1 $\mu$M TTX and 25 $\mu$M bicuculline-methiodide in the bath solution to block neuronal

Figure 5.6.: **Disruption of Astrocytic Coupling Leads to Behavioral Deficits in Adult Mice**
**(A)** Assessment of sensorimotor performance in ctrl (n = 7) and cKO mice (n = 13) before treatment (pretam) and at 30, 60 and 90 dpi. Higher score values obtained from individual sensorimotor tests (gait test, ledge test, hindlimb clasping and two horizontal wire tests) indicate sensorimotor deficits. We observed higher scores in cKO mice over time compared to ctrl mice (**pretam**: $\beta$= 0.20, t(43.9) = 0.26, $p$ = 0.7970; **30 dpi**: $\beta$= 1.53, t(43.9) = 1.99, $p$ = 0.0531; **60 dpi**: $\beta$= 2.32, t(43.9) = 3.01, $p$ = 0.0043; **90 dpi**: $\beta$= 3.21, t(43.9) = 4.18, $p$ = 0.0001).
**(B)** Novel object recognition was tested at pretam and at 90 dpi. Tests were performed 3h and 24h after object familiarization (scheme, upper panel). No differences were observed in short term (3h) or long-term (24h) object recognition memory between ctrl and cKO mice (n = 6-7; **3h-pretam**: $\beta$= 2.5, t(44) = 0.58, $p$ = 0.5667 and **3h-90 dpi**: $\beta$= 1.8, t(44) = 0.41, $p$ = 0.6813; **24h-pretam**: $\beta$= 0.7, t(44) = 0.16, $p$ = 0.8735 and **24h-90 dpi**: $\beta$= 0.4, t(44) = 0.09, $p$ = 0.9268).
**(C)** Left, scheme of Barnes maze table with 22 holes, with one escape hole (target) and spatial cues (blue symbols). Right, experimental procedure to test spatial learning (4 days acquisition phase) and memory retrieval (test day 5, with target hole sealed). Arrow heads indicate sessions.
**(D, E)** Assessment of spatial learning, latency (s) to find target hole, at pretam **(D)** and at 90 dpi **(E)**. At pretam, ctrl (n = 9) and cKO mice (n = 13) learned equally well with a significant drop in latencies from day 1 to 4 (**ctrl**: $\beta$= 41.76, t(56.2) = 2.52, $p$ = 0.0145 and **cKO**: $\beta$= 45.94, t(56.2) = 3.34, $p$ = 0.0015). However, at 90dpi, only ctrl mice showed a significant learning effect by day 4 (**ctrl**: $\beta$= 42.77, t(56.2) = 2.28, $p$ = 0.0264; and **cKO**: $\beta$= 6.11, t(56.2) = 0.44, $p$ = 0.6589).
**(F, G)** At pretam, both genotypes had a similar spatial memory performance. Bar graphs represent number of head pokes into each hole during a 90 s session on test day 5. Ctrl (n = 9) and cKO mice (n = 13) clearly distinguished the target hole (**ctrl**: comparison to hole -1, $\beta$= -3.56, z = -5.60, $p$ < 0.0001; and **cKO**: comparison to hole -1, $\beta$= -3.56, z = -6.28, $p$ < 0.0001).
**(H)** No difference in walking performance on test day 5 between genotypes at pretam (n = 9-13, t(20) = -1.07, $p$ = 0.2096, unpaired *t* test).
**(I, J)** At 90 dpi, only ctrl mice **(I)** but not cKO mice **(J)** were able to distinguish the target hole on test day 5 (**ctrl**: comparison to hole -1: $\beta$= -3.29, z = -5.55, $p$ < 0.0001; and **cKO**: comparison to hole -7: $\beta$= -1.38, z = -2.51, $p$ = 0.1414,).
**(K)** No difference in walking performance on test day 5 between genotypes at 90 dpi (n = 9-13, t(20) = -0.96, $p$ = 0.3470, unpaired *t* test).
Data are presented as mean ± SEM. n = number of mice. Significance was tested with linear mixed effects models and post-hoc pairwise comparisons (in A, B, D, E) or Dunnett's post-hoc tests (in F, G, I, J).

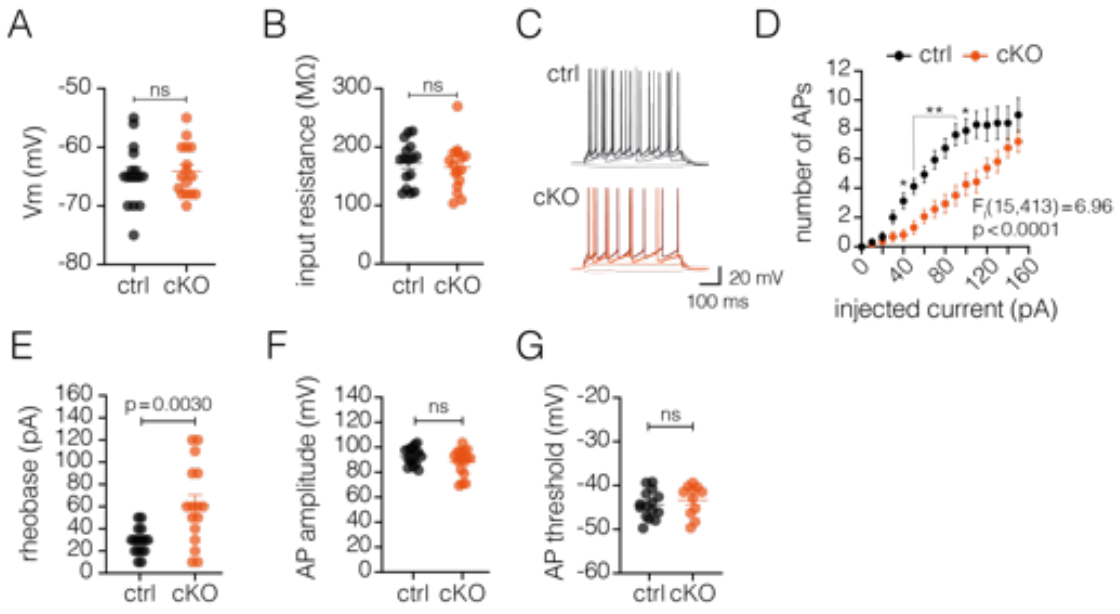

**Figure 5.7.: Reduced Excitability in CA1 Pyramidal Cells From cKO Mice**
**(A, B)** Resting membrane potential, $V_m$ **(A)** and input resistance **(B)** in CA1 pyramidal cells were similar in ctrl (n = 16 cells) and cKO mice (n = 16 cells). **(A)** Average $V_m$ of ctrl = -64.7 ± 1.3 mV and of cKO = -64.1 ± 1.1 mV (t(30) = 0.37, $p$ = 0.7127, unpaired $t$ test). **(B)** Average input resistance of ctrl = 172.4 ± 9.1 MΩ and of cKO = 165.1 ± 10.1 MΩ (t(30) = 0.54, $p$ = 0.5937, unpaired $t$ test).
**(C)** Representative traces of CA1 pyramidal cell firing action potentials (APs) from ctrl and cKO mice. Responses to -20, +30, +80 and +130 pA current injections for 500 ms are shown.
**(D)** Reduced AP firing in pyramidal cells from cKO mice (n = 16 cells) compared to ctrl (n = 16 cells, $F_{interaction}$(15, 413) = 6.96, $p < 0.0001$, mixed-effects analysis with Sidak's multiple comparisons test: $*p < 0.05$, $**p < 0.01$).
**(E)** Reduced AP firing in cKO mice resulted from a higher rheobase compared to ctrl ((t(18.3) = 3.41, $p$ = 0.003, Welch's $t$ test).
**(F, G)** AP amplitude **(F)** and AP threshold **(G)** were unchanged in pyramidal cells from cKO mice. AP thresholds were obtained from +80 pA current injections.
Data are presented as mean ± SEM.

spiking activity and inhibitory input, respectively (Figure 5.8A-C). Analysis of AMPAR mEPSCs revealed a significant increase in event frequency (Figure 5.8A) as well as amplitudes in cKO mice (Figure 5.8B, C), indicating an enhanced synaptic excitatory transmission in slices from cKO animals compared to controls. Ultrastructural analysis of excitatory synapses in CA1 stratum radiatum showed no difference in synaptic density between the genotypes (Figure 5.8D), suggesting that the increase in mEPSC frequency may result from changes in synaptic release probability. However, excitatory paired-pulse facilitation of

Schaffer collateral synapses was not altered in adult cKO mice (Figure 5.8E), indicating that presynaptic glutamate release is not affected. To determine whether postsynaptic alterations may be involved in shaping the increased synaptic excitatory transmission in cKO mice, we compared the AMPAR and NMDA receptor (NMDAR) components of evoked EPSCs and found that the AMPA/NMDA ratio was increased by 70 ± 26% ($p = 0.0162$) in cKO mice (Figure 5.8F). Given that AMPAR mEPSC frequency and amplitudes were increased without any overt changes in presynaptic glutamate release, the increase in the AMPA/NMDA ratio likely indicates a higher postsynaptic AMPAR density in cKO mice. Indeed, increased postsynaptic AMPAR density in CA1 pyramidal neurons and a higher AMPA/NMDA ratio were reported in *Cx30*$^{-/-}$*:Cx43*$^{fl/fl}$*:hGFAP-Cre* mice (Pannasch et al., 2011). Moreover, developmental knockout mice were shown to have a decreased astroglial glutamate clearance, which impacts NMDAR current kinetics (Pannasch et al., 2011). To determine whether adult cKO mice may also show impaired glutamate clearance, we investigated the decay kinetics of evoked NMDAR EPSCs at different stimulation frequencies. At single pulse, 50 Hz or 100 Hz stimulations, we observed no difference in the decay kinetics of NMDAR currents in cKO mice compared to controls (Figure 5.8G), suggesting that glutamate uptake is not altered in adult cKO mice. As expected, increasing synaptic stimulation frequencies to 50 Hz prolonged NMDAR EPSCs (Figure 5.8G), which is likely due to slower glutamate uptake by astrocytes during high frequency synaptic activity (Romanos et al., 2019). Of interest to note is that NMDAR current decay kinetics were significantly faster at 100 Hz compared to 50 Hz ($p = 0.046$ in controls and $p = 0.012$ cKO mice, paired $t$ test), similar to that which has been described for pyramidal neurons in the anterior cingulate cortex (Romanos et al., 2019). This suggests that the high frequency-induced increase in glutamate uptake capacity also occurs at CA1 synapses and is unchanged in cKO mice (Figure 5.8G).

The changes in neuronal excitability and AMPAR-mediated synaptic transmission observed in cKO mice may also alter synaptic plasticity. To investigate this, we examined long-term potentiation (LTP) in cKO mice and littermate controls, by recording field potentials induced by theta-burst stimulation (three 2-s trains of 100 Hz, 20 s apart) of Schaffer collaterals. We saw that induction of LTP was significantly decreased in cKO mice compared to controls (Figure 5.8H), a finding that may contribute to observed deficits in hippocampus-dependent spatial learning in cKO mice (Figure 5.6E, J).

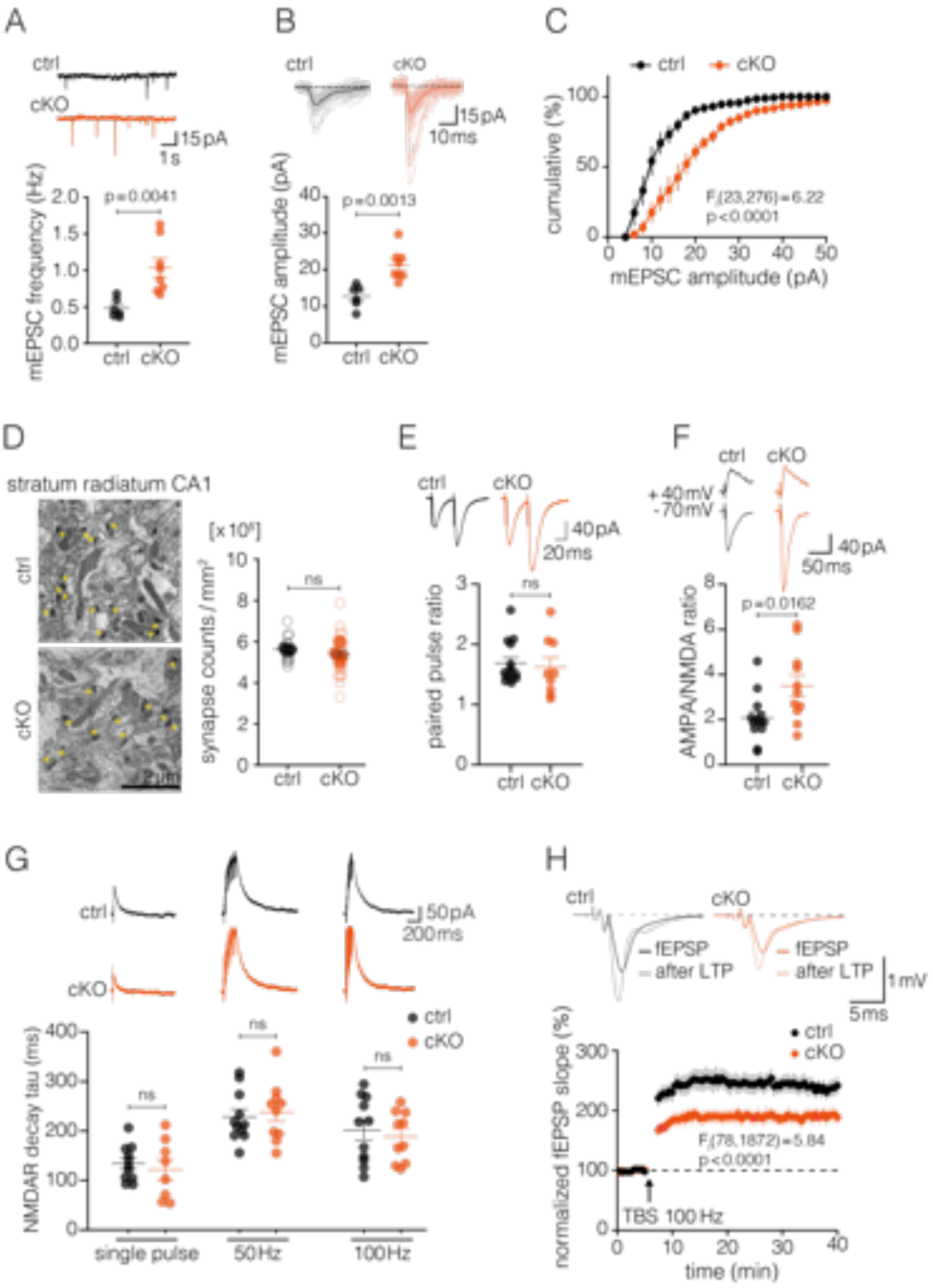

# Discussion

Astrocytes are involved in a wide range of brain functions across many brain regions (Adamsky et al., 2018; Clasadonte et al., 2017; Nagai et al., 2019; Saab

**Figure 5.8.: Excitatory Synaptic Transmission of Hippocampal CA1 Pyramidal Cells and Long-Term Potentiation Are Altered in cKO Mice**

**(A-C)** AMPAR-mediated mEPSC (recorded at -70 mV in the presence of 1 $\mu$M TTX and 25 $\mu$M bicuculline-methiodide) frequency **(A)** and amplitudes **(B, C)** are increased in cKO mice. Upper panel in **(A)** shows sample mEPSC traces from ctrl (n = 6 cells) and cKO (n = 8 cells) recordings. mEPSC frequency in cKO mice was increased by 0.56 ± 0.16 Hz compared to ctrl (t(12) = 3.54, $p = 0.0041$, unpaired *t* test). **(B)** mEPCS amplitudes were increased by 8.5 ± 2.0 pA in cKO mice compared to ctrl (t(12) = 4.16, $p = 0.0013$, unpaired *t* test). **(C)** Cumulative distribution of mEPSC amplitudes differed between ctrl and cKO mice ($F_{interaction}(23,276) = 6.215$, $p < 0.0001$), two-way ANOVA).

**(D)** No difference in synaptic density in CA1 stratum radiatum between ctrl and cKO mice (n = 3-5 mice (solid circles), N = 15-25 images (open circles), $\beta$= 22358, t(6.65) = 0.79, $p = 0.4557$, linear mixed effects models with post-hoc pairwise comparison). Synapses are indicated by yellow arrows in representative electron microscopy images (left).

**(E)** Paired pulse ratio was not altered in cKO mice (n = 9 cells) compared to ctrl (n = 14 cells, U = 50.50, $p = 0.4479$, Mann Whitney). Sample EPSC traces (50 ms interstimulus interval) are shown above the graph.

**(F)** AMPA/NMDA EPSC ratio was increased in cKO mice (n = 11 cells) compared to ctrl (n = 13 cells, t(22) = 2.61, $p = 0.0162$, unpaired *t* test), likely due to increased AMPAR activity in cKO mice. Representative NMDAR and AMPAR EPSC traces are shown above the graph.

**(G)** Decay kinetics of NMDAR EPSCs evoked with a single pulse stimulation or with 10 pulses at 50 Hz and 100 Hz were similar in ctrl (n = 8-10 cells) and cKO mice (n = 11 cells; **single pulse**: t(17) = 0.55, $p = 0.5868$; **50 Hz**: t(19) = 0.43, $p = 0.6753$; and **100 Hz**: t(19) = 0.49, $p = 0.6271$, unpaired *t* tests). In both genotypes, decay kinetics increased from single pulse to 50 Hz stimulations (**ctrl:** t(10) = 5.80, $p = 0.0002$; and **cKO:** t(7) = 3.70, $p = 0.0081$, paired *t* test) and decreased from 50 Hz to 100 Hz stimulation (**ctrl:** t(10) = 2.27, $p = 0.0463$; and **cKO:** t(9) = 3.20, $p = 0.0117$, paired *t* test).

**(H)** Theta-burst stimulation (TBS)-induced LTP (arrow, three 2-s trains of 100 Hz, 20 s apart) was reduced in cKO mice (n = 14 slices) compared to ctrl (n = 12 slices; $F_{interaction}(78, 1872) = 5.84$, $p < 0.0001$, two-way ANOVA; and comparison 32-42 min after TBS: t(24) = 2.7, $p = 0.0125$, unpaired *t* test). Sample traces (top) represent averaged field excitatory postsynaptic potentials (fEPSPs) before and 40 min after TBS.

Data are presented as mean ± SEM.

et al., 2012; Suzuki et al., 2011; Yu et al., 2018). They form large intercellular networks as they are coupled by gap junction channels, mainly comprising Cx30 and Cx43 connexin proteins (Giaume et al., 2010; Griemsmann et al., 2015). However, in the adult brain, the functional relevance of the astroglial network *in vivo* , for both behavior and cellular integrity, remains poorly understood. This is because most of our current understanding is obtained from studies in the developmental brain of mice lacking Cx30 and Cx43 (Chever et al., 2016, 2014; Lutz et al., 2009; Pannasch et al., 2012; Rouach et al., 2008; Wallraff et al., 2006). It therefore remained challenging to properly discriminate the various, developmental contributions of Cx30 and Cx43 (Cina et al., 2009; Cohen-Salmon et al., 2007; Elias et al., 2007; Ghézali et al., 2018; Teubner et al., 2003) from the functional role of the astroglial gap junction network in adult mice. To study astrocyte coupling, and to avoid possible developmental adaptations, we selectively deleted Cx30 and Cx43 from astrocytes in a tamoxifen-inducible manner in adult mice. Disruption of astrocyte coupling caused activation of astrocytes and microglia in gray and white matter brain regions. This was accompanied by impairments in sensorimotor performance and hippocampus-dependent spatial learning. Recordings from hippocampal CA1 neurons revealed a decreased neuronal excitability, while excitatory synaptic transmission was increased. Also, long-term synaptic plasticity was affected, determined by a compromised LTP induction in CA1. Our findings are the first demonstration that an intact astroglial network is required for cognitive abilities in the adult brain.

Following induction of gene recombination in adult animals, astroglial network coupling was reduced on average by around 75%, when assessed in the hippocampus of cKO mice around 90 days after tamoxifen treatment (dpi; Figure 5.2). Since astrocytic coupling is completely lost in mice with a total deletion of Cx30 and Cx43 (Pannasch et al., 2011; Wallraff et al., 2006), the residual coupling observed in cKO mice likely reflects an incomplete Cre recombination mediated by the GLAST-CreERT2 driver line (Jahn et al., 2018; Mori et al., 2006). Indeed, immunohistochemistry revealed sparsely labeled cells still expressing Cx30 and Cx43 in cKO brain sections at 90 dpi. And we confirmed that not all cortical astrocytes were targeted for recombination by Cre reporter analysis. Nevertheless, a 90% and 60% reduction in Cx30 and Cx43 expression, respectively, was achieved in both cortex and hippocampus (Figure 5.1). The different extent of Cx30 and Cx43 protein depletion could be explained by potential differences in recombination efficiency between the two floxed alleles. Another possibility is that Cx43, unlike Cx30, may not be exclusively expressed by astrocytes (Reichenbach et al., 2019; Rouach et al., 2002), which could lead to an underestimation of astrocytic Cx43 depletion.

In this study, we primarily explored the consequences of disconnecting the astroglial network on tissue integrity, cellular functions, hippocampal neurotransmission, and behavior. Adult cKO mice developed a prominent activation of astrocytes and microglia reminiscent of a reactive gliosis (Figure 5.3). The hypertrophy of astrocytes and microglia was already detected around 30 dpi and became more pronounced and widespread at 90 dpi in gray and white matter. However, we did not observe any visible signs of tissue damage or neuronal loss (Figure 5.4), suggesting the gliosis in cKO mice is unlikely to be neurotoxic, at least not within the initial 3-5 months after the induction of Cx30 and Cx43 deletion. On the contrary, mice with developmental ablation of Cx30 and Cx43 (Lutz et al., 2009) display an early onset white matter pathology that comprises dysmyelination, myelin vacuolation and axonal degeneration. Vacuole formations were also observed in the CA1 region of the hippocampus (Lutz et al., 2009). In these mice, tissue damage was associated with astrogliosis, but microglial activation was not observed (Lutz et al., 2009). Surprisingly, in adult cKO mice microglia were clearly activated in the absence of pathology, likely suggesting that microglia react to alterations in astrocytic homeostasis. Indeed, a complex dialogue between microglia and astrocytes is known to shape tissue homeostasis and cellular functions in central nervous system (CNS) health and disease (Vainchtein and Molofsky, 2020) and their cross talk can engender both beneficial or detrimental effects (Aguzzi et al., 2013; Liddelow et al., 2017; Rothhammer et al., 2018). Hence, further studies on microglial activation upon inducibly decoupling astrocytes could provide novel insights into the intercellular dynamics of microglia and astrocytes.

Since overall brain myelination and myelin integrity was preserved in adult cKO mice (Figure 5.5), we can safely conclude that the previously reported deficits are primarily caused by a developmental disruption of the glial network, before and during the peak phase of CNS myelination (Lutz et al., 2009). Similarly, early onset white matter pathology with severe dysmyelination, vacuolation, loss of oligodendrocytes and axons, was reported in mice lacking oligodendroglial connexins Cx32 and Cx47 (Menichella et al., 2006, 2003). Importantly, oligodendrocytes are coupled to astrocytes by gap junction channels, forming a panglial syncytium that is suggested to maintain potassium siphoning (Menichella et al., 2006; Orthmann-Murphy et al., 2007; Rash, 2010) as well as the supply of metabolites between capillaries and axonal compartments (Meyer et al., 2018; Morrison et al., 2013; Saab et al., 2013). This astrocyte-oligodendrocyte network is primarily mediated by heterotypic Cx30-Cx32 and Cx43-Cx47 gap junction coupling. In Cx30/Cx43 double-deficient mice, coupling between astrocytes and oligodendrocytes was diminished (Maglione et al., 2010). A complete loss of panglial coupling was also reported in mice lacking astrocytic Cx30 and oligodendroglial Cx47 (Griemsmann et al., 2015), further substantiating heterotypic coupling between astrocytes and oligodendrocytes. Hence, the early onset dysmyelination and myelin vacuole formations reported in either mice double-deficient in Cx30/Cx43 (Lutz et al., 2009), Cx32/Cx47 (Menichella et al., 2006), or Cx30/Cx47 (Tress et al., 2012) strongly underscores the importance of astrocyte-oligodendrocyte coupling for myelin formation during brain development. However, it is still unclear whether panglial coupling is also required for adult myelin maintenance and axonal integrity. In our adult cKO mice, coupling between astrocytes and oligodendrocytes should also be compromised, including in white matter, given that mRNA levels of Cx30 and Cx43 were reduced and gliosis was apparent in white matter tracts. However, brain myelination as well as myelin sheath thickness and axonal integrity in optic nerves appeared unperturbed in cKO mice. This suggests that panglial coupling is not critical for adult myelin maintenance and axonal health, at least in the absence of specific challenges. Alternatively, the residual panglial syncytium in cKO mice might be sufficient to maintain myelin and axonal integrity. The extent to which intercellular coupling is reduced in white matter tracts of cKO animals remains to be determined and follow-up studies could further address whether alterations in panglial coupling impact axonal conduction properties and energy homeostasis (Looser et al., 2018; Saab et al., 2016).

Developmental deletion of Cx30 and Cx43 was reported to cause motor deficits and impairments in the object relocation test. However, these $Cx30^{-/-}$:$Cx43^{fl/fl}$: *mGFAP-Cre* mice also developed gray and white matter pathologies that could have substantially contributed to behavioral impairments (Lutz et al., 2009). Moreover, $Cx30^{-/-}$ mice have a severe hearing impairment (Teubner et al., 2003), which could independently influence exploratory behavior (Dere et al., 2003). Since our adult cKO mice showed no visible tissue damage and are devoid of unspecific developmental complications, behavioral alterations should primarily mirror the contributions of the glial-coupled network. Adult cKO mice did not develop a severe motor phenotype, as general cage behavior, locomotion, and running on an accelerating rotarod (not shown) was indistinguishable from

littermate controls. However, closer inspection revealed a subtle increase in sensorimotor deficits between 1 and 3 months after tamoxifen treatment (Figure 5.6). The gradual appearance of sensorimotor deficits might reflect a slow increase in glial decoupling over time, following induction of Cx30 and Cx43 deletions. Yet, it also correlates with the progressive increase in gliosis in cKO mice (Figure 5.3), which may additionally contribute to behavioral changes.
We also tested cognitive abilities related to learning and memory in cKO animals before and around 3 months after tamoxifen treatment (Figure 5.6) and observed no deficits in object recognition memory. However, hippocampus-dependent spatial learning was completely abolished following astrocyte decoupling. Interestingly, astrocyte functions are known to contribute to spatial and contextual memory formation (Adamsky et al., 2018; Suzuki et al., 2011), which also involves lactate mobilization from glycogen stores and lactate release from astrocytes (Alberini et al., 2018; Duran et al., 2013; Zuend et al., 2020). We demonstrate here that spatial memory formation requires an intact astrocytic network, which has been shown to facilitate lactate supply to neurons (Clasadonte et al., 2017; Rouach et al., 2008). However, we cannot rule out the contribution of a Cx43 hemichannel function, which has been suggested to play a role in fear memory consolidation (Stehberg et al., 2012). Moreover, astrocytic coupling in the lateral hypothalamus has recently been shown to influence the sleep-wake cycle (Clasadonte et al., 2017) and an increased sleepiness may impact memory consolidation (Brown et al., 2012). Whether cKO mice have an altered sleep-wake cycle that contributes to spatial memory deficits remains to be demonstrated.

The spatial learning deficits in adult cKO mice likely indicate alterations in hippocampal circuits. The involvement of astrocytic connexins and gap junction coupling in regulating hippocampal neuron excitability, synaptic transmission, plasticity and network coordination has been well-studied in Cx30- and Cx43-deficient mice during postnatal development (Chever et al., 2016, 2014; Pannasch et al., 2014, 2012, 2011; Wallraff et al., 2006). In the adult brain however, it is not clear how hippocampal neuronal activity and neurotransmission are affected upon decoupling of the astroglial network. We found that hippocampal CA1 neuronal excitability was reduced in cKO mice (Figure 5.7). Additionally, excitatory AMPAR-mediated synaptic transmission was increased, most likely due to postsynaptic changes and not due to alterations in presynaptic release properties or a reduction in glutamate clearance at CA1 synapses (Figure 5.8). Furthermore, we also recorded stimulus-evoked fEPSPs and found that LTP induction was reduced by about 50% in cKO mice, confirming that an intact astroglial network is critical for synaptic plasticity (Pannasch et al., 2011). Our results are partially in line with previous findings in postnatal recordings from *Cx30*$^{-/-}$*:Cx43*$^{fl/fl}$*:hGFAP-Cre* mice, which have reported increased excitatory synaptic transmission and changes in postsynaptic properties at CA1 synapses (Pannasch et al., 2011). In contrast, excitability in CA1 pyramidal cells was enhanced (Pannasch et al., 2011), whereas we found a strongly reduced neuronal excitability upon injections of depolarizing currents. This discrepancy is best explained by technical differences in the recordings. Pannasch et al. performed their measurements in the presence of picrotoxin to block inhibitory input, while we evaluated cellular excitability in the absence of synaptic blockers. Hence, it may well be that inhibitory transmission is also increased in CA1 pyramidal cells of cKO mice, similar to that previously reported (Pannasch et al., 2011). Such an increase in inhibitory transmission could shift the stimulus intensity required to generate action potentials in CA1 pyramidal neurons (Pavlov et al., 2009). Astrocytes are known to regulate extracellular $\gamma$-aminobutyric acid (GABA) homeostasis and tonic inhibition of neurons (Mederos and Perea, 2019; Yu et al., 2018), which could also impact hippocampal long-term synaptic plasticity (Wu et al., 2014). However, further investigation is needed to show how the inhibition-excitation balance may be altered following astrocyte decoupling in adult mice. Nonetheless, the reduced excitability of CA1 pyramidal cells strongly indicates that hippocampal neuronal computation is perturbed in cKO mice.

Furthermore, the astroglial network was reported to contribute to glutamate clearance during postnatal development (Pannasch et al., 2011). And NMDAR currents are sensitive to extracellular glutamate elevations and inadequate glutamate uptake (Asztely et al., 1997; Pannasch et al., 2011; Romanos et al., 2019). Surprisingly, the kinetics of evoked NMDAR currents were not altered in cKO mice, even at high stimulation frequencies, suggesting that the activity-induced glutamate uptake capacity is not affected when astroglial connectivity is reduced in adulthood. Hence, the elevated excitatory synaptic transmission in cKO mice is unlikely to be related to insufficient glutamate uptake. The astrocytic network has also been described to play an important role in buffering extracellular potassium released during synaptic activity (Pannasch et al., 2011; Wallraff et al., 2006). Since resting membrane potentials of CA1 pyramidal neurons and astrocytes were unchanged in cKO mice, basal extracellular potassium levels should be normal as reported earlier (Pannasch et al., 2011). However, we cannot exclude possible deficits in spatial buffering of potassium during elevated neuronal activity in cKO mice. This could be addressed in future studies. Yet, it was recently demonstrated that astrocytic gap junction coupling is not required for buffering potassium transients evoked by synaptic activity in CA1 stratum radiatum (Breithausen et al., 2020). Moreover, in line with previous EEG recordings in *Cx30*$^{-/-}$*:Cx43*$^{fl/fl}$*:hGFAP-Cre* mice (Chever et al., 2016), throughout all our behavioral tests in cKO mice, we never noticed any spontaneous seizures, which might be expected if potassium clearance was severely perturbed (Du et al., 2018; Larson et al., 2018).

Finally, astrocyte networks serve metabolic coupling between neurons and astrocytes (Clasadonte et al., 2017; Murphy-Royal et al., 2020; Rouach et al., 2008). Hippocampal LTP and memory consolidation requires a lactate supply from astrocytes to neurons (Alberini et al., 2018; Suzuki et al., 2011). Lactate release from cortical astrocytes has been recently demonstrated upon arousal (Zuend et al., 2020). And lactate delivery to neurons through the astrocytic network has been shown to regulate excitability and basal firing activity of hypothalamic orexin neurons (Clasadonte et al., 2017). Lactate metabolism is also involved in spatial memory acquisition (El Hayek et al., 2019; Harris et al., 2019). Hence, the deficits in cKO mice related to spatial learning, hippocampal CA1 neuronal excitability and synaptic plasticity may also partly derive from alterations in neuron-glia metabolic coupling that require an intact astroglial network. Future studies using genetically encoded metabolite sensors *in vivo* (Diaz-Garcia et al., 2017; Mächler et al., 2016; Zuend et al., 2020) could determine the dynamics of metabolite distribution across the glial network to sites of neuronal activity and high energy demand. Taken together, our study introduces a novel mouse model that allows us to dissect the functional impact of the glial network in the adult mouse brain and demonstrate that an intact glial syncytium is critical for neuronal information processing and brain function.

# Materials and Methods

## Key Resources Table

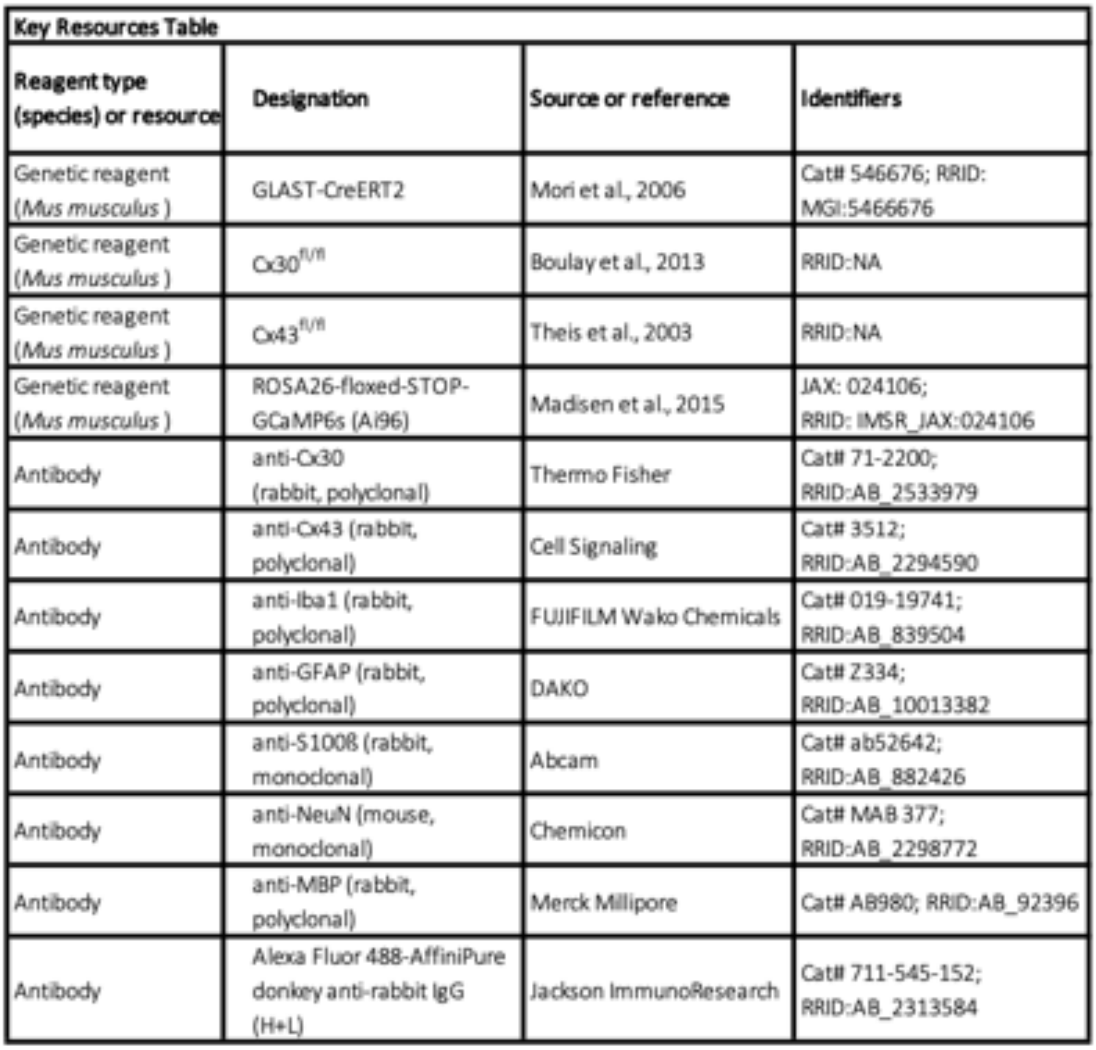

**Key Resources Table**

| **Reagent type (species) or resource** | **Designation** | **Source or reference** | **Identifiers** |
|---|---|---|---|
| Genetic reagent (*Mus musculus* ) | GLAST-CreERT2 | Mori et al., 2006 | Cat# 546676; RRID: MGI:5466676 |
| Genetic reagent (*Mus musculus* ) | $Cx30^{fl/fl}$ | Boulay et al., 2013 | RRID:NA |
| Genetic reagent (*Mus musculus* ) | $Cx43^{fl/fl}$ | Theis et al., 2003 | RRID:NA |
| Genetic reagent (*Mus musculus* ) | ROSA26-floxed-STOP-GCaMP6s (Ai96) | Madisen et al., 2015 | JAX: 024106;<br>RRID: IMSR_JAX:024106 |
| Antibody | anti-Cx30 (rabbit, polyclonal) | Thermo Fisher | Cat# 71-2200;<br>RRID:AB_2533979 |
| Antibody | anti-Cx43 (rabbit, polyclonal) | Cell Signaling | Cat# 3512;<br>RRID:AB_2294590 |
| Antibody | anti-Iba1 (rabbit, polyclonal) | FUJIFILM Wako Chemicals | Cat# 019-19741;<br>RRID:AB_839504 |
| Antibody | anti-GFAP (rabbit, polyclonal) | DAKO | Cat# Z334;<br>RRID:AB_10013382 |
| Antibody | anti-S100B (rabbit, monoclonal) | Abcam | Cat# ab52642;<br>RRID:AB_882426 |
| Antibody | anti-NeuN (mouse, monoclonal) | Chemicon | Cat# MAB 377;<br>RRID:AB_2298772 |
| Antibody | anti-MBP (rabbit, polyclonal) | Merck Millipore | Cat# AB980; RRID:AB_92396 |
| Antibody | Alexa Fluor 488-AffiniPure donkey anti-rabbit IgG (H+L) | Jackson ImmunoResearch | Cat# 711-545-152;<br>RRID:AB_2313584 |

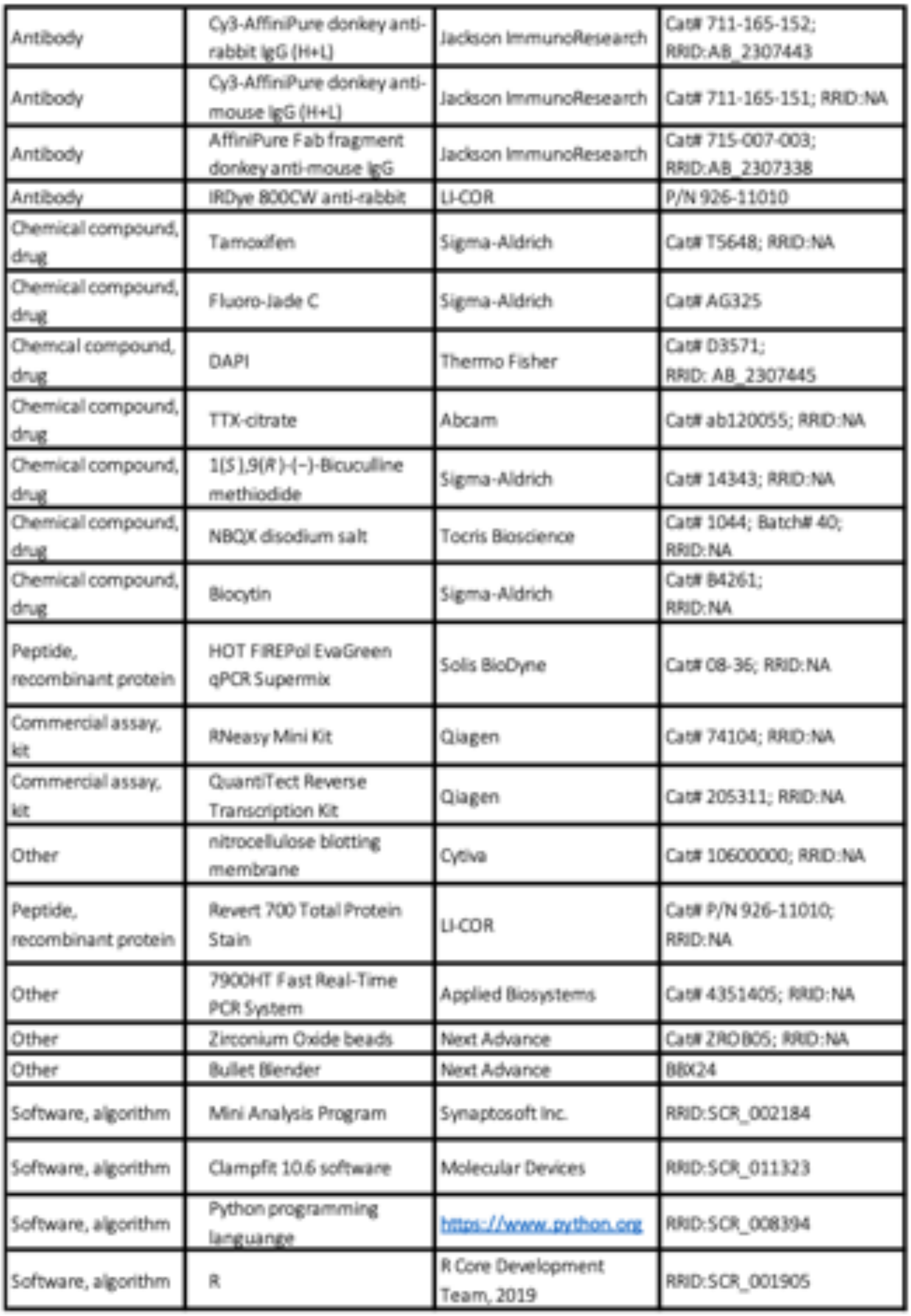

| | | | |
|---|---|---|---|
| Antibody | Cy3-AffiniPure donkey anti-rabbit IgG (H+L) | Jackson ImmunoResearch | Cat# 711-165-152;<br>RRID:AB_2307443 |
| Antibody | Cy3-AffiniPure donkey anti-mouse IgG (H+L) | Jackson ImmunoResearch | Cat# 711-165-151; RRID:NA |
| Antibody | AffiniPure Fab fragment donkey anti-mouse IgG | Jackson ImmunoResearch | Cat# 715-007-003;<br>RRID:AB_2307338 |
| Antibody | IRDye 800CW anti-rabbit | LI-COR | P/N 926-11010 |
| Chemical compound, drug | Tamoxifen | Sigma-Aldrich | Cat# T5648; RRID:NA |
| Chemical compound, drug | Fluoro-Jade C | Sigma-Aldrich | Cat# AG325 |
| Chemcal compound, drug | DAPI | Thermo Fisher | Cat# D3571;<br>RRID: AB_2307445 |
| Chemical compound, drug | TTX-citrate | Abcam | Cat# ab120055; RRID:NA |
| Chemical compound, drug | 1(*S*),9(*R*)-(−)-Bicuculline methiodide | Sigma-Aldrich | Cat# 14343; RRID:NA |
| Chemical compound, drug | NBQX disodium salt | Tocris Bioscience | Cat# 1044; Batch# 40;<br>RRID:NA |
| Chemical compound, drug | Biocytin | Sigma-Aldrich | Cat# B4261;<br>RRID:NA |
| Peptide, recombinant protein | HOT FIREPol EvaGreen qPCR Supermix | Solis BioDyne | Cat# 08-36; RRID:NA |
| Commercial assay, kit | RNeasy Mini Kit | Qiagen | Cat# 74104; RRID:NA |
| Commercial assay, kit | QuantiTect Reverse Transcription Kit | Qiagen | Cat# 205311; RRID:NA |
| Other | nitrocellulose blotting membrane | Cytiva | Cat# 10600000; RRID:NA |
| Peptide, recombinant protein | Revert 700 Total Protein Stain | LI-COR | Cat# P/N 926-11010;<br>RRID:NA |
| Other | 7900HT Fast Real-Time PCR System | Applied Biosystems | Cat# 4351405; RRID:NA |
| Other | Zirconium Oxide beads | Next Advance | Cat# ZROB05; RRID:NA |
| Other | Bullet Blender | Next Advance | BBX24 |
| Software, algorithm | Mini Analysis Program | Synaptosoft Inc. | RRID:SCR_002184 |
| Software, algorithm | Clampfit 10.6 software | Molecular Devices | RRID:SCR_011323 |
| Software, algorithm | Python programming languange | https://www.python.org | RRID:SCR_008394 |
| Software, algorithm | R | R Core Development Team, 2019 | RRID:SCR_001905 |

## Animals and Genotyping

$Cx30^{fl/fl}$:$Cx43^{fl/fl}$:$GLASTCre^{ERT2/+}$ mice were generated by crossbreeding mice expressing the tamoxifen-sensitive Cre recombinase CreERT2 under the control of the murine *Slc1a3* (GLAST) promoter (Mori et al., 2006) with mice carrying floxed *Gjb6* ($Cx30^{fl/fl}$; Boulay et al., 2013) and floxed *Gja1* ($Cx43^{fl/fl}$; Theis et al., 2003) alleles. As controls, $Cx30^{fl/fl}$:$Cx43^{fl/fl}$:$GLAST^{+/+}$ littermates were used. Mice of either sex were used for experiments. The primer sequences used for genotyping were: for Cx30 flox; 5'-TTCCCTATGCTGGTAGAGTGCTTGT-3' and 5'-GCAGTAACTTATT GAAACCCTTCACCT-3'; for Cx43 flox: 5'-GGGATACAGACCCTTGGACTCC-3' and 5'-TCACCCCAAG CTGACTCAACCG-3'; and for GLAST-CreERT2, 5'-GAGGCACTTGGCTAGGCTCTGAGGA-3' and 5'-GAGGAGATCCTGACCGATCAGTTGG-3' and 5'-GGTGTACGGTCAGTAAATTGGACAT-3'. For Cre reporter analysis, GLAST-CreERT2 mice were crossed with ROSA26-floxed-STOP-GCaMP6s (Ai96) reporter mice (Madisen et al., 2015; JAX: 024106). Mice were kept on an inverted 12/12 hr light/dark cycle in standardized cages with food and water *ad libitum*. All experimental procedures were approved by the local veterinary authorities according to the guidelines of the Swiss Animal Protection Law, Veterinary Office, Canton Zurich (Animal Welfare Act, 16 December 2005 and Animal Welfare Ordinance , 23 April 2008).

## Tamoxifen Treatment

Tamoxifen treatment was performed as previously reported (Saab et al., 2012). Briefly, mice received daily intraperitoneal (i.p.) injections of tamoxifen at a dose of 100 mg/kg body weight for 5 consecutive days. Tamoxifen solution (10 mg/ml dissolved in corn oil) was always freshly prepared for each experimental cohort injected at the same time. Injections were performed in mice at the ages of 4-5 weeks (for acute slice experiments) or 8-12 weeks. Experiments were executed around 30 to 180 days post tamoxifen treatment, as specified in the text.

## Immunohistochemistry and Histology

Mice were anesthetized with pentobarbital and transcardially perfused with ice-cold 4% paraformaldehyde (PFA, Paraformaldehyde Granular, Electron Microscopy Sciences, Hatfield, PA) in phosphate-buffered saline (PBS, pH 7.4, (10X Dulbecco's)-Powder, Axon Lab AG, Baden-Dättwil, Switzerland) with a flow of 20 ml/min. Brains were dissected, halved coronally and post-fixed in 4% PFA for 3 hr at 4 °C. Tissue was cryoprotected in 30% sucrose in PBS for ca. 2 days at 4 °C, and then stored at -80 °C until needed for cutting. Coronal sections (40 $\mu$m) were cut using a microtome (Hyrax KS 34) and then stored in antifreeze solution (50 mM sodium phosphate buffer pH 7.4, 1 M glucose, 35% ethylene glycol and 3.5 mM sodium azide) at -20 °C until further processing. Free floating sections were washed with 0.05% Triton X-100 (Sigma-Aldrich, Buchs, Switzerland) in Tris buffer (50 mM, pH 7.4) and then transferred to 0.3% Triton X-100 and 5% donkey serum in Tris buffer (blocking solution) for 1 hr at room temperature (RT). Sections were then incubated with primary antibodies diluted in blocking solution overnight at 4 °C. See Key Resources Table for a full list of antibodies used. For Cx30 labeling, before incubation in blocking solution, antigen retrieval was required and sections were heated (2x 7 min) in sodium citrate buffer (10 mM, 0.05% Tween 20, pH 6) using a commercially available microwave (at 40% of full microwave power). For immunostainings involving primary antibodies raised in mouse, a pretreatment with anti-mouse IgG Fab fragments was performed. Fab fragments were added to the blocking solution and sections were preincubated overnight at 4 °C. Following primary antibody incubation, sections were washed in Tris buffer and then incubated in Alexa Fluor 488- and Cy3-conjugated secondary antibodies for 45 min at RT. For nuclei labeling, DAPI (1:10000) was added to the secondary antibody solution. To evaluate gap junctional coupling in slices that were 4%-PFA fixed immediately after dye diffusion experiments, biocytin (Sigma-Aldrich) was visualized using Alexa Fluor 555-conjugated streptavidin (Thermo Fisher Scientific, Waltham, MA). Sections were mounted on SuperFrost Plus slides (Thermo Scientific) in Dako Fluorescence Mounting Medium (Dako, Jena, Germany).

For Fluoro-Jade C stainings, coronal brain slices (40 $\mu$m) were mounted on SuperFrost Plus slides, air-dried and then immersed in a solution containing 1% NaOH in 80% ethanol for 5min. Slides were then rinsed with 70% ethanol (2 min) and in distilled water (2 min) before incubation in a 0.06% potassium permanganate (Sigma-Aldrich) solution for 10 min. Slides were then rinsed in distilled water before incubation in Fluoro-Jade C staining solution (0.0001% Fluoro-Jade C dye (Sigma-Aldrich) in 0.1% acetic acid solution) for 10 min. After washing in distilled water (3x 1 min), slides were air-dried, cleared with xylene and coverslipped with Eukitt (Merck Millipore, Burlington, MA). Mice subjected to cortical microinfarcts caused by occlusion of penetrating arterioles (Shih et al., 2013) were used as positive controls to detect degenerating neurons.

For hematoxylin and eosin (H&E) stainings, post-fixed brains were embedded in paraffin and sagittal (2 $\mu$m) sections cut using a microtome. Sections were then deparaffinized, then rehydrated and successively incubated for 3-5 min in 0.1% hematoxylin (color blue; basic tissue compartments) and 0.1% eosin (color red, acidic tissue compartments).

## Image Acquisition and Analysis

Confocal images were acquired using a Zeiss LSM 700 or Zeiss LSM 800 confocal laser scanning microscope equipped with a 10x (Plan-Apochromat, NA 0.45), a 25x (LCI Plan-Neofluar, NA 0.8) or a 40x objective (Plan-Apochromat, NA 1.4, Oil DIC (UV) VIS-IR). Whole brain section pictures of H&E-stained sections were taken with a Zeiss Axio Scan.Z1 slide scanner with a Plan-Apochromat 10x (NA 0.45) air objective and tiled images were automatically aligned with the built-in microscope software (ZEN software, Zeiss). Image analysis was performed with ImageJ (Fiji, Version 2.0.0-rc-69/1.52) or Ilastik (Version 1.3.0). Confocal images present single plane and maximum intensity projections of z-stacks. For Cx30 and Cx43 expression analysis, fluorescent particles were counted. For GFAP and Iba1 analysis, the fluorescent particle area was determined using ImageJ. At least 3 images (per brain region) from each 3-4 brain sections per animal were analyzed. Pictures were taken in defined, comparable brain areas for all mice (using DAPI channel for selection), and the experimenter was blinded to the genotypes.

## Real Time Quantitative PCR

Mice were deeply anesthetized with isoflurane, decapitated and brains quickly dissected on ice. Tissue was homogenized in RNeasy Lysis Buffer (RLT, Qiagen, Hilden, Germany) using 0.5 mm Zirconium Oxide beads (ZROB05, Next Advance, Troy, NY) and the tissue homogenizer Bullet Blender (BBX24, Next Advance; 2x 15 s cycles on setting 4). RNeasy Mini Kit (Qiagen) and QuantiTect Reverse Transcription Kit (Qiagen) were used for RNA isolation and cDNA synthesis, respectively, according to the manufacturer's instructions, including a genomic DNA removal step. Using EvaGreen (HOT FIREPol, Solis BioDyne, Tartu, Estonia) and an ABI 7900HT Fast Real-Time PCR System (Applied Biosystems, Foster City, CA), we performed real-time qPCR to quantify the relative loss of *Gjb6* and *Gja1* mRNA following gene recombination. The following primers were used for mRNA expression analysis: for *Gjb6* (5'-GGCCGAGTTGTGTTACCTGCT-3', 5'-TCTCTTTCAGGGCATGGTTGG-3'); for *Gja1* (5'-GGTGGACTGCTTCCTCTCAC-3', 5'-GAGCGAGAGACACCAAGGAC-3'). As endogenous gene controls Actb, hprt and tbp were used: for Actb (5'-CTTCCTCCCTGGAGAAGAGC-3', 5'-ATGCCACAGGA TTCCATACC-3'), for hprt (5'-ACAGGCCAGACTTTGTTGGA-3', 5'-CACAAACGTGATTCAAATCCCTGA-3') and for tbp (5'-CACAGGAGCCAAGAGTGAAGAA-3', 5'-GCTGGGAAGCCCAACTTCTG-3'). For each reaction three technical replicates were averaged per animal.

## Western Blotting

Tissue lysis was performed in RIPA buffer (150 mM NaCl, 0.1% Triton X-100, 0.5% sodium deoxycholate, 0.1% SDS, 50 mM Tris HCl, pH 8.0, and protease inhibitors (Roche, Basel, Switzerland)) using 0.5 mm Zirconium Oxide beads and the Bullet Blender tissue homogenizer. Protein concentration was determined by bicinchoninic acid analysis (BCA Protein Assay, Merck Millipore, Burlington, MA). Protein lysate (40 $\mu$g) was size-separated by SDS-PAGE on 12% (w/v) polyacrylamide gels and then transferred to a nitrocellulose blotting membrane (0.1 $\mu$m pore size, Amersham Protran, Cytiva, Washington, DC). Following a 1hr incubation in blocking solution (5% Blocking Reagent (Roche) in PBS) membranes were probed overnight at 4 °C with rabbit anti-MBP antibody (1:500, Merck Millipore). After rinsing with 0.05% PBS-Tween, blots were incubated with IRDye 800CW anti-rabbit secondary antibody (1:10'000, LI-COR, Lincoln, NE) and infrared fluorescence was detected using an Odyssey Imaging System (Odyssey CLx, LI-COR). Normalization was performed by Revert 700 Total Protein Stain (LI-COR).

## Electron Microscopy and Analysis

Following anesthesia using pentobarbital, mice were perfused with PBS (pH 7.4) and subsequently with fixative solution (4% PFA, 2.5% glutaraldehyde in phosphate buffer with 0.5% NaCl, pH 7.4). Brains and optic nerves were dissected and postfixed in the same fixative overnight at 4 °C. Tissue preparation and electron microscopy was performed as previously described (Möbius et al., 2010). Briefly, for embedding, pieces of tissue were postfixed with 2% OsO4 (Science

Services, Munich, Germany) in 0.1 M phosphate buffer pH 7.3 and embedded in EPON (Serva, Heidelberg, Germany) after dehydration with acetone. Ultrathin sections were prepared with a Leica UC7 ultramicrotome (Leica, Vienna, Austria) and stained with UranylLess™ (Science Services, Munich, Germany). EM pictures were taken with a Zeiss EM912 electron microscope (Carl Zeiss Microscopy GmbH, Oberkochen, Germany) using an on-axis 2k CCD camera (TRS, Moorenweis, Germany).
Image analysis was performed with ImageJ (Fiji, Version 2.0.0-rc-69/1.52). For g-ratio analysis, 6-7 random overview EM pictures (at 8000x magnification) from optic nerve sections were taken and 300-350 axons per animal were analyzed. G-ratios (axon diameter divided by the axon diameter including the myelin sheath) were determined from circular areas equivalent to the measured areas. For analysis of synaptic density in the CA1 stratum radiatum, synapses were counted in 5 randomly taken images (116.6 $\mu m^2$ areas) from coronal hippocampal sections per animal, and 3-5 animals were analyzed. Glutamatergic excitatory synapses were identified by their prominent postsynaptic densities (electron-dense material) of around 30 nm thickness. The experimenter was blinded to the images.

## Behavioral Experiments

For all behavioral testing and analyses, the experimenter was blinded to the genotypes. Experiments were performed in adult mice before and after tamoxifen treatment, as specified in the text. All behavioral tests were conducted during the dark (active) phase of the animals, between Zeitgeber time ZT14 and ZT20.
**Sensorimotor scoring** was performed by adapting a previous protocol (Guyenet et al., 2010) and mainly focusing on gait, ledge test, hindlimb clasping, thin (3 mm) and thick (6 mm) horizontal wire tests. Each test was individually scored between 0-3, or 0-4 for the horizontal wire tests, with a combined total score of 0-17 for all tests. Briefly, the following scoring parameters were used for each test: **1) Gait** was assessed on a flat surface from behind the animal, i.e. facing away from experimenter; Score 0: mouse moves normally, body weight supported on all limbs, not shaking, abdomen not touching the ground; Score 1: shows a light tremor; Score 2: walks haltingly, feet point away from the body, uncoordinated walk ("duck feet"); Score 3: severe tremor, hesitant walk, drags abdomen and tail along the surface. **2) Ledge test** was performed by placing the mouse on the edge of a cage starting with its forepaws; Score 0: mouse walks along the ledge without losing footing or balance, appears coordinated and descends into the cage using its forepaws; Score 1: minor slips while walking but otherwise coordinated; Score 2: mouse slips often with hindlimbs and minor shakes while walking; Score 3: severe shaking, unable to place hindlimbs on the edge, falls off the ledge or lands on its head when descending. **3) Hindlimb clasping** was evaluated by lifting the mouse by its tail near the base for 10 s about 30-40 cm above a table; Score 0: hindlimbs are stretched out away from abdomen for 10 s; Score 1: one hindlimb is withdrawn towards the abdomen for at least 5 s; Score 2: both hindlimbs are partially withdrawn towards the abdomen for at least 5 s; Score 3: both hindlimbs are completely withdrawn for more than 5 s. **4) Horizontal wire** tests were performed by placing the mouse with its forepaws on the center of a suspended wire (3 or 6 mm diameter, 30 cm above cushioned ground) and measuring the latency to fall; Score 0: falling after 30 s or reaching the bars at the side; Score 1: falling between 21 and 30 s. Score 2: falling between 11 and 20 s. Score 3:

falling between 6 and 10 s. Score 4: falling between 1 and 5 s. Each paradigm was scored four times (two sessions on two consecutive days, same time of the day) and the average score of each test was used to calculate the sum of scores for every animal. Animals with higher score values showed sensorimotor deficits.

**Novel object recognition memory** was tested following a previous protocol (Leger et al., 2013). For the experiment, a custom-made box (W25 x D25 x H15 cm) with transparent Plexiglass walls was used and its position in the room was kept constant throughout the tests. Animals were handled before testing, allowed to explore the arena, and experiments were performed with dimmed lights to ensure a stress-free environment. Then two identical objects were placed in the box, 5 cm away from the walls, and mice were given 10 min to familiarize with the objects. For the test sessions (3h and 24h post familiarization), one object was exchanged with a novel object placed at the same location, and mice could explore the objects for 5 min. The novel object differed in brightness, shape, color, and texture from the old object. All sessions were recorded with a GoPro camera (HERO4; at 2704 x 1520 resolution and 24 frames per s) for analysis. The time spent exploring the old and novel object was measured. Our definition of exploratory behavior of the objects only included nose-directed behavior at a distance $\leq$ 2 cm to the object. Random chewing, climbing, or leaning on the object was excluded. The ratio of the exploratory time of the novel object to the total exploratory time (old and novel objects) determined the recognition index.

**Barnes maze test** was performed to assess spatial learning and memory, adapted from earlier protocols (Sunyer et al., 2007). A custom-made Barnes maze table (105 cm diameter) with 22 holes (5 cm diameter, 6 cm apart) was used. All holes were closed from underneath the table, except for one escape (target) hole to which an escape box was attached. Visual and optical cues (in the room and on the table) were used for spatial orientation. Since experiments were performed with the same groups of mice before and after tamoxifen treatment, the table orientation, spatial guidance cues, and the target hole were changed completely between the timepoints to avoid potential memory recall. To increase the motivation of animals to search and find the escape hole, weak, aversive stimuli (buzzer, bright light and fan pointing to the table) were used. All behavioral sessions were recorded with a GoPro camera (HERO4). The complete paradigm comprised an initial adaption day (day 0), a 4-day spatial acquisition phase (day 1-4) followed by a final test day (day 5). On the adaptation day, each mouse was placed in the center of the table beneath a dark box for 10 s. The box was lifted as soon as the aversive stimuli were turned on. Once the mouse entered the escape hole (with gentle guidance) the stimuli were turned off and the mouse was allowed to rest in the escape box for 2 min. During the spatial acquisition days, the same procedure was performed but now mice had to find the escape hole on their own. Each mouse had three training sessions per day (ca. 1 h between sessions) and the latencies to find the escape hole were recorded. Latency cutoff time was 180 s. The average latency per day was used for analysis. On test day 5, the escape hole was sealed like the other holes and mice were allowed to search for the target hole for 90 s. The number of head pokes into each hole were counted. Walking distance was assessed from video recordings and analyzed using a custom-written Python (v3.6.2) code (available at https://github.com/martinholub/motrack). Briefly, mouse location on the table was identified and segmented in each frame based on distinct HSV (hue, saturation, value) color profile spectra, and then tracked in consecutive frames with mean-shift algorithm, that identifies two corresponding objects in consecutive frames based on the probability of finding a bounding box with a similar HSV color profile. The centroid coordinates of the mouse were saved together with the timestamp for each frame, which allowed further analysis of motion, distance, and time to reach the escape hole.

## Acute Brain Slice Preparation

Mice (3-5 months old) were anesthetized with isoflurane, decapitated, and brains were quickly dissected and placed in an ice-cold cutting solution containing (in mM): 130 K-gluconate, 15 KCl, 0.2 EGTA, 20 HEPES, and 25 glucose (pH 7.4 adjusted with NaOH). Transversal hippocampus slices (300-350 $\mu$m thick) were cut using a vibratome (Vibration microtome, HM 650V, VWR) and then briefly immersed for 1 min at RT in a solution containing (in mM): 225 D-mannitol, 25 glucose, 2.5 KCl, 1.25 $NaH_2PO_4$, 26 $NaHCO_3$, 0.8 $CaCl_2$, 8 $MgCl_2$ (pH 7.4). Slices were then transferred to an artificial cerebral spinal fluid (ACSF) solution composed of (in mM): 125 NaCl, 2.5 KCl, 25 $NaHCO_3$, 1.25 $NaH_2PO_4$, 2 $MgCl_2$, 1 $CaCl_2$, 25 glucose, maintained at 34 °C for 30 min and then at RT thereafter. Solutions were continuously bubbled with 95% $O_2$ and 5% $CO_2$.

## Electrophysiology and Analysis

Hippocampal slices were transferred to a submerged recording chamber (RC-26, Warner Instruments, Hamden, CT) mounted on an upright Olympus microscope (BX61WI) equipped with differential interference contrast and were perfused with ACSF (containing in mM: 125 NaCl, 2.5 KCl, 25 $NaHCO_3$, 1.25 $NaH_2PO_4$, 2 $MgCl_2$, 2 $CaCl_2$, 25 glucose, saturated with 95% $O_2$ and 5% $CO_2$) maintained at 30 °C by an in-line solution heater (TC-344C, Warner Instruments). Cells were visualized using a 40x water-immersion objective (LUMPlanFL/IR 40x/0.80 W, Olympus). Somatic whole-cell recordings were performed, without series resistance compensation, from CA1 pyramidal cells and stratum radiatum astrocytes, using 4-10 M$\Omega$ glass pipettes filled with (in mM): 135 K-gluconate, 4 KCl, 2 NaCl, 10 HEPES, 4 EGTA, 4 Mg-ATP, 0.3 Na-GTP (pH 7.3, adjusted with KOH); or for neuronal synaptic activity recordings (in mM): 8 NaCl, 145 $CsMeSO_3$, 10 HEPES, 10 Na2-phosphocreatine, 2 Na2-ATP, 0.5 Na-GTP, 0.3 EGTA, 5 lidocaine N-ethyl bromide (QX-314), and 10 TEA (pH 7.25 adjusted with CsOH). Astrocytes were identified by their small cell bodies, linear IV-curves, high resting potentials (around -80 mV) and low input resistance (around 20 M$\Omega$). For intercellular coupling experiments, biocytin (2 mg/ml, Sigma-Aldrich) was added to the internal solution and passive diffusion was limited to 20 min in current-clamp mode. Immediately after recordings, slices were fixed in 4% PFA for 12-24 hr and then processed for immunohistochemical analysis. Intrinsic properties of CA1 pyramidal neurons were measured in current clamp mode (in the absence of synaptic blockers) and depolarizing current injection steps of 500 ms duration were used to elicit action potentials and to measure the input-output relationship. For miniature excitatory postsynaptic current (mEPSC) recordings, cells were voltage-clamped at -70 mV in the presence of bicuculline-methiodide (25 $\mu$M, Sigma-Aldrich) and tetrodotoxin TTX (1 $\mu$M, Abcam, Cambridge, UK) in the bathing solution to block inhibitory input and neuronal spiking activity, respectively. Evoked EPSCs were induced by stimulating Schaffer collaterals in CA1 stratum radiatum using ACSF-filled theta glass electrodes placed 100-200 $\mu$m from recorded cells. Recordings were performed in the presence of 25 $\mu$M bicuculline-methiodide. Evoked

AMPAR-mediated EPSCs were measured at -70 mV and the responses from 5 single pulses at 0.05 Hz were averaged per cell. Paired-pulse stimulations were performed with an interstimulus interval of 50 ms (averaging 5 paired-pulses, 20 s apart) and the ratio between the second and the first AMPA-EPSC peak amplitude was calculated. For recordings of evoked NMDAR-mediated EPSCs, cells were voltage-clamped at +40 mV and AMPARs were blocked by 10 $\mu$M 2,3-Dioxo-6-nitro-1,2,3,4-tetrahydrobenzo[f]quinoxaline-7-sulfonamide (NBQX, Tocris Bioscience, Bristol, UK) added to the ACSF. Evoked NMDAR-EPSCs were induced by single pulse stimulations (averaging 5 pulses, 20 s apart) and by high frequency stimulations (10 pulses at 50 Hz and 100 Hz, 20 s apart). NMDAR decay kinetics were measured by fitting a double exponential function from the current peak to the baseline (Cathala et al., 2000), and the weighted mean decay time constant was used to compare decay times between genotypes and stimulation frequencies. Extracellular field responses were induced by stimulating Schaffer collaterals using a theta electrode and fEPSPs were recorded with a glass pipette (1-2 M$\Omega$) filled with ACSF and placed in CA1 stratum radiatum close to the pyramidal layer. Long-term potentiation (LTP) was induced by theta-burst stimulations consisting of three 2-s trains of brief 100 Hz pulses (each train was composed of 10 stimulus epochs delivered at 5 Hz and each epoch contained four pulses at 100 Hz) delivered 20 s apart. Before LTP induction, baseline recordings were performed at 0.03 Hz stimulations and stimulus intensity was adjusted to evoke 40-50% of the maximum fEPSP slope. The same recording parameters were used to record fEPSP responses up to 45 min after LTP initiation. Recordings were acquired with a MultiClamp 700B amplifier (Axon Instruments, Union City, CA), low-pass filtered at 2 kHz, digitized at 20 kHz (using Digidata 1550B, Axon Instruments) and stored to disk using pClamp 10 software (Molecular Devices, Sunnyvale, CA). Data analysis was performed offline using Clampfit 10.6 software (Molecular Devices) and Mini Analysis Program (Synaptosoft Inc.,Fort Lee, NJ, USA).

## Statistics

Statistical analyses were performed using R (version 3.6.1, R Core Development Team, 2019) and GraphPad Prism (Version 8.4.2, Graphpad Software). We used the lme4 package for linear mixed effects models (lmer function of lme4: R package version 1.1.21; Bates et al., 2015) For histological analyses, we used *genotype* and *brainArea*, and where appropriate, *timepoint* as fixed effects. We added *picture* as a covariate and we allowed for random intercepts for the sections nested within animals (1|animal/section) as a random effect. Defining picture as a covariate was included when images were always taken in the same locations (e.g. picture1 in cortical layer II/III, picture2 in layer IV and picture3 in layer V/VI). For behavioral analyses, we used *genotype* and *timepoint*, and where appropriate, experiment or *testday* as fixed effects and we allowed for random intercepts for the animals (1|animalID). When inspection of residual plots revealed obvious deviations from homoscedasticity or normality, the response variable was log-transformed for statistical analysis. Values for differences between *genotypes* (and *timepoints*) were obtained post-hoc using the emmeans package with pairwise comparisons (R package version 1.4.4; Lenth et al., 2019). For log-transformed or non-transformed response variables, the ratio (r) or the difference ($\beta$) between compared pairs, respectively, is stated in the figure legends. Also, where appropriate, multiple comparisons data were analyzed with two-way ANOVA and inter-group comparisons were made using a Mann Whitney U test, paired or unpaired student's *t* test, as indicated in the figure legends. All data is presented as mean ± SEM. $p$ values $\leq 0.05$ were considered statistically significant and are stated together with each sample size in the figure legends. For whole-cell recordings, each recorded cell was considered a biological replicate. For extracellular LTP recordings, each brain slice was considered a biological replicate. Sample sizes were not determined in advance, since they were constrained by the availability of age-matched transgenic mouse cohorts.

# Acknowledgements

We thank Martine Cohen-Salmon (CIRB, Paris) for providing *Gjb6*$^{fl/fl}$ mice, Michael J. Stobart for technical assistance with qPCR analysis, Jennifer Romanos and Mirko Santello (IPT, Zurich) for technical advice on electrophysiology recordings, Frank Kirchhoff (CIPMM, Homburg) for help in initiating the study, members of the Center for Microscopy and Image Analysis of UZH for provision of microscopes and remote access to image analysis tools, the Institute of Epidemiology, Biostatistics and Prevention of UZH for statistical consulting, Karen Everett for critical reading of the manuscript, and all members of the Weber lab for support and frequent discussions

# Additonal Information

## Competing Interests

The authors declare that no competing interests exist.

## Funding

Aiman S. Saab received support from a Synapsis Career Fellowship Award, the Neuroscience Center Zurich (ZNZ) and the Cloëtta Foundation. Bruno Weber is supported by the Swiss National Science Foundation (SNF number:31003A_156965).

## Author Contributions

Ladina Hösli, Conceptualization, Data curation, Formal analysis, Validation, Investigation, Visualization, Methodology, Writing—original draft, Writing—review and editing; Noemi Binini, Data curation, Formal analysis, Validation, Investigation, Methodology, Writing—review and editing; Laetitia Thieren, Formal analysis, Investigation, Methodology, Writing—review and editing; Zoe J. Looser, Investigation, Methodology, Writing—review and editing; Kim David Ferrari, Data curation, Software, Methodology, Writing—review and editing; Marc Zuend, Investigation, Methodology, Writing—review and editing; Stewart Berry, Investigation, Methodology; Martin Holub, Software, Methodology; Wiebke Möbius, Investigation, Methodology, Writing—review and editing; Torben Ruhwedel, Investigation, Methodology; Klaus-Armin Nave, Resources, Writing—review and editing; Christian Giaume, Conceptualization, Resources; Bruno Weber, Conceptualization, Resources, Funding acquisition, Project administration, Writing—review and editing; and Aiman S. Saab, Conceptualization, Resources, Data curation, Investigation, Supervision, Funding acquisition, Visualization, Methodology, Project administration, Writing—original draft, Writing—review and editing.

## Author ORCIDs

Aiman S. Saab, https://orcid.org/0000-0003-3886-8369
Marc Zuend, https://orcid.org/0000-0002-4683-8250
Martin Holub, https://orcid.org/0000-0002-8365-0927
Wiebke Möbius, http://orcid.org/0000-0002-2902-7165
Klaus-Armin Nave, http://orcid.org/0000-0001-8724-9666

## Ethics

All experimental procedures were approved by the local veterinary authorities according to the guidelines of the Swiss Animal Protection Law, Veterinary Office, Canton Zurich (Animal Welfare Act, 16 December 2005 and Animal Welfare Ordinance, 23 April 2008).

# References

Adamsky A, Goshen I. 2018. Astrocytes in Memory Function: Pioneering Findings and Future Directions. Neuroscience 370:14–26. DOI:10.1016/j.neuroscience.2017.05.033, PMID:28571720

Adamsky A, Kol A, Kreisel T, Doron A, Ozeri-Engelhard N, Melcer T, Refaeli R, Horn H, Regev L, Groysman M, London M, Goshen I. 2018. Astrocytic Activation Generates De Novo Neuronal Potentiation and Memory Enhancement. Cell 174:1–13. DOI:10.1016/j.cell.2018.05.002, PMID:29804835

Aguzzi A, Barres BA, Bennett ML. 2013. Microglia: scapegoat, saboteur, or something else? Science 339:156–61. DOI:10.1126/science.1227901, PMID:23307732

Alberini CM, Cruz E, Descalzi G, Bessières B, Gao V. 2018. Astrocyte glycogen and lactate: New insights into learning and memory mechanisms. Glia 66:1244–1262. DOI:10.1002/glia.23250, PMID:29076603

Araque A, Parpura V, Sanzgiri RP, Haydon PG. 1999. Tripartite synapses: glia, the unacknowledged partner. Trends Neurosci 22:208–215. DOI:10.1016/S0166-2236(98)01349-6, PMID:10322493

Asztely F, Erdemli G, Kullmann DM. 1997. Extrasynaptic glutamate spillover in the hippocampus: Dependence on temperature and the role of active glutamate uptake. Neuron. DOI:10.1016/S0896-6273(00)80268-8, PMID:9052798

Bates D, Mächler M, Bolker B, Walker S. 2015. Fitting Linear Mixed-Effects Models Using lme4. J Stat Softw 67. DOI:10.18637/jss.v067.i01,

Boulay A-C, del Castillo FJ, Giraudet F, Hamard G, Giaume C, Petit C, Avan P, Cohen-Salmon M. 2013. Hearing is normal without connexin30. J Neurosci 33:430–4. DOI:10.1523/JNEUROSCI.4240-12.2013, PMID:23303923

Breithausen B, Kautzmann S, Boehlen A, Steinhäuser C, Henneberger C. 2020. Limited contribution of astroglial gap junction coupling to buffering of extracellular K+ in CA1 stratum radiatum. Glia 68:918–931. DOI:10.1002/glia.23751, PMID:31743499

Broadbent NJ, Squire LR, Clark RE. 2004. Spatial memory, recognition memory, and the hippocampus. Proc Natl Acad Sci U S A. DOI:10.1073/pnas.0406344101, PMID:15452348

Brown RE, Basheer R, McKenna JT, Strecker RE, McCarley RW. 2012. Control of sleep and wakefulness. Physiol Rev. DOI:10.1152/physrev.00032.2011, PMID:22811426

Cathala L, Misra C, Cull-Candy S. 2000. Developmental Profile of the Changing Properties of NMDA Receptors at Cerebellar Mossy Fiber–Granule Cell Synapses. J Neurosci 20:5899–5905. DOI:10.1523/JNEUROSCI.20-16-05899.2000, PMID:10934236

Chao H, Lin C, Zuo Q, Liu Y, Xiao M, Xu X, Li Z, Bao Z, Chen H, You Y, Kochanek PM, Yin H, Liu N, Kagan VE, Bayır H, Ji J. 2019. Cardiolipin-Dependent Mitophagy Guides Outcome after Traumatic Brain Injury. J Neurosci 39:1930–1943. DOI:10.1523/JNEUROSCI.3415-17.2018, PMID:30626699

Chever O, Dossi E, Pannasch U, Derangeon M, Rouach N. 2016. Astroglial networks promote neuronal coordination. Sci Signal 9:ra6. DOI:10.1126/scisignal.aad3066, PMID:26758214

Chever O, Pannasch U, Ezan P, Rouach N. 2014. Astroglial connexin 43 sustains glutamatergic synaptic efficacy. Philos Trans R Soc Lond B Biol Sci 369:20130596. DOI:10.1098/rstb.2013.0596, PMID:25225090

Cina C, Maass K, Theis M, Willecke K, Bechberger JF, Naus CC. 2009. Involvement of the cytoplasmic c-terminal domain of connexin43 in neuronal migration. J Neurosci 29:2009–2021. DOI:10.1523/JNEUROSCI.5025-08.2009, PMID:19228955

Clasadonte J, Scemes E, Wang Z, Boison D, Haydon PG. 2017. Connexin 43-Mediated Astroglial Metabolic Networks Contribute to the Regulation of the Sleep-Wake Cycle. Neuron 95:1365-1380.e5. DOI:10.1016/j.neuron.2017.08.022, PMID:28867552

Cohen-Salmon M, Regnault B, Cayet N, Caille D, Demuth K, Hardelin JP, Janel N, Meda P, Petit C. 2007. Connexin30 deficiency causes instrastrial fluid-blood barrier disruption within the cochlear stria vascularis. Proc Natl Acad Sci U S A. DOI:10.1073/pnas.0605108104, PMID:17400755

Dere E, De Souza-Silva MA, Frisch C, Teubner B, Sohl G, Willecke K, Huston JP. 2003. Connexin30-deficient mice show increased emotionality and decreased rearing activity in the open-field along with neurochemical changes. Eur J Neurosci 18:629–638. DOI:10.1046/j.1460-9568.2003.02784.x, PMID:12911759

Diaz-Garcia CM, Mongeon R, Lahmann C, Koveal D, Zucker H, Yellen G. 2017. Neuronal Stimulation Triggers Neuronal Glycolysis and Not Lactate Uptake. Cell Metab 26:361-374 e4. DOI:10.1016/j.cmet.2017.06.021, PMID:28768175

Du M, Li J, Chen L, Yu Y, Wu Y. 2018. Astrocytic Kir4.1 channels and gap junctions account for spontaneous epileptic seizure. PLoS Comput Biol. DOI:10.1371/journal.pcbi.1005877, PMID:29590095

Duran J, Saez I, Gruart A, Guinovart JJ, Delgado-Garcia JM. 2013. Impairment in long-term memory formation and learning-dependent synaptic plasticity in mice lacking glycogen synthase in the brain. J Cereb Blood Flow Metab 33:550–556. DOI:10.1038/jcbfm.2012.200, PMID:23281428

El Hayek L, Khalifeh M, Zibara V, Abi Assaad R, Emmanuel N, Karnib N, El-Ghandour R, Nasrallah P, Bilen M, Ibrahim P, Younes J, Abou Haidar E, Barmo N, Jabre V, Stephan JS, Sleiman SF. 2019. Lactate Mediates the Effects of Exercise on Learning and Memory through SIRT1-Dependent Activation of Hippocampal Brain-Derived Neurotrophic Factor (BDNF). J Neurosci 39:2369–2382. DOI:10.1523/JNEUROSCI.1661-18.2019, PMID:30692222

Elias LAB, Wang DD, Kriegstein AR. 2007. Gap junction adhesion is necessary for radial migration in the neocortex. Nature 448:901–7. DOI:10.1038/nature06063, PMID:17713529

Garcia ADR, Doan NB, Imura T, Bush TG, Sofroniew M V. 2004. GFAP-expressing progenitors are the principal source of constitutive neurogenesis in adult mouse forebrain. Nat Neurosci. DOI:10.1038/nn1340, PMID:15494728

Ghézali G, Calvo C-F, Pillet L-E, Llense F, Ezan P, Pannasch U, Bemelmans A-P, Manneville SE, Rouach N. 2018. Connexin 30 controls astroglial polarization during postnatal brain development. Development 145:dev155275. DOI:10.1242/dev.155275, PMID:17355401

Giaume C, Koulakoff A, Roux L, Holcman D, Rouach N. 2010. Astroglial networks: a step further in neuroglial and gliovascular interactions. Nat Rev Neurosci 11:87–99. DOI:10.1038/nrn2757, PMID:20087359

Goulart BK, de Lima MNM, de Farias CB, Reolon GK, Almeida VR, Quevedo J, Kapczinski F, Schröder N, Roesler R. 2010. Ketamine impairs recognition memory consolidation and prevents learning-induced increase in hippocampal brain-derived neurotrophic factor levels. Neuroscience 167:969–973. DOI:10.1016/j.neuroscience.2010.03.032, PMID:20338225

Griemsmann S, Höft SP, Bedner P, Zhang J, Von Staden E, Beinhauer A, Degen J, Dublin P, Cope

DW, Richter N, Crunelli V, Jabs R, Willecke K, Theis M, Seifert G, Kettenmann H, Steinhäuser C. 2015. Characterization of panglial gap junction networks in the thalamus, neocortex, and hippocampus reveals a unique population of glial cells. Cereb Cortex 25:3420–3433. DOI:10.1093/cercor/bhu157, PMID:25037920

Guyenet SJ, Furrer SA, Damian VM, Baughan TD, La Spada AR, Garden GA. 2010. A simple composite phenotype scoring system for evaluating mouse models of cerebellar ataxia. J Vis Exp 2–4. DOI:10.3791/1787, PMID:20495529

Harris RA, Lone A, Lim H, Martinez F, Frame AK, Scholl TJ, Cumming RC. 2019. Aerobic Glycolysis Is Required for Spatial Memory Acquisition But Not Memory Retrieval in Mice. eneuro 6:ENEURO.0389-18.2019. DOI:10.1523/ENEURO.0389-18.2019, PMID:30809587

Jahn HM, Kasakow C V., Helfer A, Michely J, Verkhratsky A, Maurer HH, Scheller A, Kirchhoff F. 2018. Refined protocols of tamoxifen injection for inducible DNA recombination in mouse astroglia. Sci Rep 8:5913. DOI:10.1038/s41598-018-24085-9, PMID:29651133

Kunze A, Congreso MR, Hartmann C, Wallraff-Beck A, Hüttmann K, Bedner P, Requardt R, Seifert G, Redecker C, Willecke K, Hofmann A, Pfeifer A, Theis M, Steinhäuser C. 2009. Connexin expression by radial glia-like cells is required for neurogenesis in the adult dentate gyrus. Proc Natl Acad Sci U S A 106:11336–41. DOI:10.1073/pnas.0813160106, PMID:19549869

Lagos-Cabré R, Burgos-Bravo F, Avalos AM, Leyton L. 2019. Connexins in Astrocyte Migration. Front Pharmacol 10:1546. DOI:10.3389/fphar.2019.01546, PMID:32009957

Larson VA, Mironova Y, Vanderpool KG, Waisman A, Rash JE, Agarwal A, Bergles DE. 2018. Oligodendrocytes control potassium accumulation in white matter and seizure susceptibility. Elife 7. DOI:10.7554/eLife.34829, PMID:29596047

Leger M, Quiedeville A, Bouet V, Haelewyn B, Boulouard M, Schumann-Bard P, Freret T. 2013. Object recognition test in mice. Nat Protoc. DOI:10.1038/nprot.2013.155, PMID:24263092

Lenth R, Singmann H, Love J, Buerkner P, Herve M. 2019. emmeans: Estimated Marginal Means, aka Least-Squares Means. cran.r-project.org.

Liddelow SA, Guttenplan KA, Clarke LE, Bennett FC, Bohlen CJ, Schirmer L, Bennett ML, Münch AE, Chung W, Peterson TC, Wilton DK, Frouin A, Napier BA, Panicker N, Kumar M, Buckwalter MS, Rowitch DH, Dawson VL, Dawson TM, Stevens B, Barres BA. 2017. Neurotoxic reactive astrocytes are induced by activated microglia. Nature 541:481–487. DOI:10.1038/nature21029, PMID:28099414

Looser ZJ, Barrett MJP, Hirrlinger J, Weber B, Saab AS. 2018. Intravitreal AAV-Delivery of Genetically Encoded Sensors Enabling Simultaneous Two-Photon Imaging and Electrophysiology of Optic Nerve Axons. Front Cell Neurosci 12:377. DOI:10.3389/fncel.2018.00377, PMID:30405358

Lutz SE, Zhao Y, Gulinello M, Lee SC, Raine CS, Brosnan CF. 2009. Deletion of astrocyte connexins 43 and 30 leads to a dysmyelinating phenotype and hippocampal CA1 vacuolation. J Neurosci 29:7743–52. DOI:10.1523/JNEUROSCI.0341-09.2009, PMID:19535586

Mächler P, Wyss MT, Elsayed M, Stobart J, Gutierrez R, von Faber-Castell A, Kaelin V, Zuend M, San Martín A, Romero-Gómez I, Baeza-Lehnert F, Lengacher S, Schneider BL, Aebischer P, Magistretti PJ, Barros LF, Weber B. 2016. In Vivo Evidence for a Lactate Gradient from Astrocytes to Neurons. Cell Metab 23:94–102. DOI:10.1016/j.cmet.2015.10.010, PMID:26698914

Madisen L, Garner AR, Shimaoka D, Chuong AS, Klapoetke NC, Li L, van der Bourg A, Niino Y, Egolf L, Monetti C, Gu H, Mills M, Cheng A, Tasic B, Nguyen TN, Sunkin SM, Benucci A, Nagy A, Miyawaki A, Helmchen F, Empson RM, Knöpfel T, Boyden ES, Reid RC, Carandini M, Zeng H. 2015. Transgenic mice for intersectional targeting of neural sensors and effectors with high specificity and performance. Neuron 85:942–58. DOI:10.1016/j.neuron.2015.02.022, PMID:25741722

Magistretti PJ, Allaman I. 2018. Lactate in the brain: from metabolic end-product to signalling molecule. Nat Rev Neurosci 19:235–249. DOI:10.1038/nrn.2018.19, PMID:29515192 Maglione M, Tress O, Haas B, Karram K, Trotter J, Willecke K, Kettenmann H. 2010. Oligodendrocytes in mouse corpus callosum are coupled via gap junction channels formed by Connexin47 and Connexin32. Glia 58:1104–1117. DOI:10.1002/glia.20991, PMID:20468052

Magnotti LM, Goodenough DA, Paul DL. 2011. Functional heterotypic interactions between astrocyte and oligodendrocyte connexins. Glia 59:26–34. DOI:10.1002/glia.21073, PMID:21046554

Mederos S, Perea G. 2019. GABAergic-astrocyte signaling: A refinement of inhibitory brain networks. Glia 67:glia.23644. DOI:10.1002/glia.23644, PMID:31145508

Menichella DM, Goodenough DA, Sirkowski E, Scherer SS, Paul DL. 2003. Connexins are critical for normal myelination in the CNS. J Neurosci. DOI:10.1523/jneurosci.23-13-05963.2003, PMID:12843301

Menichella DM, Majdan M, Awatramani R, Goodenough DA, Sirkowski E, Scherer SS, Paul DL. 2006. Genetic and physiological evidence that oligodendrocyte gap junctions contribute to spatial buffering of potassium released during neuronal activity. J Neurosci 26:10984–10991. DOI:10.1523/JNEUROSCI.0304-06.2006, PMID:17065440

Meyer N, Richter N, Fan Z, Siemonsmeier G, Pivneva T, Jordan P, Steinhäuser C, Semtner M, Nolte C, Kettenmann H. 2018. Oligodendrocytes in the Mouse Corpus Callosum Maintain Axonal Function by Delivery of Glucose. Cell Rep 22:2383–2394. DOI:10.1016/J.CELREP.2018.02.022, PMID:29490274

Möbius W, Cooper B, Kaufmann WA, Imig C, Ruhwedel T, Snaidero N, Saab AS, Varoqueaux F. 2010. Electron Microscopy of the Mouse Central Nervous SystemMethods in Cell Biology. pp. 475–512. DOI:10.1016/S0091-679X(10)96020-2

Mori T, Tanaka K, Buffo A, Wurst W, Kühn R, Götz M. 2006. Inducible gene deletion in astroglia and radial glia–a valuable tool for functional and lineage analysis. Glia 54:21–34. DOI:10.1002/glia.20350, PMID:16652340

Morrison BM, Lee Y, Rothstein JD. 2013. Oligodendroglia: metabolic supporters of axons. Trends Cell Biol 23:644–651. DOI:10.1016/j.tcb.2013.07.007, PMID:23988427

Moser EI, Krobert KA, Moser MB, Morris RG. 1998. Impaired spatial learning after saturation of long-term potentiation. Science 281:2038–42. DOI:10.1126/science.281.5385.2038, PMID:9748165

Murphy-Royal C, Johnston AD, Boyce AKJ, Diaz-Castro B, Institoris A, Peringod G, Zhang O, Stout RF, Spray DC, Thompson RJ, Khakh BS, Bains JS, Gordon GR. 2020. Stress gates an astrocytic energy reservoir to impair synaptic plasticity. Nat Commun 11:2014. DOI:10.1038/s41467-020-15778-9, PMID:32332733

Nagai J, Rajbhandari AK, Gangwani MR, Hachisuka A, Coppola G, Masmanidis SC, Fanselow MS, Khakh BS. 2019. Hyperactivity with Disrupted Attention by Activation of an Astrocyte Synaptogenic Cue. Cell 177:1280-1292.e20. DOI:10.1016/j.cell.2019.03.019, PMID:31031006

Orthmann-Murphy JL, Freidin M, Fischer E, Scherer SS, Abrams CK. 2007. Two Distinct Heterotypic Channels Mediate Gap Junction Coupling between Astrocyte and Oligodendrocyte Connexins. J Neurosci 27:13949–13957. DOI:10.1523/JNEUROSCI.3395-07.2007, PMID:18094232

Pannasch U, Derangeon M, Chever O, Rouach N. 2012. Astroglial gap junctions shape neuronal network activity. Commun Integr Biol 5:248–54. DOI:10.4161/cib.19410, PMID:22896785

Pannasch U, Freche D, Dallérac G, Ghézali G, Escartin C, Ezan P, Cohen-Salmon M, Benchenane K, Abudara V, Dufour A, Lübke JHR, Déglon N, Knott G, Holcman D, Rouach N. 2014. Connexin 30 sets synaptic strength by controlling astroglial synapse invasion. Nat Neurosci 17:549–558. DOI:10.1038/nn.3662, PMID:24584052

Pannasch U, Rouach N. 2013. Emerging role for astroglial networks in information processing: From synapse to behavior. Trends Neurosci. DOI:10.1016/j.tins.2013.04.004

Pannasch U, Vargova L, Reingruber J, Ezan P, Holcman D, Giaume C, Sykova E, Rouach N. 2011. Astroglial networks scale synaptic activity and plasticity. Proc Natl Acad Sci 108:8467–8472. DOI:10.1073/pnas.1016650108, PMID:21536893

Pavlov I, Savtchenko LP, Kullmann DM, Semyanov A, Walker MC. 2009. Outwardly rectifying tonically active GABAA receptors in pyramidal cells modulate neuronal offset, not gain. J Neurosci. DOI:10.1523/JNEUROSCI.2747-09.2009, PMID:19955387

R Core Development Team. 2019. R: A language and environment for statistical computing. Rash JE. 2010. Molecular disruptions of the panglial syncytium block potassium siphoning and axonal saltatory conduction: pertinence to neuromyelitis optica and other demyelinating diseases of the central nervous system. Neuroscience 168:982–1008. DOI:10.1016/j.neuroscience.2009.10.028, PMID:19850107

Reichenbach N, Delekate A, Plescher M, Schmitt F, Krauss S, Blank N, Halle A, Petzold GC. 2019. Inhibition of Stat3-mediated astrogliosis ameliorates pathology in an Alzheimer's disease model. EMBO Mol Med 11. DOI:10.15252/emmm.201809665, PMID:30617153

Romanos J, Benke D, Saab AS, Zeilhofer HU, Santello M. 2019. Differences in glutamate uptake between cortical regions impact neuronal NMDA receptor activation. Commun Biol 2:127. DOI:10.1038/s42003-019-0367-9, PMID:30963115

Rook JM, Xiang Z, Lv X, Ghoshal A, Dickerson JW, Bridges TM, Johnson KA, Foster DJ, Gregory KJ, Vinson PN, Thompson AD, Byun N, Collier RL, Bubser M, Nedelcovych MT, Gould RW, Stauffer SR, Daniels JS, Niswender CM, Lavreysen H, Mackie C, Conde-Ceide S, Alcazar J, Bartolomé-Nebreda JM, Macdonald GJ, Talpos JC, Steckler T, Jones CK, Lindsley CW, Conn PJ. 2015. Biased mGlu5-Positive Allosteric Modulators Provide In Vivo Efficacy without Potentiating mGlu5 Modulation of NMDAR Currents. Neuron 86:1029–1040. DOI:10.1016/j.neuron.2015.03.063, PMID:25937172

Rothhammer V, Borucki DM, Tjon EC, Takenaka MC, Chao CC, Ardura-Fabregat A, De Lima KA, Gutiérrez-Vázquez C, Hewson P, Staszewski O, Blain M, Healy L, Neziraj T, Borio M, Wheeler M, Dragin LL, Laplaud DA, Antel J, Alvarez JI, Prinz M, Quintana FJ. 2018. Microglial control of astrocytes in response to microbial metabolites. Nature. DOI:10.1038/s41586-018-0119-x, PMID:29769726

Rouach N, Avignone E, Même W, Koulakoff A, Venance L, Blomstrand F, Giaume C. 2002. Gap junctions and connexin expression in the normal and pathological central nervous system. Biol cell 94:457–75. DOI:10.1016/s0248-

4900(02)00016-3, PMID:12566220

Rouach N, Koulakoff A, Abudara V, Willecke K, Giaume C. 2008. Astroglial metabolic networks sustain hippocampal synaptic transmission. Science 322:1551–5. DOI:10.1126/science.1164022, PMID:19056987

Saab AS, Neumeyer A, Jahn HM, Cupido A, Simek AAM, Boele H-J, Scheller A, Le Meur K, Gotz M, Monyer H, Sprengel R, Rubio ME, Deitmer JW, De Zeeuw CI, Kirchhoff F. 2012. Bergmann Glial AMPA Receptors Are Required for Fine Motor Coordination. Science (80- ) 337:749–753. DOI:10.1126/science.1221140, PMID:22767895

Saab AS, Tzvetavona ID, Trevisiol A, Baltan S, Dibaj P, Kusch K, Möbius W, Goetze B, Jahn HM, Huang W, Steffens H, Schomburg ED, Pérez-Samartín A, Pérez-Cerdá F, Bakhtiari D, Matute C, Löwel S, Griesinger C, Hirrlinger J, Kirchhoff F, Nave KA. 2016. Oligodendroglial NMDA Receptors Regulate Glucose Import and Axonal Energy Metabolism. Neuron 91:119–132. DOI:10.1016/j.neuron.2016.05.016, PMID:27292539

Saab ASAS, Tzvetanova IDID, Nave KAK-A. 2013. The role of myelin and oligodendrocytes in axonal energy metabolism. Curr Opin Neurobiol 23:1065–1072. DOI:10.1016/j.conb.2013.09.008, PMID:24094633

Santello M, Toni N, Volterra A. 2019. Astrocyte function from information processing to cognition and cognitive impairment. Nat Neurosci 22:154–166. DOI:10.1038/s41593-018-0325-8, PMID:30664773

Shih AY, Blinder P, Tsai PS, Friedman B, Stanley G, Lyden PD, Kleinfeld D. 2013. The smallest stroke: occlusion of one penetrating vessel leads to infarction and a cognitive deficit. Nat Neurosci 16:55–63. DOI:10.1038/nn.3278, PMID:23242312

Stehberg J, Moraga-Amaro R, Salazar C, Becerra A, Echeverría C, Orellana JA, Bultynck G, Ponsaerts R, Leybaert L, Simon F, Sáez JC, Retamal MA. 2012. Release of gliotransmitters through astroglial connexin 43 hemichannels is necessary for fear memory consolidation in the basolateral amygdala. FASEB J. DOI:10.1096/fj.11-198416, PMID:22665389

Sunyer B, Patil S, Höger H, Lubec G. 2007. Barnes maze, a useful task to assess spatial reference memory in the mice. Protoc Exch. DOI:10.1038/nprot.2007.390

Suzuki A, Stern SA, Bozdagi O, Huntley GW, Walker RH, Magistretti PJ, Alberini CM. 2011. Astrocyte-neuron lactate transport is required for long-term memory formation. Cell 144:810–23. DOI:10.1016/j.cell.2011.02.018, PMID:21376239

Teubner B, Michel V, Pesch J, Lautermann J, Cohen-Salmon M, Söhl G, Jahnke K, Winterhager E, Herberhold C, Hardelin J-P, Petit C, Willecke K. 2003. Connexin30 (Gjb6)-deficiency causes severe hearing impairment and lack of endocochlear potential. Hum Mol Genet 12:13–21. DOI:10.1093/hmg/ddg001, PMID:12490528

Theis M, Jauch R, Zhuo L, Speidel D, Wallraff A, Döring B, Frisch C, Söhl G, Teubner B, Euwens C, Huston J, Steinhäuser C, Messing A, Heinemann U, Willecke K. 2003. Accelerated hippocampal spreading depression and enhanced locomotory activity in mice with astrocyte-directed inactivation of connexin43. J Neurosci 23:766–76. PMID:12574405

Theis M, Söhl G, Eiberger J, Willecke K. 2005. Emerging complexities in identity and function of glial connexins. Trends Neurosci 28:188–95. DOI:10.1016/j.tins.2005.02.006, PMID:15808353

Tress O, Maglione M, May D, Pivneva T, Richter N, Seyfarth J, Binder S, Zlomuzica A, Seifert G, Theis M, Dere E, Kettenmann H, Willecke K. 2012. Panglial Gap Junctional Communication is Essential for Maintenance of Myelin in the CNS. J Neurosci 32:7499–7518. DOI:10.1523/JNEUROSCI.0392-12.2012, PMID:22649229

Vainchtein ID, Molofsky A V. 2020. Astrocytes and Microglia: In Sickness and in Health. Trends Neurosci. DOI:10.1016/j.tins.2020.01.003, Wallraff A, Köhling R, Heinemann U, Theis M, Willecke K, Steinhäuser C. 2006. The impact of astrocytic gap junctional coupling on potassium buffering in the hippocampus. J Neurosci 26:5438–47. DOI:10.1523/JNEUROSCI.0037-06.2006, PMID:16707796

Wang J, Liu S, Fu Y, Wang JH, Lu Y. 2003. Cdk5 activation induces hippocampal CA1 cell death by directly phosphorylating NMDA receptors. Nat Neurosci 6:1039–47. DOI:10.1038/nn1119, PMID:14502288

Wang L, Liu YH, Huang YG, Chen LW. 2008. Time-course of neuronal death in the mouse pilocarpine model of chronic epilepsy using Fluoro-Jade C staining. Brain Res. DOI:10.1016/j.brainres.2008.07.097, PMID:18708038

Weber B, Barros LF. 2015. The Astrocyte: Powerhouse and Recycling Center. Cold Spring Harb Perspect Biol 7. DOI:10.1101/cshperspect.a020396, PMID:25680832

Wiencken-Barger AE, Djukic B, Casper KB, McCarthy KD. 2007. A role for Connexin43 during neurodevelopment. Glia 55:675–686. DOI:10.1002/glia.20484, PMID:17311295

Wu Z, Guo Z, Gearing M, Chen G. 2014. Tonic inhibition in dentate gyrus impairs long-term potentiation and memory in an Alzhiemer' s disease model. Nat Commun. DOI:10.1038/ncomms5159, PMID:24923909

Yu X, Taylor AMW, Nagai J, Golshani P, Evans CJ, Coppola G, Khakh BS. 2018. Reducing Astrocyte Calcium Signaling In Vivo Alters Striatal Microcircuits and Causes Repetitive Behavior. Neuron 99:1170-1187.e9. DOI:10.1016/j.neuron.2018.08.015, PMID:30174118

Zhuo L, Theis M, Alvarez-Maya I, Brenner M, Willecke K, Messing A. 2001. hGFAP-cre transgenic mice for manipulation of glial and neuronal function in vivo. Genesis 31:85–94. DOI:10.1002/gene.10008, PMID:11668683

Zuend M, Saab AS, Wyss MT, Ferrari KD, Hösli L, Looser ZJ, Stobart JL, Duran J, Guinovart JJ, Barros LF, Weber B. 2020. Arousal-induced cortical activity triggers lactate release from astrocytes. Nat Metab 2:179–191. DOI:10.1038/s42255-020-0170-4

# Additional Files

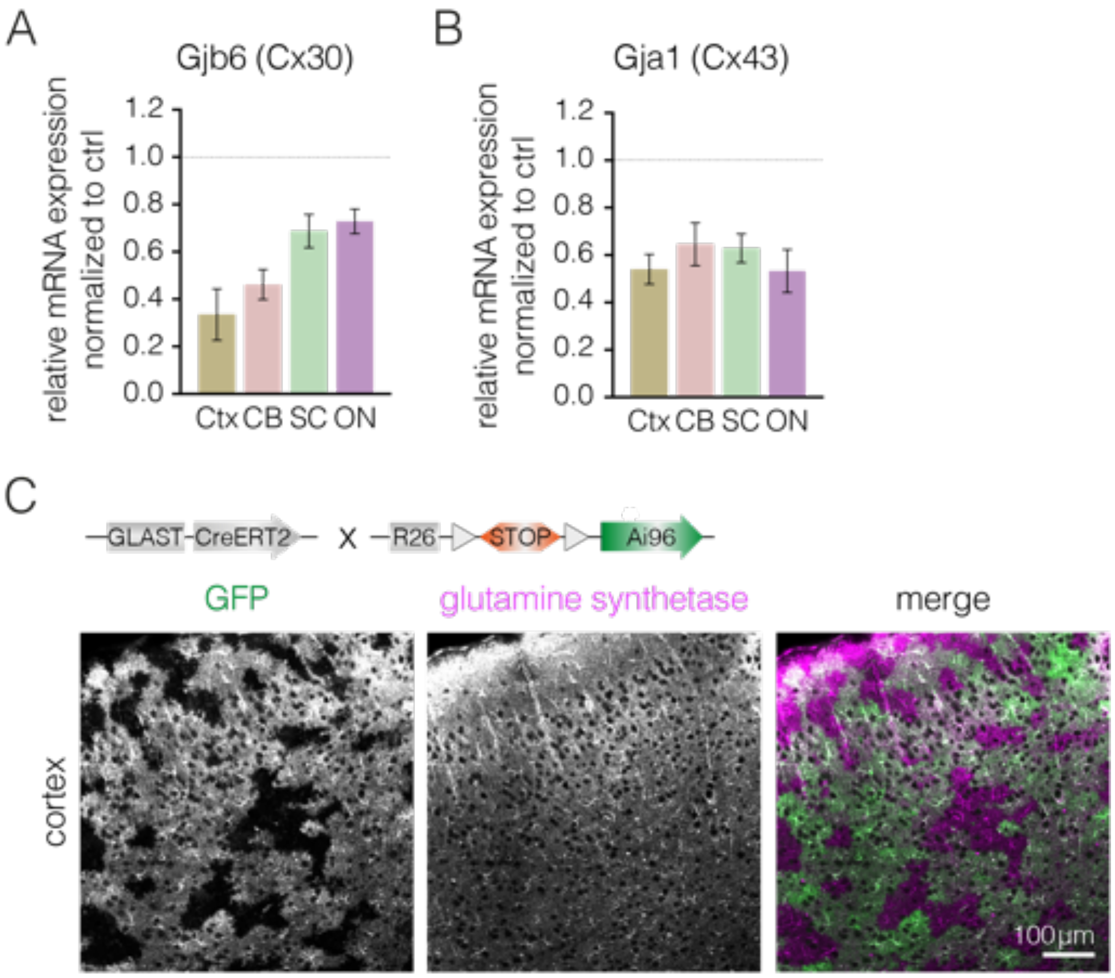

**Fig. 5.1 – Fig. suppl. 1.: Reduced mRNA Expression of *Gjb6* (Cx30) and *Gja1* (Cx43) in cKO Mice.**
**(A, B)** *Gjb6* and *Gja1* mRNA expression was reduced in different brain regions of cKO mice (n = 5) compared to ctrl (n = 5) at 30dpi (***Gjb6***: cortex (Ctx), t(4.7) = 5.88, $p$ = 0.0024; cerebellum (CB), t(7.4) = 5.21, $p$ = 0.0010; spinal cord (SC), t(7.1) = 3.71, $p$ = 0.0073; optic nerve (ON), t(7.3) = 3.1, $p$ = 0.0157; ***Gja1***: Ctx, t(6.3) = 6.38, $p$ = 0.0006, CB, t(6.3) = 2.18, $p$ = 0.0699, SC, t(7.2) = 5.06, $p$ = 0.0014, ON, t(5.1) = 4.87, $p$ = 0.0044, unpaired $t$ test). Data is presented as mean ± SEM.
**(C)** GLASTCre$^{ERT2/+}$:ROSA26-floxed-STOP-GCaMP6s(Ai96) mice revealed reporter gene expression in recombined astrocytes at 60 dpi. Depicted is a confocal overview of cortex immunostained for GCaMP6s (with anti-GFP antibody) and the astrocytic marker glutamine synthetase. Note that not all cortical astrocytes are targeted for recombination.

---

Blank page to keep figures and captions aligned

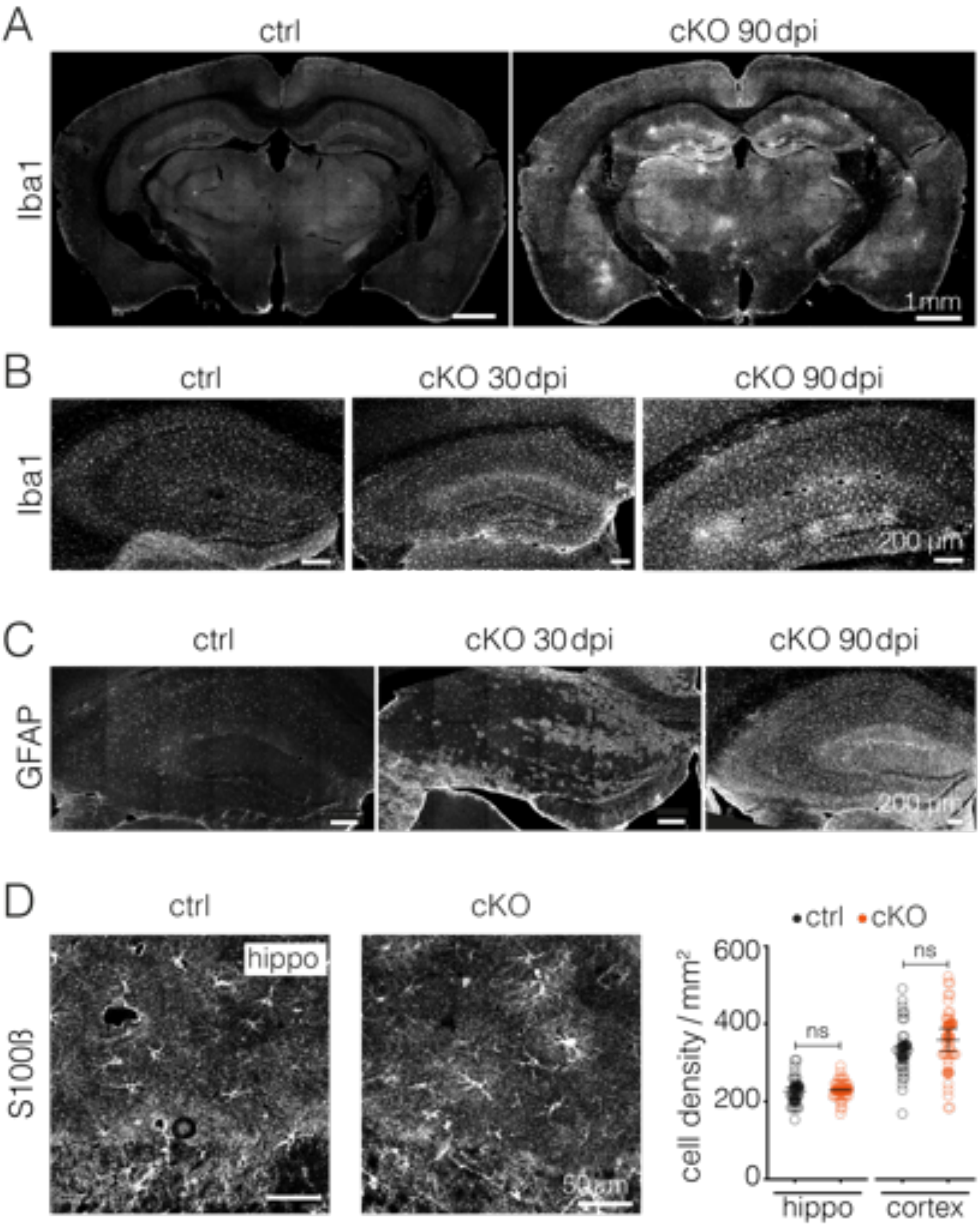
A
ctrl
cKO 90dpi
Iba1
1mm
B
ctrl
cKO 30dpi
cKO 90dpi
Iba1
200 µm
C
ctrl
cKO 30dpi
cKO 90dpi
GFAP
200 µm
D
ctrl
cKO
S100β
hippo
50 µm
•ctrl •cKO
cell density / mm²
600
400
200
0
ns
ns
hippo
cortex

**Fig. 5.3 – Fig. suppl. 1.: Overviews of Activated Astrocytes and Microglia, and Quantification of Astrocytic Density.**

**(A)** Representative overviews of coronal sections immunostained for the microglial marker Iba1 from ctrl and cKO brains at 90 dpi. Note the widespread microglial activation in cKO brains, and bright spots likely indicating activated microglial clusters.

**(B, C)** Representative hippocampal overviews immunostained for Iba1 **(B)** and GFAP **(C)** at 30 dpi and 90 dpi. Note the increase of gliosis in cKO from 30 to 90 dpi.

**(D)** Astrocytic density assessed by the astrocytic marker S100$\beta$in hippocampus and cortex was not altered in cKO mice compared to ctrl (n = 3-4 mice (solid circles), N = 26-27 images (empty circles), **hippocampus** (hippo): $\beta$= 3.4, t(8.59) = 0.17, $p$ = 0.8722; and **cortex**: $\beta$= 25.2, t(8.59) = 1.23, $p$ = 0.2517, linear mixed effects models with post-hoc pairwise comparisons). Confocal images show S100$\beta$labeling in hippocampus from ctrl and cKO sections.

Data are presented as mean ± SEM of animal means.

# 6

# Preview: Direct Vascular Contact, a Hallmark of Cerebral Astrocytes?

## Summary

Astrocytes actively participate in the formation and maintenance of the blood-brain barrier (BBB). Astrocytic perivascular end-feet almost completely cover cerebral microvessels. Therefore, astrocytes are in a powerful position to control the exchange of metabolites between vasculature and brain parenchyma. Metabolites, ions and other molecules are thought to be distributed via the vast astrocytic network formed by gap junction (GJ) channels. Due to indirect vascular contact mediated via astrocytic GJ coupling, a direct contact to blood vessels for every single astrocyte would become redundant. As of today, the proportion of cerebral astrocytes associated with blood vessels is not known. In this study, we used immunohistochemistry and confocal microscopy to investigate the interaction of sparsely labeled astrocytes with vasculature in four different brain areas. Further, by combining various viral approaches for sparse labeling with two-photon microscopy, we examined the full extent of astrocytic connections with blood vessels in the cortex *in vivo*. In total, we examined 1300 astrocytes from cortex, midbrain, thalamus and hypothalamus. On average, an individual astrocyte contacted 3.3 ± 0.04 (mean ± SEM) vessels. Not a single astrocyte was found lacking a connection to the vasculature. Our morphometric data strongly suggests that forming contacts with blood vessels is a ubiquitous feature of astrocytes.

# Introduction

The precisely balanced microenvironment in the brain is maintained by an intact BBB, separating the central nervous system (CNS) parenchyma from the systemic blood stream (Keaney and Campbell, 2015). The BBB is an elaborate multicellular complex, in which astrocytes are a part of. Astrocytic perivascular end-feet maintain close contact with the basal lamina of the vessel wall (Abbott *et al.*, 2006) and almost completely cover cerebral microvessels (Mathiisen *et al.*, 2010). As part of the neuro-vascular unit, astrocytes are thought to be important for regulating blood flow, metabolite availability and neuronal activity (Keaney and Campbell, 2015). Astrocytes engulf synapses with their perisynaptic processes, allowing them to sense neuronal activity (Araque *et al.*, 1999). Therefore, astrocytes are perfectly located to locally regulate blood flow in an activity-dependent manner (Otsu *et al.*, 2014; Attwell *et al.*, 2010; Gordon *et al.*, 2008). Astrocytic end-feet express glucose transporter (GLUT) type 1, enabling the import of glucose (Simpson *et al.*, 2007) that can be converted to lactate and used for astrocytic metabolic supply of neurons (Zuend *et al.*, 2020; Pellerin and Magistretti, 1994; Volkenhoff *et al.*, 2015; Suzuki *et al.*, 2011; Gibbs *et al.*, 2006). Metabolite distribution may be facilitated via the extensive GJ coupled network formed by astrocytes (Rouach *et al.*, 2008; Clasadonte *et al.*, 2017; Murphy-Royal *et al.*, 2020). Given the functional roles of astrocytes in neuro-vascular coupling and metabolic supply to neurons, a tight interaction of the astrocytic population with brain vasculature is to be expected. However, the vast coupled network formed by astrocytes would allow a division of labor, making a connection of every single astrocyte to vasculature redundant. To our knowledge, it is not known how and to what extent cerebral astrocytes participate in BBB formation. In this study, we aimed to quantify the proportion of cerebral astrocytes associated with vasculature by means of morphometric analysis. We found that all analyzed astrocytes in all investigated brain areas were associated with at least one blood vessel.

# Preliminary Results

We aimed at acquiring quantitative information about the interaction of the astrocytic population with the vasculature. To unambiguously assign perivascular end-feet to the respective astrocyte we sparsely labeled astrocytes using

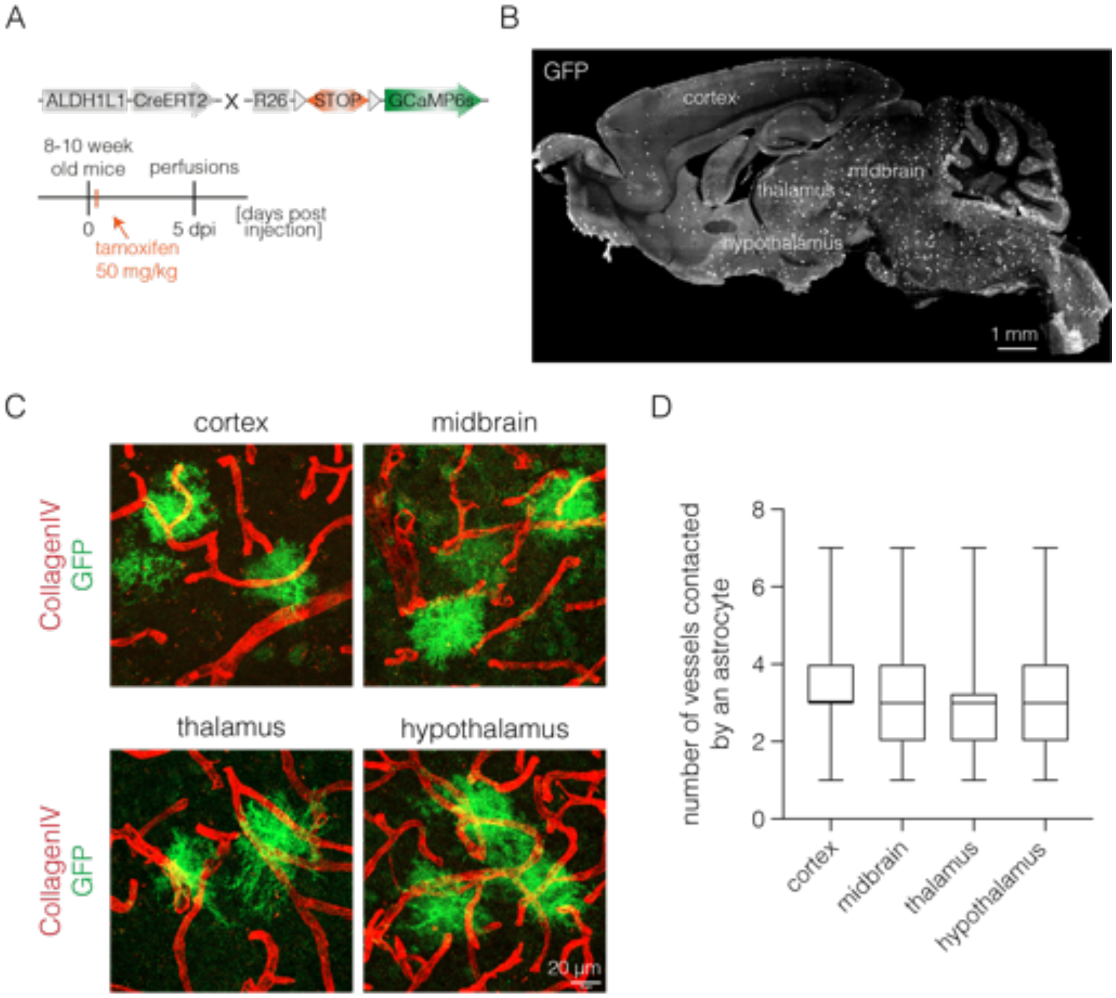

**Figure 6.1.: All Analayzed Astrocytes in Four Different Brain Regions Are Connected to Bloodvessels**

**(A)** Experimental approach for sparsely labeled astrocytes. ALDH1L1$^{\mathrm{CreERT2/+}}$:ROSA26-floxed-STOP-GCaMP6s mice were injected with tamoxifen once and perfused 5 days post-injection (dpi).

**(B)** Confocal overview image showing sparsely labeled astrocytes in all brain regions of a sagittal brain section (40 $\mu$m).

**(C)** Immunohistological example z-projections from cortical, midcerebral, thalamic and hypothalamic astrocytes, all connected to at least one blood vessel.

**(D)** Analysis of the number of contacted vessels per astrocyte residing in the cortex (n = 115, 3.2 ± 0.10 vessels/astrocyte), midbrain (n = 277, 3.1 ± 0.07 vessels/astrocyte), thalamus (n = 130, 2.84 ± 0.10 vessels/astrocyte) and hypothalamus (n = 75, 2.94 ± 0.14 vessels/astrocyte)

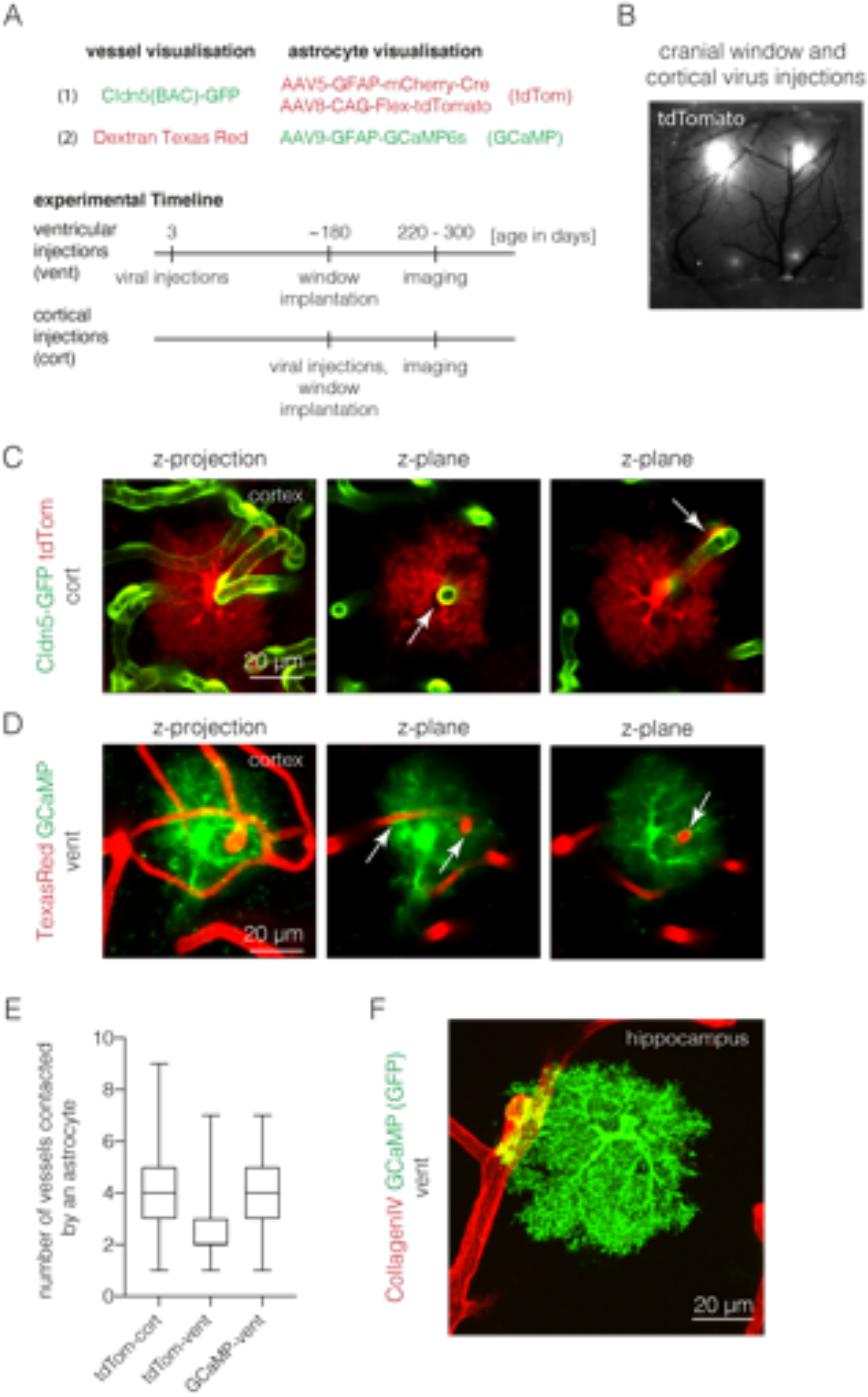
A
vessel visualisation
astrocyte visualisation
(1)
Cldn5(BAC)-GFP
AAV5-GFAP-mCherry-Cre
AAV8-CAG-Flex-tdTomato
(tdTom)
(2)
Dextran Texas Red
AAV9-GFAP-GCaMP6s
(GCaMP)
experimental Timeline
ventricular injections (vent)
3
~180
220 - 300
[age in days]
viral injections
window implantation
imaging
cortical injections (cort)
viral injections, window implantation
imaging
B
cranial window and cortical virus injections
tdTomato
C
z-projection
z-plane
z-plane
Cldn5-GFP tdTom
cort
cortex
20 µm
D
z-projection
z-plane
z-plane
TexasRed GCaMP
vent
cortex
20 µm
E
number of vessels contacted by an astrocyte
0
2
4
6
8
10
tdTom-cort
tdTom-vent
GCaMP-vent
F
CollagenIV GCaMP (GFP)
vent
hippocampus
20 µm

ALDH1L1$^{\text{CreERT2/+}}$:ROSA26-floxed-STOP-GCaMP6s mice. These mice express CreERT2 under the astrocytic promoter aldehyde dehydrogenase 1 family member L1 (ALDH1L1; Srinivasan *et al.*, 2016) and GCaMP6s in a Cre-dependent manner (Madisen *et al.*, 2015), which is used as a fluorescent reporter. A single tamoxifen injection (50 mg/kg bodyweight) at half the dose typically used for efficient recombination of most astrocytes led to sparse labeling, allowing for a clear distinction of single cells (Figure 6.1B, C). Z-stacks of every GCaMP6s-expressing astrocyte in cortex, midbrain, thalamus and hypothalamus (Figure 6.1C) were acquired and the number of vessels contacted by a single astrocyte was analyzed (Figure 6.1D). A total of 597 astrocytes imaged by confocal microscopy contacted an average of 3.0 ± 0.05 (mean ± SEM) vessels per astrocyte. We failed to find

Figure 6.2.: **Viral Approaches for Sparse Astrocyte Labeling Reveal a Vascular Connection of Every Single Astrocyte in the Somatosensory Cortex**
**(A)** Approach for vessel visualisation and sparse astrocyte labeling for 2-photon microscopy in the somatosensory cortex. Several approaches were used: **(1)** A genetic mouse model expressing green fluorescent protein (GFP) in endothelial cells, controlled by the Claudin5 (Cldn5) promoter was used for vessel visualisation. Sparse labeling of astrocytes in Cldn5-GFP mice was achieved by dual virus injections combining AAV5-GFAP-mCherry-Cre (expressing Cre in astrocytes) and AAV8-CAG-Flex-tdTomato (Cre-dependent tdTomato expression; termed tdTom). **(2)** Sparse astrocyte labeling by injections of AAV9-GFAP-GCaMP6s in wildtype mice (termed GCaMP). Vessels were visualized by intravenous injections of Dextran Texas Red before imaging. Viruses were either injected in the lateral ventricle of 3 day old pubs (vent) or in the somatosensory cortex of adult mice (cort). Imaging was always performed in adult mice.
**(B)** Example of a cranial window implantation and four intracortical injections of AAV5-GFAP-mCherry-Cre and AAV8-CAG-Flex-tdTomato (tdTom-cort).
**(C, D)** 2-photon microscopy example images of tdTomato-expressing astrocytes in Cldn5-GFP mice after cortical virus injections in adult mice **(C**, tdTom-cort), or GCaMP-expressing astrocytes after a viral ventricular injection and visualisation of the vessels with TexasRed **(D**, GCaMP-vent). White arrows in the single z-plane images indicate contact sites of astrocytes with vessels.
**(E)** Quantification of the number of vessels contacted by a single astrocyte revealed at least one connected vessel per astrocyte independent of the visualisation approach. Astrocytes of tdTom-cort mice show connections to 3.7 ± 0.07 vessels (n = 267), and those of tdTom-vent mice show connections to 2.3 ± 0.06 vessels (n = 276). Astrocytes of GCaMP-vent mice show connections to 3.9 ± 0.1 vessels (n = 160).
**(F)** Confocal image of a GCaMP6s-vent mouse, showing a GCaMP-expressing (enhanced with an anti-GFP antibody) astrocyte in the hippocampus connected to a blood vessel immunostained with an anti-CollagenIV antibody.

a single astrocyte without a vessel connection. Considering the average volume of an astrocytic territory ($\sim$ 30000 $\mu$m$^3$; Grosche *et al.*, 2013; Wilhelmsson *et al.*, 2006) and the distance of any given point in the tissue to the closest vessel (10 - 30 $\mu$m; Sakadžić *et al.*, 2014; Risser *et al.*, 2009; Shaw *et al.*, 2019), it is not surprising to find at least one vessel contacted by every astrocyte. Nevertheless, tamoxifen is injected systemically and likely enters the brain via the bloodstream. Therefore, astrocytes with intimate vessel contact could recombine faster than astrocytes potentially lacking a vascular connection. This could introduce a bias towards labeling of vessel-associated astrocytes. Morevoer, the full astrocyte morphology may not be appreciated in a 40 $\mu$m-thick brain slice, as it was used for confocal imaging (see figure 6.1C). Therefore, the estimated number of contacted vessels per astrocyte may be underestimated.

To address the two major disadvantages arising from the tamoxifen-induced immunohistological approach, we made use of a bloodstream-independent viral strategy for astrocyte labeling and acquired *in vivo* data using 2-photon microscopy. By using two different viral approaches and delivery strategies to label astrocytes (see figure 6.2A), we excluded the possibility that astrocytes may be neglected due to a lack of vascular contact. Sparse labeling of astrocytes was either achieved by direct intracortical injections of AAV5-GFAP-mCherry-Cre and AAV8-CAG-Flex-tdTomato in adult mice (termed tdTom-cort), intraventricular injections of AAV5-GFAP-mCherry-Cre and AAV8-CAG-Flex-tdTomato in 3-day old pubs (termed tdTom-vent), or intraventricular injections of AAV9-GFAP-GCaMP6s in 3-day old pubs (termed GCaMP-vent). By mixing AAV5-GFAP-mCherry-Cre and AAV8-CAG-Flex-tdTomato we achieved Cre expression specifically in astrocytes (directed by the glial fibrillary acidic protein (GFAP) promoter) and Cre-dependent expression of tdTomato in single astrocytes. This viral mix was injected into Cldn5(BAC)-GFP mice expressing GFP in endothelial cells for visualisation of the vasculature (Figure 6.2A(1), C). AAV9-GFAP-GCaMP6s was injected in wildtype mice, therefore we used Dextran Texas Red for visualisation of the blood vessels during imaging (figure 6.2A(2), D). For a full appreciation of astrocyte morphology and vascular interaction we used 2-photon laser scanning microscopy in the somatosensory cortex *in vivo* (see figure 6.2C, D). A total of 703 cortical astrocytes were analyzed using the three sparse labeling techniques described, invariably revealing astrocytic contact to at least one blood vessel ( Figure 6.2E). The intraventricular viral injections (tdTom-vent and GCaMP-vent) should not only lead to fluorophore expression in cortical astrocytes, but should also label astrocytes residing in other brain areas, inaccessible to 2-photon microscopy. Indeed, confocal imaging of a sagittally sectioned GCaMP-vent brain revealed labeled astrocytes in deeper cortical layers, hippocampus and cerebellum, that also connected to vasculature (Figure 6.2F). Thus, all astrocytes analyzed, independently of the strategy used to induce sparse labeling, showed a connection to at least one vessel.

## Discussion

In the present study we hypothesize that vascular contact is a ubiquitous hallmark of astrocytes. Astrocytes have long been seen as a homogeneous cell population. However, recent research highlights the heterogeneity of these glial cells (Khakh and Deneen, 2019; Chai *et al.*, 2017; Lin *et al.*, 2017; Morel *et al.*, 2017; Lanjakornsiripan *et al.*, 2018). We are aware of the challenges involved in investigating the entire astrocytic population. However, by using two different, widely expressed, promoters (ALDH1L1 and GFAP) to target fluorophore expression in single astrocytes, we are confident of having covered the vast majority of astrocytic subpopulations (Srinivasan *et al.*, 2016; Pannasch *et al.*, 2011). Moreover, by choosing two different strategies for viral delivery at two different ages we minimize the risk of investigating a specific subpopulation of astrocytes.

The methods used in this study are purely morphometric, hence, the functionality of the documented astrocytic vascular connections was not investigated. Considering recently reported intraregional astrocytic diversity (Lanjakornsiripan *et al.*, 2018), it is fascinating to think that astrocytes cooperate with each other implementing some sort of labor division. The astrocytic syncytium established by GJ coupling between astrocytes enables rapid intercellular communication (Giaume *et al.*, 2010) and may allow distribution of tasks among astrocytes. In addition, the astroglial network constitutes a redundant (indirect) connection to vasculature for every cell participating in the network.

Interestingly, the astrocytic network is limited to neuronal functional units, such as the barrel cortex in the somatosensory cortex or the glomeruli of the olfactory bulb (Roux *et al.*, 2011; Houades *et al.*, 2008). Astrocytes within these functional domains cultivate tight GJ coupling, but form only weak connections to astrocytes located outside of the functional unit. Likewise, astrocytic processes are structurally confined within neuronal functional units, with only few crossings between functional units (Eilam *et al.*, 2016). Capillaries, on the other hand, are evenly distributed and do not respect borders defined by neuronal functional domains (Eilam *et al.*, 2016). This implies that astrocytes may be responsible for efficient regulation of blood flow seen within functional units (Woolsey *et al.*, 1996). In the light of the present findings, however, it remains to be clarified whether every single astrocyte within a functional unit participates in blood flow regulation or whether this is an organized network effort.

Both, astrocytes as well as the astrocytic network have been implicated in metabolic support of neurons (Bernardinelli *et al.*, 2004; Rouach *et al.*, 2008; Clasadonte *et al.*, 2017; Murphy-Royal *et al.*, 2020; Dringen *et al.*, 1993; Suzuki *et al.*, 2011; Tadi *et al.*, 2015). However, why is GJ coupling required for metabolic support when every astrocyte has access to blood vessels - the metabolic source? Decoupling the astrocytic network in adulthood (see chapter 5) has no effects on critical functions, which would overtly affect neuronal viability or animal lifespan. Disconnecting GJ coupling does, however, have an impact on higher cognitive functions, such as learning and memory. This could implicate that during steady-state brain activity the support of a single astrocyte is enough to maintain neuronal functionality. Activation of a functional neuronal unit, however, may require the concerted support of an organized astroglial network. Indeed, astrocytic activation was shown to promote memory allocation and to be required for memory enhancement (Adamsky *et al.*, 2018).

Many important biological systems display a robustness against perturbations, which can be ascribed to functionally redundant pathways (Hartman *et al.*, 2001). This includes redundant genes compensating for loss of gene function (Wagner, 2005), redundant intranodal pacemakers maintaining heart rhythm (Li *et al.*, 2017) or the circle of Willis generating redundant connections ensuring brain perfusion (Alpers *et al.*, 1959). Metabolic pathways are at the heart of cellular processes required for cellular function. Not surprisingly, metabolic pathways show some degree of redundancy (Behre *et al.*, 2008). However, redundant pathways may also have distinct functional roles under certain circumstances (Harrison *et al.*, 2007; Sambamoorthy and Raman, 2018). In the brain, proper distribution of metabolites to neuronal compartments is vital for neuronal function (Menichella *et al.*, 2003; Menichella *et al.*, 2006; Odermatt *et al.*, 2003; Magnotti *et al.*, 2011). Therefore, it is quite conceivable that redundant pathways for efficient metabolite distribution exist. Direct astrocytic contact to the vasculature and an indirect vascular connection via GJ coupling, may be an example of such redundancy. These two pathways may substitute each other during basal brain activity, but possibly both are required for complex cognitive functions, such as learning and memory (see chapter 5).

In summary, using various approaches for sparsely labeling astrocytes we examined a total of 1300 astrocytes in four different brain regions. All imaged astrocytes were connected to at least one blood vessel. On average, a single astrocyte contacted roughly 3 vessels. Our data strongly suggests that direct vascular contact is a hallmark of cerebral astrocytes.

# General Discussion

# 7

During the past century the simplistic view of astrocytes representing metabolically inert cells changed toward the image of an active and dynamic astroglial network. Astrocytes are now well-known to sense and respond to neuronal activity with membrane depolarization (Kettenmann *et al.*, 1984) and gliotransmission (Bezzi and Volterra, 2001). Hence, it is broadly acknowledged that astrocytes actively participate in information processing and modulation of cognitive behaviours, but also contribute to the brain's energy budget (Barros *et al.*, 2018).

In this thesis we investigated the role of astrocytes in brain energy metabolism and cognitive behaviour. The first study, designed to better understand neuronal adaptations to fluctuating workloads, discovered a permissive role of the $Na^+$ pump controlling ATP production in mitochondria, an entirely novel mechanism. We continued by studying mechanisms underlying lactate dynamics in astrocytes and neurons, and found that arousal-induced cortical activation promotes lactate shuttling from astrocytes to neurons *in vivo*. We could demonstrate that lactate surges were partly mediated by β-adrenergic receptor activation and lactate mobilization from glycogen stores. In addition, we have generated and characterized a new mouse model that allows us to study the role of astroglial gap junction (GJ) coupling in the adult brain. We demonstrate the influence of the astroglial network on neuronal excitability, neuronal plasticity and on spatial learning and memory. Finally, preliminary data suggest that vascular contact is a universal feature of astrocytes, possibly representing a redundant pathway for metabolite distribution together with the astroglial syncytium.

Using fluorescence resonance energy transfer (FRET) sensors and ion-sensitive probes article 1 approaches the fundamental question of neuronal metabolic adaptation to changes in workload. The presented protocols allowed for a quantitative analysis of ATP consumption during the first few seconds following synaptic activity. In more detail, a short theta burst (STB) evokes a $Na^+$ rise in neurons that was used to estimate ATP consumption of the $Na^+$ pump. Transport-stop protocols based on the $Na^+$ pump, glucose or lactate transporters in concert with $Na^+$-sensitive dyes, glucose- or lactate-sensitive FRET sensors were used to measure the respective consumption. Next to the main finding, that the $Na^+$ pump controls mitochondrial ATP production in neurons, other important discoveries were made: (1) resting neurons consume glucose and lactate, (2) activity stimulates glucose flux and lactate flux in neurons, (3) energy is accumulated in mitochondria before ATP is released to the cytosol.

Using the genetically-encoded ATP sensor ATeam 1.03 (Imamura *et al.*, 2009) and the ADP:ATP reporter Perceval high range (HR) (Tantama *et al.*, 2013) we showed that ATP and ADP levels are unaffected by neuronal activity induced by STB *in vitro*. *In vivo* measurements using a transgenic mouse expressing ATeam in neurons (B6-Tg(Thy1.2-ATeam1.03$^{YEMK}$)$^{AJhi}$; Trevisiol *et al.*, 2017) also revealed invariant ATP levels during whisker stimulation. Thus, during physiological activity ATP consumption by the $Na^+$ pump and ATP production by mitochondria must be matched at any given moment. This excludes adenine nucleotides as homeostatic feedback regulators for the tight coupling of ATP consumption and production.

Signaling of cytosolic (Gellerich *et al.*, 2009; Gellerich *et al.*, 2013) and mitochondrial $Ca^{2+}$ (Glancy and Balaban, 2012; Denton *et al.*, 2016; Denton, 2009) has also been implicated in the regulation of mitochondrial energy production. However, here we show that mitochondrial $Ca^{2+}$ levels barely rise in response to STB, making signaling very unlikely. Regarding cytosolic $Ca^{2+}$, there is a mismatch between $Ca^{2+}$ dynamics and ATP production. This mismatch fails to explain the invariant ATP and ADP levels during STB. The increasing $Na^+$ levels would be another possibility to regulate oxidative phosphoryltion. Although the increase in cytosolic $Na^+$ levels correlated with ATP production, the massive $Na^+$ increase during $Na^+$ pump blockage failed to increase ATP production, also eliminating $Na^+$ levels as a potential signal. Thus, we excluded the regulation of mitochondrial ATP production via adenine nucleotides, cytosolic or mitochondrial $Ca^{2+}$, and $Na^+$. The perfect matching between $Na^+$ pump activity and ATP production, and the immediate adaptation in ATP production upon blockage of the $Na^+$ pump, implies a direct control of the $Na^+$ pump. Additionally to increasing pyruvate consumption by mitochondria, $Na^+$ pump activity also stimulated glucose consumption in neurons. This may constitute the direct link between the $Na^+$ pump and mitochondrial respiration. In astrocytes, the co-compartmentalization of the $Na^+$ pump with glutamate transporter 1 (GLT-1), glycolytic enzymes (especially hexokinase, the enzyme phosphorylating glucose to glucose-6-phosphate), mitochondrial proteins and other enzymes was observed, forming so called multiprotein complexes (Genda *et al.*, 2011; Buck *et al.*, 2003; Rose *et al.*, 2009). Thus, in astrocytes the $Na^+$ pump is thought to regulate glycolytic activity via these multiprotein complexes (Bittner *et al.*, 2011; Fernández-Moncada and Barros, 2014). Such complexes may also form in neurons, establishing a physical interaction between the $Na^+$ pump, mitochondrial proteins and glycolytic enzymes. However, the exact mechanism involved in the regulation of oxidative phosphorylation via the $Na^+$ pump is a matter for future investigations.

Interestingly, STB had no effect on either pyruvate, lactate or glucose levels in neurons, suggesting a tight regulation of cytosolic metabolites, i.e. increasing metabolite uptake in response to increased consumption. However, metabolite fluxes immediately became visible when transport-stop protocols were applied. Pyruvate was readily consumed by mitochondria upon STB stimulation. Glucose consumption, however, increased with a delay compared to pyruvate consumption. This implies that to keep pyruvate and lactate levels stable during activity, the pyruvate pool is sustained by extracellular lactate, as there is a delay in the activation of glycolysis. This extracellular lactate might be of astrocytic origin, as it has been proposed by Pellerin and Magistretti, 1994 almost 20 years ago. Indeed, with article 2 we provide *in vivo* evidence for activity-dependent lactate release by astrocytes.

In article 2 we use an arousal stimulus to robustly evoke startle responses in awake, head-fixed mice. By means of two-photon microscopy of genetically-encoded lactate (San Martin *et al.*, 2013) and $Ca^{2+}$ sensors in neurons (Ohkura *et al.*, 2012) and astrocytes (Chen *et al.*, 2013) we followed lactate dynamics during the transition into arousal state. A brief isoflurane puff elicited an immediate arousal response in mice that was detected by pupil dilation, increase in high-frequency spectrum of electroencephalography (EEG) recordings and $Ca^{2+}$ transients in neurons and astrocytes, all of which have been shown to be hallmarks of arousal before (Zerbi *et al.*, 2019; Reimer *et al.*, 2014; Berridge and Foote, 1991; Paukert *et al.*, 2014; Ding *et al.*, 2013).

Upon induction of arousal we observed an immediate and fast $Ca^{2+}$ response in neurons and astrocytes. In astrocytes the $Ca^{2+}$ transient was accompanied by a simultaneous dip in lactate levels followed by a lactate surge. The initial lactate dip seemed to be exclusive to astrocytes as neurons only showed an increase in lactate levels. The lactate dip in astrocytes could indicate lactate consumption that is not met by net production, or, it could represent a lactate release, as has been observed by others following stimulation of astrocytes (Sotelo-Hitschfeld *et al.*, 2015; Ruminot *et al.*, 2019; Pierre and Pellerin, 2005). A measurable consequence of astrocytic lactate release would be a lactate raise in the extracellular space (ECS). Indeed, by means of a precalibrated Pinnacle lactate biosensor we observed an initial fast increase in ECS, concurrent with the lactate dip in astrocytes. In a second phase we noticed a slowing of the ECS lactate rise, coinciding with the lactate surge in neurons. Even though neurons were recently suggested to produce, and possibly release lactate upon stimulation (Diaz-Garcia *et al.*, 2017), the lack of a lactate dip in neurons as well as the concurrence of neuronal lactate surge and the deceleration of the ECS lactate rise, indicate neuronal lactate uptake following arousal. Moreover, if neurons indeed released lactate, they would have to rapidly increase glycolytic activity in order to prevent an initial lactate drop (as is seen in astrocytes). However, as discussed in article 1, neuronal glycolysis *in vitro* was shown to only start after pyruvate consumption by mitochondria (Baeza-Lehnert *et al.*, 2019). In the case of neuronal lactate release this would consequently be visible as a lactate dip in neurons.

Noradrenaline released by the locus coeruleus during arousal is an important neuromodulator, that was also shown to affect astrocyte metabolism by binding to adrenergic receptors (Magistretti *et al.*, 1981; Subbarao and Hertz, 1991; Dienel and Cruz, 2016). Especially the activation of $\beta_2$-adrenergic signaling in astrocytes was linked to astrocytic lactate release and to long-term memory formation (Gao *et al.*, 2016; Descalzi *et al.*, 2019; Alberini *et al.*, 2018). By pharmacological inhibition of β-adrenoceptors with propranolol we showed that astrocyte lactate production is partially dependent on β-adrenergic signaling via noradrenaline. Interestingly, the lactate dip in astrocytes was not affected, indicating that lactate release is not mediated by β-adrenoceptors.

Glycogen breakdown is also stimulated by noradrenaline (Sorg and Magistretti, 1991) and glycogen-derived lactate release by astrocytes has been implicated in learning and memory (Suzuki *et al.*, 2011; Newman *et al.*, 2011). Using genetically modified mice deficient of glycogen stores in the brain, we demonstrate that lactate mobilization during arousal requires glycogen metabolism. To summarize, we show that arousal triggers β-adrenergic-dependent and glycogen-derived lactate release from astrocytes. Our data provides *in vivo* evidence for the astrocyte-neuron lactate shuttle (ANLS), highlighting that an increase in cortical activity triggers lactate release from astrocytes.

Astrocytic networks are activated during arousal (Paukert *et al.*, 2014; Ding *et al.*, 2013) and lactate released by astrocytes was shown to regulate neuronal excitability (Sada *et al.*, 2015), neuronal mRNA translation (Descalzi *et al.*, 2019), cognitive behaviours, including learning and memory (Alberini *et al.*, 2018) and cannabinoid-dependent social behavior (Jimenez-Blasco *et al.*, 2020). In addition, astrocytic lactate release in the lateral hypothalamus is vital for normal orexinergic neuronal activity and wakefulness (Clasadonte *et al.*, 2017) and in the hippocampus and neocortex it is critical for long-term potentiation (Murphy-Royal *et al.*, 2020). Interestingly, Murphy-Royal *et al.*, (2020) demonstrated that stress compromises lactate and glucose distribution via the astroglial network, thereby impairing plasticity. Similarly, Clasadonte *et al.*, (2017) revealed that disrupting the astrocytic GJs network diminishes lactate shuttling to orexin neurons and impairs the sleep-wake cycle. Studies in the past two decades have implicated astrocytic GJ coupling in functions such as glutamate clearance and $K^+$ buffering (Wallraff *et al.*, 2006; Pannasch *et al.*, 2011), metabolic support of neurons (Clasadonte *et al.*, 2017; Murphy-Royal *et al.*, 2020; Rouach *et al.*, 2008), regulation of synaptic activity (Pannasch *et al.*, 2011), modulation of whole neuronal networks (Chever *et al.*, 2016) and even control of complex behaviors (Clasadonte *et al.*, 2017; Murphy-Royal *et al.*, 2020). It is therefore exciting to assume that lactate distributed through the astrocytic network and released by astrocytes not only exerts metabolic functions, but also neuromodulatory effects that contribute to state-dependent network signaling. Unfortunately, most of our current knowledge on GJs coupling in the brain is based on mouse models with connexin (Cx) deletions during brain development. Hence, it remained difficult to disentangle developmental perturbations caused by the Cx deletions from their functions as GJ coupling forming networks.

In article 3 we present a newly generated conditional knock out (cKO) mouse model that enables the inducible, astrocyte-specific deletion of Cx30 and Cx43, the major Cxs involved in astrocytic GJ channel formation. Disruption of GJ coupling in adult mice caused widespread activation of astrocytes and microglia, but no tissue damage or neuronal loss. In comparison, developmental disruption of the astroglial network caused activation of astrocytes together with tissue damage, such as vacuolation and axonal degeneration, but no microglia activation (Lutz *et al.*, 2009). Astrocytes and microglia dynamically interact with each other during inflammatory processes (Farina *et al.*, 2007; Min, 2006; Norden *et al.*, 2014) and can adopt neuroprotective or neurotoxic activation states (Clarke *et al.*, 2018; Liddelow *et al.*, 2017; Martinez and Gordon, 2014). A young and interesting field of investigation is the metabolic profile of microglia that changes upon microglia activation. However, while some report the metabolic switch from oxidative phosphorylation to a more glycolytic metabolism (with the release of lactate) during activation (Baik *et al.*, 2019), others propose the existence of an astrocyte-microglia lactate shuttle under specific conditions, e.g. the neuroinflammatory disease tuberculous meningitis (Mason *et al.*, 2015). Nevertheless, extracellular lactate has been shown to have neuroprotective effects (Berthet *et al.*, 2009; Berthet *et al.*, 2012; Vohra *et al.*, 2019; Jimenez-Blasco *et al.*, 2020) and it is an interesting idea that microglia could release lactate to the ECS under certain inflammatory conditions. Likewise, it might be worth investigating the concept of a metabolic trinity (neuron-astrocyte-microglia). This newly generated mouse line could represent a simplified model to investigate neuron-astrocyte-microglia interactions in a time-dependent manner.

Further, developmental Cx30 and Cx43 knock out (KO) mice were shown to display motor deficits and impairments in the object relocation task (Lutz *et al.*, 2009). Similarly, we demonstrate that decoupling of the astroglial network in the adult brain leads to deficits in sensorimotor performance and to impaired spatial learning and memory. Since we circumvented developmental perturbations and did not detect any tissue damage in our mice, the observed impairments should primarily reflect the contribution of the glial network. Therefore, we conclude that acquisition of spatial memory requires an intact panglial network, that was demonstrated before to be involved in the distribution of (glycogen-derived) lactate, implicated in learning and memory (Clasadonte *et al.*, 2017; Murphy-Royal *et al.*, 2020; Suzuki *et al.*, 2011; Duran *et al.*, 2013; Alberini *et al.*, 2018).

The underlying cause of the observed deficits in cognitive functions could be evoked by alterations in synaptic activity. Indeed, extensive characterization of developmental Cx30 and Cx43 KO mice revealed changes in neuronal excitability, synaptic transmission, plasticity, and network coordination (Chever *et al.*, 2014; Chever *et al.*, 2016; Pannasch *et al.*, 2011; Pannasch *et al.*, 2012; Pannasch *et al.*, 2014; Wallraff *et al.*, 2006). In article 3 we report decreased neuronal excitability, increased AMPA receptor-mediated synaptic transmission and reduced long-term potentiation induction in the CA1 region of the hippocampus. Previously, an increased inhibitory transmission was reported in developmental Cx30 and Cx43 KO mice (Pannasch *et al.*, 2011). Astrocytes are known to regulate the excitation/inhibition balance in the brain (Perea *et al.*, 2016; Yu *et al.*, 2018; Mederos and Perea, 2019). An increase in inhibitory input may explain the decreased neuronal excitability that we see in our cKO mice. However, further studies on inhibitory transmission are needed to resolve the impact of the astroglial network on excitation/inhibition balance. The observed increase in synaptic transmission in our cKO was not due to changes in presynaptic release mechanisms or a reduction in glutamate clearance, but rather alterations in postsynaptic receptor composition. As the astrocytic network was reported to be important for buffering of extracellular $K^+$ (Pannasch *et al.*, 2011), we cannot exclude that the $K^+$ buffering capacity is altered in cKO mice and may contribute to the phenotype. However, recently it was shown that astrocytic GJ coupling is mainly required for buffering of large and localized $K^+$ increases, but has a limited contribution during basal activity (Breithausen *et al.*, 2020).

Interestingly, even though efficient metabolite distribution is vital for neuronal functionality (Clasadonte *et al.*, 2017; Murphy-Royal *et al.*, 2020), decoupling of the astroglial network in the adult mouse does not show grave detrimental effects. An explanation may be that every single astrocyte seems to maintain a connection to vasculature (see Preview, chapter 6). Therefore, all astrocytes in the brain may possess the machinery to support neuronal metabolism on their own. However, during activation of neuronal networks, as is the case during learning and memory, the concerted action of a whole astrocytic network might be required. This is exemplified by the new mouse model that shows impaired spatial learning and memory after decoupling of the astroglial network.

A fascinating thought is, that metabolic processes represent the core of cellular function and, therefore, the uninterrupted supply of metabolites may be ensured via redundant pathways. In case of the brain, this redundancy possibly developed in form of gap junction coupling in addition to vascular connection of every single astrocyte. Therefore, an alternative route of metabolite distribution is available in case of an interrupted vascular connection.

To summarize, we demonstrate the importance of the astroglial network for normal neuronal activity and cognitive functions in the adult brain. This mouse model represents and interesting tool for further investigation regarding lactate distribution via the network, contribution to the general excitation/inhibition balance in the brain or possible astrocyte-microglia interactions. Furthermore, the finding that vascular connection is a universal feature of astrocytes opens an array of new questions, some of which may be answered by means of the inducible Cx cKO mouse.

# Concluding Remarks

# 8

This thesis adds to the basic understanding of a fundamental regulatory mechanism in the neuronal metabolic equilibrium. By identifying the $Na^+$ pump as the principal regulator for ATP production in mitochondria we challenge the classical view on energy regulation. The stability of the ATP:ADP pool during physiological activity is a remarkable finding. Nevertheless, ATP depletion is reported during very high frequency stimulation, such as seizure-like activity or NMDA application (Rueda *et al.*, 2015; Toloe *et al.*, 2014; Lange *et al.*, 2015). However, it remains to be clarified if these ATP depletions occur under physiological conditions, or if they represent a pathological hallmark. Further, the exact mechanism by which the $Na^+$ pump interacts with mitochondrial ATP production and release remains to be illuminated.

Next, we provide evidence for an activity-dependent, neuron-directed lactate release by astrocytes, that, in the case of arousal, is partly dependent on β-adrenergic signaling and glycogen stores. Importantly, these experiments were conducted in awake mice, excluding possible confounding effects of anaesthesia. Lactate is not only a metabolite, but can also act as a signaling molecule (Magistretti and Allaman, 2018). How and to which extend lactate modulates brain state-dependent sensory processing is still to be investigated. Further studies on mice with impaired lactate release mechanisms in astrocytes will provide some knowledge on the importance of a quick astrocytic lactate release for network activity during arousal.

Finally, by disrupting the GJ coupled network in the adult mouse brain, we demonstrate that an intact glial network is crucial for normal information processing and cognitive behaviour. Further studies, using genetically-encoded calcium and metabolite sensors *in vivo* will allow to investigate the role of the glial syncytium in metabolic distribution and network synchronicity in brain-state-dependent paradigms. Especially in light of the presented preliminary results, suggesting a vascular connection of all astrocytes, these future experiments will be of value to better understand metabolic distribution in the brain.

To summarise, the studies presented new discoveries and tools that open the eye for new concepts and pave the way for further scientific breakthroughs.

# Limitations

# 9

## 9.1 Limitations of Cell Culture in the Context of Article 1

Conducting cell culture experiments has advantages compared to *in vivo* studies, some of which are: (1) calibration of genetically-encoded sensors, therefore, allowing the comparison between different cell types; (2) application of pharmacological compounds to study fluxes.

Article 1 took advantage of these benefits to quantitatively analyze ATP, glucose and pyruvate consumption with a transport-stop protocol. However, some of the experiments require the removal of extracellular glucose and/or lactate to quantify the consumption of a metabolite. This interferes with the physiological "environment" of the cell and might trigger a nonphysiological response. Expressing metabolite sensors of interest directly in mitochondria may facilitate quantification of metabolite consumption without recquiring major perturbations of the extracellular milieu.

Another disadvantage of cell culture is the lack of a "brain environment". Compared to *in vivo* conditions, cells in culture are more distant to each other. Therefore, micro-environments with local fluctuations of ions, signaling molecules and metabolites do not exist *in vitro*. These molecules, as soon as released by the cell, would immediately dilute in the cell culture medium and remain unseen by neighbouring cells (F. Barros, personal communication). To study astrocyte-neuron interaction this might be a suboptimal scenario, as astrocytes and neurons might not establish the proximity needed for interaction *in vitro*. Therefore, *in vivo* verification of concepts established in cell culture must be the next step.

## 9.2 Limitations of Genetically-Encoded Sensors in the Context of Article 2

In article 2 we circumvent the lack of a "brain environment" by conducting the experiements *in vivo* in awake mice. Therefore, any confounding effects of anaesthesia are omitted. By using two-photon laser scanning microscopy we achieve high-resolution imaging of neurons and astrocytes in the somatosensory cortex layer 2/3. However, a disadvantage of using genetically-encoded sensors *in vivo* is a lack of accurate calibration. Therefore, instead of reporting absolute metabolite concentrations, we can only measure relative changes (San Martin *et al.*, 2013; Bittner *et al.*, 2011). Fluorescence-lifetime imaging microscopy (FLIM) was introduced as a method that allows for absolut concentration measurements with some of the current sensors at hand (Becker, 2012). Instead of measuring the fluorescence intensity of the sensor, FLIM measures the fluorescence lifetime, which is dependent on the concentration of the target molecule or ion. The quantitative measurements of metabolites, ions and signaling molecules in astrocytes and neurons *in vivo* is an important advance towards resolving the extent of neuron-astrocyte interaction.

# References

A

Abbott N. J., L. Rönnbäck, and E. Hansson (2006). „Astrocyte–endothelial interactions at the blood–brain barrier“. In: *Nature Reviews Neuroscience* 7.1, pp. 41–53.

Achanta L. B., B. D. Rowlands, D. S. Thomas, G. D. Housley, and C. D. Rae (2017). „$\beta$-Hydroxybutyrate Boosts Mitochondrial and Neuronal Metabolism but is not Preferred Over Glucose Under Activated Conditions“. In: *Neurochemical Research* 42.6, pp. 1710–1723.

Adamsky A., A. Kol, T. Kreisel, *et al.* (2018). „Astrocytic Activation Generates De Novo Neuronal Potentiation and Memory Enhancement“. In: *Cell* 174.1, pp. 1–13.

Alberini C. M., E. Cruz, G. Descalzi, B. Bessières, and V. Gao (2018). „Astrocyte glycogen and lactate: New insights into learning and memory mechanisms“. In: *Glia* 66.6, pp. 1244–1262.

Allen N. J. and B. A. Barres (2005). „Signaling between glia and neurons: focus on synaptic plasticity“. In: *Current Opinion in Neurobiology* 15.5, pp. 542–548.

Allen N. J. and B. a. Barres (2009). „Neuroscience: Glia - more than just brain glue.“ In: *Nature* 457.February, pp. 675–7.

Alpers B. J., R. G. Berry, and R. M. Paddison (1959). „Anatomical Studies of the Circle of Willis in Normal Brain“. In: *Archives of Neurology And Psychiatry* 81.4, p. 409.

Amédée T., A. Robert, and J. A. Coles (1997). „Potassium homeostasis and glial energy metabolism.“ In: *Glia* 21.1, pp. 46–55.

Andriezen W. L. (1893). „The Neuroglia Elements in the Human Brain“. In: *BMJ* 2.1700, pp. 227–230.

Araque A., G. Carmignoto, P. G. Haydon, S. H. Oliet, R. Robitaille, and A. Volterra (2014). „Gliotransmitters Travel in Time and Space“. In: *Neuron* 81.4, pp. 728–739.

Araque A., V. Parpura, R. P. Sanzgiri, and P. G. Haydon (1999). „Tripartite synapses: glia, the unacknowledged partner“. In: *Trends in Neurosciences* 22.5, pp. 208–215.

Arcuino G., J. H.-C. Lin, T. Takano, C. Liu, L. Jiang, Q. Gao, J. Kang, and M. Nedergaard (2002). „Intercellular calcium signaling mediated by point-source burst release of ATP.“ In: *Proceedings of the National Academy of Sciences of the United States of America* 99.15, pp. 9840–5.

Ashrafi G., Z. Wu, R. J. Farrell, and T. A. Ryan (2017). „GLUT4 Mobilization Supports Energetic Demands of Active Synapses“. In: *Neuron* 93.3, 606–615.e3.

Attwell D., A. M. Buchan, S. Charpak, M. Lauritzen, B. A. Macvicar, and E. A. Newman (2010). „Glial and neuronal control of brain blood flow.“ In: *Nature* 468.7321, pp. 232–43.

Attwell D. and S. B. Laughlin (2001). „An Energy Budget for Signaling in the Grey Matter of the Brain“. In: *Journal of Cerebral Blood Flow & Metabolism* 21.10, pp. 1133–1145.

Azevedo F. A., L. R. Carvalho, L. T. Grinberg, J. M. Farfel, R. E. Ferretti, R. E. Leite, W. J. Filho, R. Lent, and S. Herculano-Houzel (2009). „Equal numbers of neuronal and nonneuronal cells make the human brain an isometrically scaled-up primate brain“. In: *The Journal of Comparative Neurology* 513.5, pp. 532–541.

Baeza-Lehnert F., A. S. Saab, R. Gutiérrez, *et al.* (2019). „Non-Canonical Control of Neuronal

Energy Status by the Na+ Pump.“ In: *Cell metabolism* 29.3, 668–680.e4.

Baik S. H., S. Kang, W. Lee, H. Choi, S. Chung, J. I. Kim, and I. Mook-Jung (2019). „A Breakdown in Metabolic Reprogramming Causes Microglia Dysfunction in Alzheimer’s Disease“. In: *Cell Metabolism* 30.3, 493–507.e6.

Bak L. K. and A. B. Walls (2018). „CrossTalk opposing view: lack of evidence supporting an astrocyte-to-neuron lactate shuttle coupling neuronal activity to glucose utilisation in the brain“. In: *Journal of Physiology* 596.3, pp. 351–353.

Bak L. K., A. Schousboe, and H. S. Waagepetersen (2006). „The glutamate/GABA-glutamine cycle: aspects of transport, neurotransmitter homeostasis and ammonia transfer.“ In: *Journal of neurochemistry* 98.3, pp. 641–53.

Barros L. F., A. Brown, and R. A. Swanson (2018). „Glia in brain energy metabolism: A perspective“. In: *Glia* 66.6, pp. 1134–1137.

Bartheld C. S. von, J. Bahney, and S. Herculano-Houzel (2016). „The search for true numbers of neurons and glial cells in the human brain: A review of 150 years of cell counting“. In: *Journal of Comparative Neurology* 524.18, pp. 3865–3895.

Bear M. F., B. Connors, and M. Paradiso (2007). *Neuroscience: Exploring the brain. 2007*. Vol. Third Edit.

Becker W. (2012). „Fluorescence lifetime imaging - techniques and applications“. In: *Journal of Microscopy* 247.2, pp. 119–136.

Behre J., T. Wilhelm, A. von Kamp, E. Ruppin, and S. Schuster (2008). „Structural robustness of metabolic networks with respect to multiple knockouts“. In: *Journal of Theoretical Biology* 252.3, pp. 433–441.

Bélanger M., I. Allaman, and P. J. Magistretti (2011). „Brain energy metabolism: focus on astrocyte-neuron metabolic cooperation.“ In: *Cell metabolism* 14.6, pp. 724–38.

Berg J., J. Tymoczko, and L. Stryer (2002). *Biochemistry*. 5th. New York: W.H. Freeman and Co.

Bergmann K. (1857). „Notiz über einige Strukturverhältnisse des Cerebellums und Rükenmarks“. In: *Z Med* 8, pp. 360–363.

Bernardinelli Y., P. J. Magistretti, and J.-Y. Chatton (2004). „Astrocytes generate Na+-mediated metabolic waves“. In: *Proceedings of the National Academy of Sciences* 101.41, pp. 14937–14942.

Berridge C. and S. Foote (1991). „Effects of locus coeruleus activation on electroencephalographic activity in neocortex and hippocampus“. In: *The Journal of Neuroscience* 11.10, pp. 3135–3145.

Berthet C., X. Castillo, P. J. Magistretti, and L. Hirt (2012). „New Evidence of Neuroprotection by Lactate after Transient Focal Cerebral Ischaemia: Extended Benefit after Intracerebroventricular Injection and Efficacy of Intravenous Administration“. In: *Cerebrovascular Diseases* 34.5-6, pp. 329–335.

Berthet C., H. Lei, J. Thevenet, R. Gruetter, P. J. Magistretti, and L. Hirt (2009). „Neuroprotective Role of Lactate after Cerebral Ischemia“. In: *Journal of Cerebral Blood Flow & Metabolism* 29.11, pp. 1780–1789.

Bevan S. and M. Raff (1985). „Voltage-dependent potassium currents in cultured astrocytes“. In: *Nature* 315.6016, pp. 229–232.

Bezzi P. and A. Volterra (2001). „A neuron–glia signalling network in the active brain“. In: *Current Opinion in Neurobiology* 11.3, pp. 387–394.

Bittner C. X., R. Valdebenito, I. Ruminot, *et al.* (2011). „Fast and Reversible Stimulation of Astrocytic Glycolysis by K+ and a Delayed and Persistent Effect of Glutamate“. In: *Journal of Neuroscience* 31.12, pp. 4709–4713.

Boddum K., T. P. Jensen, V. Magloire, U. Kristiansen, D. A. Rusakov, I. Pavlov, and M. C. Walker (2016). „Astrocytic GABA transporter activity modulates excitatory neurotransmission“. In: *Nature Communications* 7.1, p. 13572.

Bolaños J. P. and J. M. Medina (1996). „Induction of nitric oxide synthase inhibits gap junction permeability in cultured rat astrocytes.“ In: *Journal of neurochemistry* 66.5, pp. 2091–9.

Bosco D., J.-A. Haefliger, and P. Meda (2011). „Connexins: key mediators of endocrine function“. In: *Physiological reviews* 91.4, pp. 1393–1445.

Bowman C. L. and H. K. Kimelberg (1984). „Excitatory amino acids directly depolarize rat brain astrocytes in primary culture“. In: *Nature* 311.5987, pp. 656–659.

Brand M. D. and D. G. Nicholls (2011). „Assessing mitochondrial dysfunction in cells“. In: *Biochemical Journal* 435.2, pp. 297–312.

Breithausen B., S. Kautzmann, A. Boehlen, C. Steinhäuser, and C. Henneberger (2020). „Limited contribution of astroglial gap junction coupling to buffering of extracellular K+ in CA1 stratum radiatum“. In: *Glia* 68.5, pp. 918–931.

Brightman M. W. (1969). „Junctions between intimately apposed cell membranes in the vertebrate brain“. In: *The Journal of Cell Biology* 40.3, pp. 648–677.

Brown A. M. and B. R. Ransom (2007). „Astrocyte glycogen and brain energy metabolism.“ In: *Glia* 55.12, pp. 1263–71.

Buck C. R., M. J. Jurynec, D. K. Gupta, A. K. Law, J. Bilger, D. C. Wallace, and R. J. McKeon (2003). „Increased adenine nucleotide translocator 1 in reactive astrocytes facilitates glutamate transport“. In: *Experimental Neurology* 181.2, pp. 149–158.

Bushong E. A., M. E. Martone, Y. Z. Jones, and M. H. Ellisman (2002). „Protoplasmic Astrocytes in CA1 Stratum Radiatum Occupy Separate Anatomical Domains“. In: *Journal of Neuroscience* 22.1, pp. 183–192.

Chai H., B. Diaz-Castro, E. Shigetomi, *et al.* (2017). „Neural Circuit-Specialized Astrocytes: Transcriptomic, Proteomic, Morphological, and Functional Evidence“. In: *Neuron* 95.3, 531–549.e9.

Chance B. and G. R. Williams (1955). „Respiratory enzymes in oxidative phosphorylation. III. The steady state.“ In: *The Journal of biological chemistry* 217.1, pp. 409–27.

Chen T.-W., T. J. Wardill, Y. Sun, *et al.* (2013). „Ultrasensitive fluorescent proteins for imaging neuronal activity“. In: *Nature* 499.7458, pp. 295–300.

Chever O., E. Dossi, U. Pannasch, M. Derangeon, and N. Rouach (2016). „Astroglial networks promote neuronal coordination“. In: *Science signaling* 9.410, ra6.

Chever O., U. Pannasch, P. Ezan, and N. Rouach (2014). „Astroglial connexin 43 sustains glutamatergic synaptic efficacy.“ In: *Philosophical transactions of the Royal Society of London. Series B, Biological sciences* 369.1654, p. 20130596.

Chouhan A. K., M. V. Ivannikov, Z. Lu, M. Sugimori, R. R. Llinas, and G. T. Macleod (2012). „Cytosolic Calcium Coordinates Mitochondrial Energy Metabolism with Presynaptic Activity“. In: *Journal of Neuroscience* 32.4, pp. 1233–1243.

Cina C., K. Maass, M. Theis, K. Willecke, J. F. Bechberger, and C. C. Naus (2009). „Involvement of the cytoplasmic c-terminal domain of connexin43 in neuronal migration“. In: *Journal of Neuroscience* 29.7, pp. 2009–2021.

Clarke L. E., S. A. Liddelow, C. Chakraborty, A. E. Münch, M. Heiman, and B. A. Barres (2018). „Normal aging induces A1-like astrocyte reactivity“. In:

Clasadonte J., E. Scemes, Z. Wang, D. Boison, and P. G. Haydon (2017). „Connexin 43-Mediated Astroglial Metabolic Networks Contribute to the Regulation of the Sleep-Wake Cycle“. In: *Neuron* 95.6, 1365–1380.e5.

Claus L., C. Philippot, S. Griemsmann, A. Timmermann, R. Jabs, C. Henneberger, H. Kettenmann, and C. Steinhäuser (2018). „Barreloid Borders and Neuronal Activity Shape Panglial Gap Junction-Coupled Networks in the Mouse Thalamus“. In: *Cerebral cortex (New York, N.Y. : 1991)* 28.1, pp. 213–222.

Cornell-Bell A. and S. Finkbeiner (1991). „Ca2+ waves in astrocytes“. In: *Cell Calcium* 12.2-3, pp. 185–204.

Danbolt N. C., D. N. Furness, and Y. Zhou (2016). „Neuronal vs glial glutamate uptake: Resolving the conundrum.“ In: *Neurochemistry international* 98, pp. 29–45.

Denton R. M. (2009). „Regulation of mitochondrial dehydrogenases by calcium ions“. In: *Biochimica et Biophysica Acta (BBA) - Bioenergetics* 1787.11, pp. 1309–1316.

Denton R. M., T. J. Pullen, C. T. Armstrong, K. J. Heesom, and G. A. Rutter (2016). „Calcium-insensitive splice variants of mammalian E1 subunit of 2-oxoglutarate dehydrogenase complex with tissue-specific patterns of expression“. In: *Biochemical Journal* 473.9, pp. 1165–1178.

Descalzi G., V. Gao, M. Q. Steinman, A. Suzuki, and C. M. Alberini (2019). „Lactate from astrocytes fuels learning-induced mRNA translation in excitatory and inhibitory neurons“. In: *Communications Biology* 2.1, p. 247.

Diaz-Garcia C. M., R. Mongeon, C. Lahmann, D. Koveal, H. Zucker, and G. Yellen (2017). „Neuronal Stimulation Triggers Neuronal Glycolysis and Not Lactate Uptake“. eng. In: *Cell Metab* 26.2, 361–374 e4.

Dienel G. A. (2017). „Lack of appropriate stoichiometry: Strong evidence against an energetically important astrocyte-neuron lactate shuttle in brain“. In: *Journal of Neuroscience Research* 00.September 2016.

Dienel G. A. and N. F. Cruz (2016). „Aerobic glycolysis during brain activation: adrenergic regulation and influence of norepinephrine on astrocytic metabolism“. In: *Journal of Neurochemistry* 138.1, pp. 14–52.

Ding F., J. O’Donnell, A. S. Thrane, D. Zeppenfeld, H. Kang, L. Xie, F. Wang, and M. Nedergaard (2013). „$\alpha$1-Adrenergic receptors mediate coordinated Ca2+ signaling of cortical astrocytes in awake, behaving mice“. In: *Cell Calcium* 54.6, pp. 387–394.

Do K. Q., B. Benz, O. Sorg, L. Pellerin, and P. J. Magistretti (1997). „$\beta$-Adrenergic Stimulation Promotes Homocysteic Acid Release from Astrocyte Cultures: Evidence for a Role of Astrocytes in the Modulation of Synaptic Transmission“. In: *Journal of Neurochemistry* 68.6, pp. 2386–2394.

Dringen R., R. Gebhardt, and B. Hamprecht (1993). „Glycogen in astrocytes: possible function as lactate supply for neighboring cells“. In: *Brain Research* 623.2, pp. 208–214.

Duchen M. R. (1992). „Ca2+-dependent changes in the mitochondrial energetics in single dissociated mouse sensory neurons“. In: *Biochemical Journal* 283.1, pp. 41–50.

Duchen M., A. Verkhratsky, and S. Muallem (2008). „Mitochondria and calcium in health and disease“. In: *Cell Calcium* 44.1, pp. 1–5.

Duran J., I. Saez, A. Gruart, J. J. Guinovart, J. M. Delgado-Garcia, and J. M. Delgado-García (2013). „Impairment in long-term memory formation and learning-dependent synaptic plasticity in mice lacking glycogen synthase in the brain.“ In: *Journal of cerebral blood flow and metabolism : official journal of the International Society of Cerebral Blood Flow and Metabolism* 33.4, pp. 550–6.

Egawa K., J. Yamada, T. Furukawa, Y. Yanagawa, and A. Fukuda (2013). „Cl homeodynamics in gap junction-coupled astrocytic networks on activation of GABAergic synapses“. In: *The Journal of Physiology* 591.16, pp. 3901–3917.

Eilam R., R. Aharoni, R. Arnon, and R. Malach (2016). „Astrocyte morphology is confined by cortical functional boundaries in mammals ranging from mice to human“. In: *eLife* 5.JUN2016, pp. 1–18.

Elias L. A. B., D. D. Wang, and A. R. Kriegstein (2007). „Gap junction adhesion is necessary for radial migration in the neocortex.“ In: *Nature* 448.7156, pp. 901–7.

Emsley J. G. and J. D. Macklis (2006). „Astroglial heterogeneity closely reflects the neuronal-defined anatomy of the adult murine CNS“. In: *Neuron Glia Biology* 2.3, pp. 175–186.

Eroglu C. and B. A. Barres (2010). „Regulation of synaptic connectivity by glia“. In: *Nature* 468.7321, pp. 223–231.

Farina C., F. Aloisi, and E. Meinl (2007). „Astrocytes are active players in cerebral innate immunity“. In: *Trends in Immunology* 28.3, pp. 138–145.

Farmer W. T., T. Abrahamsson, S. Chierzi, *et al.* (2016). „Neurons diversify astrocytes in the adult brain through sonic hedgehog signaling.“ In: *Science (New York, N.Y.)* 351.6275, pp. 849–54. arXiv: `arXiv:1011.1669v3`.

Fasciani I., P. Pluta, D. González-Nieto, P. Martínez-Montero, J. Molano, C. L. Paíno, O. Millet, and L. C. Barrio (2018). „Directional coupling of oligodendrocyte connexin-47 and astrocyte connexin-43 gap junctions“. In: *Glia* 66.11, pp. 2340–2352.

Fernández-Moncada I. and L. F. Barros (2014). „Non-preferential fuelling of the Na+ /K+ - ATPase pump“. In: *Biochemical Journal* 460.3, pp. 353–361.

Fünfschilling U., L. M. L. Supplie, D. Mahad, *et al.* (2012). „Glycolytic oligodendrocytes maintain myelin and long-term axonal integrity.“ In: *Nature* 485.7399, pp. 0–5.

Gao V., A. Suzuki, P. J. Magistretti, S. Lengacher, G. Pollonini, M. Q. Steinman, and C. M. Alberini (2016). „Astrocytic $\beta$ 2 -adrenergic receptors mediate hippocampal long-term memory consolidation“. In: *Proceedings of the National Academy of Sciences* 113.30, pp. 8526–8531.

Gellerich F. N., Z. Gizatullina, O. Arandarcikaite, D. Jerzembek, S. Vielhaber, E. Seppet, and F. Striggow (2009). „Extramitochondrial Ca2+ in the Nanomolar Range Regulates Glutamate-Dependent Oxidative Phosphorylation on Demand“. In: *PLoS ONE* 4.12. Ed. by Cookson M. R., e8181.

Gellerich F. N., Z. Gizatullina, T. Gainutdinov, K. Muth, E. Seppet, Z. Orynbayeva, and S. Vielhaber (2013). „The control of brain mitochondrial energization by cytosolic calcium: The mitochondrial gas pedal“. In: *IUBMB Life* 65.3, pp. 180–190.

Genda E. N., J. G. Jackson, A. L. Sheldon, *et al.* (2011). „Co-compartmentalization of the astroglial glutamate transporter, GLT-1, with glycolytic enzymes and mitochondria“. In: *Journal of Neuroscience* 31.50, pp. 18275–18288.

Ghézali G., C.-F. Calvo, L.-E. Pillet, F. Llense, P. Ezan, U. Pannasch, A.-P. Bemelmans, S. E. Manneville, and N. Rouach (2018). „Connexin 30 controls astroglial polarization during postnatal brain development“. In: *Development* 145.4, dev155275. arXiv: `arXiv:1011.1669v3`.

Giaume C., A. Koulakoff, L. Roux, D. Holcman, and N. Rouach (2010). „Astroglial networks: a step further in neuroglial and gliovascular interactions.“ In: *Nature reviews. Neuroscience* 11.fEbRuARy, pp. 87–99.

Giaume C., L. Leybaert, C. C. Naus, J. C. Sáez, C. C. Naus, and J. C. Sáez (2013). „Connexin and pannexin hemichannels in brain glial cells: Properties, pharmacology, and roles“. In: *Frontiers in pharmacology* 4, p. 88.

Giaume C. and X. Liu (2012). „From a glial syncytium to a more restricted and specific glial networking“. In: *Journal of Physiology-Paris* 106.1-2, pp. 34–39.

Gibbs M. E., D. G. Anderson, and L. Hertz (2006). „Inhibition of Glycogenolysis in Astrocytes Interrupts Memory Consolidation in Young Chickens“. In: *Glia* 54, pp. 214–222.

Glancy B. and R. S. Balaban (2012). „Role of mitochondrial Ca 2+ in the regulation of cellular energetics“. In: *Biochemistry* 51.14, pp. 2959–2973.

Golgi C. (1870). „Sulla sostanza connettiva del cervello (nevroglia)“. In: *Rendiconti del R Instituto Lombardo di Scienze e Lettere* 3, pp. 275–277.

Golgi C. (1872). „Contribuzione alla fina Anatomia degli organi centrali del sistema nervosos“. In: *Rivista Clinica di Bologna* 2, pp. 38–46.

Gordon G. R. J., H. B. Choi, R. L. Rungta, G. C. R. Ellis-Davies, and B. A. MacVicar (2008). „Brain metabolism dictates the polarity of astrocyte control over arterioles.“ In: *Nature* 456.7223, pp. 745–9.

Griemsmann S., S. P. Höft, P. Bedner, *et al.* (2015). „Characterization of panglial gap junction networks in the thalamus, neocortex, and hippocampus reveals a unique population of glial cells“. In: *Cerebral Cortex* 25.10, pp. 3420–3433.

Grosche A., J. Grosche, M. Tackenberg, *et al.* (2013). „Versatile and Simple Approach to Determine Astrocyte Territories in Mouse Neocortex and Hippocampus“. In: *PLoS ONE* 8.7.

Halassa M. M., T. Fellin, and P. G. Haydon (2007a). „The tripartite synapse: roles for gliotransmission in health and disease“. In: *Trends in Molecular Medicine* 13.2, pp. 54–63.

Halassa M. M., T. Fellin, H. Takano, J.-H. Dong, and P. G. Haydon (2007b). „Synaptic islands defined by the territory of a single astrocyte.“ In: *The Journal of neuroscience : the official journal of the Society for Neuroscience* 27.24, pp. 6473–7.

Harris J. J., R. Jolivet, and D. Attwell (2012). „Synaptic Energy Use and Supply“. In: *Neuron* 75.5, pp. 762–777.

Harrison R., B. Papp, C. Pál, S. G. Oliver, and D. Delneri (2007). „Plasticity of genetic interactions in metabolic networks of yeast.“ In: *Proceedings of the National Academy of Sciences of the United States of America* 104.7, pp. 2307–12.

Hartman J. L., B. Garvik, and L. Hartwell (2001). „Cell Biology: Principles for the buffering of genetic variation“. In: *Science* 291.5506, pp. 1001–1004.

Hasel P., O. Dando, Z. Jiwaji, *et al.* (2017). „Neurons and neuronal activity control gene expression in astrocytes to regulate their development and metabolism“. In: *Nature Communications* May.

Henle J. and F. Merkel (1869). „Über die sogenannte Bindesubstanz der Centralorgane des Nervensystems“. In: *Z Med* 34, pp. 49–82.

Hertz L. (1965). „Possible Role of Neuroglia: A Potassium-Mediated Neuronal – Neuroglial – Neuronal Impulse Transmission System“. In: *Nature* 206.4989, pp. 1091–1094.

Hertz L. and Y. Chen (2018). „Glycogenolysis, an Astrocyte-Specific Reaction, is Essential for Both Astrocytic and Neuronal Activities Involved in Learning“. In: *Neuroscience* 370, pp. 27–36.

Hild W. and I. Tasaki (1962). „Morphological and physiological properties of neurons and glial cells in tissue culture.“ In: *Journal of Neurophysiology* 25, pp. 277–304.

Hilgetag C. C. and H. Barbas (2009). „Are there ten times more glia than neurons in the brain?“ In: *Brain Structure and Function* 213.4-5, pp. 365–366.

Houades V., A. Koulakoff, P. Ezan, I. Seif, and C. Giaume (2008). „Gap junction-mediated astrocytic networks in the mouse barrel cortex.“ In: *The Journal of neuroscience : the official journal of the Society for Neuroscience* 28.20, pp. 5207–17.

Hu X., Y. Yuan, D. Wang, and Z. Su (2016). „Heterogeneous astrocytes: Active players in CNS“. In: *Brain Research Bulletin* 125, pp. 1–18.

Hydén H. (1962). „The neuron and its glia-a biochemical and functional unit.“ In: *Endeavour* 21, pp. 144–55.

Hydén H. and E. Egyházi (1963). „Glial RNA changes during a learning experiment in rats“. In: *Proceedings of the National Academy of Sciences of the United States of America* 49.5, pp. 618–24.

Iglesias R., G. Dahl, F. Qiu, D. C. Spray, and E. Scemes (2009). „Pannexin 1: The Molecular Substrate of Astrocyte "Hemichannels"“.

In: *Journal of Neuroscience* 29.21, pp. 7092–7097.

Imamura H., K. P. Huynh, H. Togawa, K. Saito, R. Iino, and Y. Kato-yamada (2009). „Visualization of ATP levels inside single living cells with fluorescence resonance energy transfer-based“. In: 106.37, pp. 15651–15656.

Jang S., J. C. Nelson, E. G. Bend, L. Rodríguez-Laureano, F. G. Tueros, L. Cartagenova, K. Underwood, E. M. Jorgensen, and D. A. Colón-Ramos (2016). „Glycolytic Enzymes Localize to Synapses under Energy Stress to Support Synaptic Function“. In: *Neuron* 90.2, pp. 278–291.

Jimenez-Blasco D., A. Busquets-Garcia, E. Hebert-Chatelain, *et al.* (2020). „Glucose metabolism links astroglial mitochondria to cannabinoid effects“. In: *Nature* March 2018.

Karpuk N., M. Burkovetskaya, T. Fritz, A. Angle, and T. Kielian (2011). „Neuroinflammation leads to region-dependent alterations in astrocyte gap junction communication and hemichannel activity“. In: *Journal of Neuroscience* 31.2, pp. 414–425.

Katz M. J., R. J. Lasek, and J. Silver (1983). „Ontophyletics of the nervous system: development of the corpus callosum and evolution of axon tracts.“ In: *Proceedings of the National Academy of Sciences of the United States of America* 80.19, pp. 5936–40.

Kawauchi T., K. Sekine, M. Shikanai, K. Chihama, K. Tomita, K.-i. Kubo, K. Nakajima, Y.-i. Nabeshima, and M. Hoshino (2010). „Rab GTPases-Dependent Endocytic Pathways Regulate Neuronal Migration and Maturation through N-Cadherin Trafficking“. In: *Neuron* 67.4, pp. 588–602.

Keaney J. and M. Campbell (2015). „The dynamic blood-brain barrier“. In: *FEBS Journal* 282.21, pp. 4067–4079.

Kettenmann H., K. Backus, and M. Schachner (1984). „Aspartate, glutamate and $\gamma$-aminobutyric acid depolarize cultured astrocytes“. In: *Neuroscience Letters* 52.1-2, pp. 25–29.

Kety S. S. (1957). „The general metabolism of the brain in vivo“. In: *Metabolism of the Nervous System*. Elsevier, pp. 221–237.

Khakh B. S. and B. Deneen (2019). „The Emerging Nature of Astrocyte Diversity“. In: *Annual Review of Neuroscience* 42.1, pp. 187–207.

Kofuji P. and E. Newman (2004). „Potassium buffering in the central nervous system“. In: *Neuroscience* 129.4, pp. 1043–1054.

Koizumi S. (2010). „Synchronization of Ca2+ oscillations: involvement of ATP release in astrocytes“. In: *FEBS Journal* 277.2, pp. 286–292.

Kristian Enkvist M. O. and K. D. McCarthy (2002). „Astroglial Gap Junction Communication Is Increased by Treatment with Either Glutamate or High K+ Concentration“. In: *Journal of Neurochemistry* 62.2, pp. 489–495.

Kuffler S. W. and D. D. Potter (1964). „Glia in the leech central nervous system: physiological properties and neuron-glia relationship“. In: *Journal of neurophysiology* 27, pp. 290–320.

Kunze A., M. R. Congreso, C. Hartmann, *et al.* (2009). „Connexin expression by radial glia-like cells is required for neurogenesis in the adult dentate gyrus.“ In: *Proceedings of the National Academy of Sciences of the United States of America* 106.27, pp. 11336–41.

Lagos-Cabré R., F. Burgos-Bravo, A. M. Avalos, and L. Leyton (2019). „Connexins in Astrocyte Migration.“ In: *Frontiers in pharmacology* 10, p. 1546.

Lalo U., S. Rasooli-Nejad, and Y. Pankratov (2014). „Exocytosis of gliotransmitters from cortical astrocytes: implications for synaptic plasticity and aging“. In: *Biochemical Society Transactions* 42.5, pp. 1275–1281.

Lampe P. D. and A. F. Lau (2000). „Regulation of gap junctions by phosphorylation of connexins“. In: *Archives of Biochemistry and Biophysics* 384.2, pp. 205–215.

Lange S. C., U. Winkler, L. Andresen, M. Byhrø, H. S. Waagepetersen, J. Hirrlinger, and L. K. Bak (2015). „Dynamic Changes in Cytosolic

ATP Levels in Cultured Glutamatergic Neurons During NMDA-Induced Synaptic Activity Supported by Glucose or Lactate“. In: *Neurochemical Research* 40.12, pp. 2517–2526.

Lanjakornsiripan D., B. J. Pior, D. Kawaguchi, S. Furutachi, T. Tahara, Y. Katsuyama, Y. Suzuki, Y. Fukazawa, and Y. Gotoh (2018). „Layer-specific morphological and molecular differences in neocortical astrocytes and their dependence on neuronal layers“. In: *Nature Communications* 9.1.

Lee S., B.-E. Yoon, K. Berglund, S.-J. Oh, H. Park, H.-S. Shin, G. J. Augustine, and C. J. Lee (2010). „Channel-mediated tonic GABA release from glia.“ In: *Science (New York, N.Y.)* 330.6005, pp. 790–6.

Lee Y., B. M. Morrison, Y. Li, *et al.* (2012). „Oligodendroglia metabolically support axons and contribute to neurodegeneration.“ In: *Nature* 487.7408, pp. 443–8.

Lenhossék M. von (1893). „Der feinere Bau des Nervensystems im Lichte neuester Forschung“. In: *Fisher’s Medicinische Buchhandlung H. Kornfield*.

Li N., B. J. Hansen, T. A. Csepe, *et al.* (2017). „Redundant and diverse intranodal pacemakers and conduction pathways protect the human sinoatrial node from failure“. In: *Science Translational Medicine* 9.400.

Lia A., M. Zonta, L. M. Requie, and G. Carmignoto (2019). „Dynamic interactions between GABAergic and astrocytic networks“. In: *Neuroscience Letters* 689.February 2018, pp. 14–20.

Liddelow S. A., K. A. Guttenplan, L. E. Clarke, *et al.* (2017). „Neurotoxic reactive astrocytes are induced by activated microglia.“ In: *Nature* 541.7638, pp. 481–487.

Lin C.-C. J., K. Yu, A. Hatcher, *et al.* (2017). „Identification of diverse astrocyte populations and their malignant analogs“. In: *Nature Neuroscience* 20.3.

Lutz S. E., Y. Zhao, M. Gulinello, S. C. Lee, C. S. Raine, and C. F. Brosnan (2009). „Deletion of astrocyte connexins 43 and 30 leads to a dysmyelinating phenotype and hippocampal CA1 vacuolation.“ In: *The Journal of neuroscience : the official journal of the Society for Neuroscience* 29.24, pp. 7743–52.

Ma B., R. Buckalew, Y. Du, C. M. Kiyoshi, C. C. Alford, W. Wang, D. M. McTigue, J. J. Enyeart, D. Terman, and M. Zhou (2016). „Gap junction coupling confers isopotentiality on astrocyte syncytium“. In: *Glia* 64.2, pp. 214–226.

Mächler P., M. T. Wyss, M. Elsayed, *et al.* (2016). „In Vivo Evidence for a Lactate Gradient from Astrocytes to Neurons“. English. In: *Cell Metabolism* 23.1, pp. 94–102.

Madisen L., A. R. Garner, D. Shimaoka, *et al.* (2015). „Transgenic mice for intersectional targeting of neural sensors and effectors with high specificity and performance.“ In: *Neuron* 85.5, pp. 942–58.

Magistretti P. J. and I. Allaman (2018). „Lactate in the brain: from metabolic end-product to signalling molecule“. eng. In: *Nat Rev Neurosci* 19.4, pp. 235–249.

Magistretti P. J., J. H. Morrison, W. J. Shoemaker, V. Sapin, and F. E. Bloom (1981). „Vasoactive intestinal polypeptide induces glycogenolysis in mouse cortical slices: a possible regulatory mechanism for the local control of energy metabolism.“ In: *Proceedings of the National Academy of Sciences* 78.10, pp. 6535–6539.

Magistretti P. J. (2006). „Neuron-glia metabolic coupling and plasticity.“ In: *The Journal of experimental biology* 209.Pt 12, pp. 2304–11.

Magistretti P. J. and I. Allaman (2015). „A Cellular Perspective on Brain Energy Metabolism and Functional Imaging“. In: *Neuron* 86.4, pp. 883–901.

Maglione M., O. Tress, B. Haas, K. Karram, J. Trotter, K. Willecke, and H. Kettenmann (2010). „Oligodendrocytes in mouse corpus callosum are coupled via gap junction channels formed by Connexin47 and Connexin32“. In: *Glia* 58.9, pp. 1104–1117.

Magnotti L. M., D. A. Goodenough, and D. L. Paul (2011). „Deletion of oligodendrocyte Cx32 and astrocyte Cx43 causes white matter vacuolation, astrocyte loss and early mortality“. In: *Glia* 59.7, pp. 1064–1074.

Markram H., M. Toledo-Rodriguez, Y. Wang, A. Gupta, G. Silberberg, and C. Wu (2004). „Interneurons of the neocortical inhibitory system“. In: *Nature Reviews Neuroscience* 5.10, pp. 793–807. arXiv: `NIHMS150003`.

Martinez F. O. and S. Gordon (2014). „The M1 and M2 paradigm of macrophage activation: time for reassessment“. In: *F1000Prime Reports* 6.

Mason S., A. M. van Furth, L. J. Mienie, U. F. H. Engelke, R. A. Wevers, R. Solomons, and C. J. Reinecke (2015). „A hypothetical astrocyte–microglia lactate shuttle derived from a 1H NMR metabolomics analysis of cerebrospinal fluid from a cohort of South African children with tuberculous meningitis“. In: *Metabolomics* 11.4, pp. 822–837.

Mathiisen T. M., K. P. Lehre, N. C. Danbolt, and O. P. Ottersen (2010). „The perivascular astroglial sheath provides a complete covering of the brain microvessels: An electron microscopic 3D reconstruction“. In: *Glia* 58.9, pp. 1094–1103.

McKenna M. C. (2007). „The glutamate-glutamine cycle is not stoichiometric: fates of glutamate in brain.“ In: *Journal of neuroscience research* 85.15, pp. 3347–58.

Mederos S. and G. Perea (2019). „GABAergic-astrocyte signaling: A refinement of inhibitory brain networks“. In: *Glia* 67.10, glia.23644.

Menichella D. M., D. A. Goodenough, E. Sirkowski, S. S. Scherer, and D. L. Paul (2003). „Connexins are critical for normal myelination in the CNS“. In: *Journal of Neuroscience* 23.13, pp. 5963–5973.

Menichella D. M., M. Majdan, R. Awatramani, D. A. Goodenough, E. Sirkowski, S. S. Scherer, and D. L. Paul (2006). „Genetic and physiological evidence that oligodendrocyte gap junctions contribute to spatial buffering of potassium released during neuronal activity.“ In: *The Journal of neuroscience : the official journal of the Society for Neuroscience* 26.43, pp. 10984–10991.

Meyer N., N. Richter, Z. Fan, G. Siemonsmeier, T. Pivneva, P. Jordan, C. Steinhäuser, M. Semtner, C. Nolte, and H. Kettenmann (2018). „Oligodendrocytes in the Mouse Corpus Callosum Maintain Axonal Function by Delivery of Glucose“. In: *Cell Reports* 22.9, pp. 2383–2394.

Min K.-J. (2006). „Astrocytes Induce Hemeoxygenase-1 Expression in Microglia: A Feasible Mechanism for Preventing Excessive Brain Inflammation“. In: *Journal of Neuroscience* 26.6, pp. 1880–1887.

Min R. and T. Nevian (2012). „Astrocyte signaling controls spike timing–dependent depression at neocortical synapses“. In: *Nature Neuroscience* 15.5, pp. 746–753.

Montagnese C., D. A. Poulain, J.-d. Vincent, and D. T. Theodosis (1988). „Synaptic and neuronal-glial plasticity in the adult oxytocinergic system in response to physiological stimuli“. In: *Brain Research Bulletin* 20.6, pp. 681–692.

Morel L., M. S. R. Chiang, H. Higashimori, T. Shoneye, L. K. Iyer, J. Yelick, A. Tai, and Y. Yang (2017). „Molecular and Functional Properties of Regional Astrocytes in the Adult Brain“. In: *The Journal of Neuroscience* 37.36, pp. 3956–16.

Mugnaini E. (1986). „Cell junctions of astrocytes, ependyma, and related cells in the mammalian central nervous system, with emphasis on the hypothesis of a generalized functional synsytium of supporting cells“. In: *Astrocytes: Development Morphology, and Regional Specialization of Astrocytes*, pp. 329–371.

Murphy-Royal C., A. D. Johnston, A. K. J. Boyce, *et al.* (2020). „Stress gates an astrocytic energy reservoir to impair synaptic plasticity.“ In: *Nature communications* 11.1, p. 2014.

Newman L. A., D. L. Korol, and P. E. Gold (2011). „Lactate Produced by Glycogenolysis in Astrocytes Regulates Memory Processing“. In: *PLoS ONE* 6.12. Ed. by Brann D., e28427.

Nielsen B. S., D. B. Hansen, B. R. Ransom, M. S. Nielsen, and N. MacAulay (2017). „Connexin Hemichannels in Astrocytes: An Assessment of Controversies Regarding Their Functional Characteristics“. In: *Neurochemical Research* 42.9, pp. 2537–2550.

Nishida H. and S. Okabe (2007). „Direct Astrocytic Contacts Regulate Local Maturation of Dendritic Spines“. In: *Journal of Neuroscience* 27.2, pp. 331–340.

Norden D. M., A. M. Fenn, A. Dugan, and J. P. Godbout (2014). „TGF$\beta$ produced by IL-10 redirected astrocytes attenuates microglial activation“. In: *Glia* 62.6, pp. 881–895.

Odermatt B., K. Wellershaus, A. Wallraff, *et al.* (2003). „Connexin 47 (Cx47)-Deficient Mice with Enhanced Green Fluorescent Protein Reporter Gene Reveal Predominant Oligodendrocytic Expression of Cx47 and Display Vacuolized Myelin in the CNS“. In: *The Journal of Neuroscience* 23.11, pp. 4549–4559.

Oe Y., O. Baba, H. Ashida, K. C. Nakamura, and H. Hirase (2016). „Glycogen distribution in the microwave-fixed mouse brain reveals heterogeneous astrocytic patterns.“ In: *Glia*.

Ohkura M., T. Sasaki, C. Kobayashi, *et al.* (2012). „An Improved Genetically Encoded Red Fluorescent Ca2+ Indicator for Detecting Optically Evoked Action Potentials“. In: *PLoS ONE* 7.7. Ed. by Sensi S. L., e39933.

Orellana J. A., P. J. Sáez, K. F. Shoji, K. A. Schalper, N. Palacios–Prado, V. Velarde, C. Giaume, M. V. Bennett, and J. C. Sáez (2009). „Modulation of Brain Hemichannels and Gap Junction Channels by Pro-Inflammatory Agents and Their Possible Role in Neurodegeneration“. In: *Antioxidants & Redox Signaling* 11.2, pp. 369–399.

Otsu Y., K. Couchman, D. G. Lyons, M. Collot, A. Agarwal, J.-M. Mallet, F. W. Pfrieger, D. E. Bergles, and S. Charpak (2014). „Calcium dynamics in astrocyte processes during neurovascular coupling“. In: *Nature Neuroscience* advance on.

Pannasch U., L. Vargova, J. Reingruber, P. Ezan, D. Holcman, C. Giaume, E. Sykova, and N. Rouach (2011). „Astroglial networks scale synaptic activity and plasticity“. In: *Proceedings of the National Academy of Sciences* 108.20, pp. 8467–8472. arXiv: `arXiv:1408.1149`.

Pannasch U., M. Derangeon, O. Chever, and N. Rouach (2012). „Astroglial gap junctions shape neuronal network activity.“ In: *Communicative & integrative biology* 5.3, pp. 248–54.

Pannasch U., D. Freche, G. Dallérac, *et al.* (2014). „Connexin 30 sets synaptic strength by controlling astroglial synapse invasion“. In: *Nature Neuroscience* 17.4, pp. 549–558.

Panov A., Z. Orynbayeva, V. Vavilin, and V. Lyakhovich (2014). „Fatty Acids in Energy Metabolism of the Central Nervous System“. In: *BioMed Research International* 2014, pp. 1–22.

Parri H. R., T. M. Gould, and V. Crunelli (2001). „Spontaneous astrocytic Ca2+ oscillations in situ drive NMDAR-mediated neuronal excitation“. In: *Nature Neuroscience* 4.8, pp. 803–812.

Paukert M., A. Agarwal, J. Cha, V. A. Doze, J. U. Kang, and D. E. Bergles (2014). „Norepinephrine Controls Astroglial Responsiveness to Local Circuit Activity“. In: *Neuron* 82.6, pp. 1263–1270.

Pekny M. and M. Pekna (2014). „Astrocyte Reactivity and Reactive Astrogliosis: Costs and Benefits“. In: *Physiological Reviews* 94.4, pp. 1077–1098.

Pellerin L. and P. J. Magistretti (1994). „Glutamate uptake into astrocytes stimulates aerobic glycolysis: a mechanism coupling neuronal activity to glucose utilization.“ In: *Proceedings of the National Academy of Sciences of the United States of America* 91.22, pp. 10625–9.

Pelvig D., H. Pakkenberg, A. Stark, and B. Pakkenberg (2008). „Neocortical glial cell numbers in human brains“. In: *Neurobiology of Aging* 29.11, pp. 1754–1762.

Perea G., R. Gómez, S. Mederos, *et al.* (2016). „Activity-dependent switch of gabaergic inhibition into glutamatergic excitation in astrocyte-neuron networks“. In: *eLife* 5.DECEMBER2016, pp. 1–26.

Perego C., C. Vanoni, M. Bossi, S. Massari, H. Basudev, R. Longhi, and G. Pietrini (2002). „The GLT-1 and GLAST Glutamate Transporters Are Expressed on Morphologically Distinct Astrocytes and Regulated by Neuronal Activity in Primary Hippocampal Cocultures“. In: *Journal of Neurochemistry* 75.3, pp. 1076–1084.

Pfrieger F. W. (2010). „Role of glial cells in the formation and maintenance of synapses“. In: *Brain Research Reviews* 63.1-2, pp. 39–46.

Pierre K. and L. Pellerin (2005). „Monocarboxylate transporters in the central nervous system: distribution, regulation and function“. In: *Journal of Neurochemistry* 94.1, pp. 1–14.

Rash J. E., T. Yasumura, F. E. Dudek, and J. I. Nagy (2001). „Cell-specific expression of connexins and evidence of restricted gap junctional coupling between glial cells and between neurons.“ In: *The Journal of neuroscience : the official journal of the Society for Neuroscience* 21.6, pp. 1983–2000.

Reimer J., E. Froudarakis, C. R. Cadwell, D. Yatsenko, G. H. Denfield, and A. S. Tolias (2014). „Pupil Fluctuations Track Fast Switching of Cortical States during Quiet Wakefulness“. In: *Neuron* 84.2, pp. 355–362.

Retamal M. A., N. Froger, N. Palacios-Prado, P. Ezan, P. J. Sáez, J. C. Sáez, and C. Giaume (2007). „Cx43 hemichannels and gap junction channels in astrocytes are regulated oppositely by proinflammatory cytokines released from activated microglia“. In: *Journal of Neuroscience* 27.50, pp. 13781–13792.

Risser L., F. Plouraboué, P. Cloetens, and C. Fonta (2009). „A 3D-investigation shows that angiogenesis in primate cerebral cortex mainly occurs at capillary level“. In: *International Journal of Developmental Neuroscience* 27.2, pp. 185–196.

Rose C. R. and C. Karus (2013). „Two sides of the same coin: Sodium homeostasis and signaling in astrocytes under physiological and pathophysiological conditions“. In: *Glia* 61.8, pp. 1191–1205.

Rose E. M., J. C. P. Koo, J. E. Antflick, S. M. Ahmed, S. Angers, and D. R. Hampson (2009). „Glutamate Transporter Coupling to Na,K-ATPase“. In: *Journal of Neuroscience* 29.25, pp. 8143–8155.

Rouach N., A. Koulakoff, V. Abudara, K. Willecke, and C. Giaume (2008). „Astroglial metabolic networks sustain hippocampal synaptic transmission“. In: *Science* 322.5907, pp. 1551–1555.

Roux L., K. Benchenane, J. D. Rothstein, G. Bonvento, and C. Giaume (2011). „Plasticity of astroglial networks in olfactory glomeruli.“ In: *Proceedings of the National Academy of Sciences of the United States of America* 108.45, pp. 18442–6.

Rueda C. B., J. Traba, I. Amigo, I. Llorente-Folch, P. Gonzalez-Sanchez, B. Pardo, J. A. Esteban, A. del Arco, and J. Satrustegui (2015). „Mitochondrial ATP-Mg/Pi Carrier SCaMC-3/Slc25a23 Counteracts PARP-1-Dependent Fall in Mitochondrial ATP Caused by Excitotoxic Insults in Neurons“. In: *Journal of Neuroscience* 35.8, pp. 3566–3581.

Ruminot I., J. Schmälzle, B. Leyton, L. F. Barros, and J. W. Deitmer (2019). „Tight coupling of astrocyte energy metabolism to synaptic activity revealed by genetically encoded FRET nanosensors in hippocampal tissue“. In: *Journal of Cerebral Blood Flow & Metabolism* 39.3, pp. 513–523.

Saab A. S. A., I. I. D. Tzvetanova, and K.-A. A. K.-A. Nave (2013). „The role of myelin and oligodendrocytes in axonal energy metabolism.“ In: *Current opinion in neurobiology* 23.6, pp. 1065–72.

Sada N., S. Lee, T. Katsu, T. Otsuki, and T. Inoue (2015). „Targeting LDH enzymes with a stiripentol analog to treat epilepsy“. In: *Science* 347.6228, pp. 1362–1368.

Sakadžić S., E. T. Mandeville, L. Gagnon, *et al.* (2014). „Large arteriolar component of oxygen delivery implies a safe margin of oxygen supply to cerebral tissue“. In: *Nature Communications* 5.

Sambamoorthy G. and K. Raman (2018). „Understanding the evolution of functional redundancy in metabolic networks“. In: *Bioinformatics* 34.17, pp. i981–i987.

San Martin A., S. Ceballo, I. Ruminot, *et al.* (2013). „A genetically encoded FRET lactate sensor and its use to detect the Warburg effect in single cancer cells“. In: *PLoS One* 8.2, e57712.

Santello M., N. Toni, and A. Volterra (2019). „Astrocyte function from information processing to cognition and cognitive impairment“. In: *Nature Neuroscience 2019* 22.2, p. 1.

Santos G., A. Barateiro, C. M. Gomes, D. Brites, and A. Fernandes (2018). „Impaired oligodendrogenesis and myelination by elevated S100B levels during neurodevelopment“. In: *Neuropharmacology* 129, pp. 69–83.

Sayre N. L., M. Sifuentes, D. Holstein, S.-Y. Cheng, X. Zhu, and J. D. Lechleiter (2017). „Stimulation of astrocyte fatty acid oxidation by thyroid hormone is protective against ischemic stroke-induced damage.“ In: *Journal of cerebral blood flow and metabolism : official journal of the International Society of Cerebral Blood Flow and Metabolism* 37.2, pp. 514–527.

Schell M. J., M. E. Molliver, and S. H. Snyder (1995). „D-serine, an endogenous synaptic modulator: localization to astrocytes and glutamate-stimulated release.“ In: *Proceedings of the National Academy of Sciences* 92.9, pp. 3948–3952.

Schleich C. L. (1894). „Schmerzlose Operationen. Oertliche Betäubung mit indiffrenten Flüssigkeiten“. In: *Julius Springer*.

Schönfeld P. and G. Reiser (2017). „Brain energy metabolism spurns fatty acids as fuel due to their inherent mitotoxicity and potential capacity to unleash neurodegeneration“. In: *Neurochemistry International* 109, pp. 68–77.

Schousboe A., L. K. Bak, and H. S. Waagepetersen (2013). „Astrocytic control of biosynthesis and turnover of the neurotransmitters glutamate and GABA“. In: *Frontiers in Endocrinology* 4.AUG, pp. 1–11.

Seifert G., K. Huttmann, D. K. Binder, C. Hartmann, A. Wyczynski, C. Neusch, and C. Steinhauser (2009). „Analysis of Astroglial K+ Channel Expression in the Developing Hippocampus Reveals a Predominant Role of the Kir4.1 Subunit“. In: *Journal of Neuroscience* 29.23, pp. 7474–7488.

Seifert G., C. Henneberger, and C. Steinhäuser (2018). „Diversity of astrocyte potassium channels: An update“. In: *Brain Research Bulletin* 136, pp. 26–36.

Shaw K., L. Bell, K. Boyd, D. M. Grijseels, D. Clarke, O. Bonnar, H. S. Crombag, and C. N. Hall (2019). „Hippocampus has lower oxygenation and weaker control of brain blood flow than cortex, due to microvascular differences“. In: *bioRxiv*, p. 835728.

Shulman R. G., F. Hyder, and D. L. Rothman (2001). „Cerebral energetics and the glycogen shunt: neurochemical basis of functional imaging.“ In: *Proceedings of the National Academy of Sciences of the United States of America* 98.11, pp. 6417–6422.

Sickmann H. M., A. Schousboe, K. Fosgerau, and H. S. Waagepetersen (2005). „Compartmentation of lactate originating from glycogen and glucose in cultured astrocytes.“ In: *Neurochemical research* 30.10, pp. 1295–304.

Simpson I. A., A. Carruthers, and S. J. Vannucci (2007). „Supply and demand in cerebral energy metabolism: the role of nutrient transporters.“ In: *Journal of cerebral blood flow and metabolism : official journal of the Inter-

*national Society of Cerebral Blood Flow and Metabolism* 27.11, pp. 1766–91.

Söhl G. and K. Willecke (2004). „Gap junctions and the connexin protein family". In: *Cardiovascular Research* 62.2, pp. 228–232.

Sokoloff L. (1960). „The metabolism of the central nervous system in vivo". In: *Handbook of Physiology, section, I, Neurophysiology* 3, pp. 1843–1864.

Sorg O. and P. J. Magistretti (1991). „Characterization of the glycogenolysis elicited by vasoactive intestinal peptide, noradrenaline and adenosine in primary cultures of mouse cerebral cortical astrocytes". In: *Brain Research* 563.1-2, pp. 227–233.

Sotelo-Hitschfeld T., M. I. Niemeyer, P. Machler, *et al.* (2015). „Channel-Mediated Lactate Release by K+-Stimulated Astrocytes". In: *Journal of Neuroscience* 35.10, pp. 4168–4178.

Speijer D. (2011). „Oxygen radicals shaping evolution: why fatty acid catabolism leads to peroxisomes while neurons do without it: FADH/NADH flux ratios determining mitochondrial radical formation were crucial for the eukaryotic invention of peroxisomes and catabolic tissue". In: *BioEssays : news and reviews in molecular, cellular and developmental biology* 33.2, pp. 88–94.

Srinivasan R., T.-Y. Lu, H. Chai, J. Xu, B. S. Huang, P. Golshani, G. Coppola, and B. S. Khakh (2016). „New Transgenic Mouse Lines for Selectively Targeting Astrocytes and Studying Calcium Signals in Astrocyte Processes In Situ and In Vivo." In: *Neuron* 92.6, pp. 1181–1195.

Stevens B., N. J. Allen, L. E. Vazquez, *et al.* (2007). „The Classical Complement Cascade Mediates CNS Synapse Elimination". In: *Cell* 131.6, pp. 1164–1178.

Stewart P. and M. Wiley (1981). „Developing nervous tissue induces formation of blood-brain barrier characteristics in invading endothelial cells: A study using quail-chick transplantation chimeras". In: *Developmental Biology* 84.1, pp. 183–192.

Stobart J. L. and C. M. Anderson (2013). „Multifunctional role of astrocytes as gatekeepers of neuronal energy supply." In: *Frontiers in cellular neuroscience* 7, p. 38.

Stogsdill J. A., J. Ramirez, D. Liu, Y. H. Kim, K. T. Baldwin, E. Enustun, T. Ejikeme, R.-R. Ji, and C. Eroglu (2017). „Astrocytic neuroligins control astrocyte morphogenesis and synaptogenesis". In: *Nature* 551.7679, pp. 192–197.

Subbarao K. V. and L. Hertz (1991). „Stimulation of energy metabolism by ?-adrenergic agonists in primary cultures of astrocytes". In: *Journal of Neuroscience Research* 28.3, pp. 399–405.

Sun D. and T. C. Jakobs (2012). „Structural Remodeling of Astrocytes in the Injured CNS". In: *The Neuroscientist* 18.6, pp. 567–588.

Sun X. W., X. A. Cornwell, J. Li, *et al.* (2017). „SOX9 Is an Astrocyte-Specific Nuclear Marker in the Adult Brain Outside the Neurogenic Regions". In: *The Journal of Neuroscience* 37.17, pp. 4493–4507.

Suzuki A., S. A. Stern, O. Bozdagi, G. W. Huntley, R. H. Walker, P. J. Magistretti, C. M. Alberini, H. Ruth, P. J. Magistretti, and C. M. Alberini (2011). „Astrocyte-neuron lactate transport is required for long-term memory formation." In: *Cell* 144.5, pp. 810–823.

Swanson R. A., M. M. Morton, S. M. Sagar, and F. R. Sharp (1992). „Sensory stimulation induces local cerebral glycogenolysis: demonstration by autoradiography." In: *Neuroscience* 51.2, pp. 451–61.

Tadi M., I. Allaman, S. Lengacher, G. Grenningloh, and P. J. Magistretti (2015). „Learning-Induced Gene Expression in the Hippocampus Reveals a Role of Neuron - Astrocyte Metabolic Coupling in Long Term Memory." In: *PloS one* 10.10. Ed. by Coles J. A., e0141568.

Tansey F. A., M. Farooq, and W. Cammer (1991). „Glutamine Synthetase in Oligodendrocytes and Astrocytes: New Biochemical and Immunocytochemical Evidence". In: *Journal of Neurochemistry* 56.1, pp. 266–272.

Tantama M., J. R. Martínez-François, R. Mongeon, and G. Yellen (2013). „Imaging energy status in live cells with a fluorescent biosensor of the intracellular ATP-to-ADP ratio.“ en. In: *Nature communications* 4.May, p. 2550.

Tanti A., P.-E. Lutz, J. Kim, *et al.* (2019). „Evidence of decreased gap junction coupling between astrocytes and oligodendrocytes in the anterior cingulate cortex of depressed suicides.“ In: *Neuropsychopharmacology* 44.12, pp. 2099–2111.

Theis M. and C. Giaume (2012). „Connexin-based intercellular communication and astrocyte heterogeneity“. In: *Brain Research* 1487, pp. 88–98.

Theodosis D. T., D. A. Poulain, and S. H. R. Oliet (2008). „Activity-Dependent Structural and Functional Plasticity of Astrocyte-Neuron Interactions“. In: *Physiological Reviews* 88.3, pp. 983–1008.

Toloe J., R. Mollajew, S. Kügler, and S. Mironov (2014). „Metabolic differences in hippocampal ‘Rett’ neurons revealed by ATP imaging“. In: *Molecular and Cellular Neuroscience* 59, pp. 47–56.

Trevisiol A., A. S. Saab, U. Winkler, G. Marx, H. Imamura, W. Möbius, K. Kusch, K. A. Nave, and J. Hirrlinger (2017). „Monitoring ATP dynamics in electrically active white matter tracts“. In: *eLife* 6, pp. 1–17.

Verkhratsky A. and M. Nedergaard (2018). „Physiology of Astroglia“. In: *Physiological reviews*, pp. 239–389.

Virchow R. (1858). *Die Cellularpathologie in ihrer Begründung auf physiologische und pathologische Gewebelehre. Zwanzig Vorlesungen gehalten während der Monate Februar, März und April 1959 im pathologischen Institut zu Berlin.* Berling.

Vohra R., B. I. Aldana, G. Bulli, D. M. Skytt, H. Waagepetersen, L. H. Bergersen, and M. Kolko (2019). „Lactate-Mediated Protection of Retinal Ganglion Cells“. In: *Journal of Molecular Biology* 431.9, pp. 1878–1888.

Volkenhoff A., A. Weiler, M. Letzel, M. Stehling, C. Klämbt, and S. Schirmeier (2015). „Glial Glycolysis Is Essential for Neuronal Survival in Drosophila“. In: *Cell Metabolism* 22.3, pp. 437–447.

Waagepetersen H. S., S. Døring, and A. Schousboe (2008). „Metabolism of [1,6-13C]Glucose and [U-13C]Glutamine and Depolarization Induced GABA Release in Superfused Mouse Cerebral Cortical Mini-slices“. In: *Neurochemical Research* 33.8, pp. 1610–1617.

Wagner A. (2005). „Robustness, evolvability, and neutrality“. In: *FEBS Letters* 579.8, pp. 1772–1778.

Wallraff A., R. Köhling, U. Heinemann, M. Theis, K. Willecke, and C. Steinhäuser (2006). „The impact of astrocytic gap junctional coupling on potassium buffering in the hippocampus.“ In: *The Journal of neuroscience : the official journal of the Society for Neuroscience* 26.20, pp. 5438–47.

Wasseff S. K. and S. S. Scherer (2011). „Cx32 and Cx47 mediate oligodendrocyte:astrocyte and oligodendrocyte:oligodendrocyte gap junction coupling“. In: *Neurobiology of Disease* 42.3, pp. 506–513.

Wiesinger H., B. Hamprecht, and R. Dringen (1997). „Metabolic pathways for glucose in astrocytes.“ In: *Glia* 21.1, pp. 22–34.

Wilhelmsson U., E. A. Bushong, D. L. Price, B. L. Smarr, V. Phung, M. Terada, M. H. Ellisman, and M. Pekny (2006). „Redefining the concept of reactive astrocytes as cells that remain within their unique domains upon reaction to injury“. In: *Proceedings of the National Academy of Sciences of the United States of America* 103.46, pp. 17513–17518.

Witcher M. R., Y. D. Park, M. R. Lee, S. Sharma, K. M. Harris, and S. A. Kirov (2010). „Three-dimensional relationships between perisynaptic astroglia and human hippocampal synapses.“ In: *Glia* 58.5, pp. 572–87.

Wolff J. R., K. Stuke, M. Missler, H. Tytko, P. Schwarz, A. Rohlmann, and T. I. Chao

(1998). „Autocellular coupling by gap junctions in cultured astrocytes: a new view on cellular autoregulation during process formation“. In: *Glia* 24.1, pp. 121–140.

Woolsey T. A., C. M. Rovainen, S. B. Cox, M. H. Henegar, G. E. Liang, D. Liu, Y. E. Moskalenko, J. Sui, and L. Wei (1996). „Neuronal units linked to microvascular modules in cerebral cortex: response elements for imaging the brain.“ In: *Cerebral cortex (New York, N.Y. : 1991)* 6.5, pp. 647–60.

Wyss M. T., R. Jolivet, A. Buck, P. J. Magistretti, and B. Weber (2011). „In vivo evidence for lactate as a neuronal energy source.“ In: *The Journal of neuroscience* 31.20, pp. 7477–7485.

Xin W., Y. A. Mironova, H. Shen, R. A. Marino, A. Waisman, W. H. Lamers, D. E. Bergles, and A. Bonci (2019). „Oligodendrocytes Support Neuronal Glutamatergic Transmission via Expression of Glutamine Synthetase“. In: *Cell Reports* 27.8, 2262–2271.e5.

Yoon B.-E. and C. J. Lee (2014). „GABA as a rising gliotransmitter“. In: *Frontiers in Neural Circuits* 8.December, p. 141.

Yu X., A. M. W. Taylor, J. Nagai, P. Golshani, C. J. Evans, G. Coppola, and B. S. Khakh (2018). „Reducing Astrocyte Calcium Signaling In Vivo Alters Striatal Microcircuits and Causes Repetitive Behavior.“ In: *Neuron* 99.6, 1170–1187.e9.

Zerbi V., A. Floriou-Servou, M. Markicevic, *et al.* (2019). „Rapid Reconfiguration of the Functional Connectome after Chemogenetic Locus Coeruleus Activation“. In: *Neuron* 103.4, 702–718.e5.

Zuend M., A. S. Saab, M. T. Wyss, *et al.* (2020). „Arousal-induced cortical activity triggers lactate release from astrocytes“. In: *Nature Metabolism* 2.2, pp. 179–191.

# Curriculum Vitae

# B

# LADINA HÖSLI

PhD Candidate Neurobiology

Grebelackerstrasse 12
8057 Zürich
ladihoesli@bluewin.ch
+41 79 821 16 77
*18.06.1989, Samedan GR
/ ladina-hoesli

## IT Skills

- MS Office
- Adobe Illustrator
- Adobe InDesign
- Mendeley, EndNote
- R
- LaTeX

## Languages

- Romansh
- German
- English
- Italian
- French

## Interests

- Sports
- Travelling
- Sustainability
- Others

## References

are available upon request

## Education

since Oct 2014 • **PhD Candidate** University of Zurich
at the Institute of Pharmacology and Toxicology
PhD Thesis: *Investigating the Involvement of Astrocytic Functions in Brain Energy Homeostasis and Cognitive Behaviors*

2012 - Mar 2014 • **Master of Science in Neurobiology** University of Zurich
Master Thesis: *Characterization of GRP expressing neurons in the dorsal horn of the spinal cord*
(Grade: 6.0)

2009 - 2012 • **Bachelor of Science in Biologie** University of Zurich

2002 - 2008 • **Gymnasium** Academia Engiadina, Samedan
Swiss matura with focus biology/chemistry

## Work Experience

Apr 2014 - Jun 2014 • **Research Assistant** University of Zurich
at the Institute of Pharmacology and Toxicology
project design, establishment and conduct of new methods and experiments, literature research

Jul 2008 - Jan 2009 • **Nursing Internship** Cantonal Hospital Winterthur
orthopedic department
help in nursing, morning toilet, prepare entries and exits of patients, run errands, night shifts

## Part-Time

since 2019 • **External Expert** Cantonal School Zurich Nord
at oral and written school leaving examinations (Matura) in biology
review of corrected exams, presence at oral exams, review of grades, discussions with teachers

2009-2014 • **Service Staff** Zurich, St.Moritz, Zernez
in different restaurants and at caterings; on evenings, weekends and during holidays

## Voluntary

since 2020 • **step into action** Local Team Luzern
outreach to schools and teachers, customer service schools and teachers, organisation of sponsors for snacks/drinks at the event and for the content of pupil‘s ActionKit, organisation of the catering at the event, decoration of the rooms, arrange flow of the parcours

2018 - 2020 • **Students Across Borders** Zurich
1:1 tutoring, German for refugees
weekly meetings to practice German conversation, help with job and flat applications

# APPENDIX: SCIENTIFIC ACHIEVEMENTS

## Methodological Skills

| | |
|---|---|
| Histology | heart ventricle perfusions, sliding microtome slices, cryostat slices, free-floating and mounted sections for stainings, H&E stains, Nissl stains, fluorescent immunohistology, DAB, confocal microscopy (Zeiss), light and fluorescent microscopy, Apotome (Zeiss), stereology |
| Behavior | Barnes maze, novel object recognition test, sensorimotor coordination scoring, von Frey mechanical stimulation, Hargreaves thermal stimulation, behvioral video analysis, rotarod |
| Surgery | head-post fixation, craniotomy, chronic window implantation, prism implantation, cortical virus injections, tail vein catheter, intrathecal injections, intradermal injections |
| other | two-photon microscopy, PCR, genotyping, connectomics |

## Publications

2020

- Hösli, L., Binini, N., Thieren, L., Looser, Z. J., Ferrari, K. D., Zuend, M., Berry, S., Holub M., Möbius, W., Ruhwedel, T., Cohen-Salmon, M., Nave, K.-A., Giaume, C., Weber, B., Saab, A. S. (2020). Decoupling astrocytes in adult mice impairs synaptic plasticity and spatial learning. **eLife**, submitted.
- Zuend, M., Saab, A. S., Wyss, M. T., Ferrari, K. D., Hösli, L., Looser, Z. J., Sobart, J. L., Duran, J., Guinovart, J. J., Barros, L. F., and Weber, B. (2020). Arousal-induced cortical activity triggers lactate release from astrocytes. **Nature Metabolism**, 2(2):179-191.

2019

- Baeza-Lehnert, F., Saab, A. S., Gutiérrez, R., Larenas, V., Díaz, E., Horn, M., Vargas, M., Hösli, L., Stobart, J., Hirrlinger, J., Weber, B., & Barros, L. F. (2019). Non-Canonical Control of Neuronal Energy Status by the Na+ Pump. **Cell metabolism**, 29(3), 668–680.e4.
- Albisetti, G. W., Pagani, M., Platonova, E., Hösli, L., Johannssen, H. C., Fritschy, J. M., Wildner, H., & Zeilhofer, H. U. (2019). Dorsal Horn Gastrin-Releasing Peptide Expressing Neurons Transmit Spinal Itch But Not Pain Signals. **The Journal of neuroscience : the official journal of the Society for Neuroscience**, 39(12), 2238–2250.

2015

- Foster, E., Wildner, H., Tudeau, L., Haueter, S., Ralvenius, W. T., Jegen, M., Johannssen, H., Hösli, L., Haenraets, K., Ghanem, A., Conzelmann, K. K., Bösl, M., & Zeilhofer, H. U. (2015). Targeted ablation, silencing, and activation establish glycinergic dorsal horn neurons as key components of a spinal gate for pain and itch. **Neuron**, 85(6), 1289–1304.

## International Poster Presentations

2019

- **XIV European Meeting on Glial Cells in Health and Disease, Porto**

  Hösli, L., Zuend, M., Berry, S., Looser, Z., Cohen-Salmon, M., Giaume, C., Weber, B., Saab, A., The importance of the gap junction-coupled astroglial network for neuronal function and energy metabolism.

2017

- **XIII European Meeting on Glial Cells in Health and Disease, Edinburgh**

  Hösli, L., Looser, Z., Stobart, M., Giaume, C., Weber, B., Saab, A., The impact of astrocytic gap junction coupling on neuronal function and energy metabolism

2016

- **SfN, San Diego**

  Hösli, L., Saab, A. S., Zuend, M., Looser, Z., Stobart, M., Mächler, P., Wyss, M., Duran, J., Guinovart, J., Hirrlinger, J., Weber, B., Studying neuronal ATP dynamics in vivo

## Travel Grants

| | |
|---|---|
| 2019 | **Excite, ETHZ, Zurich, Switzerland** |
| 2016 | **Neuroscience Center Zurich, Zurich, Switzerland** |

# Colophon

This thesis was typeset with $\LaTeX\,2_\varepsilon$. It uses the *Clean Thesis* style developed by Ricardo Langner and adapted by Ladina Hösli. The design of the *Clean Thesis* style is inspired by user guide documents from Apple Inc.

Download the *Clean Thesis* style at `http://cleanthesis.der-ric.de/`.